Universität Rostock



Traditio et Innovatio

System Design and Performance Analysis of a Submerged Towed Docking System for Automated Launch and Recovery of Autonomous Underwater Vehicles

Doctoral Thesis

for

the academic degree of

Doktor-Ingenieur (Dr.-Ing.)

[German: Doctor of Engineering]

submitted to the Board of the Faculty of

Mechanical Engineering and Marine Technologies

at the University of Rostock

submitted by

Dirk Hinrich Hops

https://doi.org/10.18453/rosdok_id00005796

Supervisor:

Prof. Dr.-Ing. Florian Sprenger

Faculty of Mechanical Engineering and Marine Technologies

University of Rostock

Co-supervisor:

Prof. Vahid Hassani

Department of Mechanical, Electrical and Chemical Engineering

OsloMet – Oslo Metropolitan University

Doctoral committee:

Prof. Dr. Berit Zeller-Plumhoff (Chair of the committee)

Prof. Dr.-Ing. Florian Sprenger (Reviewer)

Prof. Vahid Hassani (Reviewer)

Prof. Dr.-Ing. Sven Grundmann

Prof. Dr.-Ing. Sascha Kosleck

Date of submission: 26.02.2026

Date of defence: 27.04.2026

Abstract

Autonomous Underwater Vehicles (AUVs) are increasingly used for scientific, commercial and defence applications, but their launch and recovery (L&R) from mobile host platforms remains a major bottleneck. In particular, safely establishing the initial physical connection between a free-moving AUV and a dynamically excited host vessel in sea states is challenging. Current Launch and Recovery Systems (LARS) are often highly specialised, manually assisted and limited to moderate environmental conditions. This highlights the need for an automated, more universally applicable and environmentally robust LARS concept, together with a systematic procedure to analyse its performance and operational limits.
The dissertation addresses this gap by developing and assessing a submerged towed docking device, referred to as the Launch and Recovery Device (LARD), intended to establish the initial physical connection between an AUV and a host platform. The primary objective is to design a system that fulfils defined functional and operational requirements for automation, universal applicability and resilience to adverse sea states. Robustness is achieved primarily through configuring the LARD as a passive stabilising element to reduce relative motion and misalignment during docking, rather than relying on increased algorithmic complexity in AUV control and navigation. A further objective is to identify and demonstrate a suitable and transferable evaluation framework for analysing system performance and estimating the probability of successful operation under varying environmental and operational boundary conditions.

The work combines a structured technology review and requirements analysis with concept development and detailed mechanical design of the LARD. Hydrodynamic coefficients of the device, such as drag, added mass and damping are determined using RANS-based computational fluid dynamics (CFD) and validated through towing tank experiments. Based on the hydrodynamic characterisation of the LARD, the coupled system consisting of the host platform, towing cable and LARD is analysed using multibody dynamics simulations. These simulations provide the basis for an extensive parametric study of sea state, wave direction, towing cable length, vessel length, cable attachment point, towing velocity and the use of floats and sinkers.
The results show that a proficient arrangement of the LARS can substantially reduce wave-induced relative motions of the LARD and thereby improve the robustness of the initial contact process. The simulations deliver detailed information on the motion characteristics of the system under a wide range of environmental and operational parameters, from which parameter regimes with robust and repeatable docking behaviour can be derived.

Overall, the study demonstrates that the developed LARD concept meets the key requirements of high automation, modular and universal applicability to different AUV types and significant resilience to disruptive environmental conditions, thereby contributing to an extended operational weather window and enhancing AUV operations. At the same time, the work provides a coherent contribution to the design, assessment and future optimisation of automated LARS solutions for AUVs and offers a blueprint for addressing comparable challenges in offshore operations.

Keywords: Launch and Recovery System (LARS), Launch and Recovery (L&R);
Autonomous Underwater Vehicle (AUV), Unmanned Underwater Vehicle (UUV), Marine Robots, Hydrodynamic, Ocean Engineering

Acknowledgement

I would like to take this opportunity to express my sincere gratitude to everybody who supported and accompanied me throughout my doctoral journey. The project would not have been achievable without the mentorship, support and cooperation of several persons and organisations.

First and foremost, I would like to express my deepest appreciation to Professor Dr.-Ing. Florian Sprenger for his exceptional supervision. His critical feedback and profound technical insights have significantly shaped the direction and quality of this work. His thoughtful guidance provided not only the academic foundation but also the strategic framework necessary to navigate the complexities of this research. I am especially grateful for the balance he maintained between academic rigour and constructive mentorship throughout the project.

I also extend my sincere thanks to Prof. Vahid Hassani for serving as co-supervisor and for contributing to the academic framework of this dissertation. My appreciation also extends to the members of the doctoral committee at the Faculty of Mechanical Engineering and Marine Technologies at the University of Rostock, whose support and evaluation played a significant role in the completion of this thesis.

I would like to extend my gratitude to the Chair of Fluid Mechanics at the University of Rostock for their support in organising and conducting the towing tank experiments. I appreciate their professional assistance and contributions during the experimental phase of the research.

I am particularly grateful to TKMS ATLAS ELEKTRONIK GmbH for providing the foundational framework within which this research could be conducted. The opportunity to pursue a PhD while working as a Research and Development Engineer in the Portfolio, Technology and Innovation department has been invaluable. In this regard, I would like to express my special thanks to Dr.-Ing. Jeronimo Dzaack for his strategic support and continued encouragement of the doctoral project. I also extend my sincere appreciation to Dr.-Ing. Julien Hansen, whose efforts in establishing the working environment and ongoing availability for advice were key to ensuring a productive and efficient research process.

My gratitude also goes to my colleagues in the R&D department and across various specialist departments for their expert input, collaborative spirit and feedback. Their experience and readiness to engage with complex technical issues contributed many interdisciplinary perspectives to this research.

Furthermore, I wish to acknowledge the students I had the pleasure of supervising during this project. Their engagement, curiosity and commitment brought new perspectives to the work and enriched the research process. In particular, I would like to thank Elias, Hauke, Joel, Michael, Kira, Muhammed, Julius, Djamal, Christian, Abdelhadi, Sudharani and Nirav.

Finally, I extend my heartfelt thanks to my family for their unwavering support and belief in me throughout this journey. Their encouragement has been an enduring source of strength. A very special and heartfelt word of gratitude goes to Tomke Berndt for her steadfast support, patience and motivation throughout both the demanding and the rewarding moments of this journey. I look forward with optimism and joy to stand by and celebrate in each other's challenges, achievements and growth in the years ahead.

Contents

Abstract I
Acknowledgement II
Figures VI
Tables IX
Abbreviations X
Nomenclature XII
1. Introduction 1
1.1 Problem Statement 3
1.2 Dissertation Outline 6
2. Technology Review 7
2.1 Autonomous Underwater Vehicles 8
2.1.1 Scope of tasks 9
2.1.2 Vehicle Design 10
2.1.3 Navigation & Homing 14
2.2 Lifting methods 16
2.3 Initial physical connection 19
2.3.1 Manual methods - AUV surfaced 21
2.3.2 Automatic procedures - AUV surfaced 23
2.3.3 Automatic procedures - AUV submerged 28
3. Rationale and Objectives 37
3.1 Launch and Recovery System requirements 37
3.2 Assessment of current technology against set requirements 41
3.3 Development objective and parameters 43
4. Methodology Review 46
4.1 Product Development 46
4.2 Waves 48
4.2.1 Wave theory 49
4.2.2 Wave spectrum 53
4.3 Computational Fluid Dynamics 54
4.3.1 Reynolds averaged Navier-Stokes equation 55
4.3.2 Turbulence models 56
4.3.3 CFD Software - OpenFOAM 58
4.3.4 Numerical Derivation of Drag, Damping and Hydrodynamic Mass 58

4.4 Experimental Testing 61
4.4.1 Principles of scaling in hydrodynamic testing 61
4.4.2 Forced oscillation tests 62
4.4.3 Towing Tank at the University of Rostock 64
4.5 Multibody Dynamics 65
4.5.1 Reference systems 65
4.5.2 Vessel dynamics 66
4.5.3 Dynamics of the towing cable 70
4.5.4 Dynamics of the towed body 73
4.5.5 Solution procedure for equation of motion 75
4.5.6 Simulation software OrcaFlex 75
5. Submerged Towed Docking Device 76
5.1 Functional sequence 78
5.1.1 Launch procedure 78
5.1.2 Recovery procedure 79
5.2 Concept of optimal towing depth 81
5.3 Mechanical Design 85
5.3.1 Fastening the AUV 88
5.3.2 Strength of materials 93
5.3.3 Functional extension for charging & data transfer 94
6. Hydrodynamic Properties of the Submerged Towed Docking Device 99
6.1 Simulation Setup 99
6.1.1 Geometry 100
6.1.2 Domain 100
6.1.3 Meshing 102
6.1.4 Boundary conditions 103
6.1.5 Solver and numerical settings 105
6.2 Mesh Study 105
6.2.1 Linear domain 106
6.2.2 Rotational Domain 108
6.3 Numerical Results 109
6.3.1 Translational degrees of freedom 109
6.3.2 Rotational degrees of freedom 115
6.3.3 Velocity study 117

6.4 Experimental Validation 121
6.4.1 Experimental Setup 121
6.4.2 Drag coefficient 124
6.4.3 Damping & hydrodynamic mass coefficient 128
6.4.4 Comparison of Numerical and Experimental Results 134
7. Towing Behaviour Analysis of the Submerged Towed Docking Device 140
7.1 Simulation Setup 140
7.1.1 Vessel 140
7.1.2 Waves 142
7.1.3 Towing cable 144
7.1.4 Submerged Towed Docking Device 146
7.1.5 Automation of the simulation runs for the parametric analysis 146
7.1.6 Post-processing of simulation results 147
7.1.7 Limitations, assumptions and simplifications 150
7.2 Parametric analysis 151
7.2.1 Sea state 154
7.2.2 Wave heading 155
7.2.3 Towing cable length 156
7.2.4 Vessel length 158
7.2.5 Attachment point 161
7.2.6 Floats and sinkers 165
7.2.7 Towing velocity 166
8. Conclusions 168
8.1 Perspective 174
Bibliography 178
Statement on the use of AI-assisted writing tools 193

Figures

Figure 1-1: Categories of Underwater Vehicles 1
Figure 2-1: Sub-steps of launch and recovery 7
Figure 2-2: Overview of several UUV categories 8
Figure 2-3: AUV overview 12
Figure 2-4: Crane based AUV lifting 16
Figure 2-5: AUV lifting with an A-frame 17
Figure 2-6: AUV lifting using a stinger 18
Figure 2-7: Snap-in a boat hook 21
Figure 2-8: AUV catch with a tender 21
Figure 2-9: Capturing an AUV using a floating body 22
Figure 2-10: AUV caught by a painter line 23
Figure 2-11: Surfaced AUV snatch at a painter / capture line 23
Figure 2-12: Automatic AUV caught by a painter line (according to [89]) 24
Figure 2-13: Grabbing an AUV with robot arm 25
Figure 2-14: Capturing an AUV with a net 26
Figure 2-15: AUV docks into a surfaced cradle 27
Figure 2-16: Underwater docking into cradle 29
Figure 2-17: Establishing initial contact using a ROV 33
Figure 2-18: Automatic underwater rope grab 35
Figure 3-1: carrier platform categories 37
Figure 3-2: SeaCat AUV variants and Swap Heads 44
Figure 3-3: Degrees of freedom of an AUV 45
Figure 4-1: Process model of product development according to VDI guideline 2221 [138] . 47
Figure 4-2: Definition of wave characteristics (according to [140]) 49
Figure 4-3: Wave particle motion at different water depths [140] 51
Figure 4-4: Towing Tank at the Chair of Fluid Mechanics University of Rostock [162] 64
Figure 4-5: Axis orientation of the towing carriage [162] 64
Figure 4-6: Global and local coordinate system (according to [164]) 65
Figure 4-7: Discretisation of the towing cable (according to [143]) 70
Figure 4-8: Lumped-mass model [143] 71
Figure 5-1: Schematic illustration of L&R System 76
Figure 5-2: Schematic illustration of LARD 77
Figure 5-3: AUV launch procedure 79
Figure 5-4: AUV recovery procedure 80
Figure 5-5: Map of BSH measuring stations (according to [178]) 82
Figure 5-6: Amplitude of vertical particle velocity (w) as function of depth 82
Figure 5-7: Amplitude of vertical particle velocity (w) as function of depth 83
Figure 5-8: Amplitude of horizontal particle velocity (u) as function of depth 84
Figure 5-9: LARD - mechanical design 85
Figure 5-10: LARD – components 87
Figure 5-11: AUV on inclined plane 88
Figure 5-12: Minimum clamping force depending on the slope angle 89
Figure 5-13: Simplified clamping force scheme of AUV in LARD (longitudinal section) 89
Figure 5-14: Simplified clamping force scheme of AUV in LARD (cross section) 90
Figure 5-15: Spindle-driven clamping concept 92

Figure 5-16: Spindle-driven clamping concept (detail view) 92
Figure 5-17: Additional electromechanical cylinders clamping concept (detail view) 93
Figure 5-18: Rack-and-pinion clamping concept (detail view) 93
Figure 5-19: Functional extension for charging & data transfer mounted on the LARD 96
Figure 5-20: Functional extension for charging & data transfer (detailed view) 97
Figure 5-21: Scheme (I/II) of establishing the plug connection 97
Figure 5-22: Scheme (II/II) of establishing the plug connection 98
Figure 6-1: Linear domain No. 6 for surge flow – left: side view; right: rear view 101
Figure 6-2: Rotational domain No. 3 for yaw flow – left: rear view; right: side view 101
Figure 6-3: Patches of linear (left) and rotational (right) domain 102
Figure 6-4: linear mesh - left: isometric view; right: longitudinal section at y=0 103
Figure 6-5: rotational mesh (roll) - left: isometric view; right: longitudinal section at y=0 .. 103
Figure 6-6: Detailed view on scissor-like struts M1 (left), M2 (middle) and M3 (right) 106
Figure 6-7: Mesh study for surge flow of 1 m/s 107
Figure 6-8: Convergence comparison M2: constant surge velocity vs acceleration at t=5 s . 107
Figure 6-9: Mesh study for pitch flow of 0.025 rad/s 109
Figure 6-10: Forces and moments of surge flow 110
Figure 6-11 Force Fx of surge flow (detailed view) 110
Figure 6-12: LARD pressure distribution for surge flow of 1 m/s at t=4.9 s 111
Figure 6-13: Velocity profile at t=4.9 s for surge flow of 1 m/s – x-z-plane at y=0 111
Figure 6-14 Force Fx of surge flow (zoom) 111
Figure 6-15: Forces and moments of sway flow 112
Figure 6-16: Force Fy of sway flow (detailed view) 113
Figure 6-17: Velocity profile at t=4.9 s for sway flow of 1 m/s – x-y-plane at z=0 113
Figure 6-18: Forces and moments of heave flow 114
Figure 6-19: Force Fz of heave flow (detailed view) 114
Figure 6-20: Forces and moments of roll flow of 0.025 rad/s 115
Figure 6-21: Moment Mx of roll flow (zoom) 116
Figure 6-22: Moment My of pitch flow (detailed view) 116
Figure 6-23: Moment Mz of yaw flow (detailed view) 117
Figure 6-24: Heave velocity study - forces 118
Figure 6-25: Heave velocity study – unit damping forces 119
Figure 6-26: Pitch velocity study - moments 120
Figure 6-27: Pitch velocity study – unit damping moments 120
Figure 6-28: LARD model (1:3) - side view 121
Figure 6-29: Investigated motion patterns 122
Figure 6-30: Towing carriage arrangement (surge drag and sway forced oscillation tests) .. 123
Figure 6-31: Towing carriage arrangement (sway drag and surge forced oscillation tests) .. 123
Figure 6-32: Force history Fx for surge drag run at 3 m/s 126
Figure 6-33: Comparison of force histories Fx for surge drag runs at 3 m/s 127
Figure 6-34: Motion trajectory – sway forced oscillation test (f=1 Hz; A=0.1 m) 130
Figure 6-35: Motion trajectory – sway forced oscillation test (f=0.39 Hz; A=0.5 m) 130
Figure 6-36: Comparison of force histories Fy for sway forced oscillation tests 132
Figure 6-37: Sway forced oscillation tests with different amplitudes 133
Figure 6-38: Sway forced oscillation tests with different excitation frequencies 133
Figure 6-39: Model geometry comparison 135
Figure 6-40: Twisting of the model during sway drag tests 136

Figure 6-41: Surge drag (3 m/s) experiment run 137
Figure 6-42: Surge forced oscillation tests with different excitation frequencies 138
Figure 7-1: Components of the LARS (vessel, towing cable and LARD) 140
Figure 7-2: Hull geometry 141
Figure 7-3: Wave amplitude over time - example for sea state 4 (Hs=1,6 m) 143
Figure 7-4: Towing cable arrangements 145
Figure 7-5: Towing cable attachment points 146
Figure 7-6: Scheme docking area 148
Figure 7-7: Illustration of docking success (DS) metric 149
Figure 7-8: Wave surface elevation associated with the example from Figure 7-7 149
Figure 7-9: Feature importance scores of Dataset1 153
Figure 7-10: Feature importance scores of Dataset2 153
Figure 7-11: DS and RMSE vs Sea State 154
Figure 7-12: DS and RMSE vs Wave direction grouped by Sea State 155
Figure 7-13: DS vs Cable Length grouped by Sea State 156
Figure 7-14: RMSE vs Cable Length grouped by Sea State 157
Figure 7-15: DS vs Cable Length grouped by Sea State and Vessel Length 158
Figure 7-16: RMSE vs Cable Length grouped by Sea State and Vessel Length 158
Figure 7-17: DS vs Wave Direction grouped by Vessel Length and Vessel RAOs 159
Figure 7-18: RMSE vs Wave Direction grouped by Vessel Length and Vessel RAOs 160
Figure 7-19: DS and RMSE vs Cable Length grouped by Vessel Length and Vessel RAOs 160
Figure 7-20: Towing cable attachment points in respect to the wave direction 161
Figure 7-21: DS vs Wave Direction grouped by Sea State and Attachment Point 162
Figure 7-22: RMSE vs Wave Direction grouped by Sea State and Attachment Point 163
Figure 7-23: DS and RMSE vs Cable Length grouped by Vessel Length and Clump Type . 165
Figure 7-24: DS vs Wave Direction grouped by Sea State and Towing Velocity 166
Figure 7-25: RMSE vs Wave Direction grouped by Sea State and Towing Velocity 166

Tables

Table 2-1: AUV overview 11
Table 2-2: Lifting methods 16
Table 2-3: Overview of procedures for establishing initial physical contact 19
Table 3-1: Excerpt of the identified requirements 40
Table 4-1: Douglas Sea state scale [141] 49
Table 4-2: Wave characteristics according to linear wave theory [140] 51
Table 5-1: BSH measuring stations [178] 81
Table 5-2: Hs, Ts and λ for several BSH measuring stations (sea state 4) 83
Table 6-1: Domain setups for linear flow 101
Table 6-2: Domain setups for rotational flow 102
Table 6-3: Inlet velocity over time for surge flow 104
Table 6-4: Boundary conditions for linear domain - velocity (U) and pressure (p) 104
Table 6-5: Rotational velocity over time 104
Table 6-6: Boundary conditions for rotational domain - velocity (U) and pressure (p) 105
Table 6-7: Mesh properties - linear domain 106
Table 6-8: Mesh dependent results for surge flow 108
Table 6-9: Mesh properties - rotational domain 108
Table 6-10: Translational hydrodynamic coefficients 115
Table 6-11: Rotational hydrodynamic coefficients 117
Table 6-12: Heave velocity study - hydrodynamic coefficients 118
Table 6-13: Drag run results 127
Table 6-14: Experimental drag coefficients 128
Table 6-15: Forced oscillation test matrix - surge (ux = 1 m/s) 128
Table 6-16: Forced oscillation test matrix - sway (ux = 3 m/s) 129
Table 6-17: Experimental hydrodynamic damping and added mass - surge 134
Table 6-18: Experimental hydrodynamic damping and added mass - sway 134
Table 6-19: Drag coefficients – comparison of simulation vs experimental 135
Table 7-1: Vessel parameters 140
Table 7-2: Significant wave height and peak period 142
Table 7-3: Towing cable properties 144
Table 7-4: Datasets for parametric analysis 151

Abbreviations

Abbreviation	Meaning
AUV	**A**utonomous **U**nderwater **V**ehicle
CAD	**C**omputer **A**ided **D**esign
CFD	**C**omputational **F**luid **D**ynamics
COF	**C**entre **O**f **F**lotation
COG	**C**entre **O**f **G**ravity
DNS	**D**irect **N**umerical **S**imulation
DoF	**D**egree **o**f **F**reedom
DS	**D**ocking **S**uccess
FFT	**F**ast **F**ourier **T**ransform
GNC	**G**uidance, **N**avigation and **C**ontrol
GPS	**G**lobal **P**ositioning **S**ystem
ITTC	**I**nternational **T**owing **T**ank **C**onference
JONSWAP	**Jo**int **N**orth **S**ea **Wa**ve **P**roject
KC	**K**eulegan–**C**arpenter number
L&R	**L**aunch **&** **R**ecovery
LARD	**L**aunch **A**nd **R**ecovery **D**evice
LARS	**L**aunch **A**nd **R**ecovery **S**ystem
LCF	**L**ongitudinal **C**entre of **F**lotation
LES	**L**arge **E**ddy **S**imulation
ML	**M**achine **L**earning
OpenFOAM	**Open** **F**ield **O**peration **A**nd **M**anipulation
PBOF	**P**ressure **B**alanced **O**il **F**illed

PIMPLE	merged **PI**SO–SI**MPLE** algorithm
PISO	**P**ressure-**I**mplicit with **S**plitting of **O**perators
RANS	**R**eynolds-**A**veraged **N**avier-**S**tokes (equations)
RAO	**R**esponse **A**mplitude **O**perator
RMSE	**R**oot-**M**ean-**S**quare **E**rror
ROTV	**R**emotely **O**perated **T**owed **V**ehicle
ROV	**R**emotely **O**perated **V**ehicle
SIMPLE	**S**emi-**I**mplicit **M**ethod for **P**ressure-**L**inked **E**quations
SST	**S**hear **S**tress **T**ransport
SWATH	**S**mall **W**aterplane **A**rea **T**win **H**ull
TCF	**T**ransverse **C**entre of **F**lotation
USBL	**U**ltra **S**hort **B**ase**L**ine
USV	**U**nmanned **S**urface **V**ehicle
UUV	**U**nmanned **U**nderwater **V**ehicle

Nomenclature

Scalars are denoted by italic symbols (s), vectors by an over arrow ($\vec{v}$) and matrices by bold symbols ($\boldsymbol{M}$).

The indices i and j denote the corresponding degrees of freedom in or around which the respective variable is directed and can specify a component (scalar) of a vector or matrix.

A superscript t or r indicates whether the variable refers to a translational (t) or rotational (r) coefficient (not displayed in the following table).

Symbol	Unit	Meaning
a_{b_i}	$\frac{\mathrm{m}}{\mathrm{s}^2}$	Fluid acceleration relative to the motion of the towed body
a_{e_i}	$\frac{\mathrm{m}}{\mathrm{s}^2}$	Absolute fluid accelerations
a_{f_i}	$\frac{\mathrm{m}}{\mathrm{s}^2}$	Fluid acceleration relative to the Earth
a_{l_i}	$\frac{\mathrm{m}}{\mathrm{s}^2}$	Relative acceleration between the cable segment and the fluid
$\overrightarrow{a_s}$	$\frac{\mathrm{m}}{\mathrm{s}^2}$	Acceleration vector
A	m^2	Cross-sectional area
A_i	m^2	Cross-sectional area to i
$\boldsymbol{A_m}$	kg, kgm, kgm^2	Added mass matrix
A_{wet}	%	Ratio of wetted area
AM_i	m^5	Rotational drag surface moment
$\boldsymbol{B}$	$\frac{\mathrm{Ns}}{\mathrm{m}}, \frac{\mathrm{Ns}}{\mathrm{rad}},$ Nsm	Damping matrix
c	$\frac{\mathrm{m}}{\mathrm{s}}$	Propagation speed of a wave
c_c	-	Axial damping coefficient
c_t	$\frac{\mathrm{Nms}}{\mathrm{rad}}$	Torsional damping coefficient
C_{a_i}	-	Added mass coefficient

C_{B_i}	-	Damping coefficient
C_{D_i}	-	Drag coefficient
$C_{SST\text{-}k\text{-}\omega}$	-	Model coefficient for the SST k-ω model
C_L	-	Coefficient for lift strength
C_μ	-	Model coefficient for turbulent viscosity in the k-ε simulation
C_1, C_2, C_3	-	Model coefficients contained in the k-ε simulation
d	m	Depth
d_a	m^2	Projected diameter axial to the cable's axis
d_c	-	Bending damping coefficient
d_n	m^2	Projected diameter normal to the cable's axis
D	m	Diameter
D_n	-	Effective diffusivity for n (e.g.: $D_{k_{TKE}}$, $D_{\epsilon_{TKE}}$, D_{ω_t})
DS	%	Docking success
e	$\frac{J}{kg}$	Specific internal energy
E	$\frac{N}{m^2}$	Modulus of elasticity
f	$\frac{1}{s}$	Wave frequency
f_p	$\frac{1}{s}$	Peak frequency
f_0	$\frac{1}{s}$	Excitation frequency
$\vec{F}$	N	Vector of external forces acting on the point of interest
F_a	N	Force amplitude
F_{axial}	N	Axial force
$\overrightarrow{F_{A_b}}$	N	Added mass force (towed body)

$\overrightarrow{F_{A_c}}$	N	Added mass force (towing cable)
$\overrightarrow{F_B}$	N	Hydrostatic buoyancy force
F_{clamp}	N	Clamping force
$\overrightarrow{F_{D_b}}$	N	Drag force (towed body)
$\overrightarrow{F_{D_c}}$	N	Drag force (towing cable)
$\overrightarrow{F_{DA_b}}$	N	Hydrodynamic damping force (towed body)
F_{fr}	N	Friction force
$\overrightarrow{F_L}$	N	Lift force
F_{meas}	N	Measured force
F_N	N	Normal force
F_{para}	N	Component of gravitational force parallel to incline
$\overrightarrow{F_s}$	N	Transverse force
$\overrightarrow{F_W}$	N	Weight force
$\overrightarrow{F_{wave}}$	N	Wave-induced external forces
F_1, F_2	-	Blending function for the SST k-ω model
Fr	-	Froude number
g	$\frac{\mathrm{N}}{\mathrm{kg}}$	Gravitational acceleration
G	$\frac{\mathrm{m}^2}{\mathrm{s}^3}$	Turbulence production term
G_{xyz}	-	Global coordinate system
H	m	Height
H_m	m	Arithmetic mean wave height
H_s	m	Significant wave height

$H_{1/n}$	m	Mean height of the highest n-th portion of all waves
$\mathrm{I}_{\mathrm{hydr_i}}$	kgm^2	Hydrodynamic moments of inertia of the surrounding fluid
I_{ij}	kgm^2	Moment of inertia about the respective axes i and j
k	$\frac{\mathrm{rad}}{\mathrm{m}}$	Wavenumber
k_t	Nm^2	Torsional stiffness
k_{therm}	$\frac{\mathrm{W}}{\mathrm{mK}}$	Thermal conductivity
k_{TKE}	$\frac{\mathrm{J}}{\mathrm{kg}}$	Turbulent kinetic energy
k_{tt}	Nm	Coupling coefficient
$\overrightarrow{\mathrm{k_1}}$	$\frac{\mathrm{m}}{\mathrm{s}^2}, \frac{\mathrm{rad}}{\mathrm{s}^2}$	Acceleration vector
K_i	kgm^2	Hydrodynamic moments of inertia around the x-axis
$\boldsymbol{K_L}$	$\frac{\mathrm{N}}{\mathrm{m}}, \frac{\mathrm{Nm}}{\mathrm{rad}}, \mathrm{N}$	Stiffness matrix
K_{ij}	$\frac{\mathrm{N}}{\mathrm{m}}, \frac{\mathrm{Nm}}{\mathrm{rad}}, N$	Hydrodynamic stiffness matrix
K_1, K_2, K_3	-	Coefficients of the SST k-ω model
l	m	Segment length
l_1	m	Current length of the segment
L	m	Length
L_{xyz}	-	Local body fixed coordinate system
m	kg	Mass
m_a	kg	Added mass
m_b	kg	Mass of the towed body
M_i	kgm^2	Hydrodynamic moments of inertia around the y-axis
$\overrightarrow{M_{A_b}}$	Nm	Moment resulting from added mass

$\overrightarrow{M_{D_b}}$	Nm	Drag moment (towed body)
$\overrightarrow{M_{DA_b}}$	Nm	Damping moment (towed body)
$\boldsymbol{M_m}$	kg, kgm, kgm^2	Mass matrix
$\boldsymbol{M_s}$	kg, kgm, kgm^2	Mass and inertia matrix
$\overrightarrow{M_1}, \overrightarrow{M_2}$	Nm	Bending moments (towing cable)
n_3	m^2	Surface normal component in z-direction
N_i	kgm^2	Hydrodynamic moments of inertia around the z-axis
$\overrightarrow{p_G}$	m	Position vector in the global coordinate system
$\overrightarrow{p_L}$	m	Position vector in the local coordinate system
$\overrightarrow{p_s}$	m	Position vector
P	$\frac{m^2}{s^3}$	Production rate of turbulent kinetic energy
q_i	$\frac{W}{m^2}$	Heat flux
q_1, q_2, q_3	-	Correction terms accounting for additional hydrostatic effects
$\overrightarrow{r_k}$	m	Global position vector of a node
Re	-	Reynolds number
R_{RAO_i}	m	RAO amplitude (normalized ratio of response to excitation)
$\boldsymbol{R_{rot}}$	-	Rotation matrix
RMSE		Root-mean-square error
s_i	m	Coordinate along the towing cable
S	$\frac{1}{s}$	Strain rate
$S_{ed}(f)$	-	Spectral energy density

S_n	$\frac{m^2}{s^3}$	Source term for n (e.g.: $S_{k_{TKE}}$, S_{ω_t})
S_{wet}	m^2	Wetted surface area
t	s	Time
t_{RAO}	s	Time since the wave crest passed the RAO reference point
t_s	s	Simulation time
T	s	Period
T_m	s	Arithmetic mean wave period
T_p	s	Peak period
T_{Temp}	K	Temperature
$\overrightarrow{T_{tra}}$	m	Translation vector
u	$\frac{m}{s}$	Velocity in x-direction
u_i	$\frac{m}{s}$	Velocity component in the direction i
$\overrightarrow{u_L}$	-	Direction of lift
$\overrightarrow{u_z}$	-	Unit vector (vertically downward)
UDF_i	$\frac{N}{ms}$	Unit damping force
UDM_i	$\frac{Nm}{s}$	Unit damping moment
v	$\frac{m}{s}$	Velocity in y-direction
v_{b_i}	$\frac{m}{s}$	Velocity of the towed body relative to the fluid
v_{f_i}	$\frac{m}{s}$	Fluid velocity relative to the cable
v_{f_n}	$\frac{m}{s}$	Relative fluid velocity perpendicular to the cable axis
v_{f_t}	$\frac{m}{s}$	Relative fluid velocity tangential to the cable axis
$\overrightarrow{v_s}$	$\frac{m}{s}, \frac{rad}{s}$	Velocity vector

V_b	m^3	Volume of the fully submerged body
w	$\frac{m}{s}$	Velocity in z-direction
W	m	Width
x	m	Coordinate
x_{COG}	m	Longitudinal centre of gravity
x_i	m	Spatial coordinates
x_{vessel_i}	m, rad	Vessel displacement or rotation
X_i	N	Hydrodynamic force in the x-direction
y	m	Coordinate
y_a	m	Displacement amplitude
y_{COG}	m	Transverse centre of gravity
Y_i	N	Hydrodynamic force in the y-direction
z	m	Coordinate
z_{COG}	m	Vertical centre of gravity
Z_i	N	Hydrodynamic force in the z-direction
$\alpha_{k\text{-}\omega}$	-	Model coefficient for the k-ω model
β	rad	Inclination angle of the cable axis relative to the horizontal plane
$\beta_{k\text{-}\omega}$	-	Model coefficient for the k-ω model
$\gamma_{SST\text{-}k\text{-}\omega}$	-	Model coefficient for the SST k-ω model
$\gamma_{JONSWAP}$	-	Specific constant for JONSWAP wave spectrum
Δ_b	kg	Mass of the fluid displaced by the towed body
Δ_c	kg	Mass of the fluid displaced by the towing cable
δ_{ij}	-	Kronecker delta

ϵ_{ij}	-	Strain tensor
ε_{shift}	-	Phase shift relative to the imposed motion
ϵ_{TKE}	$\frac{m^2}{s^3}$	Dissipation rate of turbulent kinetic energy
ζ_a	m	Wave amplitude
η	m	Surface elevation of a sinusoidal wave travelling in the x-direction
μ	Pas	Dynamic viscosity
θ	-	Phase of the travelling wave
ϑ_t	$\frac{m^2}{s}$	Kinematic eddy viscosity
$\vec{\kappa}$	rad	Curvature
λ	m	Wavelength
λ^*	$\frac{N}{m^2}$	Lamé parameter
μ_s	-	Static friction coefficient
$\vec{\xi}$	m, rad	Motion amplitude
ρ	$\frac{kg}{m^3}$	Fluid density
ς	°	Angle of an inclined plane
$\sigma_{JONSWAP}$	-	Specific constant for JONSWAP wave spectrum
τ	rad	Twist angle
τ_{ij}	$\frac{N}{mm^2}$	Stress tensor
ϕ	-	Flow parameter
ϕ'	-	Fluctuation of flow parameter ϕ
$\bar{\phi}$	-	Mean value of flow parameter ϕ
ϕ_{RAO_i}	-	RAO phase

$\chi_{JONSWAP}$	-	Specific constant for JONSWAP wave spectrum
ω	$\frac{1}{s}$	Angular frequency
ω_{b_i}	$\frac{rad}{s}$	Angular velocity of the towed body relative to the Earth
$\dot{\omega}_{b_i}$	$\frac{rad}{s^2}$	Angular accelerations of the towed body relative to the Earth
ω_{TKE}	$\frac{1}{s}$	Specific dissipation rate of turbulence
$\frac{\omega^2 d}{g}$	-	Non-dimensional frequency parameter
∇	-	Nabla operator

1. Introduction

The increasing importance of automation in several areas of everyday life has driven significant advances in research and development, particularly in industries where technology might exceed human capabilities. This trend is especially obvious in the maritime domain, where human activities on the oceans have markedly intensified. Offshore infrastructures for energy generation, raw material extraction, communication and research are growing and expanding towards deeper waters. Since these activities are associated with high levels of economic and technical risks, the marine industry has benefited from the advancement of automation technologies and in particular of the use of Unmanned Underwater Vehicles (UUV). [1]
The development of UUVs signifies a major shift in underwater operations. These vehicles have significantly advanced underwater technology by revolutionising the investigation of the seabed and the examination of underwater structures. The continuous improvement of the vehicles and their equipment, such as sensor systems, opens up new exploration perspectives. Furthermore, the absence of a crew on board the submersible has significantly enhanced operational efficiency and cost-effectiveness. [2]
These vehicles have expanded the range of maritime research and surveillance, including scientific, commercial and military purposes. Their applications encompass a diverse range of vital operations, including mapping the seabed, exploring limited resources, detecting and recovering unexploded ordnance and monitoring changes in undersea infrastructure, such as pipelines. These applications are in line with the overall goal of utilising technology progress for sustainable maritime exploration and resource utilisation in order to ensure prosperity. Underwater vehicles can be categorised into manned and unmanned types. Manned underwater vehicles are commonly known as submarines. Unmanned Underwater Vehicles are further categorised based on their control mechanisms. Figure 1-1 shows the different categorisation of underwater vehicles. [1, 2]

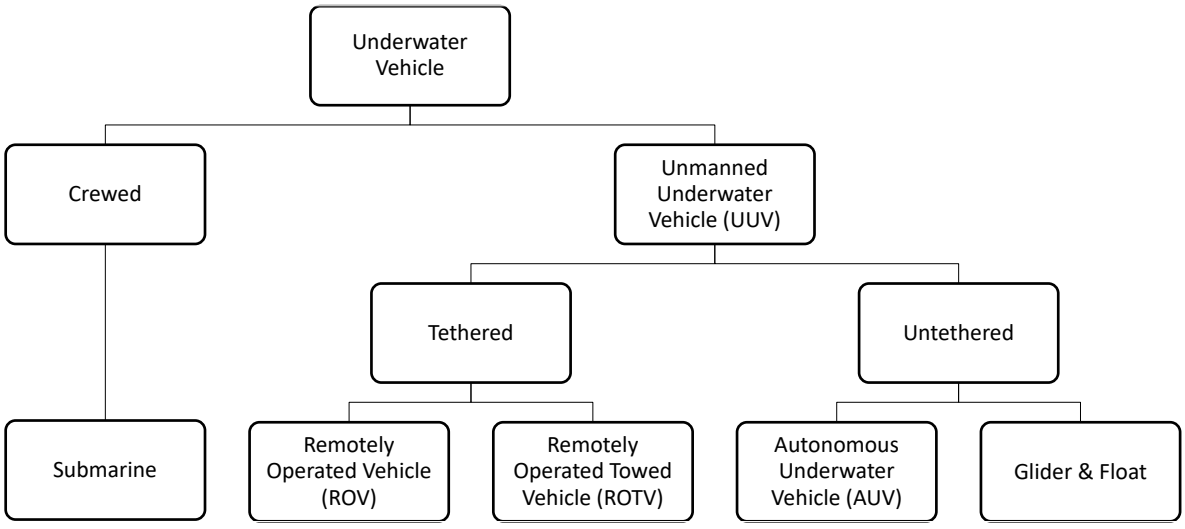


Figure 1-1: Categories of Underwater Vehicles

Tethered UUVs, such as Remotely Operated Vehicles (ROVs) and Remotely Operated Towed Vehicles (ROTVs), are connected to a carrier platform by a cable and operated by a human operator. The tether allows real-time transmission of data and energy, providing immediate results and negating the need for on-board energy storage. [2]

Untethered vehicles such as Autonomous Underwater Vehicles (AUVs), gliders and floats function without a permanent physical link. An AUV adheres to a predetermined or logic-driven trajectory, operating autonomously or in a highly automated manner, without the need for manual control. These autonomous systems have the ability to carry out intricate missions by following predetermined rules and programmes. Advanced AUVs incorporate complex algorithms for decision-making and obstacle avoidance, ensuring adaptability to the dynamic underwater environment. As a testament to their growing importance, AUVs continue to evolve with enhancements in endurance, depth capabilities and sensor technology, reflecting the ongoing innovation in marine technology. AUVs are especially advantageous in hard-to-reach areas where manned vehicles or tethered UUVs cannot operate. Nevertheless, the ability of these entities to operate and move is limited by the amount of energy they can store. [3, 4, 5]

AUVs are designed to carry out a wide range of tasks in scientific, commercial, military and environmental fields, demonstrating their flexibility and capacity to adjust to different situations. Performing specific tasks is commonly known as executing a mission.
In oceanographic research, AUVs excel in gathering data from otherwise inaccessible areas. In addition, AUVs are utilised to generate maps of the seafloor's topography, explore hydrothermal vents and analyse underwater geological processes, greatly advancing our understanding of geophysics. Furthermore, they gather samples at various depths, advancing research on marine biodiversity and ecological studies. [3, 4]
Commercially, AUVs are essential in the oil and gas sector for the purpose of conducting seabed mapping and monitoring underwater infrastructure, such as pipelines. Their role includes identifying possible dangers, assisting with maintenance and conducting ongoing surveillance of marine infrastructure. As seabed mining becomes more critical due to the global demand for resources, AUVs assist in identifying feasible mining sites and understanding geological and ecological processes. [6, 7]
In the military sector, AUVs are vital for mine countermeasures, which involve the detection and classification of underwater mines while prioritising the safety of divers. In addition, they participate in surveillance and reconnaissance activities, safeguarding harbours, clearing ports and collecting intelligence in strategically important marine areas. The covert operating capabilities of AUVs are essential for the surveillance of enemy operations and the protection of military installations. [8, 9, 10]
AUVs have a crucial role in search and rescue operations, especially in deep-water situations. They efficiently cover vast areas by employing sonar imaging to pinpoint the location of lost items or humans. In shipwreck and aeroplane crash investigations, AUVs provide insights into incidents and aid in retrieving black boxes and evidence. Underwater archaeology also benefits from AUVs, which locate and document shipwrecks and submerged settlements, preserving historical artefacts without disturbing sites. [4, 7]
From an educational standpoint, AUVs provide hands-on experience in the fields of maritime technology and robotics. Universities and research institutes employ AUVs to conduct experiments, evaluate technologies and create novel sensors and algorithms, therefore contributing to the progress of the underwater vehicle industry. [1, 7]

The various application scenarios for the use of AUVs and their versatile application possibilities are leading to increased use in various mission areas. Due to their limited velocity and range AUVs are frequently carried to the deployment area using carrier platforms like vessels, boats or other UUVs. The operational range of an AUV is contingent upon its battery capacity. In general, smaller and lighter vehicles tend to have shorter ranges. [7]

When an AUV is assigned a mission in a certain location, it has two possible methods of reaching its destination. The AUV has the capability to either navigate to the mission location itself or be carried by a host platform. Independent travel is only possible if the distance to the mission location is within the range of the AUV's battery capacity, allowing it to cover both the journey and the mission itself. This is often applicable to larger AUVs that are specifically developed for missions extending multiple days. However, smaller AUVs need to be transported to the mission site using a host platform.
Once the mission location is reached, the AUV must be launched from the host platform into the sea. After completing its mission, the AUV is recovered back onto the platform. The reasons for launch and recovery (L&R) are influenced by three main factors: transport, maintenance and the transfer of data and power. Transportation entails the process of relocating the AUV to and from the designated mission location. Maintenance can be performed on the host platform or, if necessary, the AUV can be transported to a workshop on land for more extensive repairs. Data and energy transfer involve the gathering of mission data from the AUV and the distribution of new data for future trips. Furthermore, it is necessary to recharge the batteries of the AUV in order to adequately prepare for the subsequent mission. [11]

Therefore, the L&R process is crucial to AUV operations to ensure the safe transfer of AUVs between the host platform and the underwater environment. This procedure is facilitated by Launch and Recovery Systems (LARS). These technical devices are specifically designed for deploying UUVs into the water and subsequently retrieving them. This process is fundamental to the operation of AUVs, marking the start and end of each mission. LARS therefore represent a basic requirement for the successful operation of an AUV that is not limited to operating at one location.

1.1 Problem Statement

The L&R process of AUVs has emerged as a critical bottleneck in the efficient and safe operation. While AUVs have significantly advanced in terms of autonomy, navigation and operational capabilities, the L&R phase remains fraught with risks, often overshadowing the vehicle's mission objectives.
A central concern in the L&R process is the lack of a continuous link between the AUV and the host platform. AUVs are intentionally designed without any permanent physical connections to the platforms they operate from. This autonomous nature introduces unique difficulties, particularly in adverse marine conditions, where establishing a physical connection is essential for the recovery process. Physical contact with the AUV can take many forms, such as attaching a recovery rope or securing the AUV in a device for recovery. This stage represents a shift from the autonomous operation of the AUV to controlled handling by the carrier platform.
These procedures often necessitate a close physical proximity between the AUV and the host platform for connection and lifting operations, introducing several risks. The potential for collision poses a significant danger, not just to the equipment, but also to the crew involved in the operation. This risk is particularly exacerbated in rough sea conditions where the vehicles are exposed to nearly unpredictable motions.
The physical difficulties can be explained using the simple case of two entities with disparate masses and volumes at sea. The AUV, which has a considerably smaller mass and volume compared to the carrier platform, has distinct responses to the identical sea condition, leading to varied motion patterns. In reality, this problem is far more complex, involving additional

disturbing factors such as the dynamic effects caused by the motion of the carrier platform. This motion creates a suction that can pull the AUV beneath the vessel. Likewise, the propeller jet presents a potential danger, as it might pull the AUV towards it, resulting in substantial harm to both the AUV and the propeller.
Aligning the AUV close to the carrier platform for the L&R process becomes easier with better manoeuvrability of both the AUV and the carrier platform. Carrier platforms equipped with dynamic positioning systems can maintain their position, which is advantageous. The manoeuvrability of AUVs depends on the quantity and configuration of thrusters and control elements like rudders or fins. AUVs equipped with hover capabilities are able to maintain their precise position, making the initial physical contact simpler and more straightforward. The greater challenge arises with carrier platforms and AUVs that cannot hover and instead rely on forward propulsion for efficient manoeuvring.
The efficiency of LARS is critical, especially in heavy seas, to reduce limitations regarding the maximum sea state and flow effects, thereby increasing economic and operational efficiency. When planning AUV operations, there is typically uncertainty regarding the sea conditions at the time of recovery, which may occur many hours after deployment. Unexpectedly deteriorating weather conditions can significantly impact the L&R process, leading to substantial costs such as extended platform rental periods without productive output. This uncertainty places significant constraints on the operational window of AUVs. Increasing the operating weather window is not only necessary for operations, but also has important economic implications.

This PhD thesis addresses the central concern in the L&R process of how the initial physical connection between the AUV and the host platform can be established. The focus is on the L&R process from mobile carrier platforms, such as vessels, boats or other underwater vehicles. The long-term deployment of AUVs in geographically limited areas such as wind farms or offshore oil and gas facilities and the associated challenges and simplifications are not taken into account.

The conditions and parameters guiding the development of a LARS are examined as part of a requirements analysis (outlined in chapter 3). In this context, three primary project objectives were identified. These findings are briefly summarised in the following to provide an initial overview. The LARS should incorporate an automated process to improve efficiency and reliability. It is essential that the proposed solution is universally applicable to a wide range of AUVs, ensuring wide interoperability. Furthermore, the system must possess resilience against environmental impacts, such as adverse sea conditions, to broaden the operational weather window and maintain performance as well as safety.
Automating the L&R procedure of AUVs is essential for improving safety and efficiency by eliminating the need for direct human involvement, hence making it suitable for deployment on unmanned platforms. The risks for the crew of a carrier platform related to the L&R process range from going overboard to special dangers linked to lifting operations, such as those posed by suspended loads [12]. Consequently, human intervention should be excluded, guaranteeing that the crew remains unexposed to any safety risks.
The L&R process is inherently the riskiest part of an AUV mission, as the vehicle is most susceptible to damage or loss during this phase. This is also seen in the insurance costs for AUVs. Important aspects that affect these expenses include the expertise, past performance, certifications and specialised training of the technical support and engineering personnel involved in L&R and mission planning. The expertise and past performance of vessel operators,

in conjunction with the attributes of the support vessel, have equal importance. By using automation in the process of L&R, the potential hazards associated with it are significantly reduced, resulting in improved dependability and safety of the mission. [13]

The wide range of carrier platforms and the diverse characteristics of AUVs have led to the development of a large number of LARS. These systems, often custom-designed, cater to the unique requirements posed by each AUV and its corresponding carrier platform. While many LARS utilise similar methodologies to address the challenges inherent in AUV L&R, their specific designs are usually tailored to a particular vehicle variant or type. This customisation is primarily driven by the distinctive features of the AUVs, such as size, weight, external shape, mechanical robustness of the hull and the load-bearing structure of the vehicle. Consequently, these specialised solutions are often limited in their applicability, being compatible with only certain vehicles or vehicle types. [7, 11, 12, 14]
Multiple investigations, such as those conducted by Liu et al. [15], Mischnick [11], Hanyok and Smith [12] as well as Chakrabarti [7], have highlighted a significant lack of standardisation in these systems. This lack of standardisation leads to inefficiencies and increased costs, as these systems are required for each unique combination of AUV and carrier platform.
Implementing a universally applicable LARS would streamline operations across different platforms and AUVs, reducing the need for multiple specialised systems. This would not only enhance the efficiency and flexibility of underwater missions but also lower overall costs by minimising the need for equipment. Furthermore, standardisation could lead to increased interoperability between different AUVs and carrier platforms, fostering greater collaboration and innovation within the industry.

A key objective in the development of the proposed LARS is to enable reliable L&R operations even under more demanding sea conditions. Current systems often require relatively calm weather to operate safely, which significantly limits their operational availability. To overcome this limitation, the LARS must be designed with enhanced resilience to dynamic environmental forces such as wave-induced motion and vessel motion. By ensuring functionality during higher sea states, the system can expand the operational weather window, allowing missions to proceed with fewer weather-related delays or cancellations. This not only increases the utility and responsiveness of the AUV deployment but also enhances the overall mission success rate, particularly in time-sensitive or remote operations.

In summary, improving the L&R process, particularly the initial contact phase, is vital for the efficient and safe operation of AUVs. The primary objective of this PhD project is therefore to develop a concept for safely establishing a physical connection between the AUV and the LARS. Rather than tackling L&R challenges by increasing algorithmic complexity on the vehicle side, this thesis aims to achieve robustness primarily through the overall system configuration. It therefore does not design or analyse a specific control or navigation system for the AUV. The main focus is on the system design and dynamic performance analysis of the LARS. A key aspect is to identify suitable methods and procedures for analysing the performance of the developed LARS in order to systematically assess the probability of successful operation under varying environmental and operational boundary conditions. By tuning the mechanical and hydrodynamic properties of this system, relative motion and misalignment during L&R are reduced. In this sense, complexity is shifted from active control towards mechanical design and passive dynamics, with docking performance assessed mainly via relative motion and geometric capture conditions. Within the scope of this thesis, this evaluation procedure is applied to the developed LARS concept in order to demonstrate its

practical suitability and to provide a transferable framework for addressing comparable challenges.

1.2 Dissertation Outline

In order to address the research problem outlined above, this dissertation is structured to lead from the general context of AUV L&R towards the detailed development, characterisation and assessment of a new concept for establishing the initial physical connection between an AUV and a LARS. Following this introduction, Chapter 2 presents a technology review that situates the work within the broader field of UUVs and their handling. It first introduces AUVs, their typical mission profiles, vehicle designs and navigation and homing strategies. This chapter then reviews existing lifting methods and approaches to establishing the initial physical connection between vehicle and host platform, distinguishing between manual and automatic procedures and between surfaced and submerged operations.
Building on this background, Chapter 3 formulates the rationale and objectives of the PhD project. The chapter derives functional and operational requirements for an AUV LARS from the challenges outlined in the problem statement and assesses current solutions against these requirements. On this basis, the development objective is formulated and the main design parameters are defined.

Chapter 4 reviews the methodological foundations applied throughout the dissertation. It outlines the adopted product development approach and introduces the wave theory and spectral descriptions required to model wave excitation. The numerical methods are then discussed in two parts. First, the computational fluid dynamics framework is introduced. Second, the multibody dynamics framework is presented. Finally, the principles of hydrodynamic model testing are summarised as the basis of the experimental study.
Chapter 5 describes the submerged towed docking device in detail and links the requirements to a concrete technical solution. The functional sequence of the L&R procedures is explained. Followed by a sea state analysis in the North and Baltic Sea in respect to the concept of an optimal towing depth. The mechanical design is presented with emphasis on the fastening of the AUV, relevant strength-of-materials considerations and a functional extension for charging and data transfer.

Chapter 6 investigates the hydrodynamic properties of the docking device. The chapter describes the CFD simulation setup, mesh study, followed by numerical results. These numerical coefficients are then validated experimentally through towing tank tests, in which drag, damping and hydrodynamic mass are determined and deviations between simulation and experiment are analysed.
These hydrodynamic coefficients are subsequently used in Chapter 7 to model and analyse the towing behaviour of the submerged towed docking device as part of the complete LARS consisting of the host platform, towing cable and the docking device. The parametric study examines the influence of sea state, wave heading, towing cable length, vessel length, attachment point, clump configuration and towing velocity on the system response and on the robustness of the concept, concluding with a discussion of the results.

Finally, Chapter 8 summarises the main findings and conclusions of the work and provides an outlook on potential further developments and research needs related to submerged towed docking systems for AUVs.

2. Technology Review

An AUV is a UUV that is self-propelled and contains its own sensors and power supply. An AUV may process sensor data instantly, allowing it to make judgements autonomously to execute manoeuvres or navigate around obstacles without human intervention. Vehicles perform autonomously to carry out predetermined tasks, adjusting to changing conditions using sensor information. [3, 16]

The first section of the chapter provides a more in-depth examination of AUVs. For this various types of UUVs are introduced and important characteristics such as the scope of tasks, the design and core competences of AUVs are highlighted. Based on this, the state of the art of LARS is presented. Therefore, the L&R process is divided into different sub-steps, shown in Figure 2-1. The AUV is first located on the carrier platform. The launch phase ensures the safe and efficient release of AUVs into the sea, allowing them to start carrying out their mission. This is accomplished through a single process step referred to as lifting operation. This process step involves transporting the AUV from its storage position on board the platform into the water. This step also includes the prior creation and subsequent release of a connection between the lifting tool and the AUV.

The recovery phase is essential for returning the AUVs after their mission, enabling recharging, data retrieval, maintenance work, transport and preparation for future missions. The recovery procedure involves an additional process step compared to the launch process. Prior to conducting the lifting operation, it is necessary to establish an initial physical contact with the AUV. This step is essential to facilitate the connection between the LARS and the AUV. Section 2.2 presents different ways for the lifting process based on this categorisation. Section 2.3 outlines several techniques for establishing initial physical contact.

It should be noted that individual methods are described using examples. Depending on the individual case, the implementation of a method may vary. Furthermore, it is important to note that the summary provided in this thesis only covers the physical aspects. These can be further elaborated and encompass several sub-processes. Additionally, there are other non-physical steps, such as communication for navigation and alignment, that should also be taken into account.

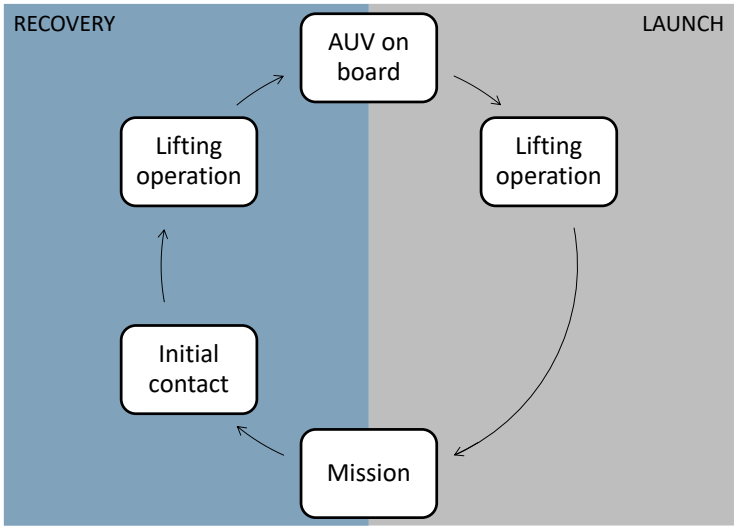


Figure 2-1: Sub-steps of launch and recovery

2.1 Autonomous Underwater Vehicles

Building on an initial overview of UUVs, this chapter will delve into the specific tasks and applications of AUVs. Furthermore, the design and structural characteristics of AUVs, such as size, weight and diving depth will be described.

Unmanned Underwater Vehicles are a diverse range of autonomous and remotely operated technology specifically developed for underwater jobs. They have the potential to greatly impact marine research and operations. The wide range of designs and purposes of these vehicles has brought about a significant transformation in oceanographic studies, military operations and offshore enterprises. [1, 4]

Figure 2-2 presents a comprehensive overview of several UUV categories, which include ROVs (Figure 2-2-1), AUVs (Figure 2-2-2&-3), gliders (Figure 2-2-4) and ROTVs (Figure 2-2-5&-6).

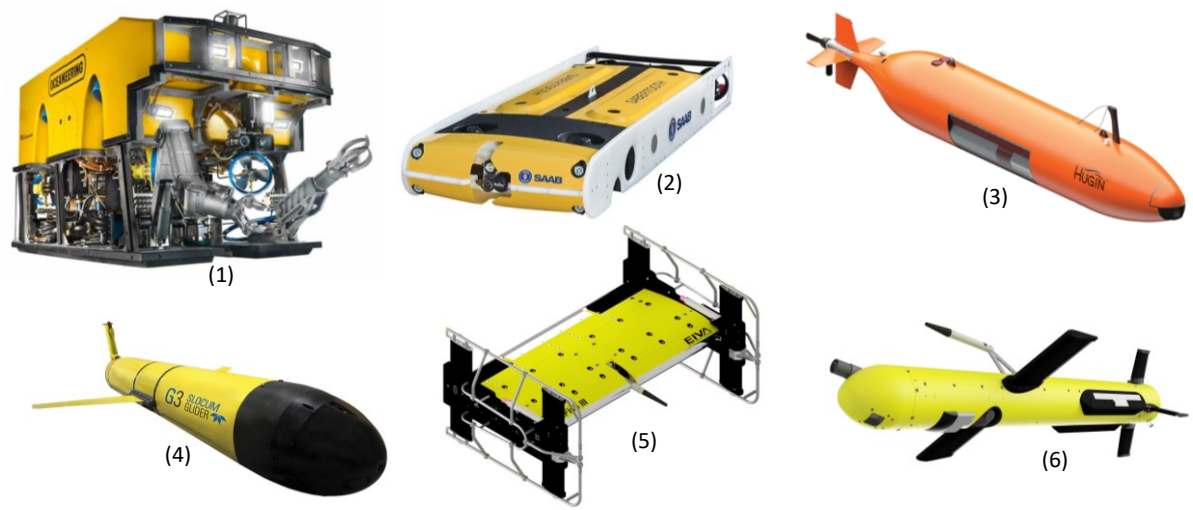


Figure 2-2: Overview of several UUV categories
(1) Oceaneering - Millennium Plus ROV [17]; **(2)**SAAB - Sabertooth AUV [18]; **(3)**Kongsberg - HUGIN AUV [19]; **(4)**Teledyne - Slocum glider [20]; **(5)**EIVA - ScanFish 3D steering ROTV [21]; **(6)**EIVA - ViperFish ROTV [22]
images are not to scale

Remotely Operated Vehicles are underwater robots that are connected by a tether. They are commonly used for tasks that need direct human direction, such as complex underwater construction, equipment installation or salvage operations. Their link facilitates both power supply and real-time data transmission, allowing for prolonged missions and intricate manipulation operations. Nevertheless, the ability to connect physically to a surface vessel or platform imposes constraints on their operational range and manoeuvrability. [3, 4, 16]

Autonomous Underwater Vehicles, in contrast, function autonomously without the need for a tether. AUVs, which are equipped with sophisticated navigation systems, sensors and occasionally manipulation capabilities, are utilised for various purposes. The robots adhere to predetermined tasks and inertial navigation systems for guidance. AUVs possess remarkable flexibility and autonomy, enabling them to gather vast amounts of data across expansive regions. However, their operational duration is constrained by the capacity of their batteries. [3, 4, 5]

Additionally, there exist hybrid variants like the Freedom AUV/ROV from Oceaneering. These UUVs can function as AUVs as well as ROVs when a tether is connected. [23]

Further subgroups of UUVs are **Gliders and Floaters**. Both are specifically engineered for doing extensive oceanographic research over extended periods of time. While Floaters are predominantly utilised for stationary observations and remain buoyant at pre-established depths, whereas gliders employ alterations in buoyancy and wings to propel themselves forward, enabling them to cover extensive distances. [4, 6, 24]

Towed devices and **Remotely Operated Towed Vehicle**s (ROTVs) can be seen as another form of UUVs. Towed behind a surface vessel or underwater vehicle, they can extend the capabilities of the towing unit. ROTVs possess enhanced manoeuvrability through actuators like adjustable wings or thrusters. They are utilised as carriers for various sensor systems. Furthermore, there exist further specialised categories of UUVs that are specifically tailored for particular purposes. [4, 6, 16]

2.1.1 Scope of tasks

AUVs are specifically engineered to perform diverse functions across several domains, encompassing scientific, commercial, military and environmental sectors. This review will provide a brief overview of the various activities that AUVs are designed to carry out, highlighting their versatility in different fields. [1]

AUVs are utilised in **oceanographic research** to gather data from areas that are inaccessible to humans. They possess sensors and tools capable of quantifying the physical, chemical and biological characteristics of the ocean. The provided data encompasses temperature, salinity, turbidity and nutrient concentrations, which are crucial for comprehending oceanic currents, climate variations and marine ecosystems. AUVs have the capability to accurately chart the topography of the seafloor, investigate hydrothermal vents and collect data on undersea volcanoes and earthquake-prone areas. These contributions greatly enhance our comprehension of geophysical phenomena. Furthermore, these vehicles gather samples from different depths to facilitate scientific research, so contributing to the examination of marine biodiversity and ecosystems. [4, 3]

In the **commercial sector**, AUVs are used for a variety of tasks, including underwater surveying for the oil and gas industry. Their work involves the process of conducting seabed mapping and inspections of pipelines and undersea infrastructure. This includes the identification of potential dangers and the facilitation of maintenance activities. Surveillance of important marine structures such as pipelines, wind farm cables and internet cables is a task that involves long-term and repetitive monitoring. This can be accomplished by deploying several AUVs that operate simultaneously. [6, 7]
Given the increasing worldwide demand for resources and the decreasing availability of land-based deposits, seabed mining is becoming a crucial undertaking. The utilisation of AUVs aids in the exploration of these marine regions, allowing for the identification of feasible mining locations and the comprehension of intricate geological processes in action. [7, 11]
The existence of unexploded ordnance on the ocean floor presents a significant threat to marine ecosystems, commercial shipping routes and underwater infrastructure. AUVs are commonly used for surveys of unexploded ordnance, as they are equipped with advanced sonar and imaging equipment. These solutions enable accurate identification and serve as the foundation for the following secure retrieval and disposal. [3, 25]

AUVs serve several roles in **military and defence** applications. These devices are utilised for the purpose of mine countermeasures, which involve the detection and classification of

underwater mines, all while ensuring the safety of human divers by eliminating their exposure to danger. AUVs are also used in surveillance and reconnaissance operations such as harbour protection tasks and port clearance operations, gathering valuable information in contested or sensitive maritime regions. They possess the ability to covertly collect information, survey adversary activities or oversee military facilities. [8, 9, 10]

Within **search and rescue operations**, particularly in deep-water environments where human divers cannot safely operate, AUVs possess the ability to rapidly traverse extensive regions and employ sonar imaging to pinpoint the whereabouts of misplaced items or individuals. In shipwreck investigations or aeroplane crashes, AUVs provide valuable insights into the cause of incidents and aid in the retrieval of black boxes and other crucial evidence. [4, 7]

AUVs contribute to underwater **archaeology exploration** by locating and documenting shipwrecks and ancient submerged settlements. They create detailed maps and images of archaeological sites, providing archaeologists with data to study without disturbing the site. This capability is crucial for preserving historical artefacts and understanding history. [4]

AUVs are also employed in **educational and technological development contexts**, offering students and researchers practical exposure to marine technology, robotics and oceanography. AUVs are utilised by universities and research institutions as platforms for conducting experiments and evaluations of novel technologies, sensors and algorithms. [1, 7]

2.1.2 Vehicle Design

AUVs possess a wide array of distinct features that are precisely designed to suit their specific purposes and operational surroundings. The performance and overall mission efficacy of AUVs are influenced by crucial criteria such as their shape, size, weight and diving depth. They are equipped with sensors to independently navigate and create maps of ocean characteristics. Common sensors used are sonars (e.g. side scan), cameras, compasses, depth sensors, thermometers, magnetometers turbidity sensors and pH sensors. [4, 26]
Table 2-1 provides an overview of various AUVs, with the corresponding Figure 2-3 illustrating these AUVs. The focus is deliberately on well-known AUV manufacturers from the European and American regions, including companies like TKMS ATLAS ELEKTRONIK GmbH (Germany), Cellula Robotics Ltd. (Canada), ECA GROUP (France), EvoLogics GmbH (Germany), General Dynamics Mission Systems (USA), Graal Tech S.r.l. (Italy), International Submarine Engineering Ltd. (Canada), IQUA Robotics (Spain), Kongsberg Maritime AS (Norway), Kraken Robotics (Canada), L3Harris Technologies (USA), Lockheed Martin Corporation (USA), Saab Ltd. (UK), Seaber (France), Teledyne Marine Technologies Incorporated (USA) and the Woods Hole Oceanographic Institution (USA). Other markets or custom-made AUVs were not considered in this context. Examples of these custom-made AUVs are the Poseidon AUV from the German GEOMAR Institute [27] and the PreToS developed by the Technical University of Berlin [7, 11].
The parameters listed in the Table 2-1 like maximum diving depth, length (L), diameter (D) for cylindrical AUVs or height/width (H/W) for box-shaped AUVs, mass in air (m) and shape (torp. = torpedo-shaped, box = box-shaped, strl. = streamlined) are explained in more detail after Figure 2-3.

Table 2-1: AUV overview

No	Organisation	AUV	Depth [m]	L [m]	D or H/W [m]	m in air [kg]	Shape	Source
1	TKMS ATLAS ELEKTRONIK	SeaCat	600	2.5-3.5	0.33	180-300	torp.	[28]
2		SeaCat ER	600	3.0-4.0	0.33	200-320	torp.	[28]
3		SeaCat SAS	300	4.0-6.0	0.33	250-500	torp.	[28]
4	Cellula Robotics	Solus-Lite	1,000/3,000/ 6,000	5.6	1.00	1,400	torp.	[29]
5		Solus-LR	3,000	8.5	1.00	3,700	torp.	[30]
6		Solus-MR	1,000/3,000 / 6,000	7.3	1.00	2,400	torp.	[31]
7	eca group	A18D	3,000	-	-	-	torp.	[32]
8	EvoLogics	Quadroin AUV	150	1.1	0.30/0.30	25	strl.	[33]
9	General Dynamics Mission Systems	Bluefin-9	200	2.4	0.26	70	torp.	[34]
10		Bluefin-12	200	4.8	0.32	250	torp.	[35]
11		Bluefin-21	4,500	4.9	0.53	750	torp.	[36]
12		Hovering AUV	30/60	1.3	0.38/0.93	72	box	[37]
13	Graal Tech	X-300	300	2.2	0.16	29	torp.	[38]
14		X-300 MCM	300	1.7	0.16	20	torp.	[39]
15	International Submarine Engineering	Explorer AUV	3,000/6,000	4.5-7.5	0.74	620-1700	torp.	[40]
16		Theseus AUV	1,000	10.7	1.27	8,600	torp.	[41]
17	IQUA Robotics	Girona 500	500	1.5	1.00	140	box	[42]
18		Sparus II	200	1.6	0.23	52	torp.	[43]
19	Kongsberg	HUGIN	3,000/4,500	5.2-6.4	0.75	850	torp.	[44]
20		HUGIN Edge	1,000	4.0	0.35	300	torp.	[45]
21		HUGIN Endurance	6,000	10.0	1.20	-	torp.	[46]
22		HUGIN Superior	6,000	6.6	0.88	2,200	torp.	[47]
23	Kraken Robotics	ThunderFish	6,000	3.5	0.50/0.95		box	[48]
24	L3Harris Technologies	IVER3 Standard	100 / 200	1.9-2.2	0.15	27-39	torp.	[49]
25		IVER4 580	300	2.0	0.15	45	torp.	[50]
26		IVER4 900	300	2.5	0.23	104	torp.	[51]
27	Lockheed Martin	Marlin	300	3.1	-	-	strl.	[52]
28	SAAB	AUV62-AT	300		0.53	800	torp.	[53]
29		Double Eagle SAROV	300	3.0	0.80/1.30	730	box	[54]
30		Sabertooth - Single hull	1,200	3.6	0.45/0.66	650	box	[55, 56]
31		Sabertooth - Double hull	3,000	4.0	0.67/1.35	1,300	box	[55, 18]
32	Seabaer	YUCO-CTD	300	1.1	0.12	10	torp.	[57]
33		YUCO-PAM	300	1.0	0.12	9	torp.	[58]
34	Teledyne Marine Technologies Incorporated	Gavia AUV	1,000	2.2-4.5	0.20	59-130	torp.	[59]
35		Osprey AUV	2,000	5.0	0.32	400	torp.	[60]
36		SeaRaptor AUV	3,000/6,000	5.5-8	0.68	2,000	torp.	[61]
37	Woods Hole Oceanographic Institution	Orpheus	11,000	1.7	1.30/1.02	250	box	[62]
38		REMUS 100	100	1.6	0.19	37	torp.	[63]
39		REMUS 600	600		0.32	240	torp.	[64]
40		REMUS 3000	3,000	3.7	0.36	335	torp.	[65]
41		REMUS 6000	6,000	3.8	0.71	862	torp.	[66]
42		Sentry	6,000	2.9	1.80/2.20	1,250	box	[67]

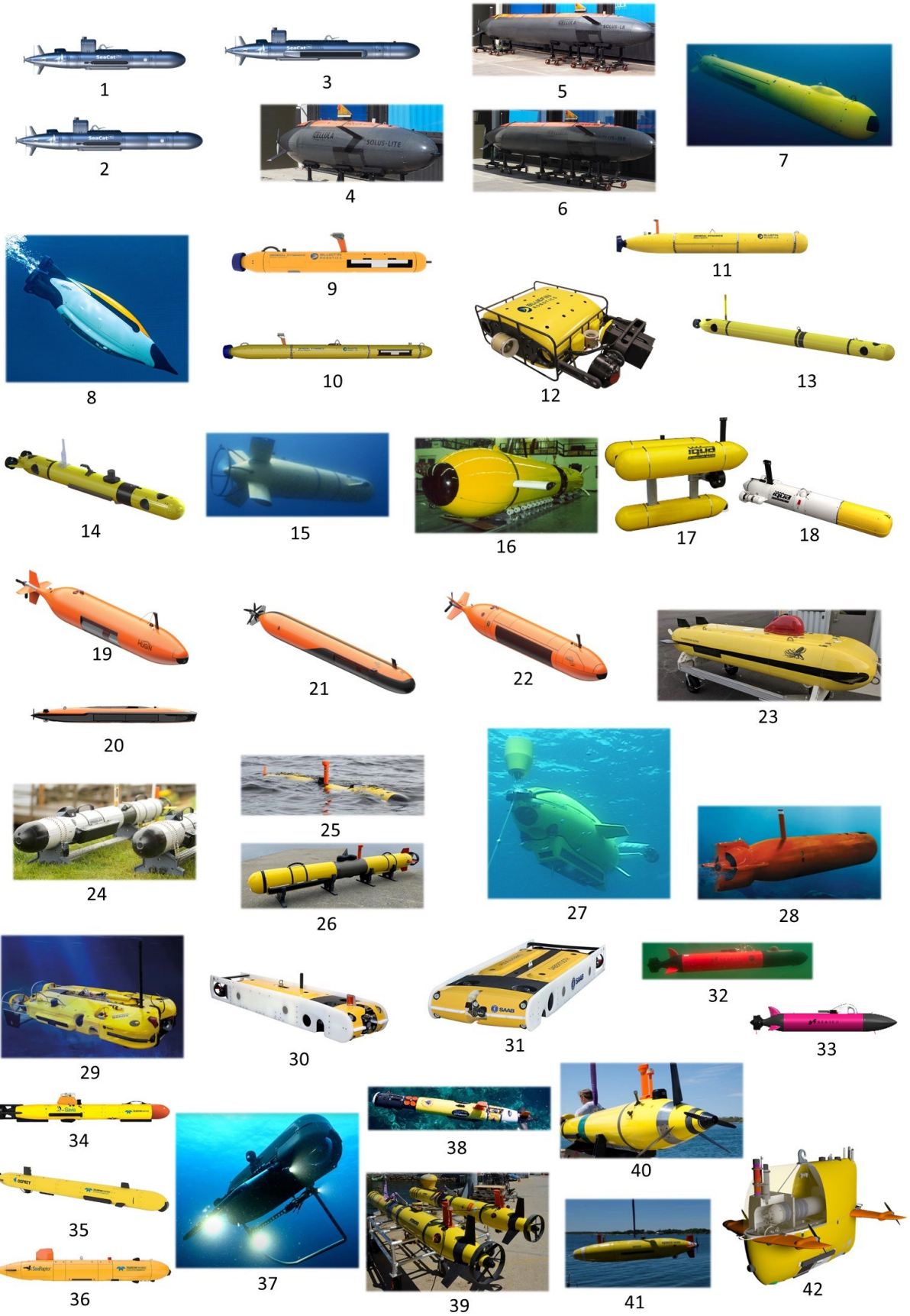


Figure 2-3: AUV overview
Description and sources are given in Table 2-1/ images are not to scale

The **shape** of an AUV is a fundamental aspect that significantly influences its hydrodynamic efficiency, stability and manoeuvrability. In general, the designs of AUVs are optimised to minimise drag and improve propulsion efficiency.
Torpedo-shaped AUVs, like the REMUS, HUGIN, SeaCat and IVER AUVs, are characterised by their streamlined and elongated cylindrical design, which is the predominant design among the examined AUVs. They are designed for efficient forward motion, making them ideal for long-duration missions in open waters. Their streamlined form minimises resistance, enabling more efficient forward motion. This design offers distinct benefits for surveying, mapping and reconnaissance operations. Torpedo-shaped AUVs, propelled by a single propeller, require forward motion for control. Their minimum controllable speed typically exceeds 0.5 m/s. [4, 28, 44, 49, 50, 64, 68]
Box-Shaped AUVs, such as the SAAB Sabertooth, are frequently employed for specialised activities that benefit from a small or boxy structure, such as operating in restricted places like offshore facilities. Although they may experience greater drag in comparison to torpedo-shaped AUVs, their design enables more versatile payload integration. Such as thruster equipment so that the vehicles are hover-capable, enabling control at low and zero speeds. This configuration allows independent motion and rotation along the x, y and z axes. [4, 18, 68]
Biomimetic AUVs, like the EvoLogics Quadroin AUV, are designed to replicate the efficient swimming mechanisms of fish or marine mammals. This design aims to achieve high manoeuvrability and energy efficiency, useful in complex underwater environments. [4, 33]

The **size** of AUVs varies greatly, depending on the intended use, payload requirements and mission duration. The diameter or height and width listed in Table 2-1 refer to the vehicle hull or pressure body and do not account for any attached or protruding parts such as fins, rudders or structures like towers.
Small AUVs like REMUS 100 from the Woods Hole Oceanographic Institution or the AUVs from Seaber in the YUCO series are portable and can be deployed manually, ideal for shallow waters, rivers and lakes. Their compact size allows for easy transportation and deployment, often from small vessels or directly from shore. [58, 63]
Medium-sized AUVs, like the REMUS 600, Bluefin-12, HUGIN Edge, Gavia, Sabertooth, IVER4 900 and SeaCat offer a balance between payload capacity and manoeuvrability. They are suited for a variety of missions, including oceanographic data collection, mine countermeasure operations and deep-sea exploration. [18, 28, 35, 45, 51, 59, 64]
Large AUVs, such as the HUGIN Endurance, are designed for extended missions, capable of carrying large payloads over long distances. These AUVs are typically used for deep-sea mapping and complex survey missions requiring extensive sensor arrays. [46]

The **weight** of an AUV has a significant impact on various crucial aspects such as buoyancy and stability. Lighter AUVs are designed for operational agility and ease of handling. Some AUVs like from Seaber's YUCO series are therefore considered man-portable and can be transported and lowered into the water without additional equipment. [58, 57]
On the other end of the spectrum, heavier AUVs such as the AUVs from Cellula Robotics in the Solus series are built to accommodate larger payloads and extended battery life. [30, 31]
It has been noted that many manufacturers commonly provide alternatives or choices for the configuration of their vehicles. These alternatives frequently include making small alterations to the vehicle, such as adding or replacing modules, which in turn result in changes to its dimensions and weight.

The operational **diving depth** of an AUV is a critical parameter that defines its applicability in various underwater environments. Many AUVs, like the Gavia, SeaCat, REMUS 600, Girona 500 and the IVER4 series, are designed for operations in coastal and shallow water environments, typically up to depths of approx. 300 up to 1,000 metres. Their applications range from environmental monitoring to underwater archaeology and surveying of shallow water regions. [28, 42, 50, 59, 64]
In contrast, deep-diving AUVs such as the HUGIN Endurance, HUGIN Superior, REMUS 6000, Sentry orpheus and Explorer AUV are engineered to withstand the extreme pressures of the deep ocean, capable of operating at depths exceeding 6000 metres. These AUVs are indispensable for deep-sea research, exploring ocean basins, underwater volcanoes and investigating deep-sea vents. [40, 46, 47, 62, 66, 67]

There is a widespread absence of established definitions when it comes to categorising AUVs. It is ambiguous if weight, size, design or a mix of these factors should be taken into account. There are a wide variety of measurements, which become much broader when considering other markets or custom-made AUVs. The primary emphasis of this research is on torpedo-shaped AUVs that have a length ranging from around 2 to 6 metres. With a weight of typically between 200 – 500 kg, these require a corresponding LARS. This is due to the fact that they are too large and heavy to be considered man-portable and at the same time they are too small to have sufficient battery capacity to travel independently to most mission locations.

The development and deployment of AUVs have seen significant growth in recent years, driven by technological advancements and increasing demand across various sectors. The AUV industry has witnessed substantial technological progress, contributing to enhanced capabilities and expanded applications. Recent advancements include improvements in energy efficiency, enabling longer missions and greater depths. Enhanced sensory and navigation systems have led to better data collection and accuracy, making AUVs invaluable for applications ranging from scientific research to military operations. [4]
Looking ahead, the AUV market is poised for continued growth. Emerging trends include the integration of artificial intelligence for autonomous decision-making, the development of swarm AUV systems for coordinated tasks and advancements in miniaturisation for cost-effective deployment. However, challenges such as regulatory hurdles, high development costs and the need for advanced infrastructure support remain.

2.1.3 Navigation & Homing

When the AUV is on the water surface, standard positioning systems such as GPS (Global Positioning System) can be used for AUV navigation. To guide an submerged AUV, dead reckoning is a common approach. After submersion AUVs lose access to GPS signals due to the inability of radio waves to sufficiently penetrate water. To improve accuracy in navigation, it is advised to use an underwater acoustic location system. One method for this is known as Long Baseline Navigation, which involves a framework of seabed-based transponders. Alternatively, Ultra-Short Baseline (USBL) or Short Baseline systems are used when a surface reference, like a support vessel, is available. The systems determine the AUV's position relative to the surface vessel's established GPS coordinates using acoustic range and attitude readings. [4, 16, 69]

To improve accuracy and reduce the accumulated mistakes of dead reckoning, AUVs may surface at intervals for GPS correction. An Inertial Navigation System on board the AUV calculates detailed positional data, including acceleration and velocity, during periods between

corrections and for precise manoeuvring. Accuracy in these measurements is improved by combining data from an Inertial Measurement Unit and possibly adding a Doppler Velocity Log, which measures the speed of motion in relation to the water or seafloor. The vehicle's vertical position (depth) is mainly measured using a pressure sensor, but it can also be determined by Doppler Velocity Log readings, providing another way to calculate depth. [68]

In the case of homing, the relative position between the AUV and the target position must be determined to compute control commands. When the AUV encounters a clearly defined, stationary target position, it can calculate its relative position to the target and generate control orders accordingly. Homing becomes more challenging when the target position is movable or not precisely defined in advance. In this case, the methods for determining the relative position are based on the sensors that are installed on the AUV. Key characteristics of a homing system include acquisition distance and direction. This is influenced by accuracy, environmental sensitivity, update rate and latency. Homing systems are either optical, acoustic or electromagnetic systems. [25, 68, 70]

Optical homing involves the use of cameras or photodetectors on the AUV to identify specific light patterns, shapes or coded signals like QR codes, ArUco markers or AprilTags that are either emitted by or placed on the target. Advanced algorithms process the visual data to determine the relative position and to guide the AUV. Although this method is suitable for above and below water, its effectiveness depends on visibility and diminishes in turbid or deep waters where light penetration is low. While passive systems work with the existing ambient light and are primarily based on contrasts, active systems need power supply to emit light waves themselves. By utilising active light sources a wider range can be achieved by using blue or green light because of the shorter wavelength of these colours. [71, 72, 73, 74, 75]

Acoustic homing is mostly utilised underwater due to the efficient propagation of sound waves in water, allowing for precise and long-range homing in deep or turbid waters. The process includes transmitting sound waves from a beacon, which are subsequently detected by the AUV's acoustic sensors. One way to calculate distance and orientation is to measure the time delay and signal strength detected by an array of sensors on the AUV. This method can involve modifying auditory sounds to encode extra navigational data. One example is a USBL system, which involves an array of hydrophones on the target or the AUV. The system calculates the relative position based on the time delay of sound pulses emitted by the transducer (e.g. target position) and received by the transceiver (e.g. AUV). [4, 14, 68, 74, 76]

Electromagnetic waves may be utilised for precise targeting at short distances. The range of this system is greatly influenced by the frequency of the electromagnetic waves utilised, as seawater's electrical conductivity plays a significant role. In general, using lower frequencies leads to a greater range. Even at very low frequencies, a maximum distance of around 10 metres is attained. [14, 68, 77, 78]
A more detailed explanation of navigation and homing is given in the review of underwater docking and charging technology for autonomous vehicles by Liu et. al. [14] and in Part B of the Springer Handbook of Ocean Engineering [79], specifically chapters 14 to 16.

2.2 Lifting methods

Lifting operations for L&R of AUVs are predominantly executed through two distinct methodologies: crane-based and ramp-based methods. The subsequent part provides an initial overview of crane-based techniques, differentiating between traditional cranes and those equipped with unique frame structures. Later on, ramp-based solutions are introduced. Table 2-2 provides a brief overview with examples of lifting systems used in each category.

Table 2-2: Lifting methods

Crane-based		**Ramp-based**
Conventional cranes	**Frame constructions**	
Portal crane / Jib crane Knuckle boom crane Davit	A-Frame J-Frame	Ramp Stinger Roller Coaster

Crane-based lifting operations, as illustrated in Figure 2-4, are mainly preferred for larger vessels. This preference stems on the significant influence that cargoes freely suspended can have on the vessel's stability. For the calculation of the vessel's stability the lifted mass is not affected by its real position but on crane's suspension point. A key aspect of this analysis involves the consideration of the ship's metacentric height (GM), which serves as a measure of the initial static stability of a floating body. When the AUV is raised and the vertical centre of gravity of the system increases, the GM decreases, which reduces the ship's stability. The greater the ratio of AUV weight to displacement of the carrier platform and the higher the point of suspension, the greater the loss of stability. [80]

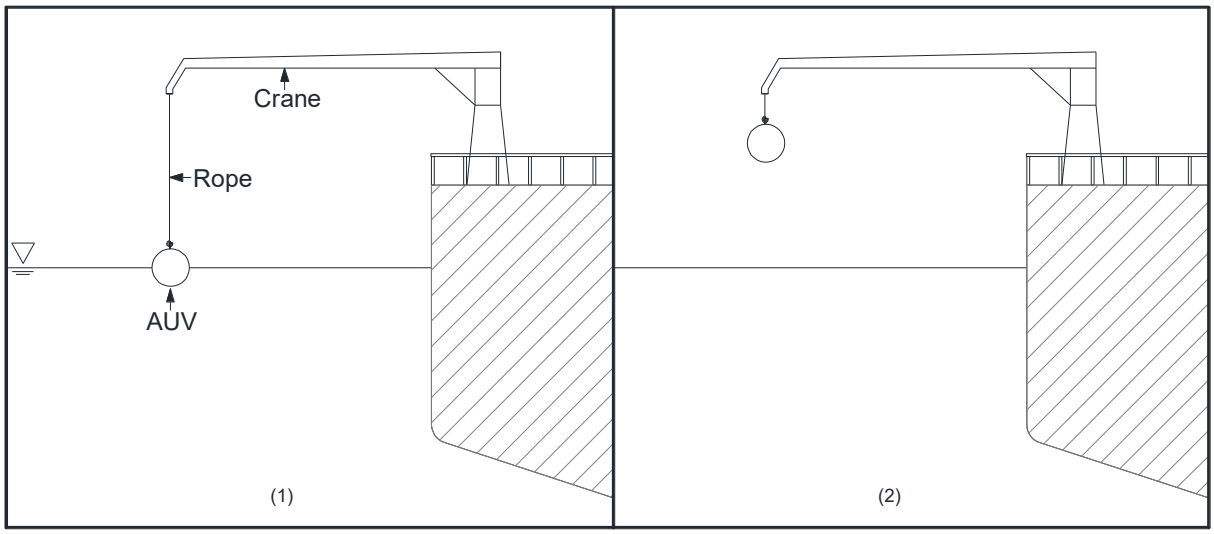


Figure 2-4: Crane based AUV lifting
Rear View **(1)** AUV attached to crane **(2)** AUV lifted / close to crane boom head

Cranes offer a foundational approach for handling AUVs because they are typically available on the respective ships. Nevertheless, they provide particular challenges and risks linked to transferring ship motions to the lifted AUV. The transfer happens mainly because the AUV, while hanging from a single lifting point, turns into a freely swinging object. Therefore, the ship's natural motions, particularly in rough seas, can cause substantial pendulum-like swinging of the AUV. The swinging action poses a significant risk to the AUV, carrier platform and deck

personnel. To avoid this, the AUV can be guided using auxiliary lines enabling precise control and limiting its unrestricted motion. Another technique involves pulling the AUV against a bearing, limiting its degrees of freedom and causing it to move in unison with the crane. Utilising a robotic arm or a knuckle boom crane for this lifting enables bringing the bearing point closer to the water surface and shortening the pendulum length to reduce the potential for pendulum motions. [7, 12]
An important aspect of crane arrangement on ships concerns its positioning relative to the ship's centre of flotation (COF). The COF is a pivotal concept in naval architecture, referring to the centroid of the ship's water plane area. It serves as the fulcrum about which a vessel rolls transversely or pitches longitudinally. This means that both the rolling and pitching axes of a ship pass through this point. Therefore, to minimise the impact of the ship's motion on the lifted AUV, it is critical to position the crane as close as possible to these rotation axes.
The optimal arrangement of the crane is contingent on the specific ship type and its operational environment. If pitching motions are a concern, the crane should be positioned towards the ship's side, close to the longitudinal centre of flotation (LCF). This positioning effectively reduces the influence of pitching during lifting operations. To prevent rolling motions, it is recommended to situate the crane amidships. This positioning corresponds with the transverse centre of flotation (TCF), located on the centreline for symmetrical vessels, providing increased stability during lifting operations.

In addition to conventional cranes, cranes with special frame constructions like A-frames and J-frames can be utilised [12]. A-frame systems, like shown in Figure 2-5, are utilised in maritime technology for launching and recovering various loads. The rotating A-frame is positioned at the stern of the vessel and often operated by a hydraulic mechanism. The winch, situated at the end of the steel frame, is primarily responsible for raising and lowering the weight. To initiate recovery of an AUV, the load is securely attached to the rope and A-frame is first swivelled overboard (Figure 2-5-a). Subsequently, the winch methodically draws it upwards (Figure 2-5-b). After this phase, the frame swings overboard, facilitating to place the load on the deck (Figure 2-5-c). The launch of an AUV runs in a reverse order when compared to the recovery process. [81]

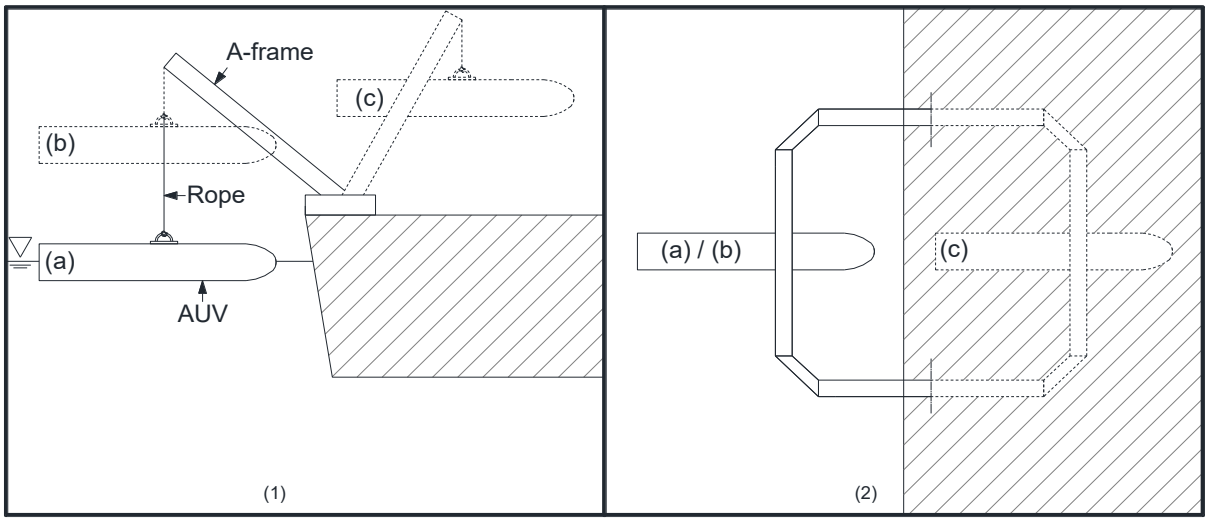


Figure 2-5: AUV lifting with an A-frame
(1) side view **(2)** top view
(a) AUV attached to winch / lifting system **(b)** AUV lifted - A-frame tilted out **(c)** AUV lifted - A-frame tilted in

A-Frame arrangements are frequently utilised as a result of their robust structure, ease of installation, operation and maintenance convenience. Another way to improve the system's efficiency is by adding a support mechanism or bearing to reduce the swinging motion of the load. The AUV can be hoisted in many positions, such as horizontally, vertically or with a specialised docking device.

Ramp-based methods are beneficial for smaller boats and are also used on larger vessels. This approach involves pulling the AUV out of the water onto the carrier platform via a ramp. The appropriateness of ramp-based techniques for smaller vessels is mostly due to the reduced deck height typical of this category of vessels. The deck's proximity to the sea surface permits the implementation of more gentle ramp gradients than would be practicable on bigger vessels. This component is essential for ensuring a smooth transfer of the AUV from the water to the deck. [12]
For boats, ramp-based solutions have a substantial benefit over crane-based operations due to their smaller impact on ship stability. This benefit arises from the strategy of maintaining the mass of the AUV as low as possible during the operation. Unlike crane-based methods, where the load is suspended and can significantly alter the vessel's centre of gravity, ramp-based methods facilitate a more gradual and controlled transfer of the AUV's weight onto the vessel.

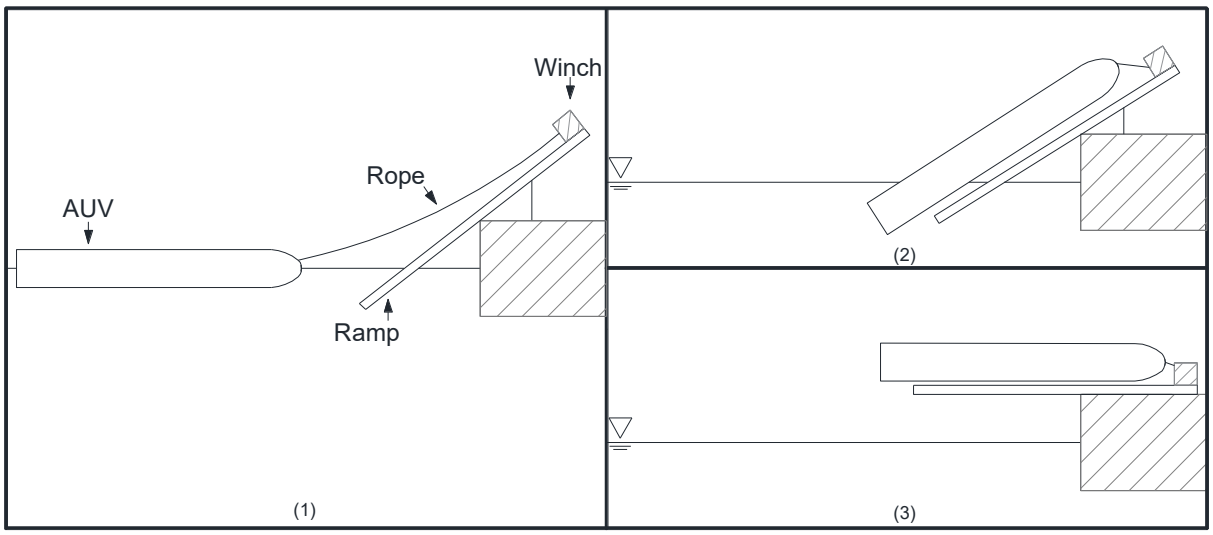


Figure 2-6: AUV lifting using a stinger
Side view **(1)** AUV attached to winch **(2)** AUV is pulled onto the ramp **(3)** Ramp is placed on the platform

The ramp, usually referred to as a stinger, is a specialised structure typically located at the stern. This strategic placement of the stinger is crucial, particularly for vessels without a dynamic positioning systems. It enables L&R operations while moving forward and this way maintaining the ship's course, reducing rolling motions and preventing drift. By positioning the stinger on or close to the rolling axis of the ship, the effects of the rolling motions on the lifting operation can be minimised. For this arrangement should be taken into account how the ship’s wake affects the approaching AUV. Although it is not commonly observed, ramps can also be mounted alongside the ship. When arranging the lifting device, it is important to consider the particular characteristics of the ship. This includes several factors, such as stability values that have significant influence on the rolling motion, as well as the presence of supplementary components like fins, which serve to soften motion. [82]
During launch, the stinger tilts down into the water, allowing the AUV to descend into the sea through gravity release. The AUV is recovered by pulling it onto the stinger using a winch

(Figure 2-6 -1 & -2). Subsequently, both the AUV and the ramp are lifted back onto the vessel (Figure 2-6 -3), completing the recovery process.

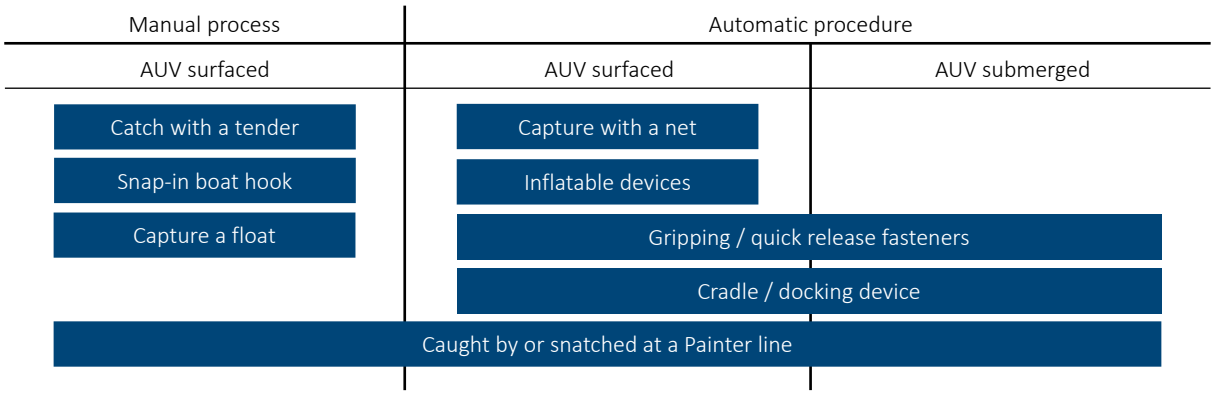
Additionally, there exist hybrid approaches combining crane and ramp-based techniques. A specific variation is outlined in the US patent US000005253605A [83]. In this example, the AUV is hoisted from the sea via a crane. A recovery line is attached to the tip of the AUV and drawn inward until the tip of the AUV emerges from the water. As the crane is horizontally displaced towards the ship, the AUV approaches the ship's side, where the ramp is placed. In this process the AUV is tilted on the ramp. Following this, the AUV is elevated onto the ramp by the process of crane retraction. [83]

L&R operations are usually carried out outboard. An exceptional scenario with a notable benefit is the utilisation of a moon pool, which is a bottom opening in the vessel's hull. This facilitates the L&R of AUVs in a manner that is largely unaffected by sea conditions and wind, therefore reducing the risks associated with L&R activities in challenging maritime environments. The lifting operation is often performed within these vehicles with either a crane or, if preferred, a ramp. [84, 85]
A more detailed explanation of various lifting methods and crane types is given by Hanyok and Smith [12] and in the Dissertation of Mr. Mischnick [11].

2.3 Initial physical connection

The initial physical connection holds significant importance in the recovery process as it marks the shift from autonomous operation to a state controllable by the host platform. The complexity of this work is caused by the continuously shifting characteristics of the maritime environment, the need for precise alignment of recovery equipment with the AUV and the overall imperative to maintain the safety and integrity of both the AUV and the carrier platform. [11]
This chapter presents a comprehensive overview of the approaches used to establish initial physical contact with AUVs. The approaches get categorised into two main types: manual and automatic. These methods are further distinguished based on whether the AUV is surfaced or submerged at the moment of contact. The researched procedures are listed in Table 2-3 and will be explained in the next sections of this chapter, providing examples and different variants for each strategy.

Table 2-3: Overview of procedures for establishing initial physical contact



The establishment of a physical connection by manual methods is common on the water surface and may involve the use of a tender, boat hook or throwing line. During the research, no manual processes were found during which the AUV was submerged. The active intervention capability from manned carrier platforms is a significant benefit of manual recovery techniques. In situations when complications develop during the process of recovery, it can be feasible to employ direct human involvement to provide assistance in the recovery operation.
Conversely, the advantages of automated operations have been particularly proven in terms of enhanced efficiency and accuracy, resulting in a significant reduction in human error and operating time. Additionally, they enable more complex and repetitive tasks to be executed with consistent accuracy and without jeopardising people, essential in challenging marine environments. It is important to acknowledge that many automated systems utilising the AUV's capabilities or actively controlled mechanisms require the energy capacity of the AUV and are consequently, not suitable for application in the event of a failure or without battery power. In comparison to manual techniques, the AUV has the capability to undergo automatic operations by either surfacing or submerging. The AUV is often surfaced for catching with a net or utilising inflatable devices. The AUV's position is irrelevant when it comes to grabbing with a robot arm or utilising a cradle, which can also be referred to as a docking cage or docking device.
Underwater recovery techniques require advanced technology to precisely locate and securely connect with the submerged AUV. Due to their ability to operate less affected by sea conditions, these approaches present an important advantage in terms of minimising operational limitations. They offer a more stable and controlled environment for recovering AUVs, especially in harsh conditions. [7]
A universally applicable technique for all categories, manual and automated as well as surfaced and submerged entails the act of capturing or seizing a painter line. This flexible method utilises a line mechanism in order to initiate contact with the AUV.

It is important to acknowledge that the domain of AUV recovery is characterised by its dynamic nature, wherein there is a constant evolution of specialised techniques and systems. A significant number of these inventions are tailored to suit certain UUVs and may remain confidential or are not conveniently distributed for research purposes. [11]
In the following sections, the procedures will be explained using general terms. As a result, variations in performance might be identified depending on the specific application, as they are reliant on the special features of the carrier platform and the AUV. A detailed examination of the unique characteristics of each variety of the diverse procedures is not conducive. Additional explanations of specific procedures can be obtained in the referenced sources, patents and recommended literature.
An example for the general and non-specialised description of the procedures is whether the manoeuvre is carried out stationary or dynamic. And if it is dynamic, which participants (AUV and carrier platform) are in motion during the manoeuvre. Certain carrier platforms, such as vessels without a dynamic positioning system, need forward motion to ensure manoeuvrability and course stability. The hydrodynamic effects caused by the flow around the hull, such as drag, can have negative effects. This addresses the manoeuvrability of the AUV and the risk of the AUV being pulled under the ship or into the propeller. The previously mentioned impacts have a correlation with velocity and appear with greater intensity as the distance between the AUV and the carrier platform decreases. In this dynamic case, at least the host platform must move. Depending on the method used to establish the initial contact, the AUV is then also in motion. In other variants of the same process the AUV may move towards a stationary carrier platform in order to minimise these challenges.

2.3.1 Manual methods - AUV surfaced

To snap in a **boat hook** is a manual approach used to establish a connection with an AUV at the surface. When the AUV appears, the host platform manoeuvres towards the UUV or the vehicle is steered to the platform. The deck crew uses a boat hook to secure a rope to the AUV's recovery eye. This procedure is illustrated in Figure 2-7. [11]
Using the boat hook gets more challenging as the gap between the sea surface and the railing increases. Mooring the AUV is made more difficult by increased seas, raising the risk of collision. Another issue is the possible suction effect created by the supply ship's motions, pulling the AUV towards the platform.

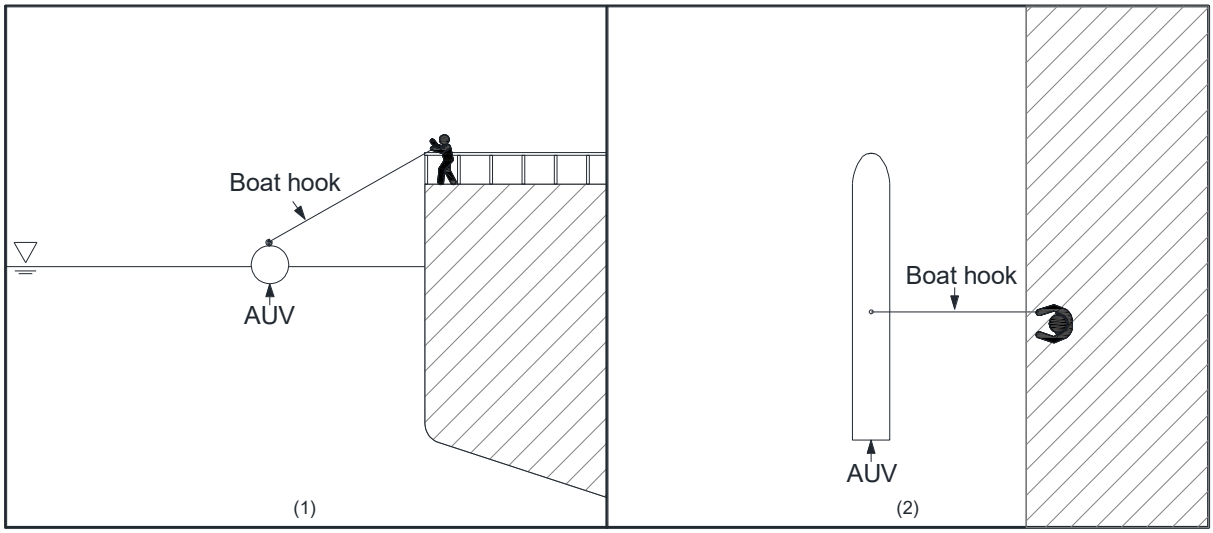


Figure 2-7: Snap-in a boat hook
A boat hook is used to make physical contact with the AUV, e.g. using an eyelet **(1)** rear view **(2)** top view

The AUV **catch with a tender**, illustrated in Figure 2-8, includes launching a tender from the carrier platform. The crew steers the tender near the AUV to connect a rope to the AUV, then secures the AUV to the tender for hauling it back to the carrier platform for the lifting. [7]

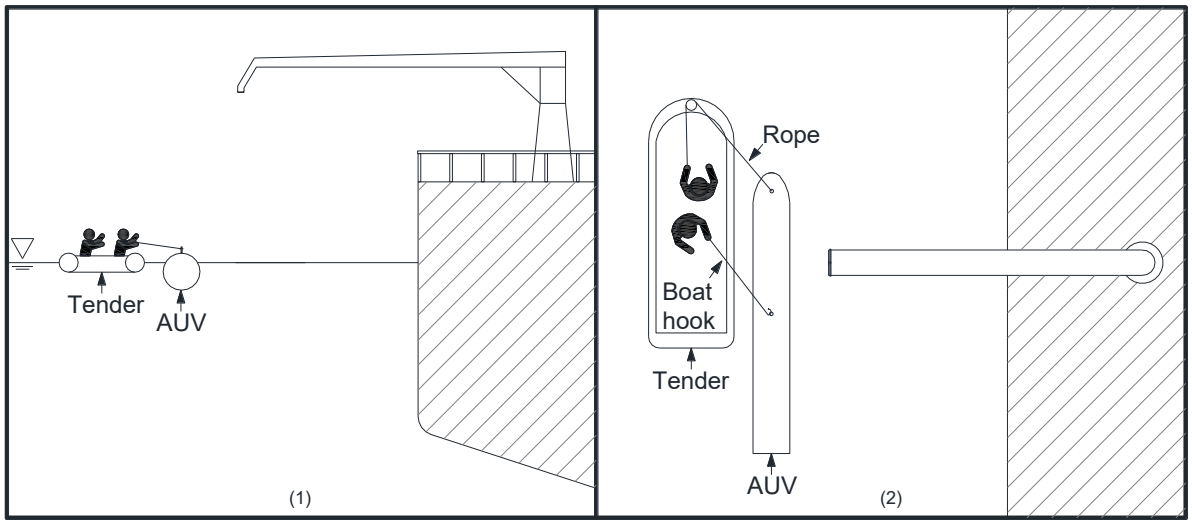


Figure 2-8: AUV catch with a tender
Initial physical contact is made manually by the crew from the tender **(1)** rear view **(2)** top view

A respective procedure is described in Patent US020220258841A1 [86]. Despite its complexity, the tender approach has clear safety benefits for the AUV. It significantly reduces the possible

damage as a collision between the tender and AUV is less harmful to the AUV than a collision with the carrier platform. This effect is further emphasised if the tender is a Rigid Inflatable Boat. However, this procedure poses a danger to the crew due to the relative motions between the carrier platform, the tender and the AUV, which demonstrate the method's constraints under severe sea conditions.

The **float method**, shown in Figure 2-9, relies on a straightforward yet efficient concept. Upon reaching the water's surface, the vehicle releases a float attached through a buoyant rope. The detachment allows the vehicle or float to move freely until the rope has been fully extended (Figure 2-9-2). The next step is to deploy a throwing anchor attached to a line over this rope. This task can be performed either manually or with specialised equipment such as a pneumatic line throwing device (Figure 2-9-3).
After the anchor goes down, the float can be pulled onto the carrier platform. This enables the attachment of the AUV's rope to a subsequent lifting system. Ramp mechanisms are often employed, if the float is positioned near the AUV's tip. When using a crane, the suspension point and the float's location should be located as near as feasible to the vehicle's centre of gravity. [11]

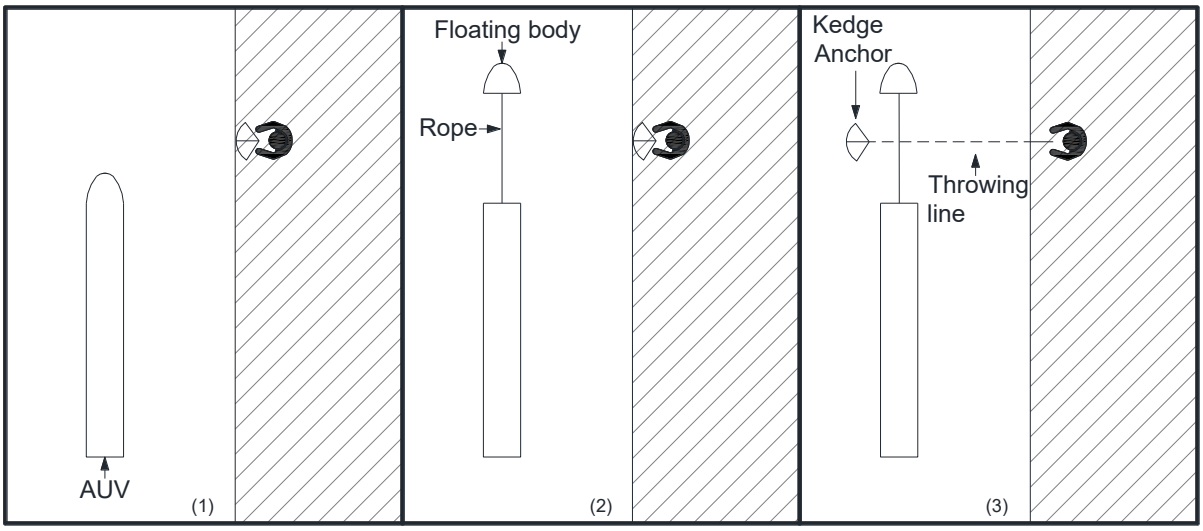


Figure 2-9: Capturing an AUV using a floating body
Top view **(1)** the AUV is positioned alongside the carrier platform **(2)** a floating body, e.g. the nose of the AUV, is ejected from the AUV and floats off, thereby tensioning a line between the AUV and the floating body **(3)** the line between the AUV and the floating body is pulled in with the aid of a kedge anchor and then connected to an lifting device

Figure 2-10 illustrates the process of capturing an AUV using a **painter line**. This procedure involves a carefully coordinated use of a crane, several ropes and a connecting piece such as an eyelet or hook on the AUV. The help rope is utilised to form an arc, which is subsequently lowered to the surface of the water. The key step in this process is hooking the arc of the rope into the eyelet of the AUV, thereby establishing a preliminary physical connection between the AUV and the recovery system (Figure 2-10 -1). The crane hook can be attached to the eyelet of the AUV by pulling on the help rope once it has been inserted into the eyelet (Figure 2-10 -2). This connects the AUV to the carrier platform via the recovery rope for lifting. The approach described in the German patent DE000019544656C1 [87] is employed to recover the SeaCat AUV from TKMS ATLAS ELEKTRONIK GmbH. [87]
In order to make an initial contact, the AUV must remain in close proximity to the carrier platform, which is constrained by the crane's range and results in a greater collision possibility.

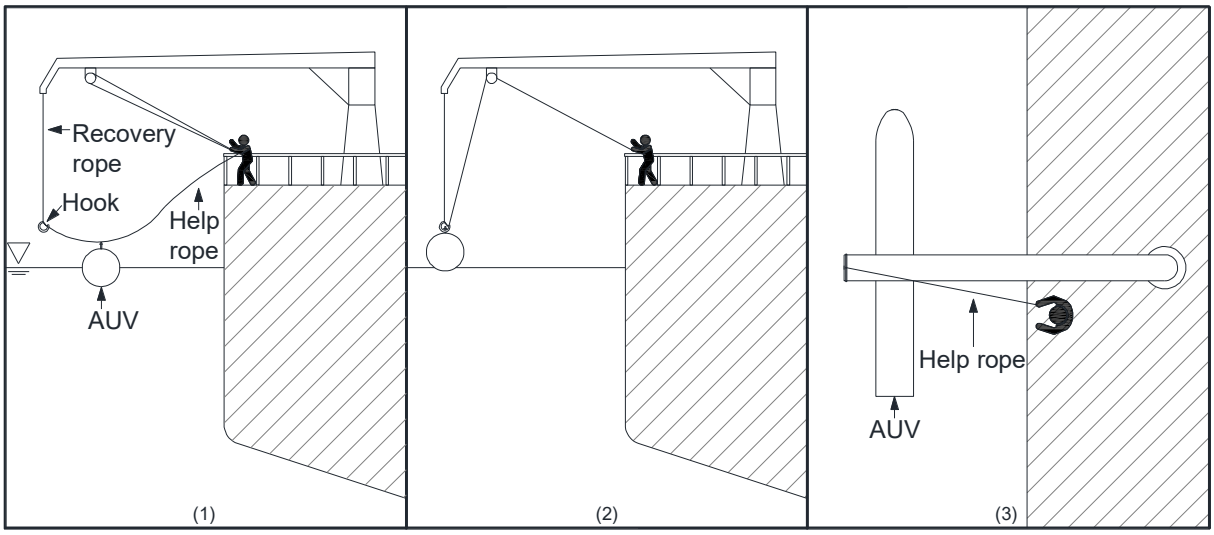


Figure 2-10: AUV caught by a painter line
(1) rear view - the AUV approaches the help rope laid out as a loop and becomes entangled in it, e.g. with an eyelet **(2)** rear view - by pulling the help rope the hook at the end of the recovery rope will get attached to the AUV **(3)** top view - shows the arrangement of AUV to carrier platform

2.3.2 Automatic procedures - AUV surfaced

Painter lines can be applied for the automatic establishing of initial physical contact in various forms. One technique is illustrated in Figure 2-11. Thereby painter line is pulled behind the carrier platform. Trawl boards are used for setting out a painter line orthogonal to the direction of travel. The AUV features a unique technique for establishing a connection with the capture line. An example of a mechanical latch is a hook. Such a capture hook is advertised, for example, by H. Henriksen on their website for L&R of AUVs using their Stinger system [88].

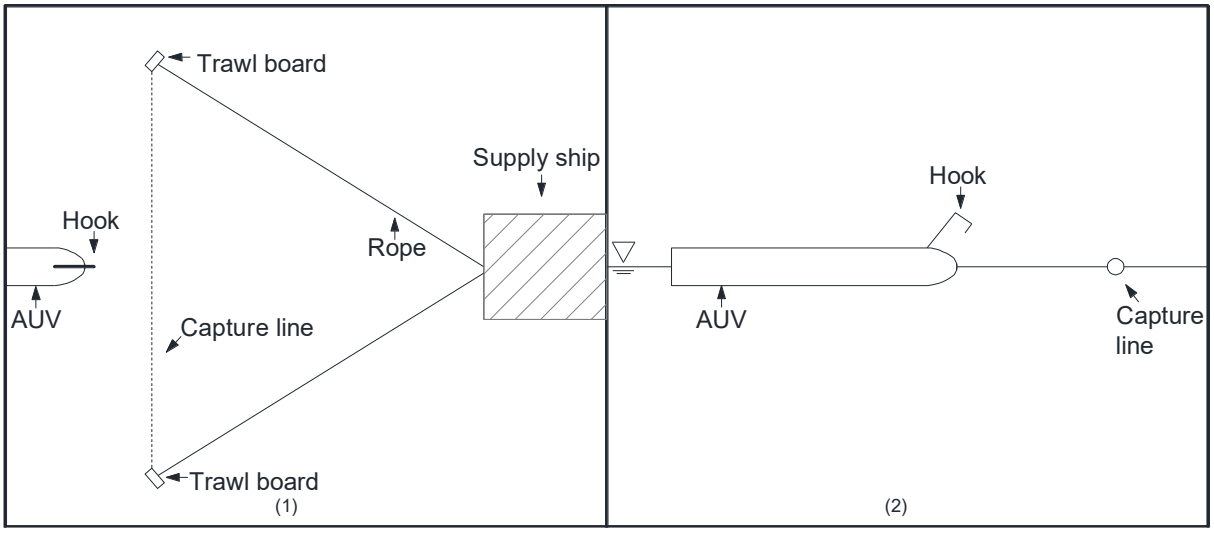


Figure 2-11: Surfaced AUV snatch at a painter / capture line
(1) top view - the AUV approaches the capture line, which is spanned perpendicular to the direction of travel with the trawl board **(2)** side view - the hook mounted on the AUV is used to grab the capture line

In the context of this automated procedure, it is essential to ensure that the line connection is securely fastened. This can be accomplished by using suitable sensors. The retrieval of the AUV poses challenges in terms of recovering both the AUV itself and the trawl boards tied to the line.

A similar version of this technique is defined in United States patent US000007350475B2 [89] and illustrated in Figure 2-12. This approach utilises a recovery rope, which is held apart on tension through the use of several trawl boards that are connected to a moving carrier platform. The primary concept is the strategic placement of a rope, either positioned on the water surface or partially submerged, below the AUV during the phase of recovery. During positioning, the rope establishes contact with a specifically engineered hook or hanging rope on the AUV. After this interaction, the line is systematically pulled back towards the carrier platform. [89]

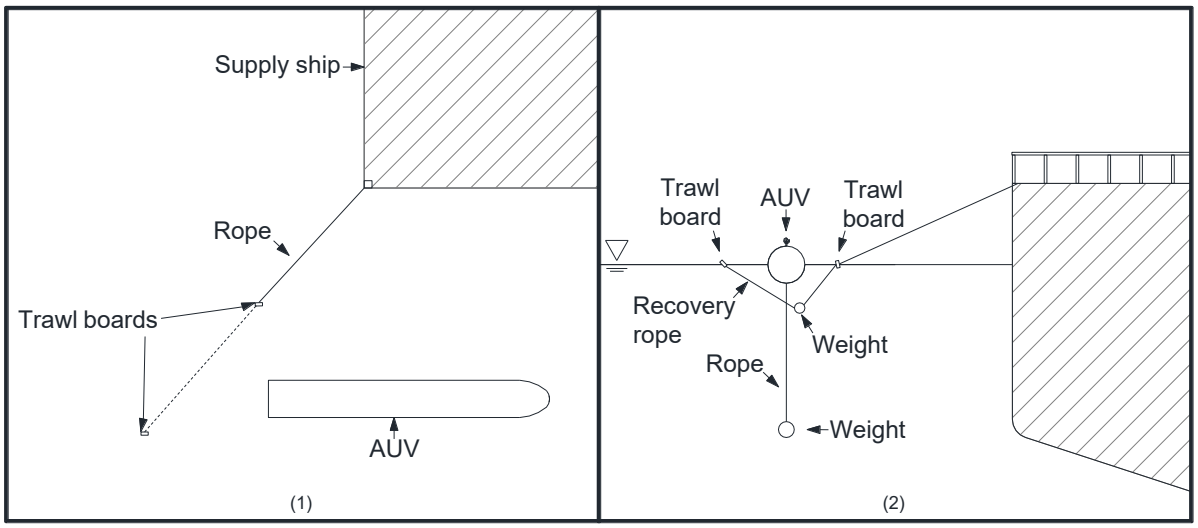


Figure 2-12: Automatic AUV caught by a painter line (according to [89])
(1) top view - the AUV is in forward motion and overtaken by the carrier platform, which is towing a recovery rope at the side **(2)** rear view - the recovery rope is tensioned by trawl boards and pulled underwater by weights - a rope released from the AUV and tensioned downwards by weights, gets caught in the recovery rope

Another painter line technique involves the release of a buoyant line from the AUV. The host platform lowers another rope that is fitted with a drogue anchor to ensure tension is maintained into the water. The initial contact is established by entangling the two lines with each other. Therefore, various manoeuvres can be performed by the AUV and host platform to achieve successful contact. In one manoeuvre, the host platform crosses the AUV's path diagonally to lay out the line in front of it. Another method involves the AUV crossing the path behind the carrier platform to capture the line. While crossing under the buoyant line, the AUV latches itself to the line by means of a recovery hook. Once the rope has been attached, it is pulled back using the winch. The line runs through the recovery hook until the drogue anchor is successfully fitted on it. [90]
A related method is described in Patent US020170259887A1 [91]. The system includes a floating body connected to the host platform by a line. During recovery, the floating body is deployed into the water, emitting location signals that guide the UUV towards it. The vehicle is equipped with a catch device designed to latch onto the line connecting the buoy and the host platform. The catch device, positioned on the vehicle's outer structure, may be fixed or retractable, allowing for streamlined operation when not in use. Once the catch is made, a spacer along the line helps prevent collision between the floating body and the vehicle. Subsequently, the host platform can retrieve the vehicle by hauling it in via the line, using a ramp or a crane system for lifting it on board. [91]
Analogue to gripping a line, solid objects such as a rod, can also be gripped. A corresponding method is explained in patent GB000002581091B. [92]

Similar to manual grabbing from a tender or, in the case of larger vessels, using an extension such as a boat hook, grabbing an AUV can also be automated. The procedure includes a **grab arm** mounted on the host platform. During the process of recovery, either the AUV manoeuvres under the crane or alternatively, the host platform positions itself and the crane above the AUV. The grab arm is designed to engage an eyelet on the watercraft or fully grab around the AUV, allowing it to be lifted on board. The procedure is illustrated in Figure 2-13.

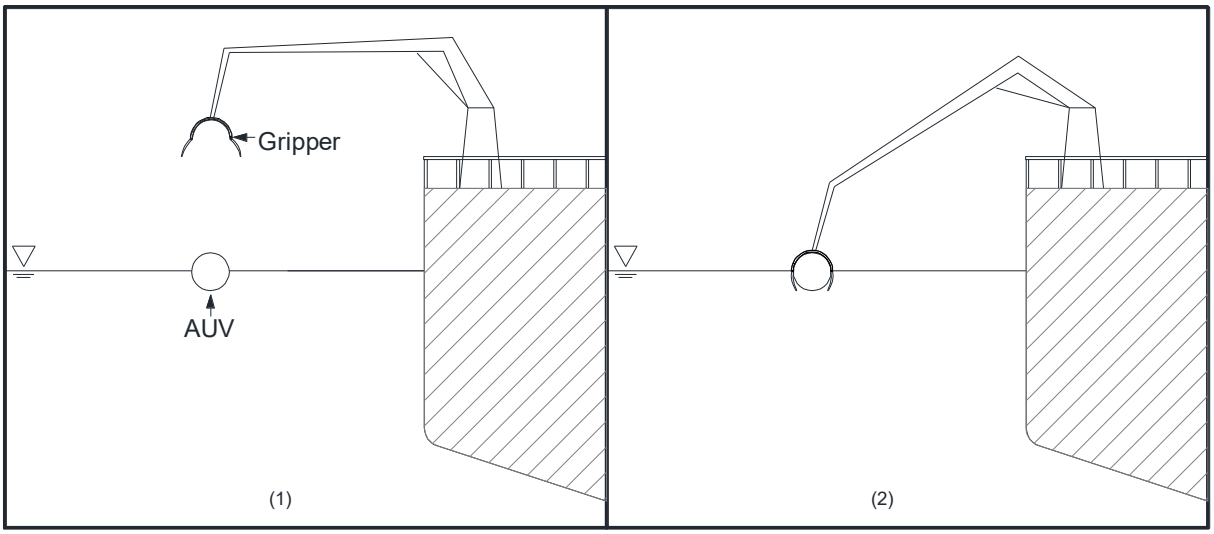


Figure 2-13: Grabbing an AUV with robot arm
(1) rear view - AUV and carrier platform are so close that the AUV is in the gripper's range
(2) rear view - the gripper encloses the AUV for the subsequently lifting operation

Companies such as DECK Marine Systems are developing these principles in the current research field by using artificial intelligence. On their website, they advertise their Artificially Intelligent Launch and Recovery System for AUV handling. This technology features an artificial intelligence-powered control system that can do complex computations and forecast the most advantageous times for capturing the AUV. For best capture, it is ideal for the AUV to be positioned horizontally, at either a wave peak or valley. The main difficulty is in precisely forecasting these motions considering the distinct sea behaviour of the AUV and the carrier platform. The gripper is designed to shadow the AUV's motion, keeping a distance of around 1 metre, until the exact moment for interaction. [93]
Critical considerations in this context include the necessary accelerations, the weight of the AUVs to be raised, wave impact loads and safety margins. These factors consistently lead to the necessity of a powerful and strong robotic arm. In this context, various ratios of recovery mechanism to AUV, such as weight or cost, must be considered. Moreover, it is essential to consider that the implementation of a gripping device may not be feasible on all carrier platforms due to constraints such as limited space, stability issues or the necessary on-board infrastructure for crane operation.

A mixed form of automatic grabbing and utilising a painter line is described in Patent EP3512767B1 [94], which details a device designed for attaching a coupling mechanism to a free-floating object, addressing challenges such as vessel motion and manoeuvrability. The invention consists of a coupling system that has two key elements: a load-bearing connection and a guiding device, which function collaboratively to stabilise and secure the floating object. The load-bearing connection, typically a rope or chain, directly supports the object’s weight upon coupling, facilitating its recovery through a lift device. [94]

The guiding device, separate from the load-bearing mechanism, enables precise alignment and controlled motion of the coupling system relative to the floating object. This guiding component often employs linear actuators, which may be pneumatic or hydraulic, to adapt quickly to the object's motion, reducing the relative motion between the coupling point and the object. This controlled manoeuvring mitigates the risk of collision or damage during recovery, even under turbulent sea conditions. [94]

The utilisation of **nets** to retrieve floating objects, such as AUVs, is a simple yet efficient approach in marine operations [11, 12]. Figure 2-14 shows the basic principle of a net based recovery. In order to achieve efficient retrieval through the utilisation of a net, it is imperative that the net maintains a consistent area. This feature enables the AUV to run into or precisely position itself over the net. After being lifted from the water, the net's adaptability allows it to adjust to the shape of the AUV. The positive aspect of this versatility is in its capacity to accommodate a wide range of forms and sizes of AUVs. Furthermore, the compact configuration of nets during periods of non-utilisation offers a notable advantage, as they may be stored in a very efficient way aboard the host platform. When stowing the AUV, the challenge is in removing the AUV from the net if it is not intended to be inserted and stored within it. Moreover, there is a high probability of causing damage to sensitive add-on components of the AUV and of becoming entangled with essential parts of the AUV, such as rudders or propeller blades. Furthermore, the suitability of nets for AUV recovery is generally limited to small and light UUVS, due to the inherent load-bearing capacity of the flexible systems.

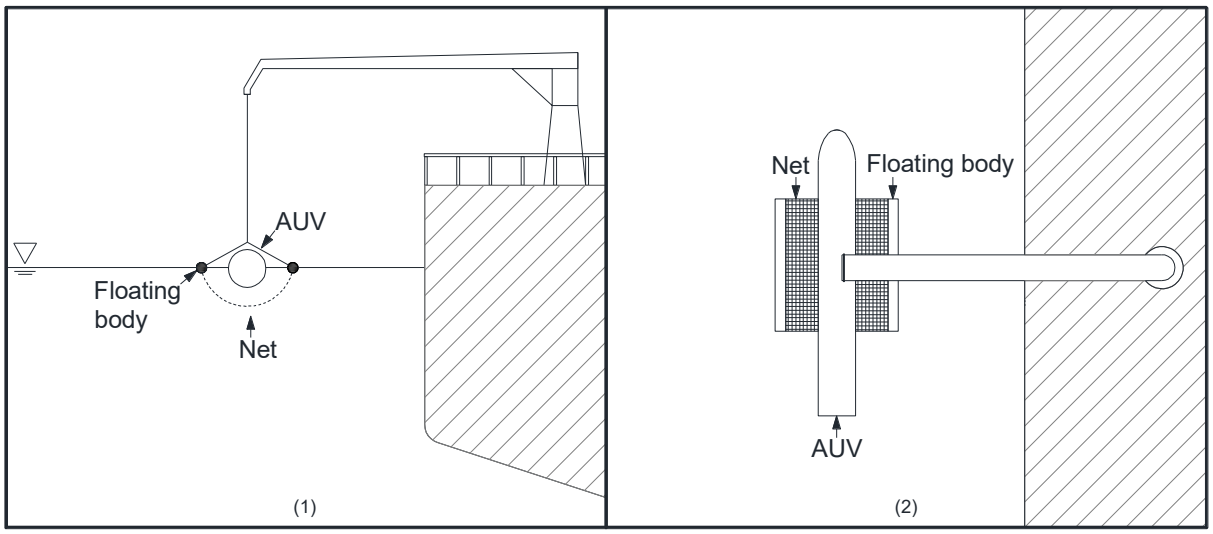


Figure 2-14: Capturing an AUV with a net
(1) rear view - the net is lowered from the crane, hangs in the water and is held on the water surface by 2 floating bodies **(2)** top view - the AUV is positioned in the net for the subsequent lifting operation

An alternative method of this technique, where the AUV is not required to actively enter the net, entails enclosing the AUV within a net. In this scenario, a net equipped with weights is placed over the AUV. The use of weights enables the encasing of the AUV within the net. [11]

Another net-based recovery approach is defined in German patent DE 100 45 911 B4 [95]. This patent describes a surface-level recovery manoeuvre involving a net towed on the water's surface. The AUV is required to position itself under the trawl net, where it becomes hooked into the net via a surface hook on the AUV. The efficacy of these systems relies on the accurate positioning of the AUV under the net. [95]

Another net based procedure is described in Patent US000011447209B2 [96]. The invention centres on a catamaran or Small Waterplane Area Twin Hull (SWATH) ship featuring a net suspended between its hulls. During recovery, the net is lowered into the water, allowing the AUV to enter the gap between the hulls. When the AUV reached the designated position the net is raised, securing the AUV for transport. [96] Similar to a net, slings can be used as described in [97].

The concept of utilising **inflatable components** for the L&R of AUVs presents a unique approach. The technology described in the study conducted by Rosie [98] is founded upon a configuration of inflatable fenders that are connected to a mat. This mat extends between two buoyancy bodies. The operational procedure begins with the lowering of the mat into the water from the stern of the host platform. The AUV places itself over the mat guided by a transponder positioned at the mat. After correctly positioning the AUV above the mat, the inflatable fenders get inflated, completely surrounding the AUV. The inflation of the fenders results in the enclosing of the AUV by the mat, thus locking it within the system. An alternative version of this method involves the inflation of the mat's sections. Furthermore, a net located at the rear of the apparatus serves as an additional layer of security, ensuring that the AUV does not accidentally slips out of the device. After the safe enclosure of the AUV, the entire assembly is then recovered onto the host platform by a ramp. Inflatable element-based recovery systems offer several benefits, including its capacity to adapt to various AUV geometries, ensure the secure encasing of the AUV during the recovery process. [98]

Another method that is also used for recovering smaller boats or surface vessels is the use of **surfaced docking devices**, also referred to as **cradles**. These cradles reveal a variety of forms and functionalities, offering the choice between a fixed or a detached connection to the carrier platform. In the latter configuration, the cradle operates independently on the water's surface, connected to the platform through tethers.

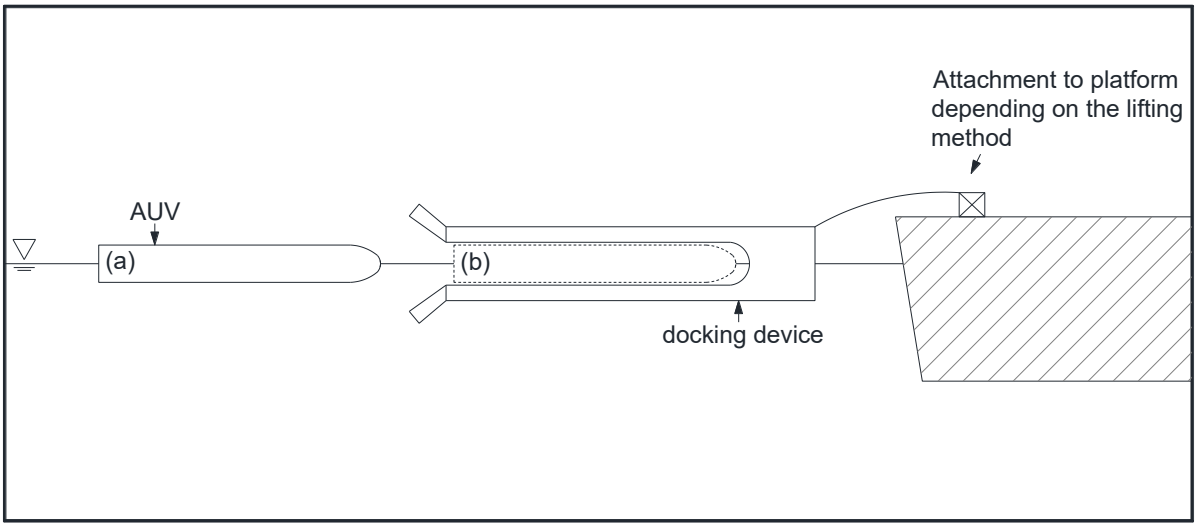


Figure 2-15: AUV docks into a surfaced cradle
Side view (a) AUV aligns itself to the towed cradle (b) after entering, the AUV is fixed in the cradle

These cradles are towed by the carrier platform for two main reasons: to minimise collision risk by maintaining a distance between the AUV and the carrier platform and to disassociate the motions of the two entities [11, 12]. A possible design of this process is described in US patent US 2010/0018449 A1 [99].
The advantage of these systems lies in their ability to facilitate docking with a moving platform,

increasing operational flexibility and lessening the necessity for the carrier platform to stop or decelerate for AUV recovery. This feature proves particularly beneficial in challenging environments where maintaining a static position could be hazardous or impractical due to the need for continuous forward propulsion. [12]
Docking entails the AUV navigating into the cradle. Typically, the AUV autonomously steers into the cradle, necessitating full operational functionality. This demands precise control and autonomy from the AUV, enabling it to independently locate and align with the moving cradle. However, there are also self-propelled cages designed to accommodate non-functional AUVs. In such scenarios, the cradle manoeuvres over the AUV, requiring technologies already present in the AUV like sensors, actuators and propulsion systems. [14]

Upon successful entry of the AUV into the cradle, the lifting process commences, involving the secure fastening of the AUV to prevent accidental release. These systems are therefore equipped with sensors and actuators for functions such as securing the AUV in place. The cradle's design is pivotal, serving not only to ease docking but also to protect the AUV from potential damage during lifting. [11]
The design and operational characteristics of a docking system, such as size, controllability and approach speed, are closely linked to the AUV's attributes. The ability of an AUV to dock precisely depends on its configuration and control capabilities. Hover-capable AUVs are particularly suitable for precision docking due to their ability to approach the dock at low speeds. [14]

2.3.3 Automatic procedures - AUV submerged

Submerged docking stations for the L&R of AUVs operate similarly to those used at the surface in function but offer distinct advantages due to their deployment underwater. One of the most significant benefits of underwater docking at sufficient depth is the independence from sea conditions. Unlike surface docking systems, which are directly influenced by waves and surface weather conditions, submerged docking stations, when positioned at an appropriate depth, are considerably less affected or even unaffected by surface sea conditions. This advantage arises because the effects of sea state, such as wave action and surface turbulence, diminish with increasing depth. Therefore, the stability of the docking environment is enhanced underwater. [7, 100]
The extent to which the sea state affects underwater operations varies and depends on several factors, including wave height, wave period and the prevailing weather conditions. Generally, the influence of surface conditions reduces with depth. This phenomenon is discussed in more detail in chapter 4.

When considering docking procedures, it is essential to differentiate between stationary and non-stationary docking techniques. Stationary docking refers to a dock that is fixed on the seabed and does not move, whereas non-stationary docking involves a docking device that is either towed or connected to a carrier platform. [14]
Stationary docking stations are widely used in marine research and offshore installations, where regular inspections of underwater structures are mandated. While these stations, often permanently installed on the seabed, are not typically utilised for the L&R of AUVs, their application offers valuable benefits. To avoid the need for AUV retrieval after each operation, these stations are equipped with power and data cables. This setup allows the specifically designed AUVs to be recharged and transmit data to the surface while docked. This reduces the necessity for frequent L&R manoeuvres. [100, 101]

Within the scope of this thesis non-stationary docking methods are examined. An example of such a method is illustrated in Figure 2-16. In Figure 2-16-a, the AUV aligns itself relative to the docking device. Subsequently, in Figure 2-16-b, the AUV enters the docking station and is then secured in the dock for the following lifting operation.
The next sections will outline the benefits and difficulties associated with this technology and provide an overview of its several variations. In addition, comparable docking techniques are being examined.

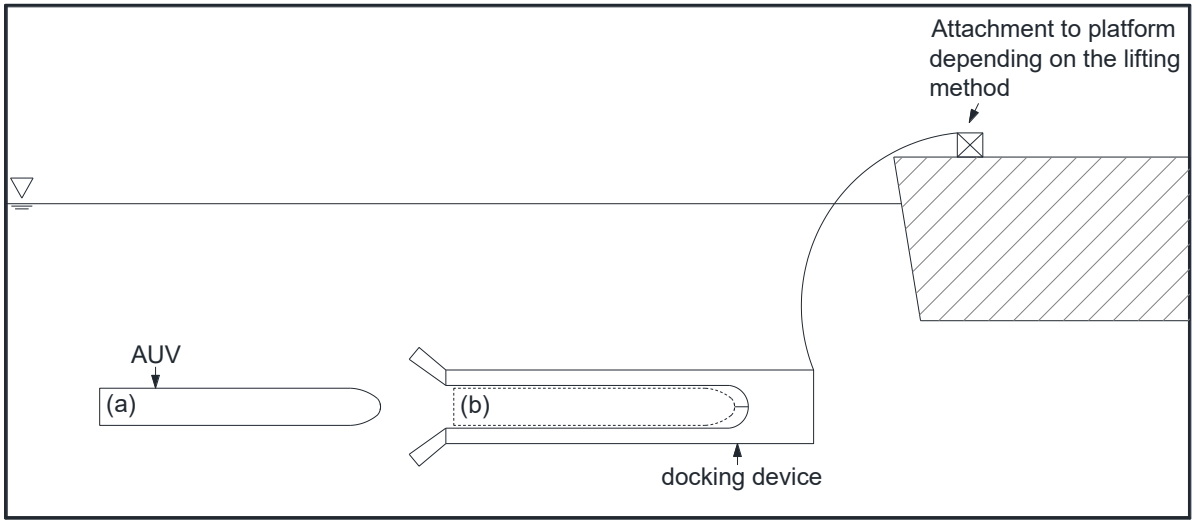


Figure 2-16: Underwater docking into cradle
Side view (a) AUV aligns itself to the towed cradle (b) after entering, the AUV is fixed in the cradle

A primary concern of towed underwater docking systems is the transfer of sea-induced motions from the carrier platform to the docking station, typically occurring through the towing connection, often a line or cable. This transfer can result in unwanted motions of the docking station, potentially complicating the docking process and posing risks to the AUV and the equipment.
To mitigate these challenges, several strategies can be implemented. Effective mitigation often involves incorporating damping elements within the towing connection. Utilising longer towing lines can provide a natural damping effect, as their length and elasticity can absorb some of the motions induced by the sea. Furthermore, the integration of sea-compensating winches represents a more sophisticated approach. These winches are designed to adjust the tension in the towing line based on real-time sea measurements, ensuring a more stable connection between the carrier platform and the docking station. Such technology is instrumental in maintaining the positional stability of the towed docking station, which is essential for smooth and successful docking operations.

The manoeuvrability of AUVs underwater compared to surfaced conditions significantly impacts their ability to dock successfully [14]. Compared to surface operations, underwater docking involves additional degrees of freedom, as depth positioning becomes a critical factor when entering the docking station. This aspect adds complexity to aligning and entering the station, making the process more intricate than it might be at the surface. To mitigate the risks of unsuccessful docking, the openings of AUV docking stations are often designed as large cones. This design allows the AUV to guide itself along the cone into the actual docking mechanism, simplifying the final stages of the docking process.

Key aspects in handling docking technologies include position determination, navigation and target recognition. The on-board inertial navigation systems of AUVs play a vital role in position determination, offering a reliable means of understanding the vehicle's location relative to the docking station. The control of underwater docking is facilitated through various systems: acoustic, optical and electromagnetic.
Especially in close proximity to the docking station, implementing an additional control system is advantageous. This redundancy ensures greater accuracy in the final approach and docking phases. In cases of unsuccessful docking, it is essential for the AUV to identify the failure, return to its former location and commence another docking attempt. Such a process requires the AUV to have a high level of autonomous decision-making capability, allowing it to adapt its behaviour based on real-time assessments of the docking procedure. [14]

Underwater docking stations can vary significantly in design and functionality, tailored to different operational needs and deployment environments. The following sections provide an overview of current research and various docking station configurations.
In Guo et al. [102] the authors present a funnel-shaped docking system designed for wired charging and data transmission. The system includes hydraulic mechanisms that actively adjust the AUV's position and orientation to ensure secure physical connection. The docking station was tested in lake trials and proved capable of guiding the AUV into position using acoustic signals and performing high-power electrical charging through direct contact. [102]
A similar cone shaped dock is presented by Sun and Han [103]. They propose a vision-based docking system that relies on optical landmarks placed around the docking station and a deep learning algorithm to identify and track these markers during the final approach. The AUV switches from acoustic to visual guidance as it nears the dock, allowing for precise alignment and positioning. The system was validated both in controlled pool environments and in natural lake settings, where it demonstrated robust performance even under visual disturbances. [103]

Zhang et al. [104] focus on the mechanical interaction between the AUV and a cone-shaped docking station. They simulate the physical impact during docking using a dynamic model and evaluate how the AUV behaves when approaching the dock under different conditions. The aim is to ensure that the AUV can enter the docking cone without damage and maintain structural alignment for energy or data transfer. [104]
Wu et al. [105] conducted a detailed computational study of the hydrodynamic interactions between an AUV and a cone-shaped dock. Using dynamic mesh simulations, they investigate how the shape of the dock and the approach strategy affect forces on the AUV. The goal was to optimise the docking procedure by minimising drag and lateral forces, ensuring that the AUV can align itself with the dock even in the presence of ocean currents. Their work identified optimal dock shapes, preferred approach velocities and control strategies under ocean current disturbances. They show that cone-shaped docks with specific geometries minimise drag and are easily identifiable via sonar. Moreover, they find that docking success in currents depends critically on the approach angle. [105]
A further study on underwater docking is documented by Meng et al. [106]. The authors examined dynamic docking systems, which involve moving docking stations towed by surface vehicles. They explored two main types: captured-style systems, where the AUV grasps a rope or rod and guided-style systems, where the AUV enters a funnel-like guide. These mobile systems are designed to extend the operational range of AUVs and reduce downtime by enabling mid-mission docking. [106]

In Patent DE 60208256 T2 [107], a L&R device for UUVs is described, focused on mitigating vertical motions that could disrupt L&R operations. The invention features a modular structure with an upper and lower frame linked by flexible cables, creating an adjustable enclosure or cage. The distance between the frames can be modified to allow the vehicle to enter and exit smoothly, avoiding the impact of wave-induced vertical oscillations on the vehicle's position within the cage. The system's cable-based linkage adjusts the frames' positions, managed by cable reels and motors, enabling swift alignment. This dynamic flexibility allows for reliable positioning of the vehicle, even as the cage itself responds to surface wave actions. The lower frame includes a concave holding plate that securely positions the vehicle upon recovery. An upper frame incorporates a holding fixture to stabilise the vehicle vertically during transport. To further aid stability and prevent damage, the invention employs damping buffers between the frames. [107]
The invention in Patent WO 2000/071415 A1 [108] aimed at stable docking, data transfer and energy replenishment. This device uses a closable cage-like frame equipped with mechanisms for precise vehicle alignment and locking. It features centring pads and guiding structures that position the vehicle during docking. A unique configuration includes adjustable cables between the frame and a counterweight or seabed anchoring point, stabilising the device while in operation. The system also incorporates inflatable bags within the frame that gently lock the vehicle into place, enabling secure docking without physical jamming. Additional stabilising wings interact with the vehicle's dorsal fin to ensure alignment within the frame and prevent unwanted motion. The device allows for battery recharging and data exchange through a specialised connector arm integrated into the frame. [108]

In DE20316247U1 [109], the system for L&R of UUVs from a surface vessel relocates the coupling point underwater, below the surface in close proximity to the host platform. The device incorporates a guidance structure that shifts between a on-board / surface-level position, used during storage or transit and a submerged L&R operational position. The guidance structure is designed to engage with the bottom of the UUV. This device is preferably articulated or swivelling, enabling it to adjust to the varying angles and positions at which the UUV may approach the docking station. It includes a latching mechanism to secure the vehicle and has a support framework with cushioning elements that support the vehicle during recovery. The docking process is further facilitated by a damping element that mitigates relative motions caused by wave action, protecting both the vehicle and the system. During recovery, the UUV is guided to the docking point where it is latched to the receiving structure. The guiding mechanism then swivels or retracts from submerged to on-board position. During this shift the UUV maintains in a stable, horizontal orientation. [109]
In US20220063780A1 [110], a docking station is designed to facilitate AUV recovery by positioning the AUV in a submerged cradle towed by the host platform. The station features a longitudinal beam and a stop mechanism that align with the AUV's body, applying a controlled pitch to maintain stability even in adverse sea conditions. This setup ensures a precise alignment between the AUV and the docking station, facilitated by a negative pitch angle of the station when fully submerged and hauled, stabilising the docking process. Key to the alignment is the hydrodynamic profiling of the docking station, along with a carefully distributed centre of gravity and buoyancy. Upon the AUV's approach, it is guided into the station by adjustable arms arranged around the stop. These arms can transition between a deployed configuration for docking and a compact state for on-board storage. Once the AUV nose contacts the stop, the AUV is pressed firmly against the dorsal beam. This configuration enables a secure connection through locking mechanisms such as latches or structural grips. [110]

Another LARS for UUVs, employing a towed docking mechanism is described in patent WO002020058408A1 [111]. It includes a towing head equipped with a locking mechanism to secure the UUV and a docking receiver, submerged to avoid wave interference in the splash zone. To minimise impact forces a dual-stage docking approach is used: the initial step occurs between the UUV and the towing head, followed by the second stage between the towing head and the docking receiver. The system ensures precise alignment between the towing head and the docking receiver through controlled mechanical motions and structural designs. The docking receiver, manipulated by a lifting device, moves along a fixed trajectory relative to the host platform. It prevents lateral shifts and allows for controlled submersion and retrieval of the UUV. Guidance is further enhanced by the use of mechanisms such as articulated arms or guiding funnels with active elements that align the vehicle. Thrusters and fins integrated into the towing head aid in fine-tuning alignment underwater. These features collectively facilitate the secure transfer of power, data and mechanical coupling during operations. [111]

The JP2015231779A [112] patent offers a storage solution and method for launching and recovering diverse UUVs. This design caters to scenarios where the UUV is vulnerable to collisions during hoisting, enhancing the durability and lifespan of both the vehicle and supporting infrastructure by reducing the potential for damage. The device features a fender structure encasing the vehicle during L&R and a connector, designed to interface seamlessly with a corresponding docking mechanism on the AUV. The AUV uses its on-board systems to precisely align and dock with the connector at the fender, securely attaching itself to the rope. By pulling in the rope, the AUV slides inside the fender towards its designated storage position within the device. [112]
In Patent CN000114426088B [113] AUV LARS employing a two-rod triggering mechanism to achieve precise alignment and secure docking is described. The platform consists of a modular support structure divided into three sections—rear, middle and front—connected by hinges and transverse rods. A cone shaped guide door, lined with cushioning material, facilitates initial alignment and protects the AUV from collision forces during entry. The guiding door adjusts minor misalignments, ensuring the AUV's successful navigation into the platform. Central to the invention is the two-rod locking mechanism, located in the middle section. This mechanism comprises a front capture rod and a rear capture rod, each pivoting on separate rotary shafts. These rods interact with fins installed on the AUV's lower structure. As the AUV advances, the front rod engages its forward fin, while the rear rod secures the rear fin, restricting motion along the longitudinal axis. A torsion spring-driven system aids this locking process without requiring external power. Further stability is achieved through a clamping groove system at the platform's front section. This groove engages a limiting rod on the AUV, ensuring precise longitudinal positioning. Once docked, the platform is lifted, with the locking mechanisms and clamping grooves securing the AUV during recovery. [113]

UUVs are also launched and recovered from other UUVs or crewed underwater vehicles such as submarines. The recovery technique is frequently challenging due to currents around the two underwater vehicles involved, as well as the relative motions between the mother underwater vehicle and the UUV to be captured.
Patent WO002013092216A1 [114] describes a system for retrieving a UUV into a flooded tender garage on an underwater host vessel. The primary feature involves a positioning flow mechanism that guides and centres the vehicle within the tender's entry zone. Strategically placed positioning nozzles around the entryway generate directed currents, creating a hydrodynamic funnel that directs the vehicle precisely toward the centre. This structured flow

minimises lateral drift and aligns the vehicle for entry. The vehicle is either self-driven or passively drawn into the garage by suction generated from a pump. This dual-purpose suction stream reinforces vehicle alignment and stabilises it within the funnel as it enters the garage. An internal capturing head secures the vehicle's front end attachment to the garage for the process of hauling in. [114]
Another related device is detailed in Patent US 020080302292 A1 [115], which outlines a telescoping, moveable tube apparatus For UUV L&R using a reconfigurable insertion/extraction mechanism. This device transitions from a retracted tube or ring to an extended funnel. During recovery, it utilises a funnel-shaped guide that compensates for slight misalignments, guiding the AUV into the apparatus. The telescopic design minimises storage demands and does not require significant modifications to the host vehicle. [115]
Patent US 000011377183 B2 [116] presents an AUV L&R device designed for extra-large unmanned underwater vehicles. This invention employs an elastic linkage mechanism combined with a hydraulic system to facilitate the controlled L&R of smaller AUVs. The device incorporates a tubular frame with a closed-end structure, where a push plate, affixed to a hydraulically driven rod, slides within a groove to activate the system. Through coordinated motion, the push plate adjusts the diameter of a ring that encircles inelastic ropes. This operation enables the opening to expand or contract by pulling on elastic rubber plates that form a cage-like structure. The invention allows the AUV to be launched or captured within a specific recovery zone and the flexibility of the cage structure reduces hydrodynamic drag on the host vehicle. [116]
A further method is described in Patent EP000002838788B1 [117], which details a recovery approach utilising wave propagation techniques to achieve precise alignment between a UUV and its recovery apparatus on a submerged host platform. Additionally, this patent describes a docking setup where the AUV is manoeuvred into alignment with a docking structure on the host platform. The docking structure can either be positioned within the garage for direct docking or extend outwards to connect with the vehicle before retracting to bring it into the garage. [117]

Docking stations can vary in size and may either fully or partially enclose the AUV. In some cases, only a **quick-release connection** is established while docking. When using a quick-release mechanism, a controllable docking device can be employed. For instance, a **ROV** can

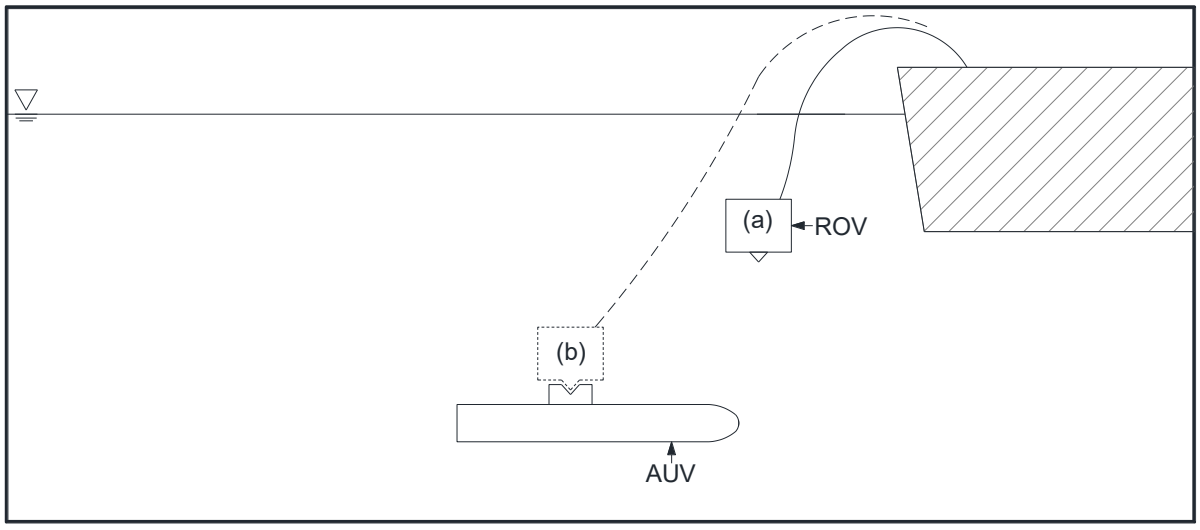


Figure 2-17: Establishing initial contact using a ROV
Side view (a) ROV approaches the AUV (b) ROV establishes a connection with the AUV

be used to create the physical connection as a docking station. This method is illustrated in Figure 2-17. Figure 2-17-a shows how the ROV, controlled from the carrier platform, approaches the AUV. In Figure 2-17-b, the ROV establishes a connection with the AUV using the quick-release mechanism.
US Patents 3 367 299 [118] and 6 189 476 B1 [119] describe the utilisation of an additional UUV to establish initial physical contact with the AUV. This UUV connects the host platform to the AUV. The inventions effectively separate the host platform from the AUV by performing the recovery operation at a depth that is not influenced by wave motions. The patents differ in their approach to this solution; Patent 3 367 299 employs a gripping device, while Patent 6 189 476 B1 utilises a coupling device. [118, 119]
Similar approaches are described by Dahn et al. [120] and by Ritz et al. [121].

The invention described in the patent WO2019207263A1 [122] outlines a system for L&R of AUVs using a ROV linked to a surface vessel via a tether. The ROV serves as an intermediary as docking station. This approach implies that the AUV does not necessarily have to run in the docking device. Rather, the docking device can be positioned on the AUV. The docking station on the ROV is conically shaped, functioning like a funnel to guide the AUV into position. Both the docking station and the AUV are equipped with docking mechanisms. The docking system enables the ROV to securely attach to the AUV. This system capitalizes on the ROV's stabilising capabilities, which allow it to maintain steady positioning despite underwater currents or surface vessel motions. The AUV's propulsion and stabilization mechanisms aid this process, ensuring a seamless and controlled connection. Once docked, the ROV carries the AUV back to the surface vessel for further operations or storage. [122]

Similar to a ROV dock onto an AUV, the AUV can dock directly to the carrier platform. Studies by Xu et. al. [123] investigate hydrodynamics of a Remora-inspired AUV approaching and docking to a benchmark submarine. This study introduces a dynamic underwater recovery mechanism leveraging the hydrodynamic advantages observed in remora fish when attached to larger marine hosts. In the Studies by Xu et. al. a remora-inspired AUV design was conceived, utilising CFD simulations to identify optimal docking locations on a submarine. [123]
Analogous the submerged submarine itself can serve as an active docking platform. Currie et al. [124] propose a dynamic docking mechanism attached to a slowly moving submarine that utilises either a actuated arm or wing to intercept an approaching AUV.

Similar to the processes on the surface, **painter lines** can also be gripped automatically underwater. A standardised procedure is illustrated in Figure 2-18. Underwater techniques are applied to reduce the impact of the sea conditions. Nevertheless, in contrast to the act of grabbing on the water surface, the AUV requires alignment in an additional amount of degrees of freedom. The length of the painter line's docking segment determines the vertical aperture, while the capture mechanism's width on the AUV specifies the horizontal aperture. A benefit of this system is the AUV's ability to approach from any direction in the x-y-plane. The execution of these processes involves the utilisation of a grabbing mechanism on the AUV, which frequently looks like an extended pair of scissors, together with a corresponding counterpart for the gripping device such as a rope or, in certain instances, a pole.

The initial step in the recovery operation of the ARTEMIS AUV involves the deployment of a recovery line from a carrier platform into the water. A depressor and an acoustic transponder are attached at the bottom end of this line. After detection of the line, the AUV starts to navigate

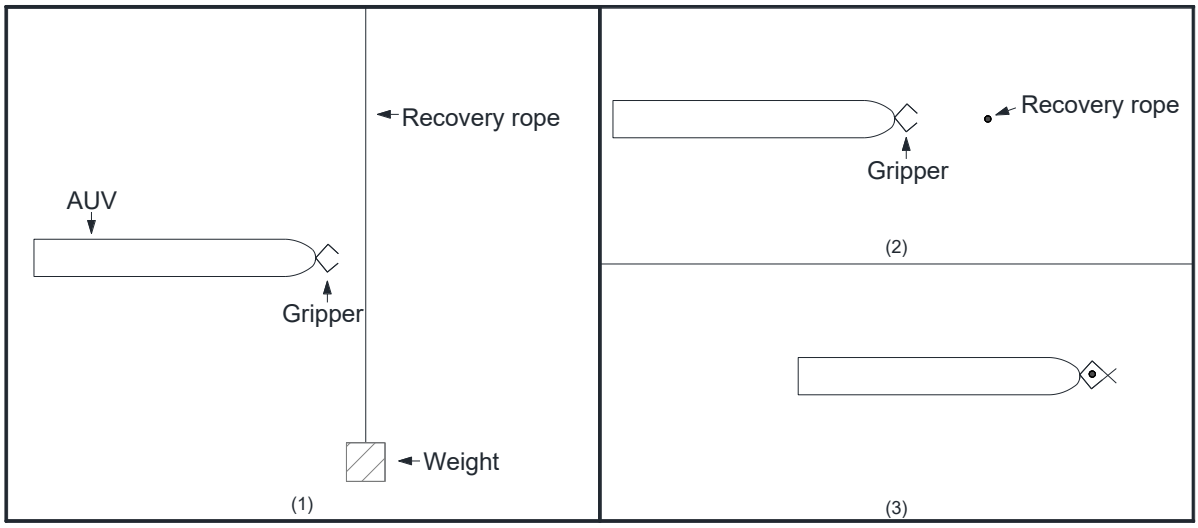


Figure 2-18: Automatic underwater rope grab
(1) side view - the AUV approaches the vertically suspended recovery rope with its gripping mechanism (2) top view - the AUV approaches the recovery rope with its gripping mechanism (3) the AUV grabs the recovery rope

towards it and utilises a grabbing mechanism mounted to its front in order to securely attach the line. [125]
The approach followed by the MARLIN AUV from Lockheed Martin differs slightly. The AUV also features a gripping mechanism at the front and docks to a recovery line equipped with an acoustic transponder at its lower end. The main difference is that the line is suspended from a docking device positioned on the surface of the water. The final recovery step involves pulling the AUV against the docking device and lifting both with a crane. [11]
The Woods Hole Oceanographic Institution's docking system demonstrates an alternative approach. The system features two frames that are joined together by a pole. The lower frame of the system contains pressured housings designed for holding electrical components. The top frame is fitted with an acoustic transponder and can be moved along the pole. The AUV specifically engineered for docking with this station is equipped with two V-shaped rods positioned at its front. The rods are interconnected by a locking mechanism. During the docking procedure, the AUV aligns itself with the pole, enabling the rods to connect and form an initial physical connection. The motorised top frame subsequently lowers, securely fastening and aligning the AUV between the two frames. [78]
Similar approaches are outlined by Wirtz et al. [126] and by Palomeras et al. [127].
A comparable cable capturing method is described in Patent CN000115009473B [128]. The system includes a cable winding and unwinding mechanism, a deflector rod mechanism and a pressing rod mechanism, which work together to achieve alignment, docking and securing of the AUV during recovery. The procedure starts with the cable mechanism releasing a mooring line attached to a buoyant sphere. The floating sphere aids in positioning via the AUV's vision system. Upon capturing the cable, the AUV is guided by retracting the floating ball toward the recovery platform. As the AUV approaches the V-shaped groove, the deflector rod mechanism adjusts its alignment. The rods, arranged symmetrically and capable of controlled rotations, ensure the AUV's axis aligns with the platform. Once positioned, the floating ball presses the AUV downward into the groove. The pressing rod mechanism locks the AUV securely by limiting its degrees of freedom. The rubber-padded V-shaped groove further restricts rotational motion, ensuring stability. [128]

Similar to grabbing the AUV with a robotic arm on the water surface, the AUV can be grabbed in a submerged state. The paper by Koch and Firvida [129] introduces an approach to perform precise docking manoeuvres with a docking station that is equipped with a robotic manipulator that actively tracks and captures the approaching AUV. The authors develop a method for analysing feasible docking poses using a novel dockability metric, which evaluates how effectively the manipulator can follow the AUV's motions. This analysis supports the selection of an optimal path for approaching the dock, ensuring that the AUV can be successfully docked even if it deviates slightly from its intended trajectory. Experiments demonstrate the feasibility of the method. The results show that while active docking is possible, the performance is affected by the AUV's lateral velocity and the controller's responsiveness. [129]

The following publications are recommended for more detailed explanations and examples of LARS: Liu et al. [14], Mischnick [11], Chakrabarti [7] and Sarda [130].

3. Rationale and Objectives

In this chapter, the findings of the requirements analysis are presented. Subsequently, an assessment is conducted on the current state of the art in LARS, which was introduced in the second chapter. According to this evaluation, the development objective is defined and the parameters for development are specified.

3.1 Launch and Recovery System requirements

Based on the theoretical foundations presented in chapter 2, a requirement analysis for a universally applicable LARS is conducted. Expert interviews are utilised to analyse the present state of operations across several carrier platforms, with the goal of identifying the requirements for distinct use cases. Expert interviews are a fundamental approach for gathering primary data. Especially in the context of qualitative content analysis, these interviews serve as a foundation for extracting significant insights from the gathered data [131].

The carrier platforms were classified into three distinct categories: ships (including survey vessels, research vessels and frigates), uncrewed surface vessels (USV / smaller boats) and extra large UUVs. Each category was analysed by examining at least one scenario through an expert interview with a person either directly involved in L&R operation (operator view) or involved in the design and layout of processes (designer view). Examples of carrier platforms were selected to illustrate and analyse the requirements. Regarding the requirements for a USV, this study focuses on the USV ARCIMS from TKMS ATLAS ELEKTRONIK UK Ltd. For the investigation of a ship, a survey vessel from Fugro N.V. was selected and for the UUV, the MUM (Modifiable Underwater Mothership) from ThyssenKrupp Marine Systems was chosen. The three carrier platform categories are illustrated in Figure 3-1.



(1) (2) (3)

Figure 3-1: carrier platform categories
(1) (Survey) vessel - Fugro Venturer [132] (2) USV - ARCIMS (3) UUV – MUM [133]

The survey vessel Fugro Venturer (Figure 3-1-1) features a large working deck equipped with various lifting devices. It belongs to Fugro N.V., a surveying company operating in 59 countries and headquartered in the Netherlands. Fugro specializes in collecting geodata to characterize and assess land and marine areas. The ARCIMS (Figure 3-1-2) is an Unmanned Surface Vehicle (USV) designed for mine hunting. A key feature of the MUM UUV (Figure 3-1-3) is its flexible adaptability to various mission requirements through its modular design. This allows the MUM UUV to be utilised in different tasks, such as scientific data collection and underwater mapping.

It is crucial to acknowledge that the findings of the conducted requirements analysis offer just a limited view of potential requirements and may not accurately reflect all vehicles of this category. This study centres on the requirements of the selected examples for each category of carrier platforms. However, it is important to point out that the criteria were formulated based on only one instance for each carrier platform. While this information offers a fundamental

basis for the needs of each vehicle category, a more extensive range of instances would result in a more comprehensive study. Therefore, doing further investigation and exploration of alternative carrier platforms may provide divergent outcomes.
The selection of interview partners is based on various criteria. Individuals directly associated with carrier platforms or involved in processes such as platform development are interviewed. Each person, due to their position and expertise, possesses knowledge, opinions and attitudes toward the subject and its implementation. The goal of these interviews is to gather information to answer the research question posed in this study through qualitative insights.

The primary research inquiry, generated from the study objectives and literature analysis, categorises requirements into two distinct categories: Application and Integration. Application addresses how the LARS is used on the carrier platform. Integration refers to the process of implementing and effectively incorporating the system into the ongoing activities on the carrier platform.
Within the realm of application, crucial elements encompass the motion profile, concurrent missions and economic aspects. The motion profile provides insights into whether the L&R operation should take place when the platform is stationary or in motion. Additionally, it is crucial to determine the maximum sea state in which the system must remain operational. The aspect of concurrent missions provides information on the requirements to minimise the impact on other tasks and optimise the system's application on the carrier platform.
For integration, important considerations are conditions on the carrier platform, safety aspects, mobility/transportability and approvals. The core aspect of conditions on the carrier platform examines how and where L&R procedures can be integrated into the platform's workspace. The feasibility of integrating the current equipment and systems into the process is assessed. Safety aspects focus on identifying, addressing and mitigating potential hazards and obstacles on the carrier platform that could arise from integrating the system. When considering transportability, it is crucial to determine if the system is designed for permanent installation or if it requires the ability to be removed and transported. Certification and approvals entail the process of determining the essential certifications and approvals needed for the system to be implemented on the carrier platform.

The research emphasised three principal aims that are not confined to any one platform. These encompass an automated process, a universal applicability for diverse AUVs and resilience to external factors such as sea conditions.
The LARS should be **automated**, eliminating the need for physical human intervention. This feature is crucial for deployment on unmanned platforms and to minimise hazards to the crew on manned vessels. Of the three platforms considered, two do not have personnel on board, necessitating a fully automated LARS. Even on platforms with human operators, the automation of this procedure is an essential measure for improving crew safety.
The LARS should possess **universal compatibility with different types of AUVs**, consequently eliminating the need for specialised designs and ensuring adaptability to varying sizes and weights. As outlined in Section 2.1, several manufacturers of AUVs create various versions of their vehicles, usually with minor modifications in dimensions or mass. Carrier platforms frequently handle a variety of AUVs or multiple variants produced by a single manufacturer. In order to reduce operational expenses, it is crucial that the LARS has the capability to accommodate many types of AUVs. The importance of this requirement is underscored in other studies, such as those conducted by Chakrabarti [7].
To ensure that the LARS can be used universally with different brands and variations on AUVs,

it has to function without requiring any extra mechanisms on the AUVs. This includes avoiding the necessity for special gripping devices, ejectable floats, quick-release fasteners or similar mechanisms. The operating efficiency is greatly improved by engineering the LARS to be adaptable and capable of handling different AUVs. This approach not only reduces costs but also simplifies logistics and maintenance, making the system more robust and versatile in diverse operational contexts.
A critical aspect of the LARS is its operational weather window and therefore its **resilience to environmental impacts** such as sea conditions. The system should operate efficiently under rough sea conditions, therefore minimising constraints related to the maximum sea states and flow disturbances. Furthermore, the system should safeguard both the AUV and the host platform from any potential damage or loss.
In general, offshore operations come to a halt if they reach a set sea condition limit, which varies depending on the specific equipment being utilised. All carrier platforms aim to attain operational effectiveness. To achieve this, it is crucial to deploy and recover AUVs under as many environmental conditions as possible, thereby maximising the operational time of the AUVs relative to the carrier platform's operational time. [7]
To broaden the range of weather conditions in which missions may be conducted in turbulent seas, ensures that the carrier platforms can operate efficiently and economically.

Table 3-1 presents an excerpt of the requirements that were formulated based on the expert interviews with operators or designers of the respective categories described in the introduction of this section. The results of various interviews were compiled and standardised. In case of disagreements between several replies of different interviewees, consultation was conducted to agree on parameters. Expanding upon this, the similarities and inconsistencies are further described. The expert interviews revealed several **commonalities in the identified requirements**. For instance, all carrier platforms necessitate a stable posture throughout operations. While survey vessels and UUVs can perform L&R operations at a standstill using dynamic positioning systems and side thrusters, the USV requires forward motion to maintain a stable course. However, it is preferable for all three platforms to carry out these operations when in motion. The speed at which the platforms are positioned for L&R varies, although an appropriate range of 2 to 4 knots is recommended.
There are also commonalities in economic aspects like time constraints. The L&R processes on the three platforms should be conducted quickly and with as minimal errors as possible to avoid delays in subsequent missions. Moreover, L&R operations must be performed day and night and under poor visibility conditions. Various types and sizes of AUVs are used on the three considered carrier platforms, resulting in a substantial need for a versatile device suitable for more than one AUV. The devices used so far are tailored to specific AUVs. A universal device would streamline operations on the carrier platform, eliminating the need for frequent equipment changes.
Another commonality from the expert interviews is that charging and data transmission would be feasible if the L&R device could establish a plug connection to the AUV. This would allow for quick energy and information transfer without needing to lift the AUV out of the water, saving time and reducing the number of L&R operations.
As a safety criterion, pendulum loads and unsecured items are not allowed due to the potential for accidents or damage. In addition, when operating on manned vessels, it is crucial to pay attention to potential obstacles and hazards such as firmly stretched ropes. The requirements for mobility and transportability are the same for all carrier platforms. The device should possess a high degree of detachability from the carrier platform and exhibit a straightforward

design for rapid assembly and disassembly, hence guaranteeing the device's constant readiness for utilisation. Furthermore, the system must possess the capability to be easily relocated between missions, enabling it to be detached from the carrier platform and transported to different sites. The devices must also be engineered for secure storage and safeguarded interim storage away from the platform.

Table 3-1: Excerpt of the identified requirements

	Host platform		
Requirement	**Ship**	**USV**	**UUV**
Course adjustment for the L&R procedure	not preferred but possible	Yes	
Motion profile for L&R for secure positioning	Forward motion and stationary	Forward motion required	Forward motion and stationary
Ideal speed for constant positioning	2 kn - 3 kn	2 kn - 5 kn	2 kn - 4 kn
Time restrictions	Quick but focus on precision		
Universal use with AUV variants	Need for a universal device / only special designs in use so far		
Functional extensions	Protection of the AUV; data transmission and power supply		
Integration of the LARS on the carrier platform	In a container or directly on the carrier platform	Directly on the carrier platform or container rack	In a container
Weight limitations	LARS does not cause stability problems	Payload and stability of USV are influenced by LARS	Aim: buoyancy-neutral design
Available lifting devices	Cranes	Ramp	Not present
Safety aspects	No unsecured objects		
Storing the AUV	Storage and protection in the LARS during lifting and storage		

In addition to shared characteristics, the assessment uncovered notable **disparities in the requirements** among the three carrier systems. These differences indicate that one or more of the carrier platforms have unique reactions to certain demands. These inconsistencies might result in certain criteria being unnecessary for one platform but crucial for another. In addition, certain criteria may be contradictory, requiring the need for solutions to resolve these conflicts or prioritise replies depending on practicality.

A significant distinction between the desired motion profiles of the three carrier platforms stems from the need for course adjustments during recovery manoeuvres. This path modification is impractical for survey vessel operations due to the vessel's predetermined path, which is synchronised with concurrent missions. Therefore, it is preferable for the LARS of survey vessels to function independently, regardless of the direction of waves or flow of currents. Nevertheless, it was underscored that course alterations are not entirely excluded and can be

taken into account if it is not possible to proceed without modifying the course or if it takes significant additional effort or a greater level of complexity in the LARS.
Different platforms exhibit substantial variations in integration approaches. For optimal installation of the LARS on the working deck of the survey vessel and the UUV, it is recommended to use a system that fits into a 10-foot or 20-foot shipping container, which is securely attached to the working deck using existing mechanisms such as twist locks. An alternative option for the survey vessel would be to establish a direct connection to the deck, such as by welded or bolted connections. The containerised installation is essential for the UUV since only containers can be incorporated into its modular design. In contrast, when it comes to the USV, it is preferable to directly integrate it on the working deck. Alternatively, container racks might also be utilised. However, the weight, height and their impact on stability make full containers unsuitable.

In addition to the specific requirements outlined, the design must also include generic needs related to marine conditions and economic considerations such as costs, time, quality and reliability.

3.2 Assessment of current technology against set requirements

In this part, procedures for establishing initial physical contact and lifting methods are assessed according to the previously outlined requirements. By using the requirement of automation, **any manual procedures** (see section 2.3.1) have been eliminated from consideration in the L&R process. The consideration of automating certain operations that were previously done manually is also taken into account. This leads to substantial similarities with current automated techniques. An example of this would be establishing an initial contact using a boat hook, which in its automated version exhibit several parallels with grabbing utilising a robotic arm.
The use of a tender boat is a unique attribute. Manual retrieval from the small boat is excluded since it violates the criterion that no crew members should be physically involved in the procedure, as previously specified. Nevertheless, employing a small vessel for retrieval also offers several benefits. Small boats have considerably higher speed and more manoeuvrability compared to the associated host platform. This agility allows flexible responses to changing conditions during approach, such as an AUV rotating due to currents and waves. This reduces the probability of collision between the AUV and the small boat. Should a collision occur, the damage to the AUV would likely be less severe than if it were struck by a larger vessel.
The primary limitation of this approach is the potential danger it presents to the crew on board the tender. For larger carrier platforms, it may be beneficial to deploy a USV equipped with an appropriate LARS for establishing the initial physical contact. Once the AUV is autonomously recovered onto the USV, both the USV and the AUV must be recovered onto the carrier platform. This represents the method's drawback that it necessitates the recovery of both the AUV onto the small boat and subsequently the small boat onto the carrier platform. However, this strategy is especially beneficial for ships that have limited manoeuvrability and want to prevent any harm to both the AUV and the carrier platform.

The assessment of the **automated methods** includes procedures in which the AUV is on the water surface (section 2.3.2) as well as in the submerged state (section 2.3.3).
The utilisation of a **robotic arm** for the recovery of AUVs leads to need of robust and therefore heavy system, mostly because of the significant mass of the AUVs. In addition, it is important to keep the AUV at a safe distance from the carrier platform to reduce the possibility of collisions, which can be made worse by hydrodynamic effects such as suction into the propeller

jet. This requires the robotic arm to have a wide reach, resulting in a long lever arm and a correspondingly heavy and robust structure. Ship accelerations in rough seas and safety factors for offshore lifting operations must also be considered. Overall, this creates a very costly and heavy system that is difficult to retrofit onto carrier platforms. For some platforms, such as smaller boats or the USV considered in the requirements analysis, this LARS is not feasible due to its impact on the vessel stability.
Nets and flexible designs have the benefit of being more space-efficient for storage in comparison to other alternatives. Nevertheless, a significant disadvantage is the ability to cause damage to fragile components. During the capture and lifting procedures, nets have the potential to become entangled in sensitive components such as rudders, propellers, sensors or further attachments. This danger means that the requirement to protect the AUV against damage cannot be fulfilled.
Flexible **inflatable devices** may easily conform to the contour of the AUV, making them very adaptable. These technologies fix the AUV by using the pressure generated by the inflatable components. The necessary pressure is dependent on the mass and shape of the AUV, as well as the resultant contact areas between the inflatable components and the AUV. It is important to take the medium utilised to inflate the components into account. When utilising air, it is necessary to consider the effect on buoyancy, whereas employing denser fluids like the surrounding water increases the overall weight of the recovery system.
Automated techniques for establishing an initial physical connection using a **painter line** require a gripping mechanism or specialised equipment aboard the AUV to establish contact with the line. This conflicts with the requirement for universal applicability without modifications or the necessity for specialised mechanisms. In addition, these processes contribute to the overall dimensions and mass of the vehicle, which might result in increased resistance.
Another challenge arises from the difficulty of placing a homing target, such as an acoustic beacon or light source, in the middle of a painter line or pole. In this configuration, the AUV must home in on a location offset from the homing signal emitter. This misalignment complicates the process, as precise navigation becomes challenging when the AUV is guided by a signal not located at the actual connection point. [68]

Automated procedures for establishing the initial physical connection with **docking devices** provide a range of benefits and drawbacks. In summary, some aspects of these approaches fulfil the requirements specified in Section 3.1. Essentially, this entails the automated execution of the process and the protection of the AUV against damage. In addition, this technology has the potential to create docking devices that may be compatible with various AUVs, although some small modifications may be required to adapt the cage to the AUV. Underwater docking cages enable the docking procedure to be independent of sea conditions, ensuring their application even in turbulent sea states. Furthermore, docking devices can be used in conjunction with various lifting techniques.
Despite these advantages, it is important to equally take into account the drawbacks. One of the main concerns is the added weight of the cage which has to be lifted with the AUV. Moreover, it is important to highlight that the AUV must be in full operational state for all manoeuvres that involve active task performance by the AUV. If a failure occurs, it is essential to have a backup strategy.

Lifting operations for AUV LARS present various advantages and disadvantages depending on the method employed. **Conventional crane systems** represent a well-proven technology,

widely available on a range of vessels. These systems often come with integrated heave compensation, which helps mitigate the effects of vessel motion, making them suitable for a variety of vehicles. Their design allows them to extend well overboard, providing significant operational flexibility during both launch and recovery.
Despite these advantages, crane systems have some limitations. One significant drawback is their limited reach, which can pose challenges in certain operational contexts. Additionally, the pendulum effect, especially in high winds, can introduce instability and increase the risk of accidents, making operations more hazardous.
Cranes with frame constructions, such as A-frames or J-frames, are also established and reliable technology. These systems have the potential to function under rough sea conditions, demonstrating robustness and reliability. Similar to traditional crane systems, they extend well overboard, facilitating easier L&R operations.
Nevertheless, these systems have their limitations. The pendulum effect in high winds remains a concern. Additionally, frame constructions tend to be large and heavy, necessitating a considerable amount of deck space. This can provide a substantial constraint for vessels that have a restricted deck space or where weight distribution is crucial for stability.
Stinger systems provide a controlled technique, which can be very advantageous for L&R operations. They are appropriate for many types of vehicles and can be particularly beneficial for smaller boats where cranes may not be feasible due to stability limitations. In addition, stinger systems provide support to the AUV during the L&R process.
Despite these advantages, stinger systems may face issues, especially in rough waters. Under such circumstances, the act of extending to the ocean surface may provide considerable difficulties, which might possibly affect the effectiveness and security of the operation. An essential juncture occurs when the AUV is hauled onto the ramp. During this stage, the AUV is in close proximity to the ramp, but has not yet made contact with it. In this scenario, the oscillating motion of the waves might result in collisions between the AUV and the ramp.

The selection of a lifting operation method for AUVs should evaluate the capabilities of the vessel, the operational environment and the special needs of the AUV. Crane systems and cranes with frame constructions offer robust, proven solutions with integrated heave compensation and high-sea state operational capabilities. However, they require significant deck space and can be affected by winds and vessel motions. Stinger systems provide a controlled approach and are suitable for smaller vessels but may face challenges in high seas. Ultimately, the choice of system should align with the operational goals, ensuring safe and efficient L&R of AUVs under various conditions.

3.3 Development objective and parameters

The aim of this research is to create a concept for establishing the initial physical connection between the AUV and the LARS that fulfils the specifications mentioned in Section 3.1. The main objectives are achieving automation, providing universal application for different types of AUVs and enhancing resistance to external factors like sea conditions.
Firstly, the LARS should operate in a fully automated manner, eliminating the need for physical human intervention. Furthermore, the LARS should possess universal compatibility with various types of AUVs, hence eliminating the demand for specialised designs and guaranteeing adaptation to diverse sizes and weights. The functionality should be independent of any supplementary mechanisms on the AUVs, such as specialised gripping devices, detachable floats or quick-release fasteners. Adapting and equipping the LARS to handle various AUVs

improves operational efficiency, decreases expenses and streamlines logistics and maintenance. Finally, a critical aspect of the LARS is its operational capability in rough seas and its resilience to environmental impacts. The system should function under challenging sea conditions, while minimising limitations associated with high sea states. This enhanced functionality not only increases the utilisation rates of AUVs but also supports efficient and cost-effective operation of the carrier platforms. To address these requirements, the developed concept is analysed for the representative case of operation from a surface vessel. Compared with a submerged towing arrangement, for example when the system is deployed from a submarine, a surface ship is expected to experience larger wave-induced motions and stronger flow disturbances. Using a surface vessel as carrier platform therefore represents a more challenging assessment case with respect to the motion of the LARS.

The L&R related lifting operation is not within the scope of this work. Further limitations involve the navigation and homing of the AUV, which are addressed through established procedures. For further information on guidance, navigation and control (GNC) than provided in section 2.1.3, literature by Fossen [134], Antonelli [135] or Paull et al. [136] is recommended. The present thesis deliberately shifts the focus towards mechanical/hydromechanical design and passive dynamics.

The basis for the development is the SeaCat AUV (illustrated in Figure 3-2) from TKMS ATLAS ELEKTRONIK GmbH. The SeaCat AUV is a versatile, moderately sized AUV designed for multipurpose use across a range of underwater missions. Built for adaptability and efficiency, the SeaCat employs a modular SwapHead technology, which allows for rapid in-field exchanges of specialised payloads, enhancing the AUV's utility across varied operational demands without the need for multiple vehicle types. This capacity to seamlessly swap mission-specific payload heads enables the SeaCat to function as a comprehensive solution for clients with specialised underwater survey, inspection and monitoring needs.

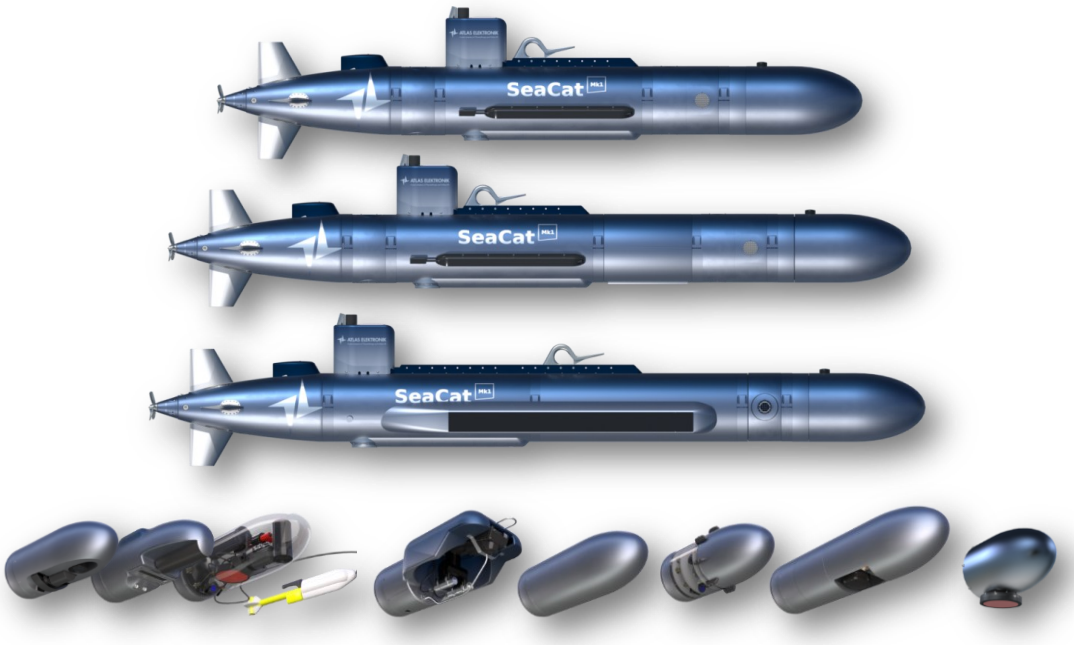


Figure 3-2: SeaCat AUV variants and Swap Heads

Depending on the battery capacity and the sonar used, the SeaCat AUV is available in different variants. The dimensions of the SeaCat AUV can be customised according to payload and battery configurations. With a diameter of 325 mm, a length varying between 2500 and 5000 mm, a width of 576 mm and a height of 670 mm (inclusive of antennas), the SeaCat is suitable for deployment in diverse marine environments. Its weight in air ranges between 180 and 500 kg depending on its specific configuration. In terms of speed and manoeuvrability, the SeaCat AUV has a maximum forward speed of 6 knots, with a minimum of 0 knots when using its hover capabilities and can reverse up to a speed of 1 knot.

As shown in Figure 3-3, a free body like the AUV has six Degrees of Freedom (DoF). Translational motions occur along the three main axes of a Cartesian coordinate system (x, y, z). Surge(x), sway (y) and heave (z) are associated with translational motion. In rotation, the origin of the coordinate system corresponds to a point on the object around which the body can rotate. For a fully submerged AUV this point corresponds to the centre of gravity (COG). The rotational axes correspond to the main axes and allow for three more DoF. Rotation around the x-axis is called roll, around the y-axis pitch and around the z-axis yaw. Figure 3-3 defines how the axes of AUVs are aligned and labelled. According to the figure, the x-axis is aligned along the main direction of motion. The z-axis points upwards and the y-axis points to the left in the direction of travel.

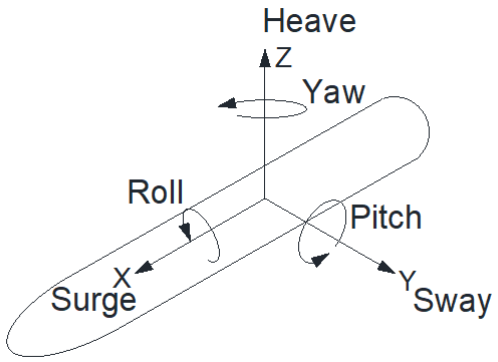


Figure 3-3: Degrees of freedom of an AUV

4. Methodology Review

This chapter presents fundamental background on the primary methodologies and theoretical principles that support this work, covering product development, waves, computational fluid dynamics (CFD), experimental testing and multibody dynamics.
The product development section examines the employed systematic design and engineering methods. Wave theory explores the theoretical foundations for predicting ocean surface interactions, explaining the assumptions and constraints of wave models in dynamic marine settings. The CFD section presents simulation techniques utilised for analysing fluid dynamics, emphasising the impact of assumptions in computational modelling on accuracy. Then, a brief introduction to model tests is presented. Subsequently, multibody dynamics is introduced, accompanied by a discourse on the employed simplifications. Collectively, these sections delineate the advantages and limitations of each methodology, offering essential context for the interpretation of the ensuing data and analysis conducted within this work.

4.1 Product Development

Product development is a methodically organised procedure aimed at solving the complex problems associated with the development of novel products or the modification of current ones. Due to the complex nature of product design, development often follows a structured plan to guarantee initial coordination and efficient cost management during the process. Product development encompasses four fundamental phases: task definition, conceptualisation, design and finalisation. Each phase offers a structure that reduces iterative cycles by continuously enhancing prior stages through knowledge transfer from subsequent phases. This iterative, feedback-driven approach is congruent with the Test-Operate-Test-Exit paradigm, which integrates ongoing testing and refinement of design activities [137].
This iterative, phase-oriented process is exemplified by guideline 2221 from the Association of German Engineers ([in German:] VDI: Verein Deutscher Ingenieure). By segmenting the process into clearly delineated phases and utilising structured approaches such as functional structuring, requirement listing, utility analysis and functional analysis, product development teams may optimise the production of new and effective products. These technologies facilitate structured processes and improve decision-making, therefore yielding optimised, high-quality design solutions that satisfy both technical and operational criteria. [138]
VDI Guideline 2221 further categorises these four phases into nine specific activities, as seen in Figure 4.1, each representing an important step in the product development cycle. This comprehensive method enhances the engineering process by guaranteeing that all facets of development are methodically considered. This project emphasises the preliminary stage of developing a prototype system in accordance with the VDI 2221 methodology, with the objective of finalising the concept phase by executing the initial four development activities.

For the product development approach outlined in VDI 2221 the functional structure (VDI 2803) serves as a fundamental instrument for product planning and conceptualisation, derived on the principles of value analysis. This method decomposes the overall function of a system into distinct sub-functions, enabling early problem detection and functional descriptions. There are two primary types of functional structures: hierarchical and transformational. The hierarchical structure organizes functions across various levels, while the transformational structure maps functional relationships via material, energy and signal flows. This division helps identify potential issues early in the design process, visualize function structures and

establish a structured layout of the product. [137, 139]
The Metaplan method, a brainstorming-inspired technique, is used to develop a functional structure for an object or system. Initially, the system is broadly described and sub-functions are collected without formal connections. These sub-functions are then organised logically, creating a coherent structure. This “playful” approach encourages open ideation, making it suitable for the early stages of product conceptualization [139].

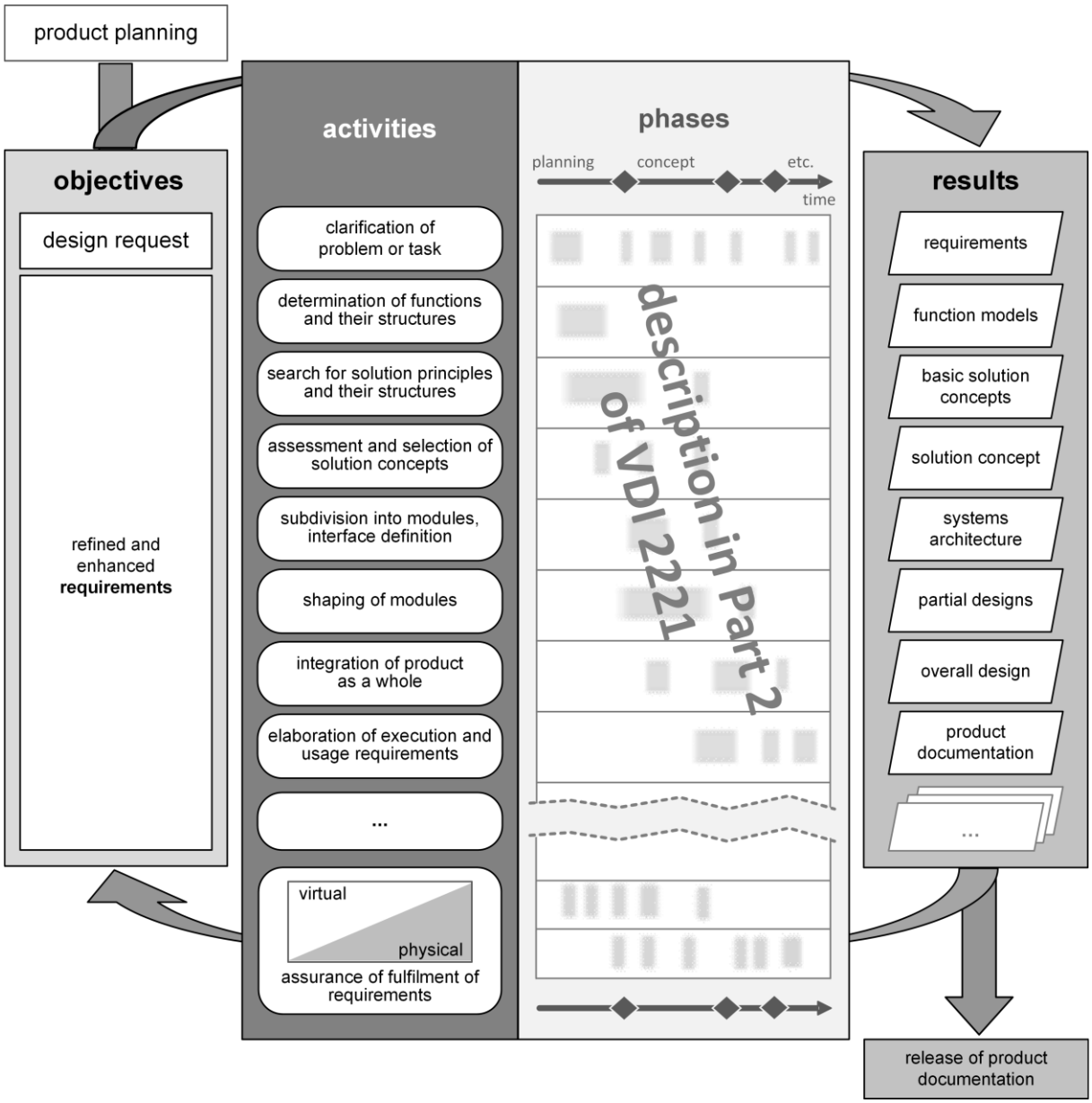


Figure 4-1: Process model of product development according to VDI guideline 2221 [138]

The requirements list is a fundamental documentation tool, especially for less complex development projects. This tabular list classifies requirements by type and importance, differentiating between necessary (essential) and optional (desirable) criteria. Each requirement is linked to sub-systems or key features, ensuring they are clear, valid, accurate, prioritised, achievable, traceable and verifiable. Quality criteria such as clarity, feasibility and traceability are essential to maintain high standards of documentation and project execution [137].
The are different techniques supporting the requirements list. Questionnaires gather requirements directly from stakeholders, either in written or verbal form, allowing for

customised feedback that can inform the requirements list. The Scenario Technique projects potential usage scenarios, identifying influences and impacts that might otherwise go unnoticed. By simulating the system's lifecycle, engineers can extract requirements that address broader environmental interactions and product life cycle stages [137].

The morphological matrix is a two-dimensional framework used during the concept or design phase to create comprehensive system solutions. The matrix lists sub-functions derived from the functional structure in the first column, with potential solutions for each function across the row. Engineers then create viable combinations, selecting one solution per sub-function to generate various design alternatives. This technique helps visualize and evaluate multiple potential solutions, offering a structured approach to innovation [139].
Utility analysis provides a systematic way to evaluate and compare multiple design options by assigning objective scores based on predetermined criteria. Each criterion is weighted according to its importance and the total score for each design is calculated by summing the weighted criteria scores. This approach is beneficial when choosing the optimal design from a pool of viable alternatives, providing a quantitative basis for decision-making [137].
Similar to utility analysis, point rating assesses different design solutions but does not employ a hierarchical structure for criteria. Instead, it evaluates each criterion in sequence, either with or without weighting. This method, consisting of six steps from defining criteria to calculating scores, is flexible and can be adapted to weighted and unweighted formats [137].
The dominance matrix or pairwise comparison, is a qualitative approach for comparing solution variants within a concept by ranking them against each other based on specific attributes. Each variant is assessed as either "better than" or "worse than" the others for each attribute. After completing all comparisons, a total score for each variant provides a ranked order. This method can also be applied to the weighting of criteria in utility analysis by adjusting comparisons to reflect "more important" or "less important" categories [139].
The argument balance method is a quick and straightforward tool for evaluating the pros and cons of various solutions or variants by listing them in a comparative table. Although easy to use, this method lacks depth, making it more suitable for preliminary evaluations rather than final decisions, particularly when complex trade-offs are involved [137].

4.2 Waves

In this section waves at the interface between water and air are considered using the term waves. Other kinds of waves e.g. acoustic, optical or pressure waves that propagate in the water are not considered in this context.
Waves are generated at the interfaces of stratified fluids with different velocities, such as air and water. For example, wind blowing across the surface of a water body transfers energy to the water through shear forces, leading to the formation of waves. This interaction occurs when the air travels faster than the water and therefore exerts pressure and tangential stress on the surface, causing periodic undulations. The energy transfer depends on factors such as wind speed, duration and fetch, which determine the size and energy of the resulting waves.
Waves can also arise from external impulses, including ship motions, coastal landslides, earthquakes or volcanic eruptions. Additionally, large-scale atmospheric pressure fluctuations and astronomical forces, such as tidal waves, contribute to wave formation. [140]

Waves are characterised by specific parameters, including wave height H (equal to twice the amplitude ζ_a), wavelength λ, propagation speed c and wave period T, which represents the time required for the wave to travel one wavelength λ. The local displacement of the water surface

caused by wave motion is measured relative to the still water level, where the depth d equals $z = 0$. Wave dynamics involve a redistribution of water masses, resulting in wave-induced currents within the water body, which can be described using velocity components u for horizontal particle motions and w for vertical particle motions. The wave characteristics are illustrated in Figure 4-2.

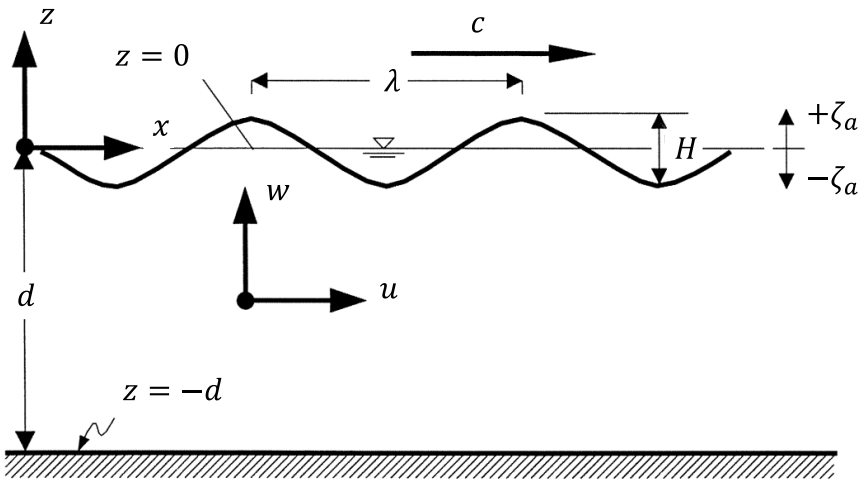


Figure 4-2: Definition of wave characteristics (according to [140])

The Douglas scale categorises the sea state into ten levels based on the wave height. The respective categorisation is given in Table 4-1.

Table 4-1: Douglas Sea state scale [141]

Sea state	Wave height [m]	Characteristics
0	0	Calm (glassy)
1	0 - 0.1	Calm (rippled)
2	0.1 - 0.5	Smooth (wavelets)
3	0.5 - 1.25	Slight
4	1.25 - 2.5	Moderate
5	2.5 - 4	Rough
6	4 - 6	Very rough
7	6 - 9	High
8	9 - 14	Very high
9	>14	Phenomenal

4.2.1 Wave theory

Wave theory provides a fundamental framework for understanding and mathematically describing wave phenomena in nature. It simplifies complex interactions by using idealised assumptions, such as small wave amplitudes in linear wave theory, allowing key parameters like wavelength, wave height and wave speed to be calculated.

Linear wave theory

The linear wave theory was developed by Airy, who derived it based on the assumption of sinusoidal, long-crested and regular waves. Additional assumptions about the fluid include the

absence of viscosity (frictionless flow), incompressibility, homogeneity, irrotationality and the lack of any underlying current. In this theory, the wave height H is considered very small compared to the water depth d and the wavelength λ, with the conditions $H \ll d$ and $H \ll \lambda$. These simplifications allow for a mathematically straightforward description of wave motion under idealised conditions.

The surface elevation $\eta(x,t)$ of a sinusoidal wave travelling in the x-direction can be expressed as:

$$\eta(x,t) = \zeta_a \cos(kx - \omega t) \tag{4.1}$$

Wherein the wavenumber k is:

$$k = \frac{2\pi}{\lambda} \tag{4.2}$$

And the angular frequency ω for a wave period T is expressed as:

$$\omega = \frac{2\pi}{T} \tag{4.3}$$

The phase of the travelling wave θ can be expressed as:

$$\theta = kx - \omega t \tag{4.4}$$

The combination of equation (4.1) and (4.4) results in the following shortened expression for the surface elevation $\eta(x,t)$:

$$\eta(x,t) = \zeta_a \cos(\theta) \tag{4.5}$$

Based on the relationship between water depth and wavelength waves can be classified into three types (illustrated in Figure 4-3): deep-water waves, intermediate waves and shallow-water waves. Deep-water waves occur when the water depth exceeds half the wavelength:

$$\frac{d}{\lambda} > \frac{1}{2} \tag{4.6}$$

In deep water, the orbital motion of water particles caused by the wave is circular and decreases exponentially with depth, with no seabed interference.
In the transition zone, where:

$$\frac{1}{20} > \frac{d}{\lambda} > \frac{1}{2} \tag{4.7}$$

interactions between the wave motion and the seabed begin to occur. Orbital motion begins to flatten into elliptical paths, especially near the seabed, as the interaction between the wave and the bottom becomes more pronounced.
Finally, shallow-water waves arise when the water depth is less than

$$\frac{d}{\lambda} < \frac{1}{20} \tag{4.8}$$

and the seabed significantly impacts wave dynamics. In shallow water, the wave motion is dominated by horizontal oscillations that extend throughout the entire water column, as the vertical component diminishes. This results in translational motion, where the wave energy moves forward, creating short, steep crests and long troughs. [140]

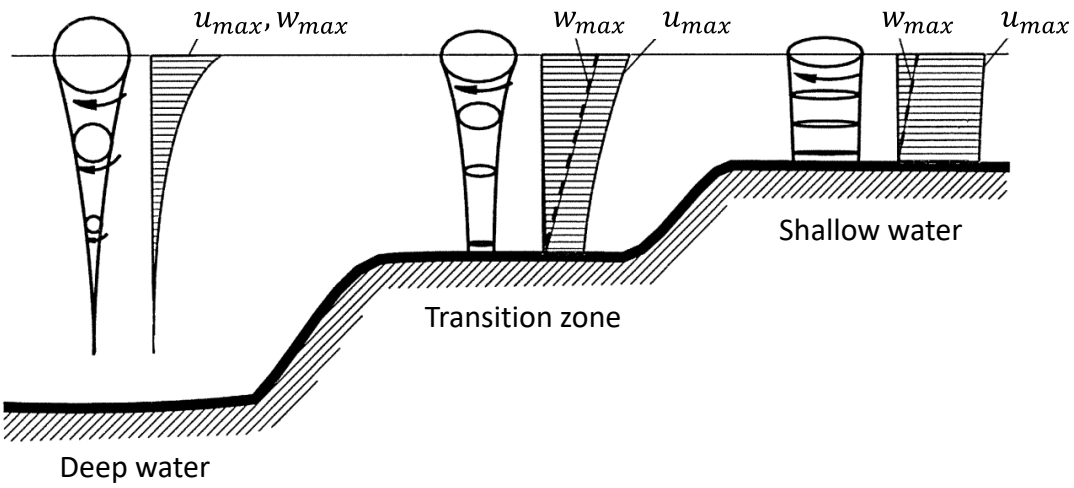


Figure 4-3: Wave particle motion at different water depths [140]

The formulae for some wave characteristics according to linear wave theory are listed in Table 4-2. The general results are in the centre column of Table 4-2. In addition to the general results, special solutions for deep water and shallow water can be developed using the profile of the $tanh\left(\frac{2\pi d}{\lambda}\right)$ function. For shallow water waves it is assumed that:

$$tanh\left(\frac{2\pi d}{\lambda}\right) = \frac{2\pi d}{\lambda} \tag{4.9}$$

and for waves in deep water the assumption is made that:

$$tanh\left(\frac{2\pi d}{\lambda}\right) = 1 \tag{4.10}$$

Table 4-2: Wave characteristics according to linear wave theory [140]

	Shallow water $\frac{d}{\lambda} < \frac{1}{20}$	**General & Transition zone** $\frac{1}{20} > \frac{d}{\lambda} > \frac{1}{2}$	**Deep water** $\frac{d}{\lambda} > \frac{1}{2}$
c $\left[\frac{\mathrm{m}}{\mathrm{s}}\right]$	$\sqrt{g \cdot d}$	$\sqrt{\frac{g \cdot \lambda}{2\pi} tanh\left(\frac{2\pi d}{\lambda}\right)}$	$\frac{T \cdot g}{2\pi}$
λ [m]	$T\sqrt{g \cdot d}$	$\frac{g \cdot T^2}{2\pi} \cdot tanh\left(\frac{2\pi d}{\lambda}\right)$	$\frac{T^2 \cdot g}{2\pi}$
u(x, z, t) $\left[\frac{\mathrm{m}}{\mathrm{s}}\right]$	$\zeta_a \cdot \sqrt{\frac{g}{d}} \cdot \cos(\theta)$	$\zeta_a \cdot \omega \frac{\cosh[k(z+d)]}{\sinh(kd)} \cos(\theta)$	$\zeta_a \cdot \omega \cdot e^{\mathrm{kz}} \cos(\theta)$
w(x, z, t) $\left[\frac{\mathrm{m}}{\mathrm{s}}\right]$	$\zeta_a \cdot \omega \left(1 + \frac{z}{d}\right) \sin(\theta)$	$\zeta_a \cdot \omega \frac{\sinh[k(z+d)]}{\sinh(kd)} \sin(\theta)$	$\zeta_a \cdot \omega \cdot e^{\mathrm{kz}} \sin(\theta)$

Nonlinear wave theory

The distinction between linear and nonlinear wave theory arises from the assumption that the wave height H is small compared to both the water depth d and the wavelength λ. This assumption forms the basis of linear wave theory, which simplifies calculations and is valid for many situations where wave heights are relatively small. However, it does not accurately describe all wave phenomena, especially in cases where wave height becomes significant. One limitation of linear theory is its inability to account for closed orbital paths of water particles, which, according to the theory, exclude mass transport.
To better align with observed phenomena, nonlinear wave theory, such as the second-order term of the Stokes wave theory, can be applied. This theory progressively approximates real-world conditions by incorporating higher-order terms, capturing more complex behaviours. However, with increasing accuracy, computational complexity also grows. The nonlinear approach becomes especially important in the transition zone between deep and shallow water, as the linear theory reaches its limits. In coastal areas, where the ratio of wave height to water depth increases and can approach 1 at the breaking point, nonlinear effects dominate. Stokes developed an advanced theory using a series expansion that includes higher-order terms, allowing the representation of surface boundary conditions more accurately. Stokes theory accounts for natural asymmetries in wave shapes. At first order it converges with the results of the linear Airy and Laplace wave theory. [140]

For simplicity, only the second-order terms of Stokes theory are considered here. For the nonlinear horizontal velocity component u_{nl} the second-order term of the Stokes equation can be expressed as follows:

$$\frac{3}{4}\left(\frac{2\pi\cdot\zeta_a}{\lambda}\right)^2 c\,\frac{\cosh[2k(z+d)]}{\sinh^4(kd)}\cos(2\theta) \tag{4.11}$$

Together with the first-order term according to linear wave theory, this results in:

$$\begin{aligned} u_{nl}(\mathrm{x,z,t}) = {} & \zeta_a\cdot\omega\frac{\cosh[k(z+d)]}{\sinh(kd)}\cos(\theta) \\ & +\frac{3}{4}\left(\frac{2\pi\cdot\zeta_a}{\lambda}\right)^2 c\,\frac{\cosh[2k(z+d)]}{\sinh^4(kd)}\cos(2\theta) \end{aligned} \tag{4.12}$$

Similar to the second-order term of the Stokes equation for u the second-order term of the Stokes equation for the vertical particle velocity w_{nl} is:

$$\frac{3}{4}\left(\frac{2\pi\cdot\zeta_a}{\lambda}\right)^2 c\,\frac{\sinh[2k(z+d)]}{\sinh^4(kd)}\sin(2\theta) \tag{4.13}$$

Which results in the following equation for w_{nl}:

$$\begin{aligned} w_{nl}(\mathrm{x,z,t}) = {} & \zeta_a\cdot\omega\frac{\sinh[k(z+d)]}{\sinh(kd)}\sin(\theta) \\ & +\frac{3}{4}\left(\frac{2\pi\cdot\zeta_a}{\lambda}\right)^2 c\,\frac{\sinh[2k(z+d)]}{\sinh^4(kd)}\sin(2\theta) \end{aligned} \tag{4.14}$$

4.2.2 Wave spectrum

Waves on the ocean surface are primarily generated by wind, which creates a velocity difference between the air and water. Initially, these waves are small but grow over time and with increasing fetch. As new waves form on existing ones, they interact and influence each other. This process results in a sea state that represents a complex superposition of numerous individual waves of varying sizes, lengths and speeds. Consequently, the ocean surface becomes a dynamic system of overlapping short and long, small and large, fast and slow waves, contributing to the overall complexity of wave behaviour. [140]

The statistical description of wave conditions involves analysing wave characteristics either in the time domain or the frequency domain. In the time domain, key parameters include the arithmetic mean wave height (H_m) and mean wave period (T_m), which represent average conditions over a given time series. Additionally, parameters such as $H_{1/n}$ describe the mean height of the highest n-th portion of all waves. Of particular importance is the significant wave height ($H_s = H_{1/3}$), which represent the average height of the highest one-third of the waves in the record. [140]
In the frequency domain, wave characteristics are analysed through spectral methods. Here, the significant wave height derived from the spectrum provides a measure of wave energy based on the distribution of wave frequencies. The peak period (T_p) and its corresponding peak frequency ($f_p = \frac{1}{T_p}$) indicate the dominant wave energy, representing the most energetically significant waves within the spectrum. [140]
By analysing waves in the frequency domain through statistical methods, the superposition of different waves can be represented in a wave spectrum. Using Fourier analysis, these overlapping waves are decomposed into their fundamental sinusoidal components. These basic waveforms are then categorised into frequency classes, with the energy contained in each wave assigned to its respective class. From the energy distribution across these frequency classes, the spectral energy density $S_{ed}(f)$ can be determined. [140, 142]
Commonly used wave spectra include the ISSC spectrum, also referred to as the Bretschneider or modified Pierson-Moskowitz spectrum, the JONSWAP spectrum, the Gaussian swell spectrum and the Ochi-Hubble spectrum. The Gaussian swell spectrum is based on the normal probability density function, while the Ochi-Hubble spectrum allows for the representation of double-peaked sea states, capturing both remotely generated swells and locally wind-generated seas. [143]
In this work, the spectral energy density $S_{JONSWAP}(f)$ for wind-generated waves in the North Sea is used. The JONSWAP spectrum derived from extensive measurements during the Joint North Sea Wave Project (JONSWAP). It is mathematically expressed as a function of wave frequency f, peak frequency f_p and specific constants $\chi_{JONSWAP}$, $\sigma_{JONSWAP}$ and $\gamma_{JONSWAP}$. The spectral energy density $S_{JONSWAP}(f)$ can be expressed as: [142]

$$S_{JONSWAP}(f) = \left(\frac{\chi_{JONSWAP}\, g^2}{16\,\pi^4}\right) f^{-5} \exp\left[-\frac{5}{4}\left(\frac{f}{f_p}\right)^{-4}\right] \gamma_{JONSWAP}^{exp\left[-\frac{1}{2\,\sigma_{JONSWAP}^2}\left(\frac{f}{f_m}-1\right)^2\right]} \tag{4.15}$$

4.3 Computational Fluid Dynamics

This chapter aims to provide an overview of the fundamental principles of fluid mechanics and CFD simulation to enhance the understanding of the CFD software used in this work. Fluid mechanics describes the physical behaviour of fluids, which are substances characterised by a molecular structure that offers no resistance to external shear forces and deform under minimal applied forces. For the present application, fluids are considered as liquids and gases and are treated as a continuum, modelled as a continuous substance. The following conservation equations, given in their differential form, apply to a continuum of fluid mechanics. [144] These include the conservation of mass:

$$\frac{\partial \rho}{\partial t} + \frac{\partial}{\partial x_i}(\rho u_i) = 0 \tag{4.16}$$

where ρ is the fluid density, t is time, x_i represents spatial coordinates and u_i is the velocity component in the direction i. This equation ensures that mass is conserved over time.
The conservation of momentum is expressed as:

$$\rho \frac{Du_i}{Dt} = \rho k_i + \frac{\partial \tau_{ij}}{\partial x_j} \tag{4.17}$$

Here, $\frac{Du_i}{Dt}$ is the derivative of velocity, representing the acceleration, ρk_i denotes body forces (e.g., gravity) and τ_{ij} is the stress tensor. This equation governs the forces acting on a fluid element.
The conservation of angular momentum is given by equation (4.18) where the symmetry of the stress tensor τ_{ij} is established, indicating the internal forces are balanced.

$$\tau_{ij} = \tau_{ji} \tag{4.18}$$

The conservation of energy is given by equation (4.19). In this equation, e represents the specific internal energy and q_i is the heat flux. The first term on the right represents work done by stress, while the second term describes heat transfer within the fluid.

$$\rho \frac{De}{Dt} = \tau_{ij} \frac{\partial u_i}{\partial x_j} - \frac{\partial q_i}{\partial x_i} \tag{4.19}$$

These equations (4.16) to (4.19) introduce 17 unknowns but provide only 8 equations, necessitating further constraints to solve the system of equations. The material law and Fourier's law simplify the stress tensor τ_{ij} and the heat flux q_i, respectively:

$$\tau_{ij} = -p\delta_{ij} + \lambda^* \delta_{ij} \epsilon_{kk} + 2\mu \epsilon_{ij} \tag{4.20}$$

Here, δ_{ij} is the Kronecker delta (1 when $i = j$, 0 otherwise), λ^* is a material constants, μ is the dynamic viscosity and ϵ_{ij} is the strain tensor.
The Fourier's law is expressed as:

$$q_i = -k_{therm} \frac{\partial T_{Temp}}{\partial x_i} \tag{4.21}$$

where k_{therm} is the thermal conductivity and T_{Temp} is the temperature.
The strain tensor ϵ_{ij}, appearing in the material law, is defined as:

$$\epsilon_{ij} = \frac{1}{2}\left(\frac{\partial u_i}{\partial x_j} + \frac{\partial u_j}{\partial x_i}\right) \tag{4.22}$$

This tensor characterizes the deformation of the fluid element due to velocity gradients. Together, the equations (4.16) to (4.22) form the basis of the Navier-Stokes equations given in equation (4.23). The Navier–Stokes equations are the fundamental conservation laws of mass and momentum for fluid motion, relating velocity and pressure fields to body forces and viscous stresses. They describe the motion of viscous fluids in space and time.

$$\rho \frac{\mathrm{Du_i}}{\mathrm{Dt}} = \rho \mathrm{k_i} + \frac{\partial}{\partial \mathrm{x}_i}\left\{-p + \lambda^* \frac{\partial \mathrm{u}_m}{\partial \mathrm{x}_m}\right\} + \frac{\partial}{\partial \mathrm{x_j}}\left\{\mu\left(\frac{\partial \mathrm{u_i}}{\partial \mathrm{x_j}} + \frac{\partial \mathrm{u_j}}{\partial \mathrm{x}_i}\right)\right\} \tag{4.23}$$

4.3.1 Reynolds averaged Navier-Stokes equation

The Navier-Stokes equations can be solved by many approaches, each varying in computing effort and accuracy. Three widely used approaches are Direct Numerical Simulation (DNS), Large Eddy Simulation (LES) and Reynolds-averaged Navier-Stokes (RANS) equations. DNS yields the most precise outcomes by directly solving the equations without approximations. This approach necessitates an exceptionally fine computing grid to get a converged solution, leading to a substantially elevated computational complexity. Owing to its resource-intensive characteristics, DNS is predominantly utilised to get profound physical understanding of simplified flow issues. [145, 146]
Large Eddy Simulation focuses on resolving the larger, energy-containing turbulent structures, while smaller-scale motions are modelled using an appropriate turbulence model. This technique balances accuracy and computing expense, as bigger structures dominate the flow dynamics. Although LES is more computationally efficient than DNS, it compromises the level of precision in the solution. This renders it appropriate for situations when addressing all turbulent scales is unfeasible, although comprehending large-scale dynamics is crucial. [147]
RANS simplifies the flow by decomposing the quantities into mean values and fluctuations. This approach significantly reduces computational effort compared to DNS and LES, but has reduced accuracy. RANS is commonly used in engineering applications where efficiency is critical and its balance between accuracy and computational feasibility makes it a practical choice. RANS produces reliable results with manageable computational resources and is particularly advantageous when the information on the flow regime obtained by DNS or LES is not required.

In the RANS method, the flow parameter ϕ is divided into a mean value $\bar{\phi}$ and a fluctuation ϕ'. The following applies for a flow variable ϕ:

$$\phi = \bar{\phi} + \phi' \tag{4.24}$$

The averaging approach applies to incompressible flows with a Mach number less than 0.3. This allows density fluctuations to be neglected. The conservation equations are expanded to include the averaged flow quantities and their fluctuations, which introduces the Reynolds stress tensor in equation (4.25) into the system of conservation equations. Therein u_i corresponds to the velocity component in the direction i. Different approximations for the fluctuations of the flow parameter and their effects result in various simulation models. [147]

$$\tau_{\mathrm{ij}} = -\rho\, \overline{u_i' u_j'} \tag{4.25}$$

Turbulence models are used to determine turbulent stresses, as different approaches yield varying degrees of agreement with experimental data depending on the application. Eddy

viscosity models are commonly employed in industrial contexts due to their lower computational cost and greater robustness. However, Reynolds stress models offer more accurate physical foundations, reducing conceptual weaknesses compared to eddy viscosity models. [148]
In eddy viscosity models, turbulent stresses are approximated using Boussinesq's hypothesis, given by equation (4.26), which simplifies the Reynolds stress tensor from six unknown components to just two: the kinematic eddy viscosity (ϑ_t) and the turbulent kinetic energy (k_{TKE}). Eddy viscosity models are classified based on how ϑ_t and k_{TKE} are solved. In zero-equation models, ϑ_t is determined using a simple algebraic equation, while k_{TKE} is neglected. In one-equation models, ϑ_t is obtained from a differential equation, but k_{TKE} remains disregarded. In two-equation models, both ϑ_t and k_{TKE} are calculated using two separate differential equations. This hierarchical complexity allows to balance computational efficiency and accuracy depending on the specific requirements of the simulations.

$$\tau_{ij} = -\rho\,\overline{u_i' u_j'} = \vartheta_t\left(\frac{\partial \overline{u}_i}{\partial x_j} + \frac{\partial \overline{u}_j}{\partial x_i}\right) - \frac{2}{3} k_{TKE}\delta_{ij} \tag{4.26}$$

4.3.2 Turbulence models

k-ε model

The k-ε model is well-suited for simulating turbulent core flows, though it tends to predict flow separation at walls to occur later, resulting in smaller separation zones [149]. The underlying differential equations are functions of the turbulent kinetic energy (k_{TKE}) and the dissipation rate of turbulent kinetic energy (ϵ_{TKE}). The differential equation for the turbulent kinetic energy is:

$$\frac{D}{Dt}(\rho k_{TKE}) = \nabla\left(\rho D_{k_{TKE}} \nabla k_{TKE}\right) + P - \rho \epsilon_{TKE} \tag{4.27}$$

In this context, ∇ denotes the Nabla operator, D_n represents the effective diffusivity for n (here $D_{k_{TKE}}$) and P signifies the production rate of turbulent kinetic energy.
The differential equation for the dissipation rate is defined as follows:

$$\frac{D}{Dt}(\rho \epsilon_{TKE}) = \nabla\left(\rho D_{\epsilon_{TKE}} \nabla \epsilon_{TKE}\right) + \frac{C_1 \epsilon_{TKE}}{k_{TKE}}\left(P + C_3 \frac{2}{3} k_{TKE} \nabla u\right) - C_2 \rho \frac{{\epsilon_{TKE}}^2}{k_{TKE}} \tag{4.28}$$

For the turbulent kinematic eddy viscosity applies:

$$\vartheta_t = C_\mu \frac{{k_{TKE}}^2}{\epsilon_{TKE}} \tag{4.29}$$

The equations and coefficients are derived from [150], which provides a comprehensive explanation of the model and the values of the coefficients utilised in the simulation model.

k-ω model

The $k-\omega$ turbulence model, in its widely adopted form, was developed by Wilcox in the late 1980s and has since undergone various refinements to improve its accuracy in near-wall and low-Reynolds-number flows. Unlike the $k-\varepsilon$ model, the $k-\omega$ formulation exhibits improved sensitivity to adverse pressure gradients and flow separation, making it particularly suitable for simulating boundary-layer flows with strong shear or separation effects. The model is governed by two transport equations: one for the k_{TKE} and the other for the specific dissipation rate of

turbulence ω_{TKE}, defined as the rate of dissipation per unit turbulent kinetic energy. [151] The transport equation for the turbulent kinetic energy is expressed with $\beta_{k\text{-}\omega}$ as a model constant as:

$$\frac{\mathrm{D}}{\mathrm{Dt}}(\rho \mathrm{k_{TKE}}) = \nabla\left(\rho \mathrm{D_{k_{TKE}}} \nabla k_{TKE}\right) + P - \beta_{k\text{-}\omega} \rho k_{TKE} \omega_{TKE} \tag{4.30}$$

The corresponding equation for the specific dissipation rate is given by:

$$\frac{\mathrm{D}}{\mathrm{Dt}}(\rho \omega_{TKE}) = \nabla\left(\rho \mathrm{D}_{\omega_{TKE}} \nabla \omega_{TKE}\right) + P \alpha_{k\text{-}\omega} \frac{\omega_{TKE}}{k_{TKE}} - \beta_{k\text{-}\omega} \rho {\omega_{TKE}}^2 \tag{4.31}$$

In this equation, $\alpha_{k\text{-}\omega}$ and $\beta_{k\text{-}\omega}$ are empirical constants that calibrate the interaction between k_{TKE} and ω_{TKE}. The diffusion terms are governed by their respective diffusivity functions, $D_{\omega_{TKE}}$ and $D_{k_{TKE}}$.
The kinematic eddy viscosity is computed using the following relationship:

$$\vartheta_{\mathrm{t}} = \frac{k_{TKE}}{\omega_{TKE}} \tag{4.32}$$

The constants and formulation used in this model are based on the standard k–ω model as described in [151], with values adjusted according to validated benchmarks for wall-bounded and free shear flows.

***SST-k-ω* model**

The *SST-k-ω* model or Shear Stress Transport model is a two-equation turbulence model that combines the advantages of the k-ω and k-ε models while minimising their respective disadvantages. The model incorporates the transport of turbulent shear stress, enhancing accuracy in predicting flow characteristics. In near-wall regions, the k-ω formulation is applied, while the k-ε formulation is used in the core flow regions.
The distinction between these regions is made through the blending function F_1, which weights the coefficients K_1 of the $k\text{-}\omega$ model and $K_2$of the $k\text{-}\varepsilon$ model to determine the SST model coefficient K_3 via:

$$K_3 = F_1 K_1 + (1 - F_1) K_2 \tag{4.33}$$

Neither the $k\text{-}\varepsilon$- nor the $k\text{-}\omega$ model alone adequately accounts for the transport of turbulent shear stress, often leading to inaccuracies in predicting eddy viscosity. To avoid overestimating eddy viscosity, the SST model introduces a limiter function $max(a_1 \omega_t, b_1 S F_2)$, where F_2 is another blending function distinguishing between near-wall and core regions, a_1 and b_1 are model constants, ω_t is the specific dissipation rate of turbulence and S represents the strain rate. The turbulent eddy viscosity is expressed as:

$$\vartheta_{\mathrm{t}} = \frac{a_1 k_{TKE}}{max(a_1 \omega_{TKE}, b_1 S F_2)} \tag{4.34}$$

The transport equation for turbulent kinetic energy is defined as:

$$\frac{\mathrm{D}}{\mathrm{Dt}}(\rho \mathrm{k_{TKE}}) = \nabla\left(\rho \mathrm{D_{k_{TKE}}} \nabla k_{TKE}\right) + \rho \mathrm{G} - \frac{2}{3} \rho k_{TKE} (\nabla \mathrm{u}) - \beta_{k\text{-}\omega} \rho k_{TKE} \omega_{TKE} + S_{k_{TKE}} \tag{4.35}$$

where G is the turbulence production term, $\beta_{k\text{-}\omega}$ is a model coefficient and $S_{k_{TKE}}$ represents the source term of the turbulent kinetic energy equation.

The transport equation for the specific dissipation rate ω_{TKE} is given in equation (4.36), where $\gamma_{SST\text{-}k\text{-}\omega}$ and $C_{SST\text{-}k\text{-}\omega}$ are model coefficients and $S_{\omega_{TKE}}$ represents the source term of the specific dissipation rate of turbulence equation

$$\frac{\mathrm{D}}{\mathrm{Dt}}(\rho\omega_t) = \nabla\left(\rho \mathrm{D}_{\omega_{TKE}} \nabla\omega_{TKE}\right) + \frac{\rho\gamma \mathrm{G}}{\vartheta} - \frac{2}{3}\rho\gamma_{SST\text{-}k\text{-}\omega}\omega_{TKE}(\nabla \mathrm{u}) - \beta_{k\text{-}\omega}\rho{\omega_{TKE}}^2 - \rho(\mathrm{F}_1 - 1)C_{SST\text{-}k\text{-}\omega}D_{k_{TKE}\omega_{TKE}} + S_{\omega_{TKE}} \tag{4.36}$$

The equations and coefficients, as formulated, are based on the work of [150], where a more detailed description of the model and the values of the coefficients implemented in the computational model can be found.

4.3.3 CFD Software - OpenFOAM

OpenFOAM (Open Field Operation And Manipulation) is an open-source programme primarily developed by OpenCFD Ltd. During the pre-processing step, the geometry is prepared and meshed, while fluid characteristics, including compressibility and turbulence models, are defined. The processing step entails the selection of solution methodologies, including solvers and convergence criteria, followed by the execution of the simulation. The post-processing stage involves assessing the simulation results. OpenFOAM distinguishes itself from conventional CFD simulation tools principally by the absence of a graphical user interface. However, the post-processing phase may optionally employ ParaView, which offers a graphical interface.

4.3.4 Numerical Derivation of Drag, Damping and Hydrodynamic Mass

Hydrodynamic coefficients define the correlation between the hydrodynamic forces exerted on a body and key flow characteristics, including velocity, acceleration and motion amplitude. These properties are required to solve the equation of motion presented in section 4.5. The characteristics thereby enable the characterisation and prediction of the dynamic behaviour of maritime structures under diverse flow conditions. Section 4.5 further defines the coefficients and clarifies their physical meaning within the equation of motion framework. The present study concentrates on the following three coefficients:

- Drag coefficients quantify the structure's resistance to incoming flow, principally linked to viscous and pressure-induced forces.
- Damping coefficients quantify energy dissipation resulting from radiated waves and viscous effects, especially pertinent in oscillatory or transient movements.
- Hydrodynamic mass coefficients consider the extra inertia caused by the acceleration of the surrounding fluid, hence increasing the apparent mass of the body.

In this section for numerical methodologies to derive these coefficients from CFD simulations the procedure outlined by Leitão et al. [152] is presented. The OpenFOAM-based workflow computes drag directly from converged steady loads in constant-velocity CFD runs, obtains damping by regressing those loads over families of linear and angular velocities to identify both linear and decoupled quadratic terms (including cross-couplings) and derives added mass from transient acceleration steps that isolate the acceleration-dependent increment in the six-component load.

The **drag** is directly calculated based on force integration in steady-velocity simulations, indicating that the surrounding flow maintains a constant (either linear or rotational) velocity along a single body axis. This is numerically derived by OpenFOAM as the sum of pressure

and viscous forces integrated throughout the wetted surface. In the translational configuration, the authors prescribe a uniform inlet velocity in the test direction, apply zero-gradient pressure at outlet and walls and enforce no-slip on the vehicle surface. They adopt an SST-k-ω turbulence model and solve the Navier–Stokes equations with the transient PISO algorithm (pisoFoam). The PISO (Pressure-Implicit with Splitting of Operators) algorithm is a pressure–velocity coupling method for incompressible CFD that advances the momentum equation and then enforces mass conservation by performing one or more pressure-correction steps. For rotational DoF, the body is placed in a rotating mesh region (a cylindrical subdomain) with "movingWallSlipVelocity" on the cylinder to impart angular motion. Here the authors employ an incompressible PISO-based solver configured for rotating frames together with a k-ε turbulence model. In both translational and rotational cases, drag is the principal component of the steady load along the excited DoF and is taken directly from OpenFOAM's force integration once steady conditions are reached.

The **damping** coefficients are obtained by repeating the steady velocity simulations over a set of velocities and regressing the resulting forces or moments against the imposed linear or angular velocity. Conceptually, damping in the 6-DoF model is the part of the hydrodynamic load proportional to velocity, arising from fluid–structure interaction via pressure gradients and wall shear. To estimate damping consistently across principal and cross-coupled terms, the authors perform families of steady runs. At each operating point, the fully converged load vector is plotted versus the corresponding linear or angular velocity yields, by coefficient-wise linear or quadratic fitting. The use of a linear model is emphasised for tractability and because it performs competitively at moderate speeds. If higher-order effects are relevant, the decoupled quadratic term estimated by the same regressions can be superposed without adopting a fully coupled quadratic form. [152]

The **hydrodynamic or added mass** is estimated with a two-phase transient protocol that isolates acceleration-dependent loads. For each DoF, the simulation first runs at a constant velocity until the steady load vector is converged. Then a step in constant acceleration is applied in the same DoF while all others remain at zero. Due to the acceleration the load increases to a new value. The difference reflects only acceleration-dependent effects. Dividing the magnitude of the load shift (difference between the force before the acceleration F_1 and the force with acceleration F_2) by the imposed (linear or angular) acceleration a_s yields the added mass coefficient associated with that DoF [152]:

$$m_{a_i} = \frac{F_{2_i} - F_{1_i}}{a_{s_i}} \tag{4.37}$$

One advantage of the presented procedures is that the simulation setup (environment, meshing and boundary conditions) needs only minor adjustments for deriving drag, damping and hydrodynamic mass. In the presented approach geometry preparation and meshing proceed via blockMesh to define the computational domain, followed by snappyHexMesh to fit the mesh to the body and to refine layers near the wall. The UUV surface is no-slip with appropriate wall functions for turbulence quantities. For translational cases, the fluid domain features a uniform inlet velocity in the studied direction of motion, zero-gradient outlet and zero-gradient pressure at boundaries. For rotational cases, a cylindrical subdomain enclosing the vehicle provides the rotating reference region. The cylinder wall uses a moving-wall slip condition to enforce angular motion while minimising viscous artefacts at the rotating boundary. These choices

allow the same model and post-processing to be used for different coefficients and across several DoF. [152]

Leitão et al. [152] validated their approach by comparing CFD against analytical solutions for a sphere and a spheroid. For the sphere, translational added mass derived from acceleration steps agrees with the analytic value within approx. 2.3 %. The validation of the damping coefficients for the sphere is assessed by simulating different constant speeds and comparing the computed drag force with the analytical value. Deviations decrease from 12.8 % at the lowest speed (0.1 m/s) to 1.9 % at the highest speed (0.6 m/s). For the spheroid, the same added mass protocol reached deviations of up to 0.9 % for translational DoF and 4.0 % for rotational DoF. Together, these results confirm that the solver settings, boundary conditions and post-processing achieve the expected analytical behaviour for bodies with known solutions. [152]

Other approaches to derive these hydrodynamic coefficients from CFD simulations using different simulation workflows and post-processing procedures are presented below. A detailed description is not provided, as these approaches represent alternative procedures that were not used in this work.
Hong et al. [153] simulate towing, rotating-arm and Planar Motion Mechanism tests, entirely in CFD to identify the hydrodynamic properties of an underactuated, torpedo-shaped vehicle. For steady motions, they solve the RANS equations with an SST-k-ω model in and replicate towing and rotating-arm tests to obtain velocity-dependent and rotary-rate-dependent damping by regressing converged loads against the prescribed linear or angular velocity. Unsteady coefficients are obtained via Planar Motion Mechanism: the body is placed in a multi-zone sliding-mesh setup and excited in pure surge, sway, heave and yaw. Decomposing the time-varying forces yields in-phase (added mass) and out-of-phase (damping) components. The mesh is unstructured with near-wall prism layers and is subjected to grid-independence checks. The geometry is simplified to remove small appendages that destabilise dynamic grids. Methodological credibility is established by comparisons to standard benchmarks like the the DARPA SUBOFF model and an ellipsoid. [153]
In Jiawei et al. [154] the focus is on an observation-class ROV and ways to compute its steady hydrodynamic coefficients. The authors run families of steady cases for longitudinal, lateral and vertical motions with inlet speeds from 0.1 to 1.0 m/s and additional “skew” (drift/heading) cases at ±10° to map yaw-related effects. For each operating point the resulting force and moment components are then regressed against the imposed velocity and heading to produce direction-wise resistance and linear damping derivatives. Because the study is restricted to steady simulations, acceleration-dependent added mass terms are not resolved. [154]
Amini Foroushani and Sabzpooshani [155] estimate rotary-plane damping and its dependence on Reynolds number by simulating a rotating-arm test for DARPA SUBOFF in a non-inertial reference frame. Instead of moving meshes, they add source terms to the steady RANS momentum equations so that the flow is solved on a fixed, high-quality mesh while the body undergoes steady turning. With this formulation, ANSYS Fluent solves the finite-volume discretization using a pressure-based SIMPLE (Semi-Implicit Method for Pressure-Linked Equations) algorithm. Boundary conditions and a user-defined function prescribe the radius-linear inlet profile and inertial-term sources. The hydrodynamic moment and lateral force components scale linearly with angular rate at fixed radius in the linear regime. Validation is achieved by comparison to published captive experiments for DARPA SUBOFF, with close agreement of linear fits.
Gadelho et al. [156] determine added mass and damping of a half-submerged circular cylinder

from fully viscous, time-domain simulations in OpenFOAM. The body is forced to oscillate harmonically in heave and sway and the solver interDyMFoam with mesh motion and a Volume of Fluid free-surface formulation provides the instantaneous hydrodynamic force history and radiated wave field. Assuming linear response at each excitation frequency, damping is obtained from the wave-energy balance: the amplitude of the radiated free surface for a given oscillation determines the linear radiation damping, which is then inserted into the linearised equation of motion so that the added mass as the remaining unknown follows directly from the measured force, prescribed displacement, velocity and acceleration. By sweeping frequency, they recover frequency-dependent added mass and damping. Convergence and plausibility are assessed against potential-flow solutions from Sutulo et al. [157]. Overall they achieve very good agreement for heave and small systematic underestimation of sway damping at higher frequencies, which the authors discuss in terms of neglected higher-harmonic force content and the predominance of inviscid pressure effects for most of the frequency range. [156]

4.4 Experimental Testing

Physical model testing is fundamental to fluid mechanics when full-scale prototype trials are unfeasible due to cost, logistical, or safety constraints. Model tests allow examination of flow behaviour, evaluating hydrodynamic performance and detecting design deficiencies at an early stage by testing scaled replicas. To ensure the findings are transferable, the model must replicate the real scaled reaction via similitude, necessitating geometric, kinematic and dynamic similarity to maintain the controlling physics across scales. In addition, experimental results are only considered robust if the test conditions are adequately controlled and the measurements are repeatable and reproducible, thereby limiting the influence of environmental variability, instrumentation drift and operator-dependent effects.
This section outlines the principles of scaling in hydrodynamic testing followed by a brief overview of forced oscillation tests employed to determine added mass and damping coefficients. In section 4.4.3 primary characteristics of the experimental towing tank facility at the University of Rostock utilised for the studies in this work are presented.

4.4.1 Principles of scaling in hydrodynamic testing

In practical applications, it is uncommon for all fluid forces such as inertia, gravity, viscosity, pressure, elasticity and surface tension to be simultaneously significant. Most problems are governed by inertia in combination with a single dominant additional force.

For example, ship resistance is typically governed by inertia and gravity, making Froude similarity the primary scaling requirement. In contrast, fully submerged bodies, pipe and channel flows at moderate-to-high Reynolds numbers are governed mainly by inertia and viscosity, so Reynolds similarity is central. Capillary-dominated phenomena, such as small droplets, thin films and microfluidic flows, are governed by inertia and surface tension (often characterised by the Weber or Capillary number). In this section only those principles of scaling in hydrodynamic testing that are relevant for the present work are considered. This includes Froude scaling, which represents the ratio of inertial to gravitational forces and Reynolds scaling, which represents the ratio of inertial to viscous forces. Dynamic similarity requires that the corresponding dimensionless numbers of the model and the full-scale configuration are equal. Equal Froude numbers preserve wave and gravitational effects making this approach particularly relevant for free-surface flows and problems in which surface waves are generated, such as vessel motions. Equal Reynolds numbers ensure similar viscous–inertial interactions

and are therefore suitable for the motion of submerged bodies or for flows around structures and other bodies fully immersed in a moving fluid.

The **Froude** number is defined as

$$Fr = \frac{v}{\sqrt{g\,L}} \tag{4.38}$$

where v denotes the characteristic velocity, L the characteristic length and g the gravitational acceleration.

Froude similarity is achieved by equating the Froude number of the real scaled model and the scaled model

$$Fr_{real} = Fr_{scaled} \tag{4.39}$$

$$\frac{v_{real}}{\sqrt{g_{real}\,L_{real}}} = \frac{v_{scaled}}{\sqrt{g_{scaled}\,L_{scaled}}} \tag{4.40}$$

The **Reynolds** number is a dimensionless quantity that characterises the ratio of inertial to viscous forces in a fluid flow. It is defined as

$$Re = \frac{\rho\, v\, L}{\mu} \tag{4.41}$$

Where ρ is the fluid density, v a characteristic flow velocity, L a characteristic length and μ the dynamic viscosity of the fluid. Low Reynolds numbers indicate laminar flows dominated by viscous effects, whereas high Reynolds numbers are associated with turbulence and inertia-dominated behaviour. In model testing and numerical simulations, matching the Reynolds number between model and full-scale is essential to achieve dynamic similarity with respect to viscous effects.

$$Re_{real} = Re_{scaled} \tag{4.42}$$

$$\frac{\rho_{\text{real}}\, v_{\text{real}}\, L_{\text{real}}}{\mu_{\text{real}}} = \frac{\rho_{scaled}\, v_{scaled}\, L_{scaled}}{\mu_{scaled}} \tag{4.43}$$

4.4.2 Forced oscillation tests

The added mass and damping coefficients of a submerged body can be determined using experimental testing by imposing a known and repeatable accelerations in a single DoF at a time. This is achieved using a standard forced oscillation test, in which a Planar Motion Mechanism drives the model with prescribed sinusoidal motions. This approach was established by the Planar Motion Mechanism (PMM), where the model oscillates with fixed amplitude and frequency while being towed at constant speed. In practice, the desired motions are realised by combining a constant towing velocity in one direction with a superimposed sinusoidal displacement in the direction perpendicular to the towing direction. [158]

In forced oscillation tests, the body is subjected to a prescribed oscillatory motion and the forces required to enforce this motion are measured. These forces are then introduced into the equation of motion for a single DoF, which can be written as [159]:

$$(m + m_a)\ddot{y} + C_{B_y}\dot{y} + cy = F_{meas} \tag{4.44}$$

where m denotes the known dry mass, m_a the added mass to be identified, C_{B_y} the damping coefficient to be identified, c the stiffness, which is set to zero in the present context and F_{meas} the measured hydrodynamic force acting in the same degree of freedom.

When body is subjected to a prescribed harmonic motion of the form

$$y = y_a \sin(\omega t) \tag{4.45}$$

with amplitude y_a and angular frequency ω

$$\dot{y} = \omega y_a \cos(\omega t) \tag{4.46}$$

and

$$\ddot{y} = -\omega^2 y_a \sin(\omega t) \tag{4.47}$$

The measured excitation force F_r can be represented by a harmonic function fitted as

$$\begin{aligned} F_{meas} &= F_a * \sin\left(\omega t + \varepsilon_{shift}\right) \\ &= F_a \sin(\omega t)\cos(\varepsilon_{shift}) + F_a \cos(\omega t)\sin(\varepsilon_{shift}) \end{aligned} \tag{4.48}$$

where F_a is the force amplitude and ε_{shift} the phase shift relative to the imposed motion.

Equation (4.48) can be inserted into equation (4.44) to form:

$$(m + m_a)\ddot{y} + C_{B_y}\dot{y} + cy = F_a \sin(\omega t)\cos(\varepsilon_{shift}) + F_a \cos(\omega t)\sin(\varepsilon_{shift}) \tag{4.49}$$

Decomposing equation (4.49) into an in-phase (acceleration related) component

$$y_a \sin(\omega t)[-\omega^2(m + m_a)] = F_a \sin(\omega t)\cos(\varepsilon_{shift}) \tag{4.50}$$

for added mass

$$m_a = -\frac{F_a \cos\left(\varepsilon_{shift}\right)\omega^2}{y_a} - m \tag{4.51}$$

and an out-of-phase (velocity related) component

$$\omega C_{B_y} y_a \cos(\omega t) = F_a \cos(\omega t)\sin(\varepsilon_{shift}) \tag{4.52}$$

for damping

$$C_{B_y} = \frac{F_a \sin(\varepsilon_{shift})}{y_a \omega} \tag{4.53}$$

In post-processing of model test data, the in-phase and out-of-phase components of the measured signal are computed from an integration over an integer number of periods of the measure signals using a first order Fourier analysis [160, 161].
For more detailed descriptions of the procedure, reference is made to literature such as e.g. Lin and Chiu. [158]

4.4.3 Towing Tank at the University of Rostock

The experiments realised within the scope of this work were conducted in the Towing Tank at the Chair of Fluid Mechanics University of Rostock, which is illustrated in Figure 4-4. The main basin is 37 m long, 5 m wide and up to 3 m deep [162].

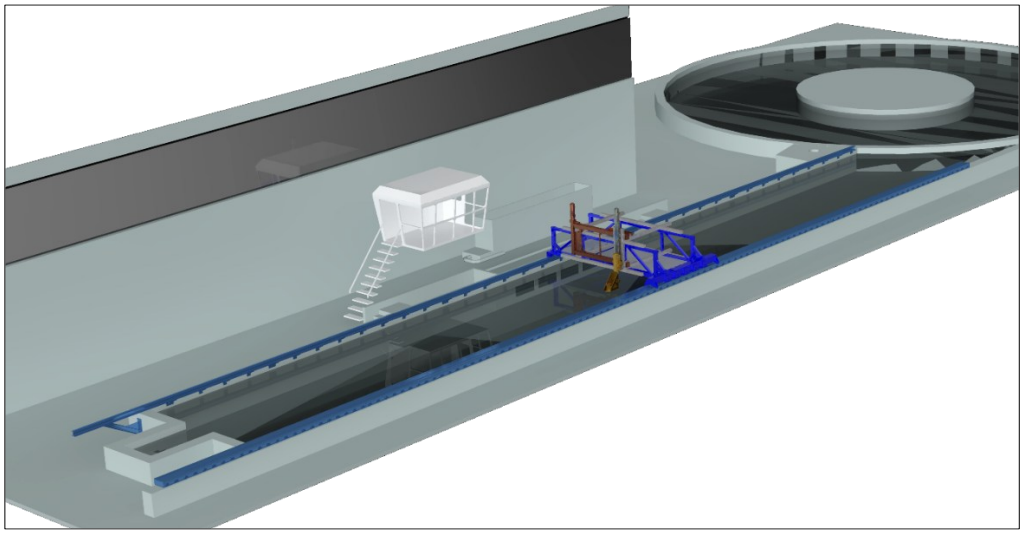


Figure 4-4: Towing Tank at the Chair of Fluid Mechanics University of Rostock [162]

The CNC-controlled towing carriage features three translational axes (X, Y, Z) and one rotational axis (C), whose orientations are illustrated in Figure 4-5. The X-axis (aligned with the towing direction) offers a measurement length of 34.7 m, a position accuracy of 0.1 mm and a maximum speed of 9 m/s depending on the payload, with corresponding maximum accelerations of 8 m/s². The transverse Y-axis provides a displacement of 2.0 m, a position accuracy of 0.1 mm, a maximum speed of 1.5 m/s, a maximum acceleration of 15 m/s² and a maximum load capacity of 450 kg. The vertical Z-axis has a travel of 1.1 m, a maximum speed of 1 m/s, a maximum acceleration of 20 m/s² and can carry up to 300 kg with weight compensation. All axes can be operated either in automated CNC path control mode or manually, enabling highly repeatable kinematics for towing tests, programmed oscillations and acceleration runs. [162]

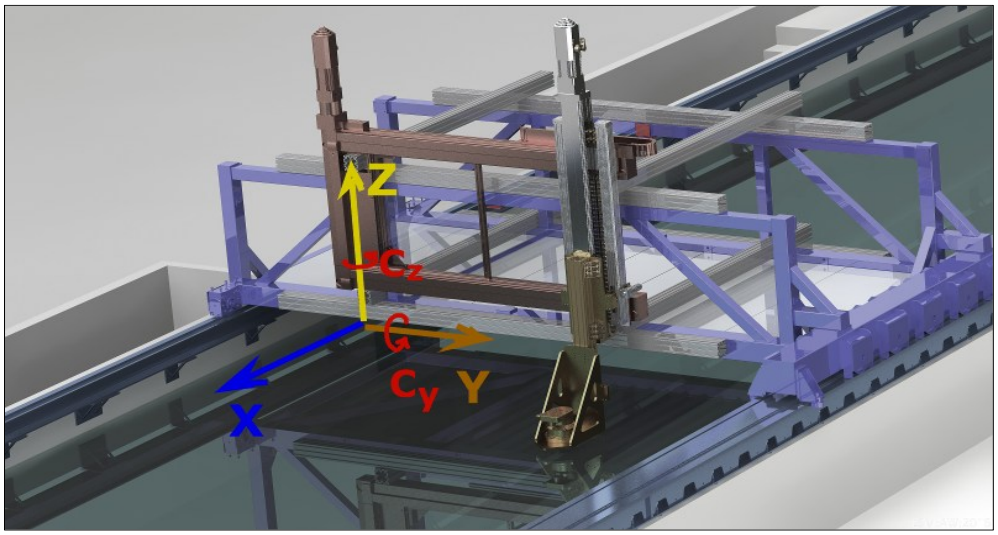


Figure 4-5: Axis orientation of the towing carriage [162]

4.5 Multibody Dynamics

By applying the fundamental principles of kinematics and kinetics for multibody systems, complex technical systems can be transformed into calculable mathematical structures. This substitution system enables the analysis of loads, dynamic behaviour or reactions. The calculations within this replacement system are carried out numerically. The accuracy of multibody simulations is influenced not only by the precision of numerical computations, but also by the complexity of the model and the correctness of the input data. [163]
These bodies, when interconnected, form a complex multibody system. The position of each body is clearly defined by position vectors and rotation matrices. By taking the time derivatives of these quantities, velocities and accelerations can be determined. Further time derivatives of angular momentum and linear momentum lead to the equations of motion, which describe the dynamics of a body within the system. [163]
The following sections first introduce the fundamental concepts of reference systems and DoF followed by a description of the basics required to simulate the towing of a submersible body by a vessel. Therefore, the vessels dynamics based on the equation of motion are described. After this, the modelling of the towing line is explained, as well as the calculation of the forces and moments that govern the cable's dynamics. Subsequently, the forces and moments responsible for the dynamics of a towed body are described. Based on these foundations, section 4.5.5, presents the solution procedure for the equation of motion.

4.5.1 Reference systems

To describe and calculate motions and forces, it is essential to define the position of each individual body with precision. In multibody dynamics, a right-handed global coordinate system G_{xyz} serves as the reference frame. Its origin is denoted as point 0 and the axes X_G, Y_G and Z_G are mutually orthogonal. The position of a body relative to the global coordinate system G_{xyz} is described by a body-fixed local coordinate system L_{xyz}, whose axes X_L, Y_L and Z_L are also orthogonal. The origin of the body-fixed coordinate system can be defined using a position vector with respect to the global system G_{xyz}. The orientation of the local coordinate system L_{xyz} is given by the alignment of its axes relative to the axes of the global system G_{xyz}. These coordinate systems are illustrated in Figure 4-6. [163]

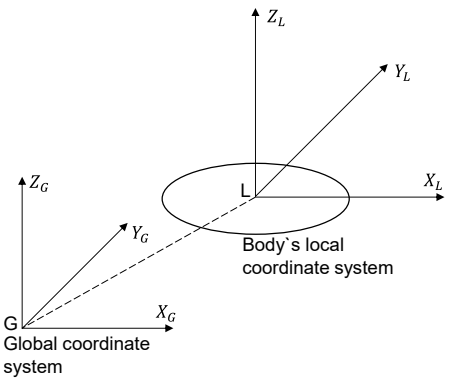


Figure 4-6: Global and local coordinate system (according to [164])

A freely moving rigid body can change its position or orientation under the influence of external forces. These changes manifest as translations, rotations or a combination of both. Since a rigid body in three-dimensional space possesses six DoF, it can translate along and rotate about each of the three spatial axes.

To describe the orientation of a rigid body with respect to the global coordinate system, Euler angles can be used. The body is rotated sequentially about the Z_L-axis, the X_L-axis and again the Z_L-axis. The initial position of the body is defined with respect to the global coordinate system. Each rotation is characterised by a specific angle. The first rotation about the Z_L-axis is defined by the angle ψ, the second about the X_L-axis by the angle Θ and the third, again about the Z_L-axis, by the angle φ. Together, these three angles fully define the body's orientation. The transformation between the two coordinate systems is achieved through the product of the three elementary rotation matrices. The rotation matrices for each axis are given as: [163]

$$\boldsymbol{R}_{\boldsymbol{Z_L}}(\psi) = \begin{bmatrix} \cos(\psi) & -\sin(\psi) & 0 \\ \sin(\psi) & \cos(\psi) & 0 \\ 0 & 0 & 1 \end{bmatrix} \tag{4.54}$$

$$\boldsymbol{R}_{\boldsymbol{X_L}}(\Theta) = \begin{bmatrix} 1 & 0 & 0 \\ 0 & \cos(\Theta) & -\sin(\Theta) \\ 0 & \sin(\Theta) & \cos(\Theta) \end{bmatrix} \tag{4.55}$$

$$\boldsymbol{R}_{\boldsymbol{Z_L}}(\varphi) = \begin{bmatrix} \cos(\varphi) & -\sin(\varphi) & 0 \\ \sin(\varphi) & \cos(\varphi) & 0 \\ 0 & 0 & 1 \end{bmatrix} \tag{4.56}$$

The overall rotation matrix $\boldsymbol{R}_{\boldsymbol{rot}}$ for the coordinate transformation is the product of these three matrices in the order given:

$$\boldsymbol{R}_{\boldsymbol{rot}} = \boldsymbol{R}_{\boldsymbol{Z_L}}(\psi) * \boldsymbol{R}_{\boldsymbol{X_L}}(\Theta) * \boldsymbol{R}_{\boldsymbol{Z_L}}(\varphi) \tag{4.57}$$

The translation of the body can be represented by the translation vector $\overrightarrow{T_{tra}}$, as shown in equation (4.58), whose components T_x, T_y and T_z define the displacement along the X-, Y- and Z-axes respectively. [165]

$$\overrightarrow{T_{tra}} = \begin{bmatrix} T_x \\ T_y \\ T_z \end{bmatrix} \tag{4.58}$$

To determine the exact position of a body, both the translation vector $\overrightarrow{T_{tra}}$ and the rotation matrix $\boldsymbol{R}_{\boldsymbol{rot}}$ are required. The translation vector specifies the displacement of the origin of the local coordinate system within the global coordinate system, while the rotation matrix describes the body's orientation. For a point $\overrightarrow{p_L}$ in the local coordinate system, with coordinates

$$\overrightarrow{p_L} = \begin{bmatrix} x_L \\ y_L \\ z_L \end{bmatrix} \tag{4.59}$$

the position $\overrightarrow{p_G}$ of this point in the global coordinate system can be determined by the following equation:

$$\overrightarrow{p_G} = \mathbf{R}_{\mathbf{rot}}\, \overrightarrow{p_L} + \overrightarrow{T_{tra}} \tag{4.60}$$

4.5.2 Vessel dynamics

A vessel (also referred to as a ship) is used in this work as a representative term for the surface-floating carrier platform. In maritime engineering, each of the six DoF of a vessel has a specific nomenclature to enable standardised and precise descriptions of vessel motions. The

translational motions along the X-, Y- and Z-axes are termed surge, sway and heave respectively, while the rotations about these axes are known as roll, pitch and yaw. The DoF are already introduced and illustrated in Figure 3-3 for AUVs in section 3.3.

The motion of a vessel on the free water surface is the result of complex interactions between hydrodynamic, aerodynamic and mechanical forces. External environmental factors such as waves, wind and currents generate hydrodynamic and aerodynamic forces that can induce or stabilise motion in various directions. Additionally, water characteristics like depth and density significantly influence drag and buoyancy forces. Internal effects, such as the hull shape, mass distribution and inertia forces of the vessel, also affect its motion. These, along with damping due to the surrounding medium and the added mass, contribute to the overall inertia of the system. The added mass refers to the additional inertia resulting from the acceleration or displacement of the surrounding fluid when an object moves within it. Mechanical influences, including thrust forces from propulsion as well as acceleration and deceleration, directly affect the vessel's direction and velocity. [166, 167, 168]

In the present study, vessel motion is calculated and simulated as a response to wave excitation. Therefore, only wave-induced motion is examined in detail at this point. The motion of a vessel in waves can be described using Displacement Response Amplitude Operators (RAOs). Each RAO consists of a pair of numerical values representing the vessel's response in a specific degree of freedom for a given wave direction and period. These linear values include an amplitude, which indicates the motion relative to the wave amplitude and a phase, which defines the time shift between the wave and the vessel response. Due to the vessel's six DoF, the RAO data consist of six amplitude-phase pairs for a wave period and heading. Amplitudes are expressed in units of length for translational motions and in degrees for rotational motions. The vessel displacement or rotation x_{vessel_i} (in the DoF i) can be described by equation (4.61), where R_{RAO_i} is the RAO amplitude as a normalized ratio of response amplitude to excitation amplitude, ζ_{a_i} the wave amplitude (excitation amplitude), ω_i the wave angular frequency, ϕ_{RAO_i} the RAO phase for the time shift and t_{RAO} the time elapsed since the wave crest passed the RAO reference point: [166]

$$x_{vessel_i} = R_{RAO_i}\,\zeta_{a_i}\,\cos\left(\omega_i\,t_{RAO} - \phi_{RAO_i}\right) \tag{4.61}$$

To model vessel motion accurately, RAOs must be determined with high precision. This can be achieved experimentally or by using computational tools that rely on diffraction analysis and linear potential theory. An example of such a tool is OrcaWave, developed by Orcina [169]. Potential theory describes fluid motion as a solution to the Laplace equation, assuming the fluid is incompressible, irrational and inviscid. For a detailed discussion of potential theory and the interaction between potential theory and wave spectrum to calculate the vessel dynamic, reference is made to literature such as the work by Rapp [170] and Clauss et al. [171].

Displacement RAOs represent the amplitudes $\vec{\xi}$ of motion in the direction of the considered DoF i, influenced by contributions from all DoF j. They are the complex amplitudes of the body's oscillatory motion relative to its equilibrium position and are expressed in the body-fixed coordinate system L_{xyz}, with ξ_x, for example, denoting motion along L_x. RAOs are obtained by solving the body's equation of motion under the assumption of first-order wave excitation. The simplified form of this equation, for a freely floating vessel with linear damping

and neglecting external damping and stiffness matrices, is adopted from [166, 172] and presented as:

$$\{-\omega^2(\boldsymbol{M_m} + \boldsymbol{A_m}) + i\omega\, \boldsymbol{B} + \boldsymbol{K_L}\}\vec{\xi} = \overrightarrow{F_{wave}} \tag{4.62}$$

In this equation, $\overrightarrow{F_{wave}}$ represents the wave-induced external forces on the vessel. The matrix $\boldsymbol{M_m}$ is the vessel's mass matrix, shown in equation (4.63). Here, m denotes the total vessel mass; I_{xx}, I_{yy} and I_{zz} are the principal moments of inertia; and x_{COG}, y_{COG}, z_{COG} are the coordinates of the centre of gravity in the vessel's local frame. The products of inertia I_{xy}, I_{xz} and I_{yz} account for inertia coupling between rotational axes.

$$\boldsymbol{M_m} = \begin{bmatrix} m & 0 & 0 & 0 & m\,z_{COG} & -m\,y_{COG} \\ 0 & m & 0 & -m\,z_{COG} & 0 & m\,x_{COG} \\ 0 & 0 & m & m\,y_{COG} & -m\,x_{COG} & 0 \\ 0 & -m\,z_{COG} & m\,y_{COG} & I_{xx} & -I_{xy} & -I_{xz} \\ m\,z_{COG} & 0 & -m\,x_{COG} & -I_{yx} & I_{yy} & -I_{yz} \\ -m\,y_{COG} & m\,x_{COG} & 0 & -I_{zx} & -I_{zy} & I_{zz} \end{bmatrix} \tag{4.63}$$

For typical marine vehicles that are symmetric about the longitudinal axis, the mass distribution implies $y_{COG} = 0$ and the products of inertia involving the y-axis vanish, which leads to $I_{xy} = I_{yx} = I_{yz} = I_{zy} = 0$. If the body-fixed origin is chosen at the COG ($x_{COG} = x_{COG} = x_{COG} = 0$), the translational–rotational coupling terms disappear. Moreover, if the body axes are aligned with the principal axes at the COG (a common "normal case" assumption), then $I_{xz} = I_{zx} = 0$. In those circumstances $\boldsymbol{M_m}$ becomes a fully diagonal matrix:

$$\boldsymbol{M_m} = \begin{bmatrix} m & 0 & 0 & 0 & 0 & 0 \\ 0 & m & 0 & 0 & 0 & 0 \\ 0 & 0 & m & 0 & 0 & 0 \\ 0 & 0 & 0 & I_{xx} & 0 & 0 \\ 0 & 0 & 0 & 0 & I_{yy} & 0 \\ 0 & 0 & 0 & 0 & 0 & I_{zz} \end{bmatrix} \tag{4.64}$$

The matrix $\boldsymbol{A_m}$ represents the added mass of the floating body. The matrix notation follows the conventions of the Society of Naval Architects and Marine Engineers [173]. It describes the hydrodynamic inertia effects resulting from fluid-structure interaction.

$$\boldsymbol{A_m} = \begin{bmatrix} X_{\dot{u}} & X_{\dot{v}} & X_{\dot{w}} & X_{\dot{p}} & X_{\dot{q}} & X_{\dot{r}} \\ Y_{\dot{u}} & Y_{\dot{v}} & Y_{\dot{w}} & Y_{\dot{p}} & Y_{\dot{q}} & Y_{\dot{r}} \\ Z_{\dot{u}} & Z_{\dot{v}} & Z_{\dot{w}} & Z_{\dot{p}} & Z_{\dot{q}} & Z_{\dot{r}} \\ K_{\dot{u}} & K_{\dot{v}} & K_{\dot{w}} & K_{\dot{p}} & K_{\dot{q}} & K_{\dot{r}} \\ M_{\dot{u}} & M_{\dot{v}} & M_{\dot{w}} & M_{\dot{p}} & M_{\dot{q}} & M_{\dot{r}} \\ N_{\dot{u}} & N_{\dot{v}} & N_{\dot{w}} & N_{\dot{p}} & N_{\dot{q}} & N_{\dot{r}} \end{bmatrix} \tag{4.65}$$

The entries, known as hydrodynamic mass coefficients, relate forces and moments to body accelerations. For example, the first entry is given by:

$$X_{\dot{u}} = \frac{\partial X}{\partial \dot{u}} \tag{4.66}$$

This coefficient characterises the sensitivity of the hydrodynamic force X in the x-direction to an acceleration $\dot{u}$ in the x-direction. $X_{\dot{u}}$ therefore quantifies how the surrounding fluid's added inertia affects force X under acceleration in the x-direction.
Other entries describe analogous effects for the remaining DoF. Terms such as $Y_{\dot{v}}$, $Z_{\dot{w}}$, etc. refer to accelerations in the translational y- and z-directions, while entries like $K_{\dot{p}}$, $M_{\dot{q}}$ and $N_{\dot{r}}$ represent hydrodynamic moments of inertia induced by angular accelerations about the x-, y- and z-axes respectively.

While moving through the fluid, the vessel is subjected to pressure and viscous forces that oppose its motion, leading to hydrodynamic damping forces and moments. The linear damping matrix $\boldsymbol{B}$, as shown in equation (4.67), captures these effects and is structured according to the six DoF:

$$\boldsymbol{B} = \begin{bmatrix} X_u & X_v & X_w & X_p & X_q & X_r \\ Y_u & Y_v & Y_w & Y_p & Y_q & Y_r \\ Z_u & Z_v & Z_w & Z_p & Z_q & Z_r \\ K_u & K_v & K_w & K_p & K_q & K_r \\ M_u & M_v & M_w & M_p & M_q & M_r \\ N_u & N_v & N_w & N_p & N_q & N_r \end{bmatrix} \tag{4.67}$$

Translational DoF are represented by entries like X_u, Y_v and Z_w, while rotational DoF are captured by terms such as K_p, M_q andN_r. Each matrix entry indicates the magnitude of hydrodynamic damping force or moment in a given degree of freedom. For instance, X_u is defined as:

$$X_u = \frac{\partial X}{\partial u} \tag{4.68}$$

This coefficient shows how the hydrodynamic force X in the x-direction responds to velocity u. It quantifies the influence of pressure and viscous fluid forces on the damping of force X during motion along the x-axis.
The hydrodynamic stiffness matrix $\boldsymbol{K_L}$, given in equation (4.69), describes the restoring forces and moments resulting from hydrostatic effects when the vessel is displaced or inclined about its equilibrium position.

$$\boldsymbol{K_L} = \rho\, g \begin{bmatrix} 0 & 0 & 0 & 0 & 0 & 0 \\ 0 & 0 & 0 & 0 & 0 & 0 \\ 0 & 0 & \int_{S_B} n_3\, dS_{wet} & \int_{S_B} n_3\, y\, dS_{wet} & -\int_{S_B} n_3\, x\, dS_{wet} & 0 \\ 0 & 0 & \int_{S_B} n_3\, y\, dS_{wet} & \int_{S_B} n_3\, y^2\, dS_{wet} + q_3 & -\int_{S_B} n_3\, x\, y\, dS_{wet} & -q_1 \\ 0 & 0 & -\int_{S_B} n_3\, x\, dS_{wet} & -\int_{S_B} n_3\, x\, y\, dS_{wet} & \int_{S_B} n_3\, x^2\, dS_{wet} + q_3 & -q_2 \\ 0 & 0 & 0 & 0 & 0 & 0 \end{bmatrix} \tag{4.69}$$

For fully submerged bodies with constant displaced volume, the hydrostatic restoring is governed primarily by the relative offset between the centre of gravity and the centre of buoyancy (yielding predominantly rotational restoring moments, while translational restoring terms are typically absent in an unstratified fluid). For partially submerged (surface-piercing)

bodies, additional and often dominant restoring contributions arise from changes in the submerged volume and waterplane area, leading to significant translational and coupled restoring terms. In this matrix, ρ is the fluid density, g gravitational acceleration, dS_{wet} is an infinitesimal surface element of the wetted surface area S_{wet}, n_3 the surface normal component in z-direction and q_1, q_2, q_3 are correction terms accounting for additional hydrostatic effects.

The equation of motion (4.62) enables the precise calculation of vessel responses ξ_j in all six DoF under wave excitation. The resulting RAOs are then used to model vessel motion behaviour for various wave conditions and amplitudes.

4.5.3 Dynamics of the towing cable

To compute the dynamic response of a towed cable, the system can be modelled using a lumped-mass approach. This method involves dividing the cable into n identical segments, which are connected by $n + 1$ nodes. Indexing starts at the first node, assigned the value 0. The segment between nodes 0 and 1 is indexed as ½. and subsequent segments are indexed as $k + ½$. The global position of a node is defined by the vector $\overrightarrow{r_k}$, comprising its x-, y- and z-components. This discretisation method is illustrated in Figure 4-7. [174]

$$\overrightarrow{r_k} = \begin{bmatrix} x_k \\ y_k \\ z_k \end{bmatrix} \tag{4.70}$$

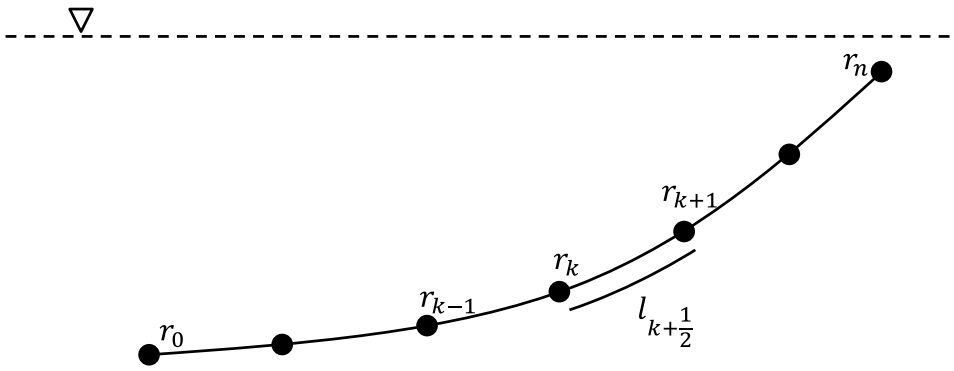


Figure 4-7: Discretisation of the towing cable (according to [143])

The individual nodes of the lumped-mass model represent short beams that include half-segments on either side (except for the first and last nodes) and account for physical properties such as mass, buoyancy and drag. The massless segments between the nodes transmit forces and capture the cable's mechanical and elastic characteristics, such as bending stiffness and elasticity. These segment properties are implemented using spring-damper elements. Arranged in parallel, these spring-damper elements (also referred to as Kelvin-Voigt elements) model the viscoelastic behaviour of the cable and its interaction with the surrounding fluid. Figure 4-8 offers a more detailed view of the lumped-mass model. Axial spring-dampers centrally placed in each segment simulate axial stiffness and damping via opposing tensile forces at the segment's nodes. Rotational spring-dampers on either side of each node model bending by aligning axial directions. Torsional spring-dampers represent torsional stiffness by applying equal and opposite torques at the segment ends. [174, 175]

The following section outlines some of the equations employed to simulate the dynamics of each node and segment. These equations are solved individually for every node and segment, relying on classical mechanics principles that account for inertia, external forces, internal

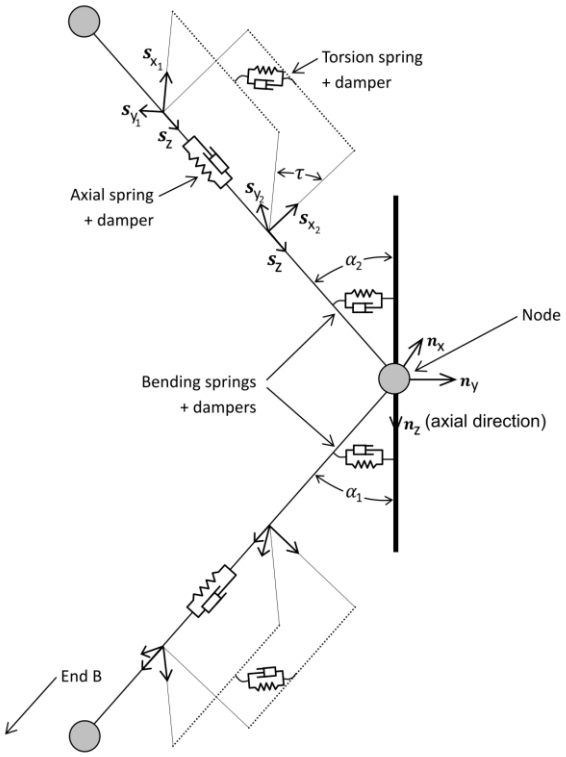


Figure 4-8: Lumped-mass model [143]

stresses and damping forces to simulate the towing cable's motion. The axial force F_{axial} in equation (4.71) is assumed to behave linearly and is modelled via axial spring-damper elements. The first term represents the axial force resulting from cable elongation, where E is the modulus of elasticity, A the cross-sectional area and l_1 the current length of the segment. The second term captures the coupling between axial force and torsion, involving the coupling coefficient k_{tt} and the twist angle τ. The third term incorporates axial damping, with c_c representing the damping coefficient, l the segment length and dl_1/dt the rate of change of segment length.

$$F_{axial} = EA\frac{(l_1 - l)}{l} + \frac{k_{tt}\,\tau}{l} + EA\,c_c\frac{dl_1}{dt}\frac{1}{l} \tag{4.71}$$

Bending stiffness is assumed to be linear, with the cable treated as an isotropic material, meaning the bending stiffness is equal in both $\overrightarrow{s_x}$ and $\overrightarrow{s_y}$ directions. This linear-elastic bending assumption is generally acceptable provided that cable curvatures and bending strains remain moderate and that the cable is not operating in regimes dominated by large rotations, contact, or significant material nonlinearity. In practical terms, the assumption is most defensible when the cable response is governed primarily by axial tension and small-to-moderate bending, which is typical for towed configurations under steady or mildly varying excitation. The linear model is also conservative in the sense that it can overpredict bending moments and local stresses if, in reality, the cable exhibits stiffness degradation, hysteresis, or geometric nonlinearities that effectively redistribute curvature. The resulting bending moment $\overrightarrow{M_2}$, as given in equation (4.72), is derived from the spring-damper elements acting between the axial direction of the node (n_z) and the segment's axial direction ($\overrightarrow{s_z}$), dependent on the angle α_2. The first term denotes the elastic bending moment, proportional to the bending stiffness EI and the curvature

magnitude $|\vec{\kappa}|$. The second term accounts for damping, where d_c is the bending damping coefficient and $d|\vec{\kappa}|/dt$ the curvature magnitude time derivative.

$$|\overrightarrow{M_2}| = EI\ |\vec{\kappa}| + d_c\ \frac{d|\vec{\kappa}|}{dt} \tag{4.72}$$

An additional bending moment M_1, acting on the opposite side of the node and resulting from curvature defined by angle α_1, induces a transverse shear force $\overrightarrow{F_s}$ at the node. This shear force is computed using equation (4.73), which involves the segment direction $\overrightarrow{s_z}$, the difference in bending moments $\overrightarrow{M_2} - \overrightarrow{M_1}$.

$$\overrightarrow{F_s} = \overrightarrow{s_z} \times \frac{1}{l}(\overrightarrow{M_2} - \overrightarrow{M_1}) \tag{4.73}$$

Torsional moment is also modelled linearly using spring-damper elements. The twist angle τ, defined between directions $\overrightarrow{s_{x1}}$ and $\overrightarrow{s_{x2}}$, governs this interaction. In equation (4.74), the first term represents the elastic restoring torque with torsional stiffness k_t. The second term models the coupling with axial strain and the third term addresses the damping torque due to twisting, with c_t denoting the torsional damping coefficient.

$$|M_t| = k_t \frac{\tau}{l_0} + k_{tt} \frac{(l_1 - l)}{l} + c_t \frac{d\tau}{dt} \tag{4.74}$$

Each node is subject to hydrodynamic forces that influence the cable's dynamics. One such force is drag $\overrightarrow{F_{D_c}}$, defined in equation (4.75). Here, A_{wet} is the ratio of the wetted area, d_n and d_a are the projected diameters normal and axial to the cable's axis. C_{D_x}, C_{D_y} and C_{D_z} are the drag coefficients in the corresponding directions. The variables v_{f_x}, v_{f_y} and v_{f_z} denote the components of the fluid velocity relative to the cable and v_{f_n} the relative velocity perpendicular to the cable axis.

$$\overrightarrow{F_{D_c}} = \frac{1}{2} A_{wet}\ \rho \begin{bmatrix} d_n\ l\ C_{D_x}\ v_{f_x}\ |v_{f_n}| \\ d_n\ l\ C_{D_y}\ v_{f_y}\ |v_{f_n}| \\ \pi\ d_a\ l\ C_{D_z}\ v_{f_z}\ |v_{f_z}| \end{bmatrix} \tag{4.75}$$

In addition to drag, the lift force $\overrightarrow{F_L}$ must be determined for each node. This dynamic lift force is influenced by the inclination angle β of the cable axis relative to the horizontal plane. The coefficient C_L characterises the lift strength, v_{f_t} is the tangential relative fluid velocity and $\overrightarrow{u_L}$ is the lift direction orthogonal to the cable axis and lying in the plane formed by the cable axis and the relative flow. Equation (4.76) quantifies this relationship.

$$\overrightarrow{F_L} = A_{wet}\ cos(\beta)\ \frac{1}{2}\ \rho\ d_n\ l\ C_L\ |v_{f_t}|^2\ \overrightarrow{u_L} \tag{4.76}$$

Finally, the added mass force $\overrightarrow{F_{A_c}}$ acting on each node due to the additional inertia of the surrounding fluid is described by equation (4.77).

$$\overrightarrow{F_{A_c}} = \begin{bmatrix} (1 + C_{a_x})\ \Delta\ a_{e_x} - C_{a_x}\ \Delta_c\ a_{l_x} \\ (1 + C_{a_y})\ \Delta\ a_{e_y} - C_{a_y}\ \Delta_c\ a_{l_y} \\ (1 + C_{a_z})\ \Delta\ a_{e_z} - C_{a_z}\ \Delta_c\ a_{l_z} \end{bmatrix} \tag{4.77}$$

The coefficients C_{a_x}, C_{a_y} and C_{a_z} represent the added mass coefficients in each direction. Δ_c denotes the mass of the displaced fluid volume of the cable segment. The terms a_{e_x}, a_{e_y} and a_{e_z} are the absolute fluid accelerations in each direction, while a_{l_x}, a_{l_y} and a_{l_z} represent the

relative acceleration between the cable segment and the fluid, defined as the difference between the respective accelerations.

4.5.4 Dynamics of the towed body

The towed body can be idealised as a simplified rigid body with six DoF, represented by a point mass. This approach offers the advantage that there is no need to import complex geometries into the simulation. Instead, properties derived from the actual structure, such as mass moment of inertia, centre of mass or cross-sectional areas, can be directly assigned to the point mass. This significantly reduces computational effort during simulation, as these properties do not have to be calculated from the detailed geometry. At the same time, this method enables an efficient simulation process by focusing on the essential dynamic aspects, without compromising the accuracy of the overall system response. The following forces and moments are described for the fully submerged condition.

The weight force $\overrightarrow{F_W}$ can be calculated using the mass of the towed body m_b and the vertically downward unit vector $\overrightarrow{u_z}$, as shown in equation (4.78). This force acts on the centre of mass of the towed body.

$$\overrightarrow{F_W} = -m_b \, g \, \overrightarrow{u_z} \tag{4.78}$$

The hydrostatic buoyancy force $\overrightarrow{F_B}$ is expressed by equation (4.79), where V_b denotes the displaced volume of the fully submerged body. The buoyancy acts on the centre of volume.

$$\overrightarrow{F_B} = \rho \, g \, V_b \, \overrightarrow{u_z} \tag{4.79}$$

During the translational motion of the towed body through water, the added mass effect must be considered. This effect arises from the acceleration of the surrounding fluid that is also set into motion by the body. The force $\overrightarrow{F_{A_b}}$, representing this effect, is provided in equation (4.80).

$$\overrightarrow{F_{A_b}} = \begin{bmatrix} \left(1 + C_{a_x}^t\right) \Delta_b \, a_{f_x} - C_{a_x}^t \, \Delta_b \, a_{b_x} \\ \left(1 + C_{a_y}^t\right) \Delta_b \, a_{f_y} - C_{a_y}^t \, \Delta_b \, a_{b_y} \\ \left(1 + C_{a_z}^t\right) \Delta_b \, a_{f_z} - C_{a_z}^t \, \Delta_b \, a_{b_z} \end{bmatrix} \tag{4.80}$$

Here, $C_{a_x}^t$, $C_{a_y}^t$ and $C_{a_z}^t$ denote the translational added mass coefficients in x-, y- and z-directions. These coefficients correspond to the diagonal elements of the added-mass matrix defined in equation (4.65). Specifically, $C_{a_x}^t$ corresponds to $X_{\dot{u}}$, $C_{a_y}^t$ to $Y_{\dot{v}}$ and $C_{a_z}^t$ to $Z_{\dot{w}}$. The notation is used deliberately to highlight that, at this point, only the principal diagonal entries of that matrix in equation (4.65) are considered. The variable Δ_b represents the mass of the fluid displaced by the towed body. The components a_{f_x}, a_{f_y} and a_{f_z} refer to the fluid acceleration relative to the Earth, while a_{b_x}, a_{b_y} and a_{b_z} denote the fluid acceleration relative to the motion of the towed body.

In addition to translational effects, the rotational influence of added mass must also be included. The moment $\overrightarrow{M_{A_b}}$, resulting from added mass, is described in equation (4.81). The terms $C_{a_x}^r$, $C_{a_y}^r$ and $C_{a_z}^r$ are the rotational added mass coefficients. Similar to the translational added mass coefficients they correspond to the diagonal elements of the added-mass matrix ($C_{a_x}^r = K_{\dot{p}}$; $C_{a_y}^r = M_{\dot{q}}$; $C_{a_z}^r = N_{\dot{r}}$) defined in equation (4.65) but are presented in a different notation to

draw attention to the fact that only the principal diagonal coefficients are considered. $\mathrm{I}_{\mathrm{hydr_x}}$, $\mathrm{I}_{\mathrm{hydr_y}}$ and $\mathrm{I}_{\mathrm{hydr_z}}$ represent the hydrodynamic moments of inertia of the surrounding fluid and $\dot{\omega}_{b_x}$, $\dot{\omega}_{b_y}$ and $\dot{\omega}_{b_z}$ are the angular accelerations of the towed body relative to the Earth.

$$\overrightarrow{M_{A_b}} = \begin{bmatrix} -C_{a_x}^r \, \mathrm{I}_{\mathrm{hydr_x}} \, \dot{\omega}_{b_x} \\ -C_{a_y}^r \, \mathrm{I}_{\mathrm{hydr_y}} \, \dot{\omega}_{b_y} \\ -C_{a_z}^r \, \mathrm{I}_{\mathrm{hydr_z}} \, \dot{\omega}_{b_z} \end{bmatrix} \tag{4.81}$$

The hydrodynamic damping force $\overrightarrow{F_{DA_b}}$ counteracts the translational motion of the towed body and is assumed to be linear and proportional to the relative velocity components v_{b_x}, v_{b_y} and v_{b_z} in the respective directions. The damping is calculated using the unit damping forces UDF_x, UDF_y and UDF_z, which represent the force per unit length at a velocity of one metre per second. Although these coefficients are contained in the damping matrix of equation (4.67), a dedicated notation is introduced here to make explicit that only the principal diagonal entries are considered. The same applies for the unit damping moments in equation (4.83).

$$\overrightarrow{F_{DA_b}} = \begin{bmatrix} -UDF_x \, v_{b_x} \\ -UDF_y \, v_{b_y} \\ -UDF_z \, v_{b_z} \end{bmatrix} \tag{4.82}$$

In addition to the damping force, the damping moment $\overrightarrow{M_{DA_b}}$, which resists rotational motion, must be considered. This moment is directly proportional to the angular velocities ω_{b_x}, ω_{b_y} and ω_{b_z}. It is computed using the unit damping moments UDM_x, UDM_y and UDM_z, which specify the resisting moment for an angular velocity of one radian per second.

$$\overrightarrow{M_{DA_b}} = \begin{bmatrix} -UDM_x \, \omega_{b_x} \\ -UDM_y \, \omega_{b_y} \\ -UDM_z \, \omega_{b_z} \end{bmatrix} \tag{4.83}$$

The drag force $\overrightarrow{F_{D_b}}$ arises from the motion of the body through the fluid, as it must displace or push away the stationary fluid particles. In addition, viscous effects contribute to deceleration. The drag force for a fully submerged body is expressed in equation (4.84). The coefficients $C_{D_x}^t$, $C_{D_y}^t$ and $C_{D_z}^t$ represent the translational drag coefficients. A_x, A_y and A_z are the cross-sectional areas and $|\overrightarrow{v_b}|$ is the magnitude of the towed body's velocity vector.

$$\overrightarrow{F_{D_b}} = \begin{bmatrix} -\frac{1}{2}\rho \, C_{D_x}^t \, A_x \; v_{b_x} \, |\overrightarrow{v_b}| \\ -\frac{1}{2}\rho \, C_{D_y}^t \, A_y \; v_{b_y} \, |\overrightarrow{v_b}| \\ -\frac{1}{2}\rho \, C_{D_z}^t \, A_z \; v_{b_z} \, |\overrightarrow{v_b}| \end{bmatrix} \tag{4.84}$$

Since rotational motion also results in displacement of the surrounding fluid, a resisting drag moment $\overrightarrow{M_{D_b}}$ acts against this motion. It is described by equation (4.85). The terms $C_{D_x}^r$, $C_{D_y}^r$ and $C_{D_z}^r$ denote the rotational drag coefficients, while AM_x, AM_y and AM_z represent the rotational drag area moments. The angular velocities ω_{b_x}, ω_{b_y} and ω_{b_z} correspond to the respective coordinate directions of the angular velocity vector $\overrightarrow{\omega_b}$. The fluid is considered irrotational and thus does not contribute angular velocity.

$$\overrightarrow{M_{D_b}} = \begin{bmatrix} -\frac{1}{2}\rho\, C_{D_x}^{r}\, AM_x\, \omega_{b_x}\, |\overrightarrow{\omega_b}| \\ -\frac{1}{2}\rho\, C_{D_y}^{r}\, AM_y\, \omega_{b_y}\, |\overrightarrow{\omega_b}| \\ -\frac{1}{2}\rho\, C_{D_z}^{r}\, AM_z\, \omega_{b_z}\, |\overrightarrow{\omega_b}| \end{bmatrix} \tag{4.85}$$

4.5.5 Solution procedure for equation of motion

In multibody dynamic simulations, the motion of each individual point of the towing cable, the vessel and the towed body is calculated as a function of time. This calculation is based on the underlying local equation of motion, as represented in equation (4.86).

$$\boldsymbol{M_s}(p_s, a_s) + \boldsymbol{B}(p_s, v_s) + \boldsymbol{K_L}(p_s) = \vec{F}(p_s, v_s, t_s) \tag{4.86}$$

In this expression, $\boldsymbol{M_s}$ denotes the mass and inertia matrix (including $\boldsymbol{M_m}$ and $\boldsymbol{A_m}$), $\boldsymbol{B}$ the linear damping matrix, $\boldsymbol{K_L}$ the stiffness matrix and $\vec{F}$ the vector of external forces acting on the point of interest. The variables p_s, v_s and a_s represent the position, velocity and acceleration vectors respectively, while t_s stands for the simulation time.
At each time step, the positions of all elements are recalculated, allowing for the inclusion of nonlinear effects and thereby yielding realistic simulation results. To solve these equations explicit or implicit numerical integration methods can be used. In the implicit method, the equations for the subsequent time step are not directly evaluated but formulated as a coupled system of equations. This system comprises both the current and future states and must therefore be solved iteratively. The implicit approach offers particularly high numerical stability. Although it theoretically allows for larger time steps, in dynamic systems the time step must still be sufficiently small to ensure convergence, which may increase computation time.

At the start of a simulation, the static equilibrium state of the system is first determined. This involves balancing all forces and moments in the system so that their resultant equals zero. The static calculation includes effects such as weight, buoyancy, drag forces, added mass, as well as tension, shear forces, bending and torsion. Before entering the dynamic simulation phase, the system undergoes a so-called build-up phase, during which vessel and wave motions are gradually introduced. This procedure is intended to avoid large transient effects between the static and dynamic solutions.

4.5.6 Simulation software OrcaFlex

OrcaFlex, developed by Orcina, is a comprehensive software tool for the static and dynamic analysis of offshore systems. Common application areas include the simulation of risers, mooring systems, installation analyses, buoy systems, hose systems and towed systems, as well as studies in defence and renewable energy contexts.
Representing such systems requires to define and parameterise the relevant physical properties and environmental conditions (e.g., geometry, mass and inertia properties, stiffness and damping characteristics, hydrodynamic coefficients and load cases). Simulations can be used to study the dynamic response of systems to influences such as waves, currents and wind. OrcaFlex supports a wide range of analysis methods, including static analysis, modal analysis, time-domain and frequency-domain dynamic analysis, as well as load and fatigue analyses.

5. Submerged Towed Docking Device

The conceptual and technical development of the concept is based on the rationale and objectives outlined in chapter 3. The functional and operational requirements as well as the comprehensive assessment of the current state of the art in AUV LARS were taken into account in order to develop the concept described within this chapter. This system design builds upon the idea of a submerged towed docking device referred to as the Launch and Recovery Device (LARD). A schematic representation of the concept is provided in Figure 5-1.

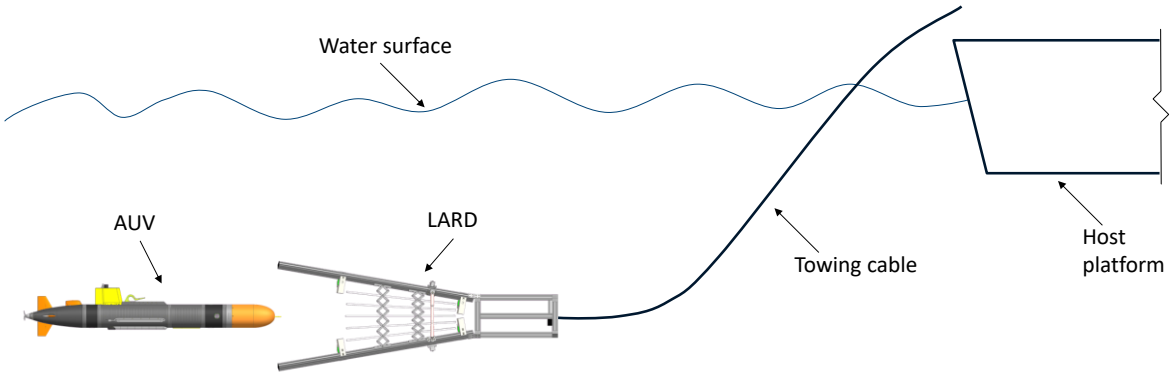


Figure 5-1: Schematic illustration of L&R System

A fundamental challenge in AUV L&R from surface host platforms lies in the differing hydrodynamic responses of the AUV and the carrier platform when subjected to wave excitation. These differences arise from distinct characteristics in size, mass distribution and geometric configuration, which lead to dissimilar motion behaviour in sea. Consequently, synchronised manoeuvring between the AUV and the host platform becomes highly unreliable. To mitigate this issue, a towed docking device is utilised. As this device's properties are more closely to the AUV's dimensions, mass and hydrodynamic properties the frequency ranges in which waves cause motion are closer compared to the carrier vessel.

Furthermore, wave-induced relative motion can be reduced by towing the LARD fully submerged in a sufficient depth below the water surface. Minimising or even eliminating the influence of wave-induced motions thereby leads to an improved docking reliability. As illustrated in Figure 5-1, the LARD is connected to the host platform via a towing cable. While the submerged configuration significantly reduces surface wave interactions, the dynamic excitations of the host platform are still transmitted through the towing cable to the LARD. To mitigate this transmission of motion, a sufficiently long and flexible towing cable, potentially combined with passive damping elements or wave-compensating winches, can decouple the motion of the towing host platform from the LARD to a large extent.

Figure 5-2 illustrates the process of AUV docking into the LARD and being captured. The LARD structure is realised in the form of a large, funnel-shaped body with a wide capture opening to simplify the AUV's approach. Integrated guiding mechanisms ensure that the AUV is centred during its entry into the LARD. To address spatial constraints on board the host platform, the funnel mechanism is designed to be collapsible. In its closed configuration, the structure wraps around the AUV and provides mechanical protection during lifting and on-board storage. The mechanism also enables the AUV to be fixed within the LARD using frictional clamping. By adjusting or interchanging the bearing elements, the system can further accommodate AUVs with different lengths and diameters, thus fulfilling the requirement of a

modular and universal docking interface. As the entire L&R process is intended to be executed without human intervention to improve operational safety and efficiency, the concept also aligns with the requirement of automation. It should also be noted that the described LARD is part of the intellectual property covered by Patent DE102023126292A1 [176] and WO002025067969A1 [177] by Hops et al.

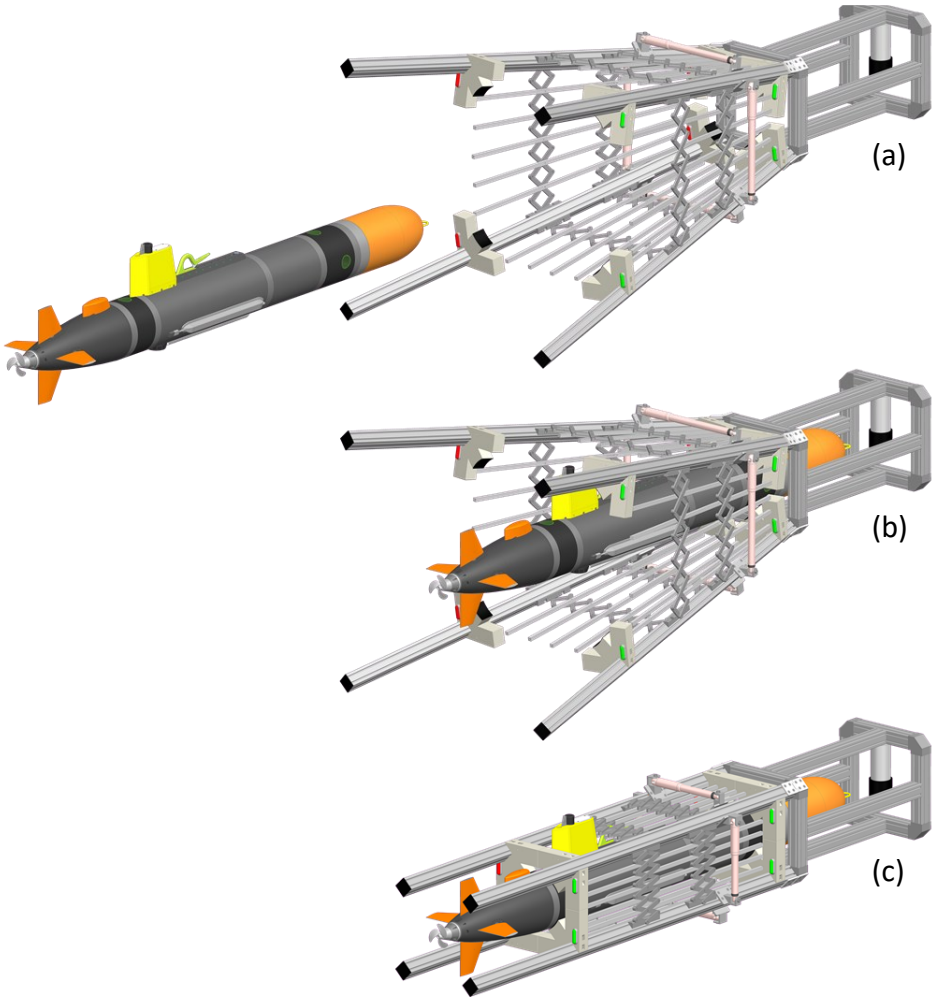


Figure 5-2: Schematic illustration of LARD
(a) The AUV aligns itself with the towed LARD and accelerates to enter the open funnel; (b) The struts begin to close when the AUV reaches the predefined end-position; (c) When the LARD is closed, the AUV is secured by friction, which ensures the subsequent lifting operation

This chapter outlines the functional sequence, offering a deeper comprehension of the intended operation of the LARD concept. Subsequently, practical instances from the German North Sea and Baltic Sea are employed to formulate preliminary principles to point out how the influence of the wave-induced motion diminishes with increasing depth. The concluding section of this chapter emphasises the mechanical design, including the selection of components and strength of materials predicated on the requirement that the AUV be secured only by frictional clamping. A brief outlook on functional extension for charging and data transfer for the AUV docked in the LARD follows.

5.1 Functional sequence

The functional sequences for the L&R process with the LARD are illustrated using simplified schemes in Figure 5-3 and Figure 5-4. This structure emphasises the relationships among three fundamental functional components for both the AUV and the LARD: position, sensors and the motion control system. The position element ensures the precise alignment and coordination of both entities. The sensor systems are crucial for motion detection and spatial awareness. The motion control systems ensure that various mechanical and operational transitions are executed. By segmenting the sequence into discrete phases, the operational flow is delineated in chronological order, emphasising the ideal protocols for the effective and safe L&R of the AUV. It should be noted that this is a significant simplification of a complex process and therefore not all components and dependencies are taken into account.

5.1.1 Launch procedure

The launch procedure in Figure 5-3 begins with the lifting operation, during which the AUV is securely fastened within the LARD to prevent unintended motions. The LARD, along with the secured AUV, is then lowered into the water using either a crane or ramp mechanism. The sensor system of the LARD ensures the AUV is positioned inside the device and that the locking mechanism is securely fastened. Concurrently, the motion control system of the LARD remains in a locked state, safeguarding the equipment during its transition to the water.
Next, the submersion process takes place. After entering the water, the LARD and the enclosed AUV will begin to descend to a predetermined depth by extending the length of the towing cable. The LARD’s sensors carefully track this submersion. For instance, an IMU and a USBL system that continuously determine the LARD's relative position to the host platform and detect its own motions until the LARD is hoisted back onto the platform. While this phase is in progress, the motion control system will make certain that the device stays closed.
Upon reaching the designated depth and achieving stabilisation, the LARD opening process commences. The LARD sensors remain in monitoring its relative position to the host platform. The AUV's on board sensors determine its position in relation to the LARD, thereby enabling coordination between the two systems. The motion control system of the LARD subsequently activates the unlocking and opening of the funnel-shaped cone. This process open state permits the AUV to exit.
In the AUV release phase the AUV exit the LARD, transitioning from a partially enclosed position to a fully outside one. In this phase, the LARD is towed at a specified depth. The sensors of the AUV monitor its relative position to the LARD, thereby ensuring a precise and controlled release process. The AUV's motion control system is responsible for regulating the release and obtaining the required steering commands from its sensors to ensure a smooth exit. The relative motions between the AUV and the LARD along the y and z axes are of minimal significance as the AUV retreats from the forward towed LARD. After the AUV has fully exited the LARD, it operates autonomously and commences its assigned mission. The AUV's role in the L&R sequence concludes here, shifting the focus entirely to the LARD.
Upon deployment of the AUV, the closure of the LARD is initiated. The LARD continues to maintain its specified depth. The motion control system subsequently facilitates the closure of the funnel-shaped opening, thereby ensuring the device is secured and ready for recovery. The subsequent phase entails the lifting operation of the LARD. The device is extracted from the water utilising a crane or ramp, thereby reversing the initial deployment procedure. At this stage, the motion control system guarantees that the LARD is securely closed and locked, thereby preventing any accidental reopening or damage throughout the lifting procedure. The process ultimately concludes with the storage of LARD on the deck of the host platform, where it is secured for maintenance, reconfiguration or future use.

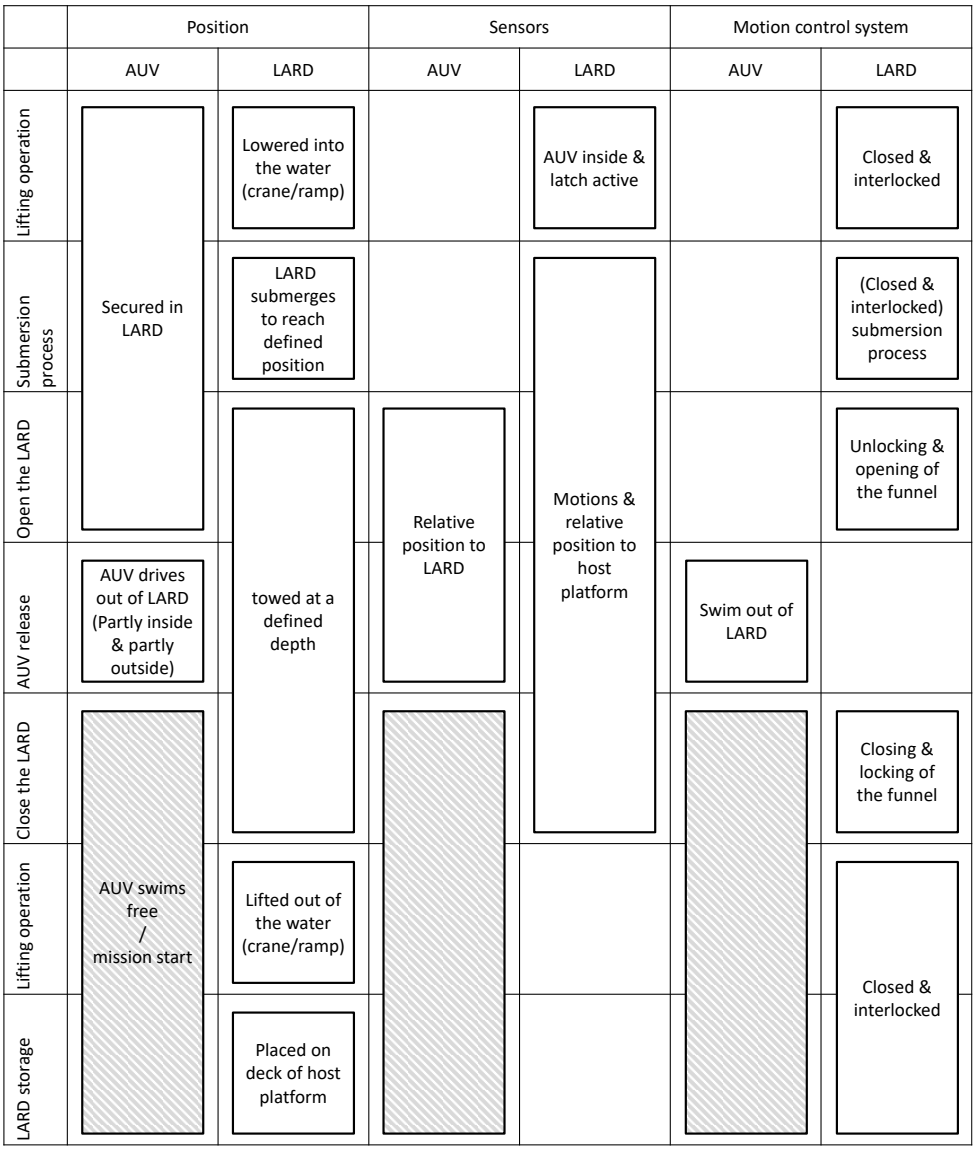


Figure 5-3: AUV launch procedure

5.1.2 Recovery procedure

Figure 5-4 illustrates the recovery procedure, which consists of a sequence of systematic stages that guarantee the safe retrieval of the AUV using the LARD. The procedure encompasses lifting operations, submersion processes, opening the LARD, course alignment, AUV catching up and docking into the LARD, closing the LARD, lifting operations and LARD storage with the AUV securely contained within.

A crane or ramp lowers the LARD into the water to start the process. At this point, the motion control mechanism of the LARD is responsible for ensuring that the device is locked. The submersion process begins once the LARD is set in the water. The device descends to a predetermined depth, attaining the designated position in relation to the host platform controlled by the cable length. The on-board sensor system of the LARD continuously monitors its motions and assesses its relative position to the platform.

Opening the LARD is the subsequent stage after a successful submersion. The device is towed at a specified depth with a forward velocity of approx. 2 knots. The motion control system subsequently unlocks and opens the structural elements of the LARD building a funnel, in preparation for the entry of the AUV. This stage necessitates that the LARD's sensor systems identify the steady towing activity. Stability is evaluated through the assessment of multiple parameters, including the absolute position and motion of the LARD across all six DoF.

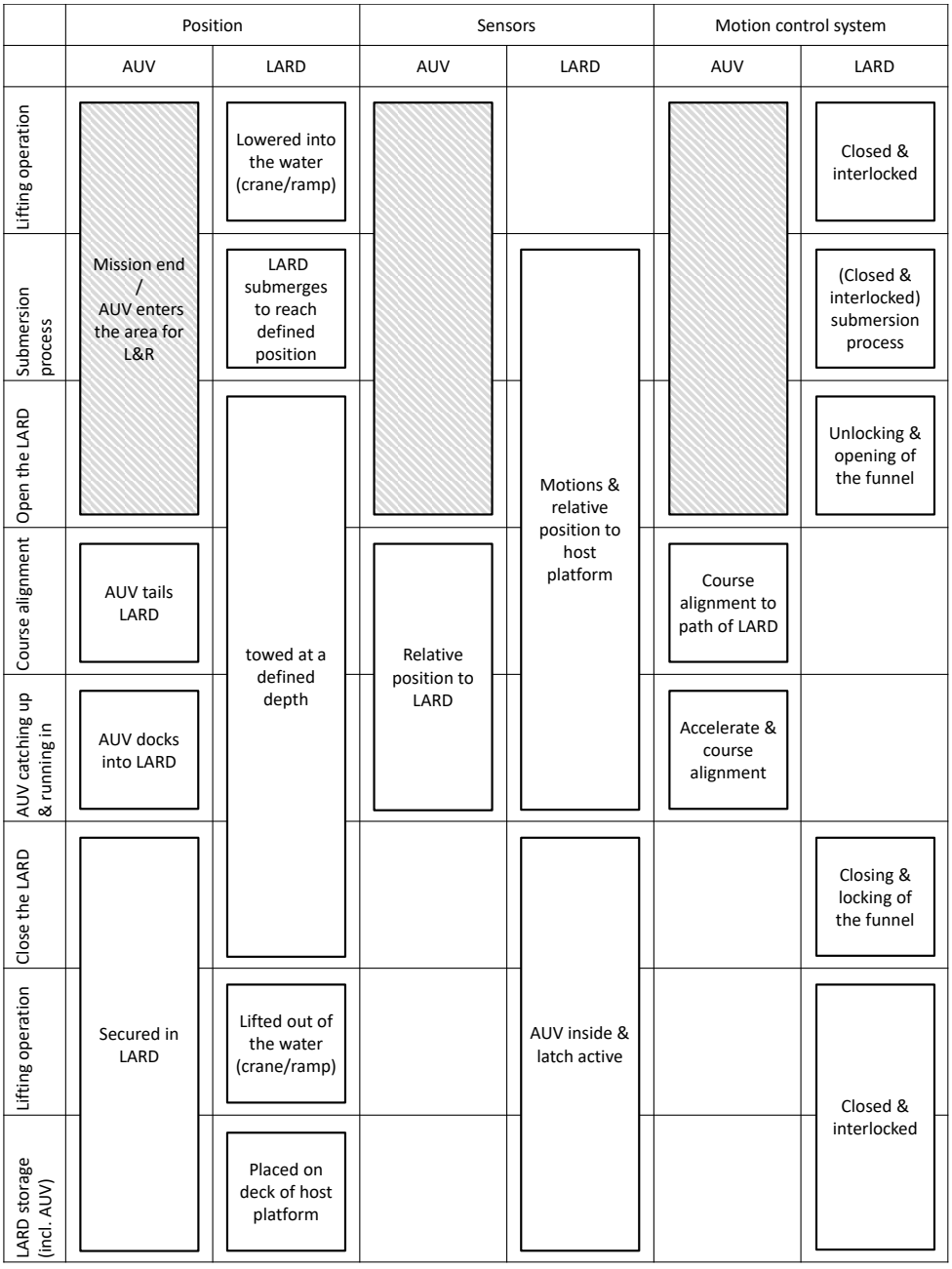


Figure 5-4: AUV recovery procedure

Upon meeting the pre-set criteria, the course alignment phase commences. In this phase, the AUV begins tracking the LARD, which remains submerged towed at the set depth. The sensors of the AUV track its relative position to the LARD. The AUV's motion control system subsequently modifies its trajectory to correspond with the LARD's path. The alignment process indicates that the AUV follows the appropriate trajectory and is optimally positioned for entry into the LARD. This operation can be interpreted as an interaction between (i) a navigation layer providing a relative pose estimate to the docking device, (ii) a guidance layer generating an approach trajectory towards the docking-area centre and (iii) a low-level control layer tracking the commanded trajectory. In the present work, these layers are treated as a baseline capability of operational AUVs. The contribution of the towed docking device is to passively shape the relative-motion environment in which this baseline GNC operates, thereby increasing the likelihood that the geometric capture conditions at the entrance are met.

The subsequent step entails the AUV approaching and entering the LARD. During this period,

the AUV adheres to the LARS's trajectory and accelerates to a speed that surpasses that of the LARD. The AUV's sensors continuously detect its relative location to the LARD, ensuring precise navigation. Under the guidance of the LARD's structural funnel layout and its own motion control system, the AUV enters the LARD.
Upon reaching a specified position within the LARD, the recovery process advances to the closing phase. The LARD's motion control system secures the AUV by closing its structural elements within the LARD. The LARD's sensor system tracks the AUV's position within the LARD and verifies that the locking mechanisms are engaged.
The second lifting operation represents the penultimate phase of the recovery procedure, wherein the LARD, containing the AUV, is lifted from the water. During this operation, the LARD's sensors confirm that the AUV is securely locked inside. This guarantees the safe handling of the combined structure of the LARD and AUV during its transition from water to the deck of the host platform.
The concluding phase of the recovery process involves the storage of the LARD containing the AUV securely within it. The LARD is closed and locked, safeguarding the AUV until subsequent operations or maintenance activities commence.

5.2 Concept of optimal towing depth

The fundamental concept of the LARD assumes that the process is conducted in a submerged state, thereby minimising or entirely eliminating the influence of surface waves. Using the wave theory explained in Section 4.2.1, exemplary data from the German North and Baltic Seas will be used to illustrate how wave influence decreases with depth. For this initial estimation, it is assumed that distance between the LARD and the host platform is considered sufficiently large to disregard excitations transmitted from the platform. This preliminary calculation serves as a first approximation to determine the required diving depths and provides a basis for the subsequent design process.

The analysis is conducted through the calculation of the equations of motion for water particles under wave excitation, the gathering of sea state data for relevant areas of operation and the estimation of local wave excitation. The calculation examples chosen for this purpose were potential use cases in the German North and Baltic Seas. Measurement stations in these regions offer a wide range of environmental data, such as wave conditions. This analysis employed wave data obtained from the German Federal Maritime and Hydrographic Agency ([German:] BSH - Bundesamt für Schiffahrt und Hydrographie) that correspond to observations conducted in 2022. Table 5-1 provides an overview of the measurement stations, while Figure 5-5 illustrates their geographical locations.

Table 5-1: BSH measuring stations [178]

No.	Name	d [m]	Position (Latitude)	Position (Longitude)
1	FINO1	30	54° 00.860' N	06° 35.031' E
2	Nordergruende	10	53° 50.100' N	08° 10.083' E
3	Helgoland	20	54° 13.164' N	07° 49.109' E
4	Butendiek	19	55° 01.480' N	07° 47.216' E
5	Arkona	46	54° 53.116' N	13° 51.644' E

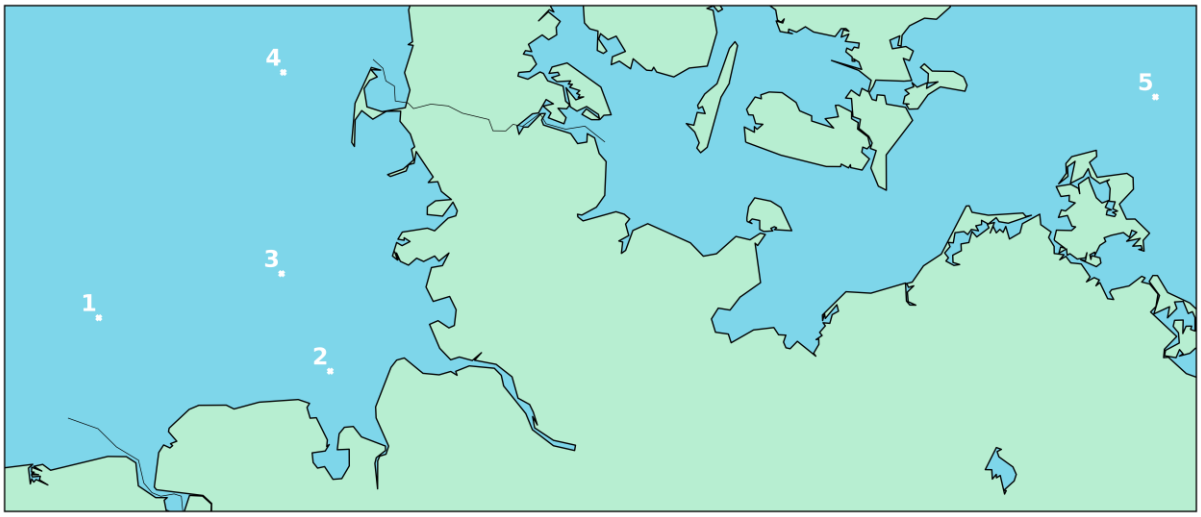


Figure 5-5: Map of BSH measuring stations (according to [178])

The wave records were analysed in monthly intervals. The primary parameters examined were the significant wave height and the corresponding wave period. A filtering process was implemented to categorise wave height and period based on sea state levels. Monthly mean values of significant wave heights (H_s) and periods (T) were subsequently calculated for each sea state to ascertain the representative wave characteristics associated with each condition.

Figure 5-6 illustrates the amplitude profiles for various months based on measurements from the FINO1 station at sea state 4. The amplitude of vertical particle velocity is graphed as a function of depth. The data encompasses the period from February to December in the year 2022. The amplitude of particle velocity as a function of depth is determined utilising the linear wave theory. Therefore, the terms $\cos(\theta)$ and $\sin(\theta)$ in equations for $u(x, z, t)$ and $w(x, z, t)$ were set

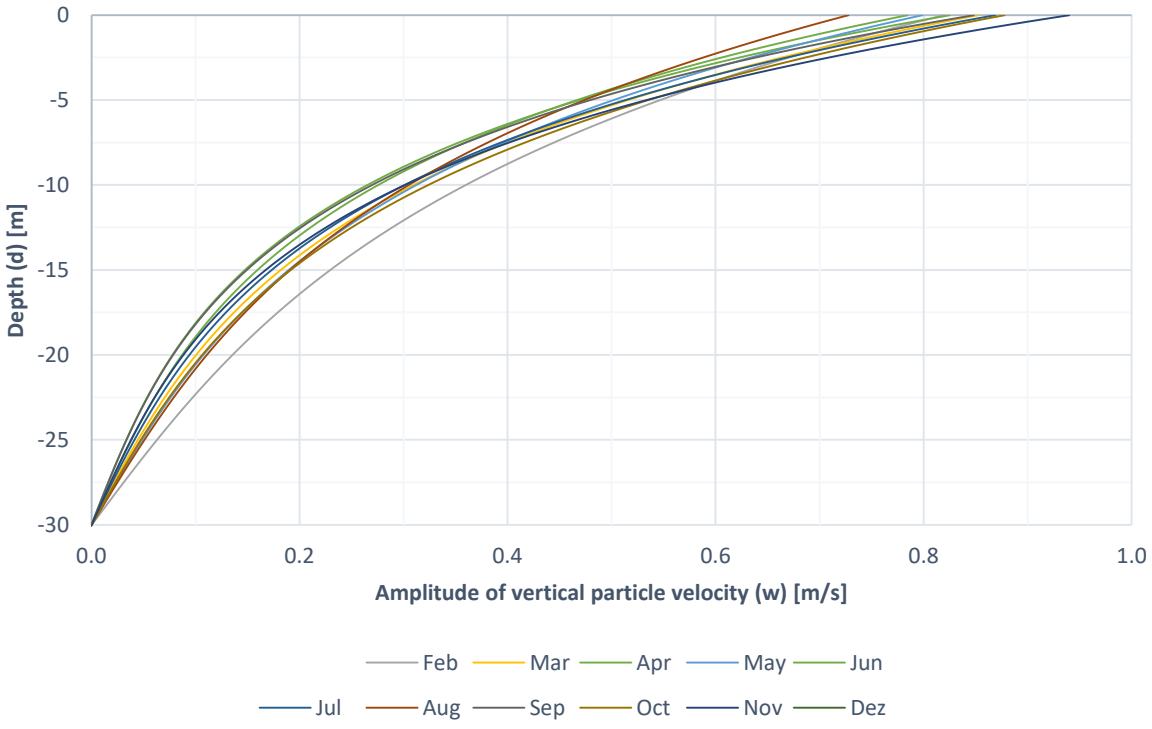


Figure 5-6: Amplitude of vertical particle velocity (w) as function of depth for BSH measuring station FINO1 at sea state 4

to their maximum, which is 1. This represents the maximum velocity at which particles experience wave-induced motion at the corresponding depths. For all calculations, the respective ratio of water depth to wavelength ($\frac{d}{\lambda}$) was used to determine whether the formulae for deep water, transition region or shallow water are applied.

Seasonal variations influence the impact of typical sea state waves on wave particles at different depths as seen in Figure 5-6. The month exhibiting the highest excitation at half the water depth was chosen for the corresponding measuring station. Figure 5-7 illustrates the amplitude of vertical particle velocity (w) as a function of depth for the BSH measuring stations: FINO1, Nordergruende, Helgoland, Butendiek and Arkona, under sea state 4. The month corresponding to each measuring station is indicated in brackets. The foundational data therefore is presented in Table 5-2, including significant wave heights, wave periods and wavelengths.

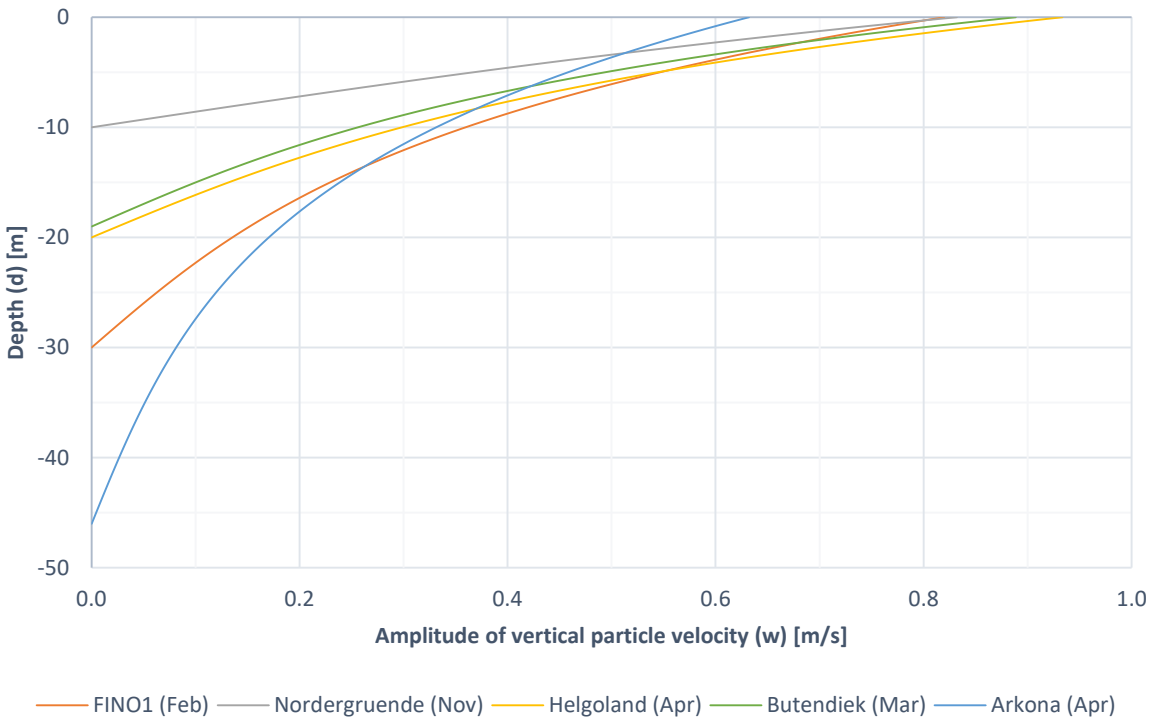


Figure 5-7: Amplitude of vertical particle velocity (w) as function of depth for several BSH measuring stations at sea state 4

Table 5-2: H_s, T_s and λ for several BSH measuring stations (sea state 4)

	FINO1	**Nordergruende**	**Helgoland**	**Butendiek**	**Arkona**
Month	Feb	Nov	Apr	Mar	Apr
H_s [m]	1.8792	1.8971	1.9012	1.7240	1.6018
T [s]	7.2026	7.1615	6.3969	6.0953	7.9595
λ [m]	79.60	61.63	61.75	56.35	98.37

Based on the values in Table 5-2, the amplitude of horizontal particle velocity (u) as a function of depth is depicted in Figure 5-8. At the seabed, where $z = -d$, the amplitude of horizontal particle velocity (u) does not diminish entirely, in contrast to the amplitude of vertical particle velocity (w), which is 0. This is a result of the hyperbolic cosine in the equation for u which is equivalent to (for $z = -d$):

$$\cosh[k(-d + d)] = \cosh[0] = 1 \tag{5.1}$$

Consequently, the amplitude of the horizontal particle velocity (u) at $z = -d$ is:

$$\frac{\zeta_a \omega}{\sinh(kd)} \tag{5.2}$$

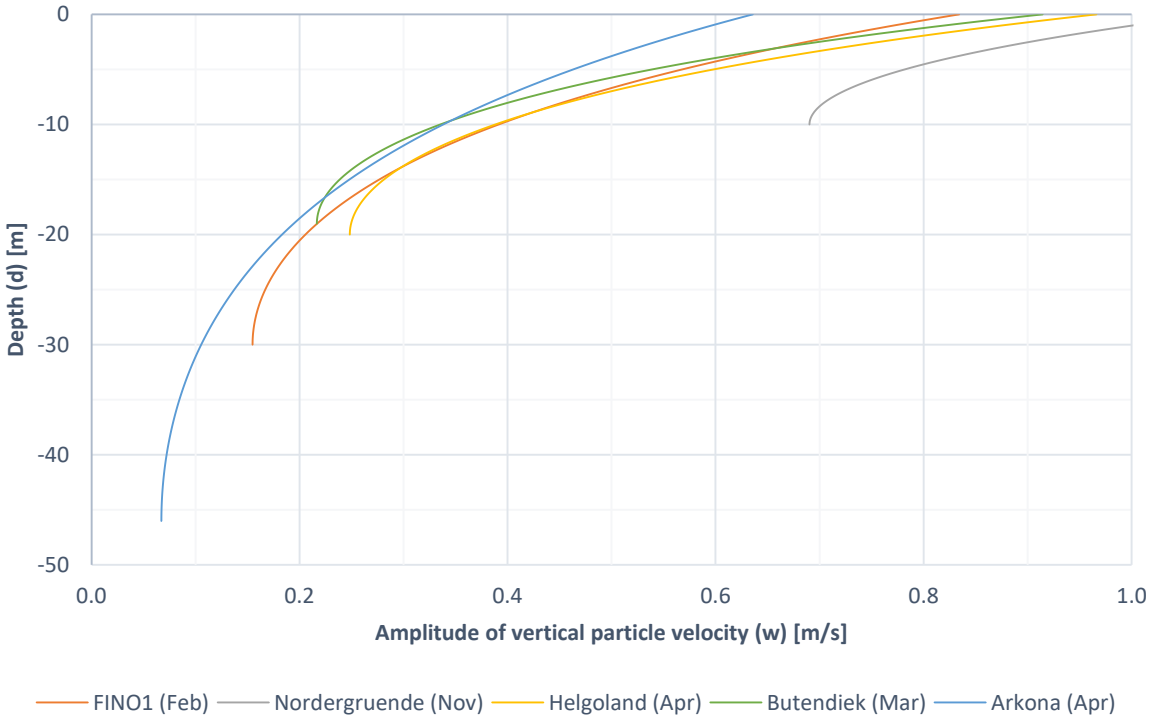


Figure 5-8: Amplitude of horizontal particle velocity (u) as function of depth for several BSH measuring stations at sea state 4

This study use equations derived from linear wave theory. The contribution of nonlinear wave theory variables was evaluated relative to linear terms to assess their precision. The impact of the nonlinear second order term was examined by utilising the available wave data. The sine and cosine functions denoting the phase of the travelling wave were adjusted to their peak value. The analysis of this ratio indicated that the nonlinear contribution is below 1 % in all cases, making it insignificant for this study. For instance, the mean values at the Helgoland measurement station under sea state 4 conditions, with $H_s = 1.9012$ m, $\lambda = 61.75$ m and $d = 20$ m, the nonlinear-to-linear ratio is at 0.14 %. The linear wave equations offer enough precision while minimising computer complexity, hence assuring dependability for the examined wave situations.

5.3 Mechanical Design

The primary function of the LARD is to capture and secure the AUV. his is achieved by using the same mechanism that opens and closes the funnel to clamp the vehicle once it has entered the capture region. The final design has an approximate mass of 175 kg. In the open configuration, the LARD is about 4m long and tapers from an approximate overall width and height of 1.5 m × 1.5 m at the widest end to about 0.6 m × 0.6 m at the narrow end, which is also the overall width and height in the closed configuration. The final solution presented in Figure 5-9 was developed using various established engineering methods, including morphological analysis and decision-making techniques such as utility analysis. Alternative designs and concepts that were not selected or explicitly excluded are not discussed here to maintain clarity and focus. These included for example variations of the head geometry, including a closed construction, as well as the potential integration of fins or rudders. In a passive implementation, such appendages could have generated additional lift or downforce. In an actively controlled implementation, they could have been used to influence the towing behaviour of the LARD. These options were ultimately not pursued due to the increased complexity of control and regulation, the additional sensor requirements, the associated susceptibility to faults and the resulting cost increase. Furthermore, different mechanisms for opening and closing the struts were also evaluated. The final configuration uses four externally mounted electromechanical cylinders, the operating principle of which is described in Section 5.3.1. Intermediate studies investigated whether the same motion could be realised with fewer actuators (e.g., a single actuator combined with mechanical transmission and force redistribution). This approach was discarded primarily due to concerns regarding robustness and fault sensitivity. Given the available installation space, the four-actuator arrangement provided a comparatively robust and straightforward implementation.

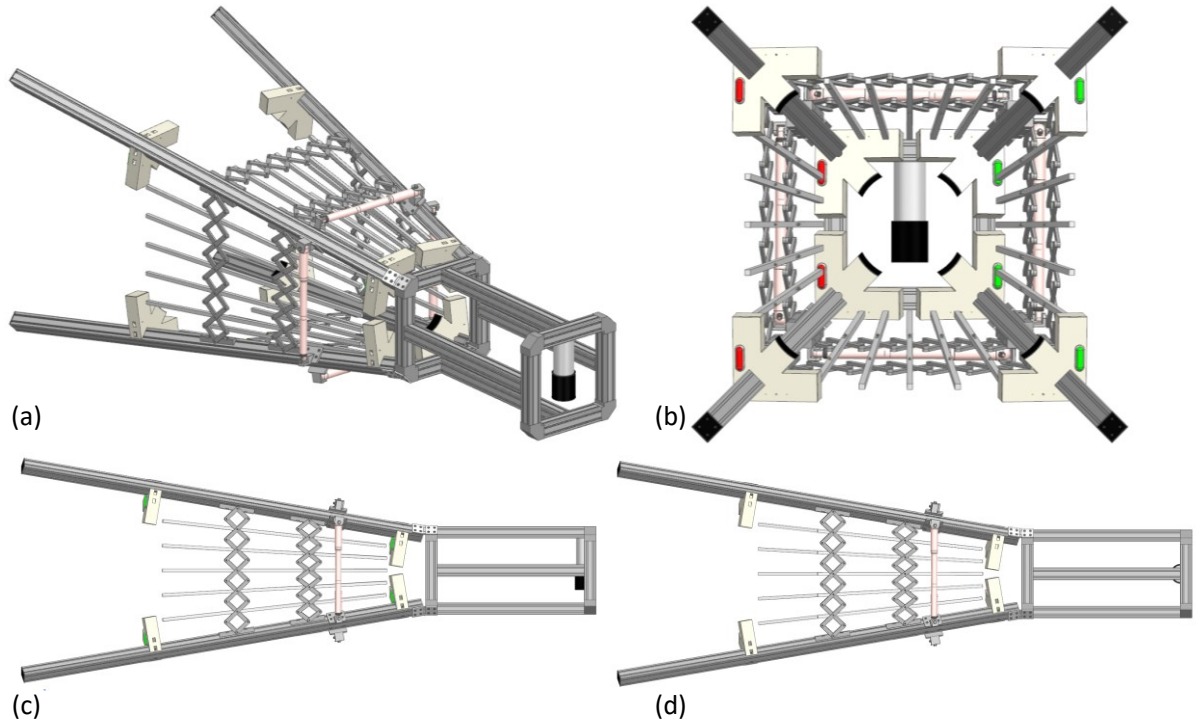


Figure 5-9: LARD - mechanical design
(a) isometric view (b) rear view (c) side view (d) top view

In order to clamp a part reliably, all of its DoF must be constrained. Grippers are mechanical devices used to grasp, hold and manipulate objects and represent the direct interface between a machine and its target component. There are various types of grippers, including mechanical, vacuum, magnetic and adhesion-based systems. This work focuses specifically on the functionality of mechanical grippers as these are used for capturing the AUV in the LARD. The effectiveness of a mechanical gripper is largely determined by its gripping force. It is important to distinguish between gripping force and holding force. The gripping force is the force required to establish contact and secure the object, while the holding force is the force necessary to maintain this grip once established. Typically, the holding force is lower than the initial gripping force.
The drive system of a gripper converts supplied energy into either rotary or linear motion, which is then transmitted via the kinematic system to produce the desired gripping motion. The kinematics determine critical parameters such as the gripping speed, gripping force and the progression of force application. Mechanical clamping gripper allow for various closing motions, including parallel motion, circular motion, arc displacement or a flexible enclosing motion. The chosen concept in this work adopts a circular movement as the primary closing action.
Grippers can be actuated pneumatically, hydraulically or electrically. In this study, an electrically driven clamping mechanism is employed to secure the AUV using clamping jaws. This configuration supports reliable, controllable gripping action, aligns with system integration requirements and provides a robust solution for underwater applications where precise control and minimal maintenance are essential. The selection of this approach reflects a careful evaluation of design alternatives and operational constraints based on functional, structural and performance considerations.

The design of the LARD is subject to a range of structural, dimensional and functional requirements. Structurally, all components must exhibit seawater resistance and sufficient mechanical strength to endure operational loads and environmental stresses. Dimensional constraints demand a compact design and low dead weight, allowing integration within the spatial and weight limits of the carrier platform. Functionally, the device must incorporate a reliable mechanism for opening and closing, be adaptable to different AUV types, guide the AUV into position, facilitate communication and localization (with the AUV and the carrier platform) and secure and protect the AUV during the L&R process as well as storage.
The developed concept meets these requirements by partially enclosing the AUV and forming a mechanical connection via a clamping mechanism. The core structure consists of a foldable, funnel-shaped opening formed by struts arranged around the front frame. A guiding mechanism (highlighted in red in Figure 5-10) is installed between the struts to support alignment. At the head of the assembly, struts connect the funnel to a frame, which in turn supports four articulated struts. Each of these is equipped with two clamping jaws (highlighted in green in Figure 5-10), forming two concentric clamping rings when closed. These rings define the contact surfaces required for secure fixation of the AUV through friction. By adjusting the position of these jaws along the struts the LARD can be configured for AUVs of different lengths. Exchanging the jaws enables L&R for AUVs with other geometries. The struts form a funnel for AUV ingress and close to create a compact structure. During hoisting and on-board handling, the enclosure provides mechanical protection for the AUV. An automated fixing process is facilitated by the integration of electromechanical actuators that control the clamping jaws. Four such actuators (highlighted in magenta in Figure 5-10) are arranged symmetrically to open and close the structure and are also part of the locking mechanism. If the force provided

by these actuators is sufficient, they can maintain the closed position and thereby eliminate the need for an additional locking mechanism. This ensures the secure retention of the AUV following insertion and closing, particularly during lifting operations.
For the guidance of the AUV into the LARD, a dedicated positioning aid (highlighted in red in Figure 5-10) is incorporated. This aid extends from the front to the rear clamping jaws and is installed between each pair of struts. To not collide with superstructures on the AUV, the upper positioning element is shortened accordingly. Inspired by folding structures such as music stands or spike strips, the positioning aid employs a series of foldable mechanisms. These are linked with rods, forming continuous guidance paths along the length of the funnel. The layout prevents the AUV from slipping between the rods or through the positioning elements, ensuring safe and reliable docking. Additionally, the foldable guidance system adds a protective layer during handling.
Navigation and positioning systems are essential to ensure spatial coordination and alignment between the LARD, the AUV and the carrier platform. One proposed solution is the use of a USBL system (highlighted in light blue in Figure 5-10). Due to uncertainties in particularly in near-field operation the USBL system is supplemented by optical systems such as cameras or light-based signals, which offer a viable alternative for short-range localization but are limited in underwater visibility conditions.

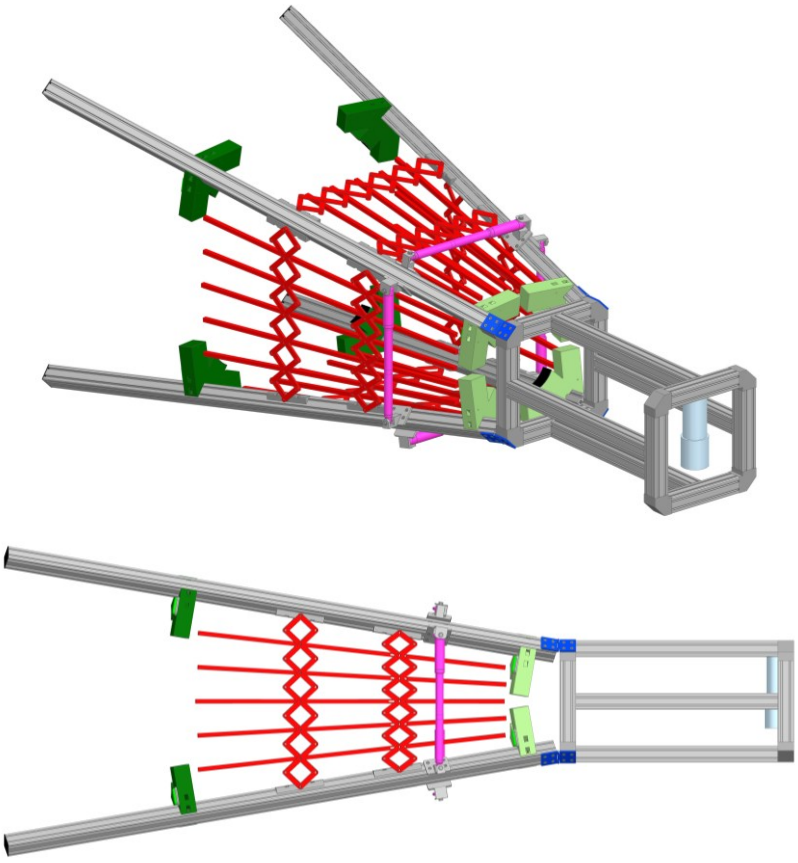


Figure 5-10: LARD – components
Green: clamping jaws (light green: front clamping ring / dark green: rear clamping ring);
Magenta: Actuators (opening and closing mechanism);
Red: Guiding mechanism (positioning aid);
Light blue: USBL System;
Dark blue: Hinges

5.3.1 Fastening the AUV

A fundamental step to ensure the secure fixation of the AUV via frictional contact is determining the necessary clamping force needed to prevent the AUV from slipping within the fixture during L&R. This force is applied by electromechanical actuators and must be sufficient to generate a reliable frictional connection between the contact surfaces of the LARD and the AUV. The design process therefore began with the evaluation of the force required to counteract gravitational forces acting on the AUV.
The clamping force was derived using a simplified model of an inclined plane with the angle ς shown in Figure 5-11. In this scenario, the downward component of the AUV's weight F_{para} acting along the slope must be fully balanced by the frictional force F_{fr} created at the contact interface. This frictional force results from the combination of the normal force F_N (perpendicular to the inclined surface) and the externally applied clamping force F_{cl}.

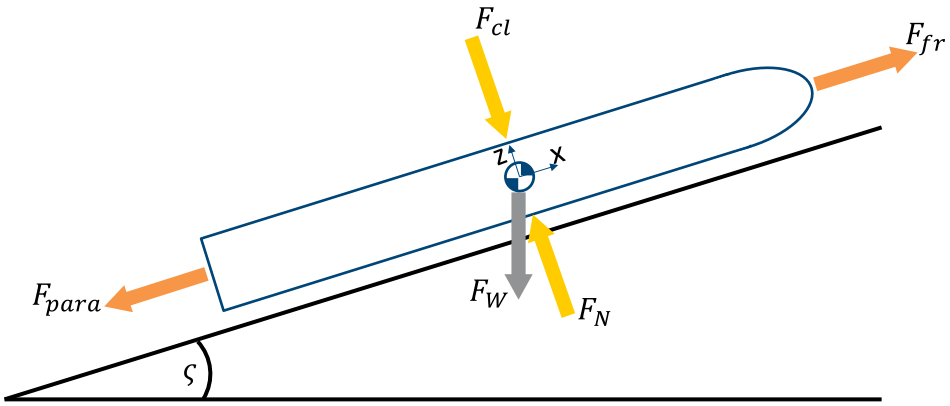


Figure 5-11: AUV on inclined plane

To secure the AUV in the LARD the frictional force must be at least the downward force:

$$F_{fr} = F_{para} \tag{5.3}$$

With F_{fr} being the product of the normal force F_N and the static friction coefficient μ_s:

$$F_{fr} = F_N \, \mu_s \tag{5.4}$$

The normal force F_N can be expressed as sum of the clamping force F_{cl} and the component of the weight force acting perpendicular to the plane, resulting in:

$$F_{fr} = (F_{cl} + F_w \cos(\varsigma)) \, \mu_s \tag{5.5}$$

The downhill force corresponds to the component of the weight force acting parallel to the plane, described by:

$$F_{para} = F_W \sin(\varsigma) \tag{5.6}$$

With equations (5.4) to (5.6) inserted into (5.3) the clamping force F_{cl} can be calculated using:

$$F_{cl} = \frac{F_W \sin(\varsigma) - \mu_s F_W \cos(\varsigma)}{\mu_s} \tag{5.7}$$

For a static friction coefficient μ_s of 0.32 () and a inclination of 90°, the required clamping force was calculated to 9.2 kN. The force depending on the slope angle is illustrated in Figure 5-12.

The friction coefficient was determined experimentally for the contact pair (AUV outer surface against a rubber coating applied to the bearing interface). To ensure a conservative estimate, the tests were conducted under lubricated conditions, representing a worst-case scenario with reduced friction, for instance to mimic contamination or biofouling (e.g. algae) at the interface.

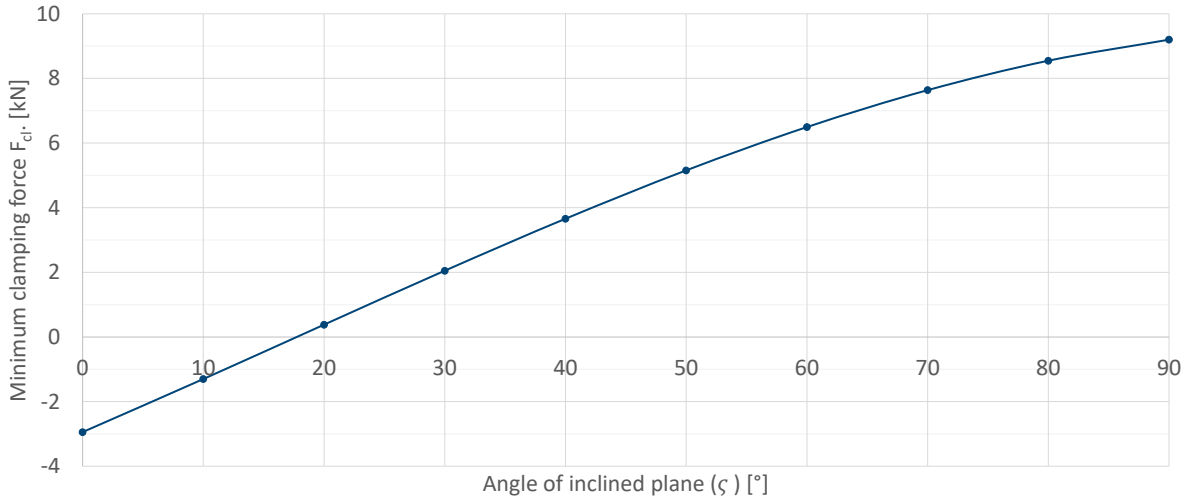


Figure 5-12: Minimum clamping force depending on the slope angle

However, the actual application of the clamping force in the LARD differs from this idealised setup. Rather than applying force in direct opposition to the gravitational component, the system transmits clamping forces via four struts arranged symmetrically around the AUV. These struts, each equipped with clamping jaws, are driven by electromechanical actuators and apply force radially toward the AUV as illustrated in Figure 5-13 and Figure 5-14.This introduces a complex set of mechanical relationships involving lever arms, joint positions and load transfer paths.

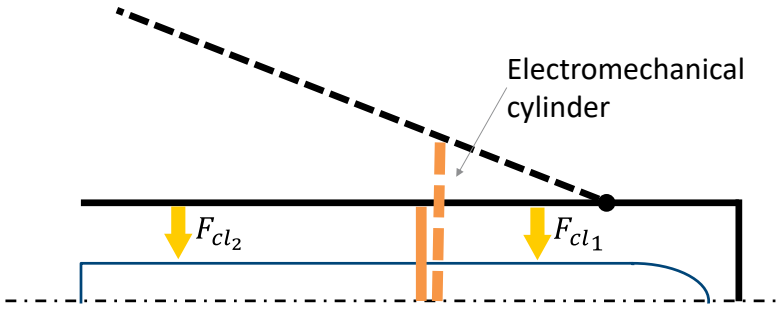


Figure 5-13: Simplified clamping force scheme of AUV in LARD (longitudinal section)

As seen in Figure 5-14, the 4 force components $F_{cl_{1_1}}$, $F_{cl_{1_2}}$, $F_{cl_{1_3}}$ and $F_{cl_{1_4}}$ of the first (front) clamping ring F_{cl_1} are arranged in a 45° angle relative to line of action of the gravitational force and relative to the line of action of the electromechanical cylinders. The same applies to the force components of the second (rear) clamping ring. This must be taken into account for the determination of how much force the electromechanical cylinders must exert in order to provide adequate pressure on the two clamping jaws, ensuring that the AUV is secured in the LARD only by friction. In this context, the dimensioning of the contact (bearing) surfaces governs the resulting contact pressure distribution and the likelihood of local overstressing or indentation of the AUV surface. Adequately sized and shaped contact surfaces promote a more uniform

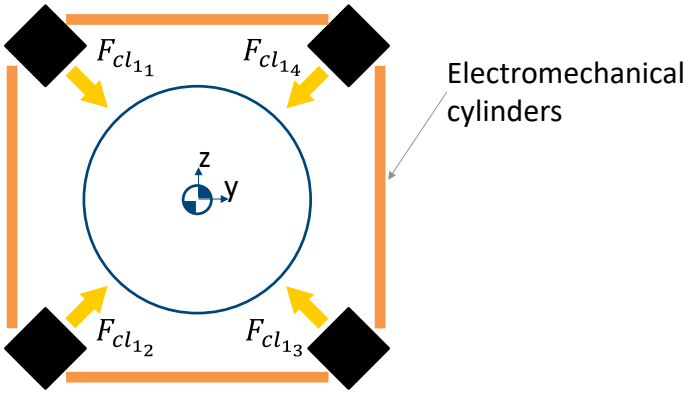


Figure 5-14: Simplified clamping force scheme of AUV in LARD (cross section)

pressure field, increase the robustness against misalignment and help maintain stable friction conditions by avoiding local pressure peaks.

It is important to acknowledge that while the spacing between the two clamping jaws is dictated by the AUV's geometry, the AUV's placement within the device is adjustable. So the position of the clamping rings and electromechanical cylinders relative to the joints for the struts are still to be determined. It is essential to ensure that no components intersect during the opening and closing motion. This is especially pertinent since the struts, positioned at a 45° angle, induce tilting or displacement along the x-axis. The positioning of the electromechanical cylinder and the clamping rings in relation to the joint results in varying lever arms.

The actuator stroke length and joint configuration were assessed to guarantee that the fixture could achieve a minimum aperture of 1 x 1 metre, facilitating the secure docking of the AUV. The actuators are responsible for producing clamping force and facilitating the folding mechanism necessary for the device's opening and closing. The multiple purposes necessitated the optimisation of actuator selection and location to reconcile stroke requirements with force capability. To ensure redundancy, the failure of a clamping ring, e.g. due to damage, is also taken into account. It is presumed that the complete clamping force must be exerted by a single clamping ring. In addition, a safety factor of 4 is selected for offshore lifting operations. This choice reflects a deliberately conservative design approach and follows recommendations provided by experienced practitioners involved in the specification and design of comparable systems.

This study involved many iterative computations of force and moment equilibria, which considered the distances among supports, actuator placements and joint positions. Subsequently, research was conducted on electromechanical actuators appropriate for underwater applications, focussing specifically on their force output and stroke length. Utilising these characteristics, the actuator position was established, from which the joint locations and support button positions were extrapolated. The outcome is a system characterised by numerous interdependencies, which was addressed iteratively through the testing of various electromechanical actuators and the identification of combinations that provided advantageous mechanical arrangements.

The calculations confirmed the mechanical viability of the design and the efficiency of force transmission via the structural elements. The specific computation procedures and collision analyses are not detailed in this context. The conclusive design is seen in Figure 5-9. The selected electromechanical cylinders deliver a stroke force of 4.5 kN with a stroke of 200 mm.

The foldable guiding mechanism used to assist in AUV positioning extends between the front and rear clamping jaws, must provide sufficient rigidity and stability while allowing for compact folding. The design was inspired by deployable structures such as collapsible barriers and was configured to avoid any risk of the AUV slipping through the mechanism.
All components were modelled using the CAD software Siemens NX. The software allowed detailed spatial analysis of the arrangement, motion paths and interference checks. It also supported the validation of actuator strokes and the integration of support structures and sensor positions. The complete design process, as outlined in [179],was influenced by repeated calculations, mechanical modelling and system-level analysis of interdependent components, guaranteeing that the final design fulfils the requirements specified in this study.

Additional clamping force

To enable the L&R of heavier AUVs than those primarily considered in this study, a mechanism was developed to generate additional clamping force [180]. In such cases, it is assumed that the AUV's weight exceeds the holding capacity of the electromechanical cylinders alone, making a clamping based on the opening and closing mechanism insufficient. It is important to note that this mechanism represents a functional extension of the system and is not considered further in the analysis of the following sections. It is presented solely as a potential enhancement for applications which require additional clamping force involving for example heavier vehicles or lower friction values. For the conceptual and mechanical design discussed in this work, the clamping force provided entirely by the electromechanical actuators is sufficient to secure the AUV. However, to address the possibility that this force may be inadequate in other applications due to increased weight or reduced friction from biofouling or debris, several alternative concepts for generating supplemental clamping force were explored. These concepts were developed to a pre-design stage and evaluated using consistent criteria, including achievable force amplification, passive safety in the event of power loss, controllability, integration complexity, susceptibility to corrosion and maintenance demands, space and weight constraints and overall life-cycle costs. A morphological box approach was used to systematically derive a broad range of potential solutions, which were then assessed using a simplified utility analysis.

The spindle-driven clamping concept illustrated in Figure 5-15 and Figure 5-16 emerged as the most suitable solution during the concept development phase. When the funnel structure closes, a spindle on one clamping jaw engages with a nut embedded in the opposite jaw, forming a mechanically robust threaded connection. To accommodate potential positional or angular misalignments the spindle and nut incorporate conical features that assist in alignment during engagement. The clamping force is applied via a rotary motor and the use of a trapezoidal thread (S16x2) ensures reliable self-locking with a pitch angle of 2.51°, maintaining force retention even in case of power or actuator failure. The design is characterised by a minimal number of components, high functional reliability due to the reduced number of moving parts, straightforward assembly and strong resistance to unintentional release. Standardised components such as the spindle, nut and bearings are predominantly off-the-shelf, which simplifies procurement and cost control. Only the conical guidance features require custom fabrication. Despite the overall positive evaluation, noted drawbacks are the complex integration of the mechanism into the clamping jaws and the limited access to the embedded actuator units inside the jaws during operation.

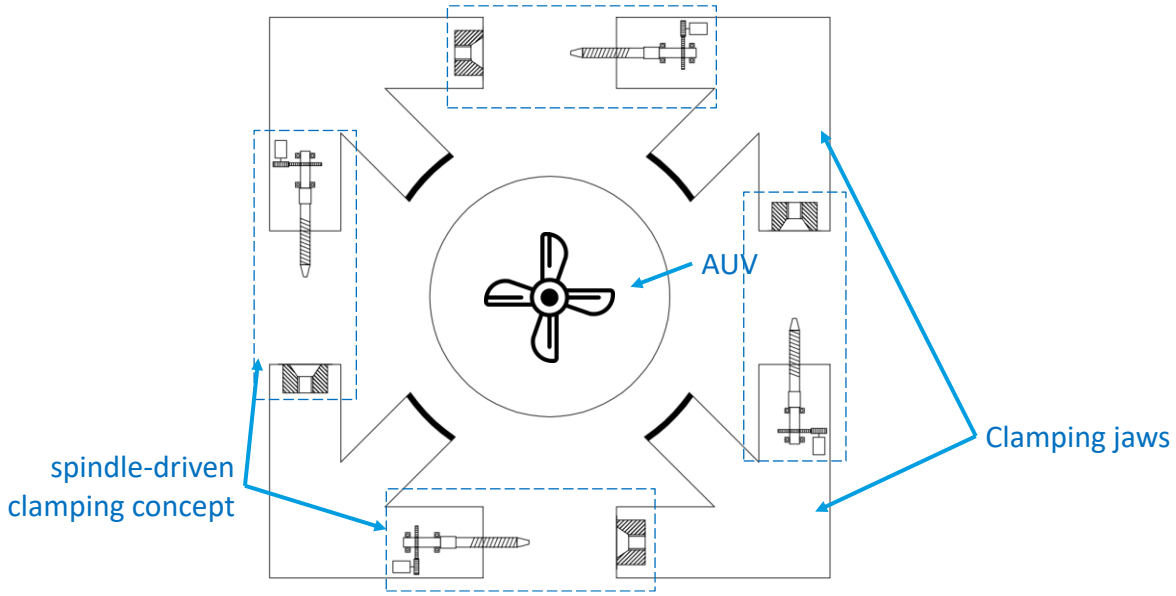


Figure 5-15: Spindle-driven clamping concept

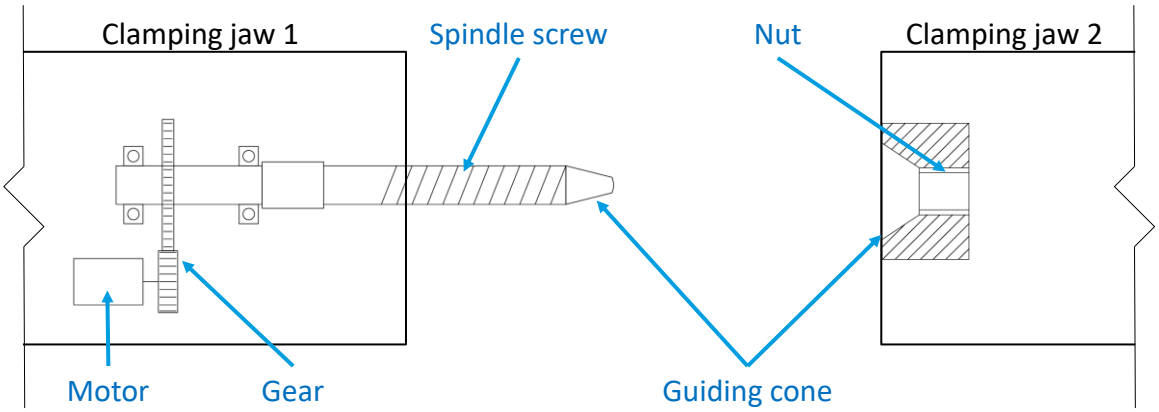


Figure 5-16: Spindle-driven clamping concept (detail view)

An alternative concept (illustrated in Figure 5-17) focuses on additional electromechanical cylinders, which extend to engage a spring-loaded locking pin housed in the opposing clamping jaw. Once the pin snaps into a designated eyelet on the piston rod, the cylinder retracts, generating the clamping force. Another concept (see Figure 5-18) utilised a rack-and-pinion system with an integrated detent rail. One clamping jaw houses a toothed rack, while the opposing jaw features a guiding cone and a pinion gear. Upon contact, the gear engages the rack and, via rotary motion, generates a tensile force. A spring-loaded side pressure pin locks the rack in place by snapping into corresponding recesses in the detent rail.

As previously mentioned, the spindle drive system can be extended for cases where the force provided by the electromechanical cylinders is insufficient. In such scenarios, the final design recommendation includes a spindle-driven clamping concept as an auxiliary or redundant mechanism. This ensures secure fixation of the AUV even under degraded conditions or in the event of actuator failure.

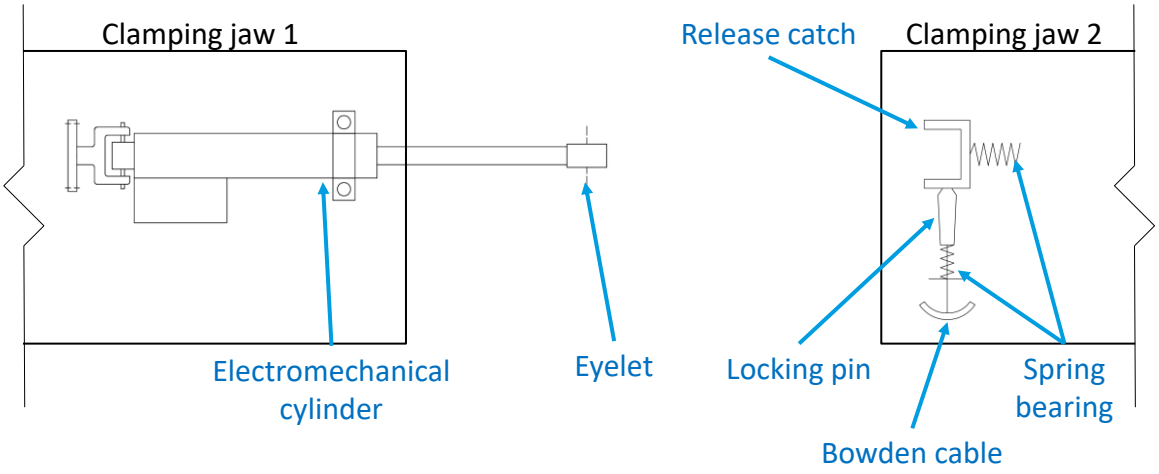


Figure 5-17: Additional electromechanical cylinders clamping concept (detail view)

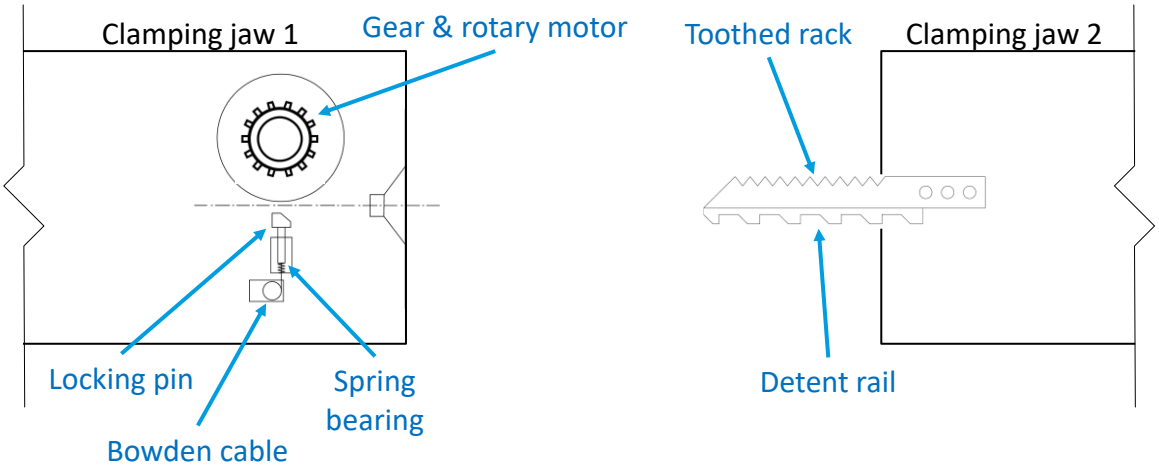


Figure 5-18: Rack-and-pinion clamping concept (detail view)

5.3.2 Strength of materials

To ensure the structural integrity of the LARD, a static strength analysis was conducted to verify that the fixture can withstand the internal stresses resulting from externally applied loads with an adequate safety margin against failure. This verification is crucial to confirm that no component of the structure will yield or fracture under operational conditions. The permissible stress levels for each component depend on the material selection, the type and nature of loading and the geometry of the parts involved. In this work, the static strength verification was carried out following the procedure outlined in the guideline published by the Research Council for Mechanical Engineering ([German:] Forschungskuratorium Maschinenbau e.V.) on the mathematical verification of the strength of mechanical components. [181]

The structural assessment includes the determination of all acting loads, including those introduced through positioning forces and clamping actions. These were used to derive the resultant transverse loads, as no significant axial forces were present in this configuration. This consideration also acknowledged that, in the case of a clamping ring failure, the full clamping force must be borne by the remaining clamping ring.

By calculating the bending moment distribution across the supporting struts, the maximum

bending moment $M_{b,max} = 1457.0935$ Nm was identified. This value served as the basis for calculating the maximum actual bending stress $\sigma_{b,max}$, which was obtained by dividing the maximum bending moment by the section modulus W_b of the profile used.

$$\sigma_{b,max} = \frac{M_{b,max}}{W_b} \tag{5.8}$$

To meet the strength requirements, a Bosch®-Rexroth® structural profile with cross-sectional dimensions of 80 × 80 mm was selected. The section modulus of this profile is:

$$W_b = 33 * 10^{-6}\ \mathrm{m}^3 \tag{5.9}$$

The corresponding limiting bending stress $\sigma_{b,F}$ is:

$$\sigma_{b,F} = 195\ \frac{\mathrm{N}}{\mathrm{m}^2} \tag{5.10}$$

With these values, it was sufficient to achieve a safety factor against yielding S_F of 4.4.

$$S_F = \frac{\sigma_{b,F}}{\sigma_{b,max}} = \frac{\sigma_{b,F}}{\left(\frac{M_{b,max}}{W_b}\right)} = \frac{195\ \frac{\mathrm{N}}{\mathrm{m}^2}}{\left(\frac{1457.0935\ \mathrm{Nm}}{33 * 10^{-6}\ \mathrm{m}^3}\right)} = 4.4393 \tag{5.11}$$

The achieved safety factor significantly exceeds the standard minimum safety factor of 2, providing robust assurance that the structure can accommodate the applied mechanical loads without reaching the material's yield strength. This comparatively high margin is primarily a consequence of the selected construction profiles. These profiles are only available in discrete standard sizes, which limited a more fine-grained sizing of the cross-sections. Consequently, the design is not optimised for minimum mass or a safety factor close to the lower bound, but rather reflects the use of readily available modular components. A further reduction of the safety factor could be achieved through a dedicated optimisation (e.g., custom profiles or more differentiated section selection). However, this would reduce conservatism and may increase manufacturing effort and cost.

5.3.3 Functional extension for charging & data transfer

In the context of increasing demands for extended AUV missions, reliable energy replenishment and high-rate data offload remain central challenges. A wide array of wireless technologies has been explored to address these issues, including inductive power transfer systems, optical and acoustic communication links and hybrid solutions. Reviews by Liu et al. (2024) [14] and Teeneti et al. (2021) [182] have comprehensively discussed the potential of these wireless systems. They highlight the benefits of wireless charging such as tolerance to misalignment, reduced mechanical complexity and immunity to seawater-induced corrosion. For instance, inductive wireless power transfer offers fault-tolerant and contact-free energy transfer, with recent systems demonstrating sufficient efficiency for practical AUV deployment.

In wireless charging, inductive power transfer is the most established technique. It involves the use of a pair of magnetically coupled coils, one on the docking station and the other on the AUV. When alternating current flows through the primary coil, it generates a time-varying magnetic field, which induces a current in the secondary coil on the vehicle, thereby delivering power without physical contact. Recent systems have demonstrated sufficient efficiency for

practical underwater operation. [14, 182]
Simultaneously, optical and electromagnetic communication channels have shown promise for high-speed data transmission under certain conditions, albeit with susceptibility to environmental interference and limited range. For wireless data transmission, three primary methods are used: acoustic, optical and radio frequency. Acoustic communication (widely used due to its long range) is constrained by low bandwidth and high latency. Optical systems, usually based on blue-green lasers or high-power LEDs, offer high data rates but require line-of-sight and are highly sensitive to turbidity and alignment. Radio frequency-based systems operate effectively over short distances using low-frequency bands that can partially penetrate seawater. While these techniques continue to evolve and despite their growing integration into commercial and academic platforms, they still face inherent limitations in energy density, transmission distance and data security. [14, 182]

However, in this project, the fundamental requirement was to avoid any modifications to the AUV. This constraint precludes the integration of additional wireless modules or coils. This necessitated the exclusive use of an existing plug-type connector already present on the AUV. The requirement for a cable-based solution is further justified on technical grounds. For energy transfer, plug connections allow higher power throughput compared to inductive methods, which are constrained by coil size, coupling efficiency and thermal limits. Wired connections therefore enable significantly faster recharging, a nontrivial advantage when minimising turnaround times is crucial. Similarly, with regard to data transfer, wired communication remains vastly superior in terms of bandwidth and reliability. High-resolution sensor packages on modern AUVs (including multibeam sonars, optical cameras and real-time navigation systems) generate large data volumes that must be offloaded efficiently. While wireless links can support mission uploads or status monitoring, they typically fall short when tasked with full dataset retrieval.
Moreover, cable-based data transmission inherently mitigates concerns over data and operational security. Unlike wireless transmission, which disperses electromagnetic, optical or acoustic signals into the surrounding medium, wired systems confine the data path, ensuring a physically secure channel. For mission profiles involving classified, commercially sensitive or high-resolution scientific data, this feature is particularly important.
The following section therefore only discusses a plug-based solution. For further technical details of wireless approaches, reference is made to Liu et al. [14] and Teeneti et al. [182].

To ensure reliable underwater charging and data transmission for AUVs, two key developments were addressed: the selection of a suitable underwater connector system and the design of a dedicated mechanical solution for its automated connection and disconnection.
For the selection of an appropriate underwater connector, it is essential to differentiate among several types: dry-mate (connectable only in air), wet-mate (connectable in moist environments) and underwater-pluggable (connectable directly under water) [183]. In the present use case, the connector must be underwater-pluggable and remain fully functional while exposed directly to the surrounding seawater even in an unplugged state. All connector components must withstand the corresponding hydrostatic pressure, dynamic pressure changes, saline corrosion and ensure a secure mechanical and electrical interface.
Due to the requirement that the plug connection must be established and disconnected underwater, most types of underwater connectors, such as rubber moulded, plastic moulded and bulkhead connectors, can be excluded. A more advanced solution is the Pressure Balanced Oil Filled (PBOF) connector. These connectors equalize internal pressure with the ambient

underwater pressure using dielectric oil, enabling functionality at great depths with reduced mechanical stress during connection and disconnection. [184, 185]
PBOF connectors from manufacturers like SEACON and GISMA can operate at depths of up to 4000 metres and support several hundred mating cycles, making them suitable for demanding underwater operations. Some versions also support hybrid configurations, offering both copper contacts for power transmission and fibre optics for high-bandwidth data transfer. [186]

PBOF connectors were identified as the most appropriate solution for the present underwater plug operation. Based on this, a suitable underwater mechanism for automating the connection and disconnection process has been developed. A comprehensive requirements analysis was performed to define both functional and technical criteria for the system. Functional requirements include the ability to integrate the connector, centre the mating parts, move one connector half along a predefined path and securely lock the connection. Technically, the system must be fully submersible and corrosion-resistant. These specifications were translated into functional structures and design elements using morphological analysis. Key design challenges include ensuring precise alignment between connector halves to avoid damage and reduce insertion forces, especially important for multi-contact connectors. Another critical requirement is the secure fixation of the mated connection to resist environmental forces such as currents and mechanical vibrations.

The result is a functional extension of the LARD that is mounted on the upper struts, enabling a plug connection to the AUV to be established and disconnected. The functional extension is coloured red in Figure 5-19. For clarity, only the rear part of the LARD, on which the mechanism is mounted, is shown.

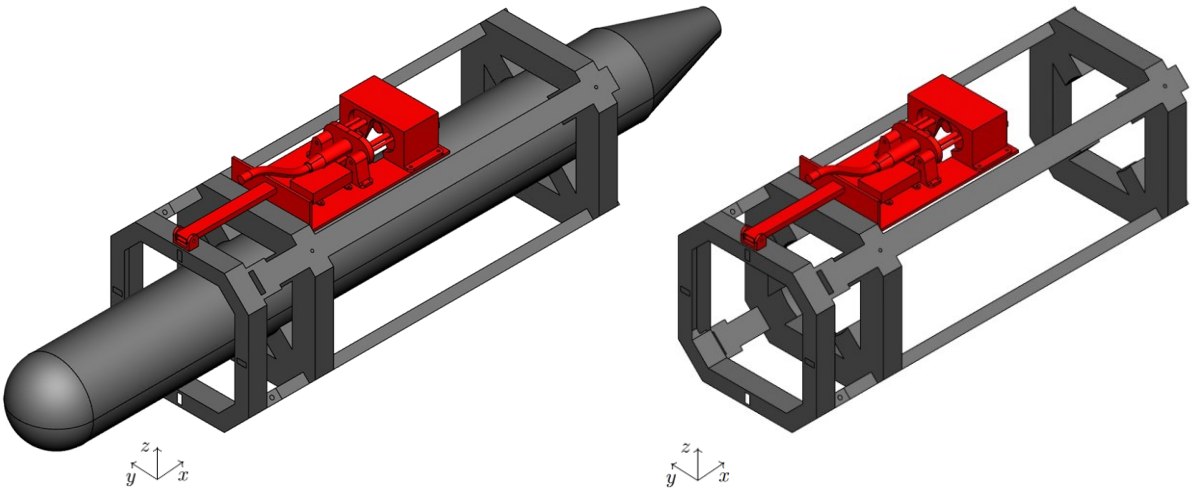


Figure 5-19: Functional extension for charging & data transfer mounted on the LARD

A detailed view on the device for the functional extension for charging & data transfer is presented in Figure 5-20. The used components and their configuration are explained prior to outlining the functioning principle through the schematics of the plug connection establishment. The device is mounted to the LARD via a hinge and a scissor mechanism, enabling it to synchronise with the opening and closing of the LARD without individual position control or driving unit. The PBOF plug is mounted on the plug guiding plate, which can be moved along a linear axis via a linear motor drive. The linear motor ensures a compact build while enabling powerful, self-locking and precisely controllable linear motion of the PBOF connector. To

maintain alignment, the guide plate moves along a linear guidance towards the centring cone. While closing the LARD, this cone is lower onto the corresponding socket mounted on the AUV. This funnel shaped centring mechanism corrects positional inaccuracies in several DoF (x, y and rotational about the x-axis) during the closing phase of the LARD. Thus, it facilitates the positioning of the AUV within the LARD and allows for axial misalignments, which are passively corrected as the docking structure closes.

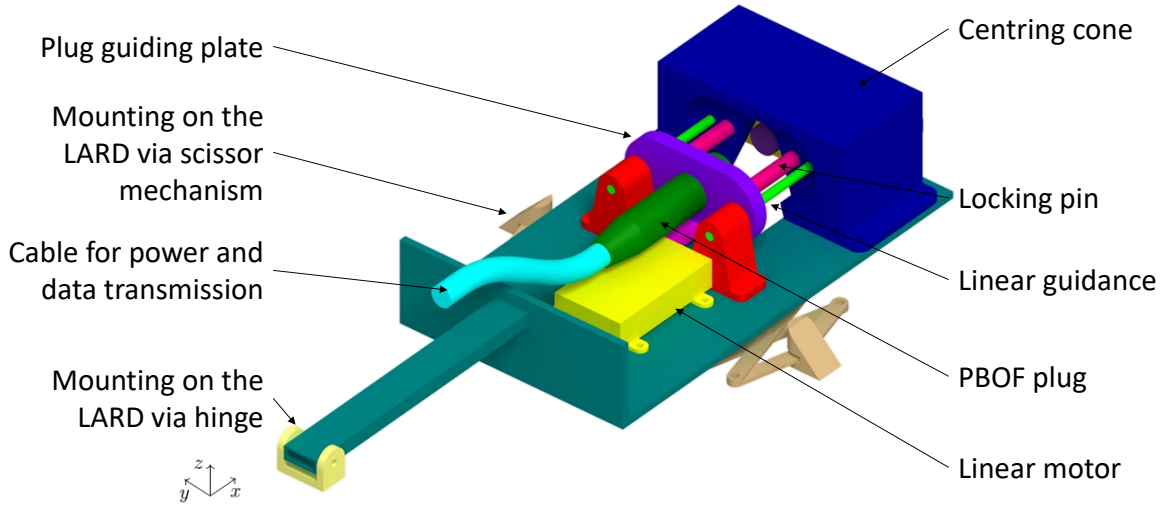


Figure 5-20: Functional extension for charging & data transfer (detailed view)

The functioning principle of the plug connection establishment is illustrated in Figure 5-21 and Figure 5-22. Once the AUV is aligned in the LARD and the docking arms are nearly closed (Figure 5-21-Position A), the centring funnel ensures that the plug connector aligns correctly

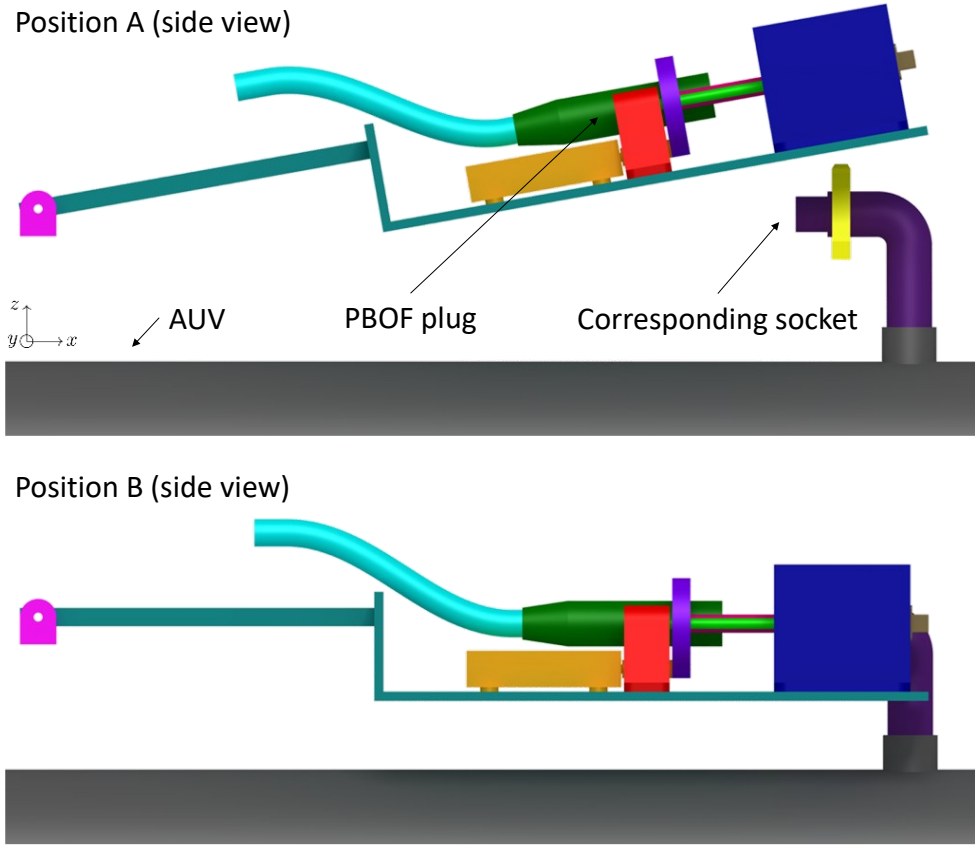


Figure 5-21: Scheme (I/II) of establishing the plug connection

with its counterpart (Figure 5-21-Position B). The guide plate of the counterpart is pressed into the centring funnel and is thus fixed in place (Figure 5-22-Position B). The electric spindle actuator then drives the connector forward along the x-axis until it reaches the socket on the AUV (Figure 5-22-Position C), completing the electrical and mechanical connection. To secure the connection against vibrations and hydrodynamic forces, mechanical locking bolts fix the locking pins in place. This arrangement ensures that the connector remains locked even under axial and torsional loads.

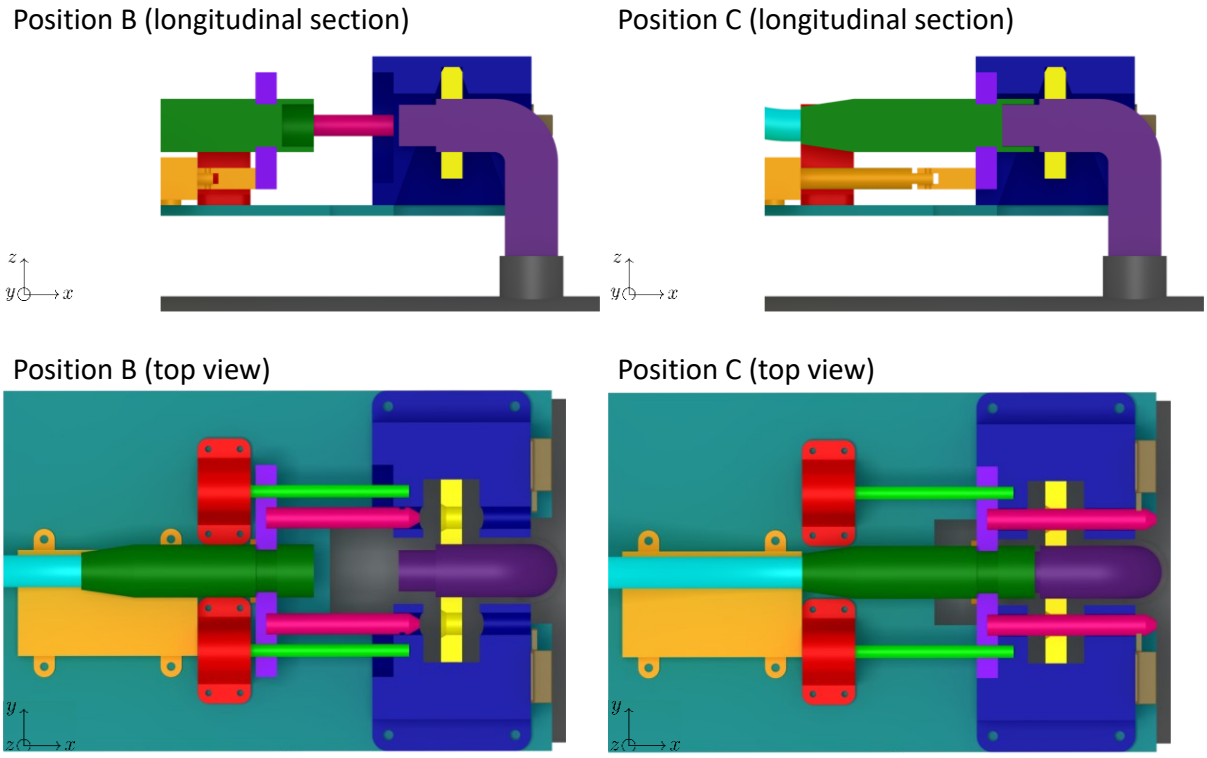


Figure 5-22: Scheme (II/II) of establishing the plug connection

After completion of data and energy transfer, the system executes the reverse sequence: the mechanical locking pins are retracted, the linear drive pulls the plug out of the socket and the entire LARD can then open. The design emphasizes robust mechanical principles to compensate the difficulty of intervention in underwater environments. The lead principle throughout the design process of the functional extension for charging & data transfer was to reduce the number of moving parts and ensure fault-tolerant operation. Ultimately, the proposed mechanism provides a solution, fully integrated into the LARD, for underwater plug-based connection and disconnection. It is essential that the towing cable is appropriate for data and energy transmission for this functional upgrade to be viable.

6. Hydrodynamic Properties of the Submerged Towed Docking Device

This chapter focuses on the hydrodynamic coefficients of the LARD, including drag, damping and hydrodynamic mass, as the basis for further analysis of the towing behaviour of the LARD, which is addressed in the following chapter.
The calculation of the drag, damping and hydrodynamic mass coefficients relies on the theoretical framework outlined in Section 4.4. According to equation (4.84) the translational drag coefficient can be expressed as:

$$C_{D_i}^t = \frac{2\,F_{D_i}}{\rho\, v_{b_i}\,|\,v_b|A_i} \tag{6.1}$$

and according to equation (4.85), for the rotational drag coefficient applies:

$$C_{D_i}^r = \frac{2\,M_{D_i}}{\rho\,\omega_{b_i}\,|\omega_b|\,AM_i} \tag{6.2}$$

The unit damping forces and moments can be determined based on equations (4.82) and (4.83).

$$UDF_i = \frac{F_{DA_i}}{v_{b_i}} \tag{6.3}$$

$$UDM_i = \frac{M_{DA_i}}{\omega_{b_i}} \tag{6.4}$$

The added mass coefficients for translational DoF ($C_{a_i}^t$) in equation (4.80) and for rotational DoF ($C_{a_i}^r$) in equation (4.81) can be calculated based on:

$$C_{a_i} = \frac{m_{a_i}}{\Delta_b} \tag{6.5}$$

This chapter includes the simulation setup which follows the approach for numerical derivation of drag, damping and hydrodynamic mass outlined section 4.3.4. Following the outcomes of these simulations are presented and discussed. To confirm the validity of the numerical results, experimental testing is carried out using scaled model tests in a towing tank. Selected examples are included to discuss the level of agreement between the simulated and experimental data.

6.1 Simulation Setup

This chapter outlines the numerical setup used to compute the LARD's hydrodynamic coefficients. All simulations were run in OpenFOAM 11 with a pressure-based, transient, incompressible formulation solved by the PIMPLE algorithm (merged PISO–SIMPLE algorithm). Two motion classes were treated:

- Linear: surge, sway and heave - modelled as rigid-body translation in a uniform inflow
- Rotational: roll, pitch and yaw - represented by a rigidly rotating inner mesh embedded in a stationary outer domain.

In this section geometry simplification, domain definition and mesh generation followed by boundary conditions like turbulence models, discretization and solver controls are described.

6.1.1 Geometry

The coordinate origin is placed at the LARD's centre of mass and the characteristic length is the overall device length $L_{LARD} \approx 4$ m. To avoid prohibitive cell counts from numerous small parts (e.g., screws, nuts, washers, pins, seals), a mesh-friendly yet hydrodynamically equivalent geometry was created. This idealisation reduces the effective surface roughness and removes small-scale cavity/gap flows; therefore, it can shift local boundary-layer transition and separation behaviour and should be regarded as a modelling assumption [187]. The aim was to preserve the outer flow contour and effective wetted area while removing or homogenising features with negligible influence on large-scale flow. Following a "shape over detail" principle, major external surfaces, edge locations and cross-sections were retained, whereas assembly-level details were omitted. Because surface forces are the primary quantities of interest, the total surface area was kept close to the original design. Concretely, small fasteners and hardware were removed; electromechanical cylinders and lines were idealised as smooth, constant-diameter cylinders and aluminium profiles were represented as solid members with the same outer dimensions, omitting internal cavities, grooves and through-holes. Sharp edges were filleted (typically with a radius of 2 mm) selecting the largest radius that did not perceptibly alter the external contour, to improve mesh quality and avoid numerical singularities. Besides improving mesh robustness, fillets can mitigate corner separation by smoothing the junction and reducing adverse transverse pressure gradients, thereby altering wake structures and force coefficients [188]. Finally, gaps were closed, overlapping surfaces removed and surface normal unified to obtain a model suitable for automated boundary-layer meshing. Sealing gaps suppresses open-cavity/gap flows that can generate recirculating vortices and self-sustained shear-layer oscillations, which would otherwise add local unsteadiness and pressure fluctuations [189].

6.1.2 Domain

The flow domain is a rectangular box, with translational and rotational cases treated separately. Each domain is sized in a way that the inflow develops without interference and the wake redevelops before the outlet. Also taking into account that further enlargement does not change the monitored quantities. This was validated for one representative linear and one representative rotational case and the resulting length ratios were applied to the remaining DoF. Because domain size directly affects the total mesh count (with a constant cell resolution), it is kept as small as possible and as large as necessary. The sensitivity of the overall cell count (and thus computational cost) to changes in mesh resolution is discussed in section 6.2. The coordinate origin is placed at the LARD's centre of mass.

For **linear motions**, six different domains were tested (Table 6-1) for surge inflow. The far-field boundaries were assessed by verifying a spatially uniform outlet profile and confirming negligible blockage effects at the lateral planes. Domain 6 (see Figure 6-1) provided undisturbed outlet and lateral planes. The final domain length ratios were cross-checked against the ITTC external-flow CFD recommendations ITTC7.5-03-02-03 [190]. However, it should be noted that these guidelines are primarily formulated for surface ships and were therefore used here as a pragmatic consistency check rather than a strict requirement for a fully submerged body. For sway and heave, the same length ratios were retained and only the LARD orientation was changed.

Table 6-1: Domain setups for linear flow

Domain ID	x-magnitude [as ratio of L_{LARD}]	z- magnitude [as ratio of L_{LARD}]	z- magnitude [as ratio of L_{LARD}]
1	-1.9 - 1.9	-1.3 - 1.3	-1.3 - 1.3
2	-3.8 - 2.5	-1.5 - 1.5	-1.5 - 1.5
3	-6.3 - 2.5	-1.3 - 1.3	-1.3 - 1.3
4	-7.5 - 2.5	-1.3 - 1.3	-1.3 - 1.3
5	-7.5 - 2.5	-1.9 - 1.9	-1.9 - 1.9
6	-7.5 - 2.5	-2.5 - 2.5	-2.5 - 2.5

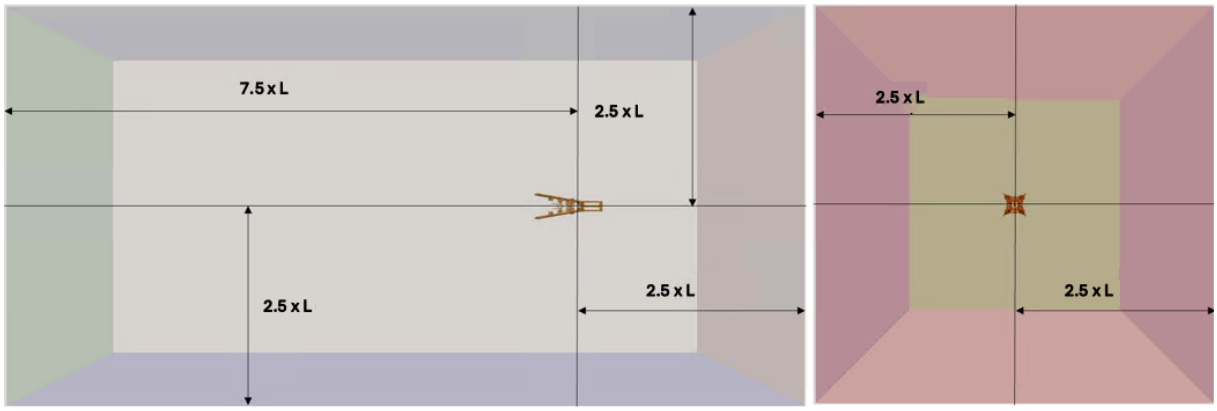


Figure 6-1: Linear domain No. 6 for surge flow – left: side view; right: rear view

For **rotational motions**, five domains were examined (Table 6-2) for yaw flow. The LARD remained stationary while an inner cylindrical mesh region enclosing the body was prescribed the rotational motion (dynamic-mesh and interface details in Section 4.3). Domain 3 (see Figure 6-2) yielded undisturbed boundary profiles and no further change in monitored quantities upon enlargement and was therefore adopted. The final domain length ratios were also cross-checked against the ITTC7.5-03-02-03 [190], analogous to the linear-motion domains. The same length ratios were reused for roll and pitch, changing only the rotation axis.

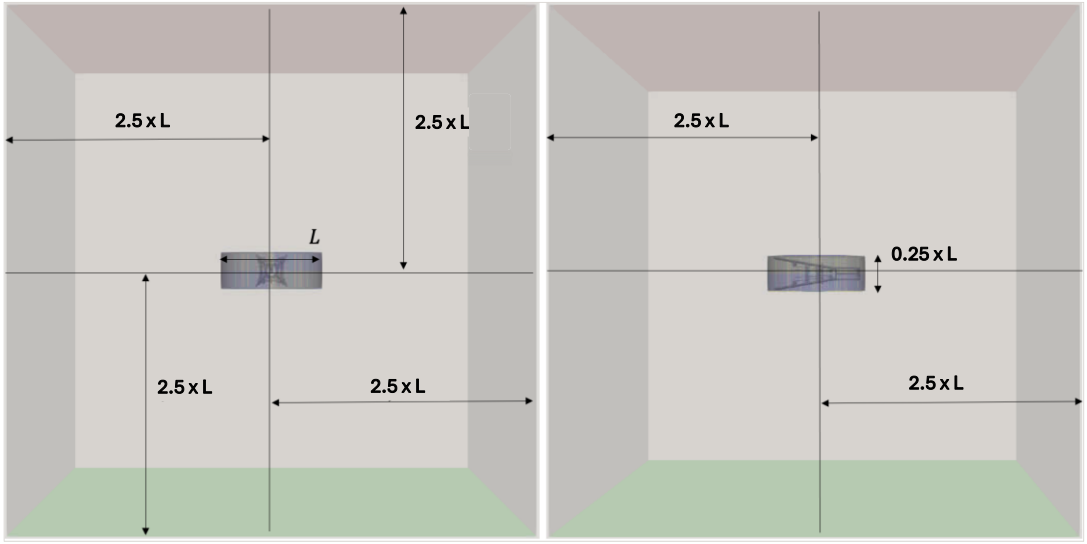


Figure 6-2: Rotational domain No. 3 for yaw flow – left: rear view; right: side view

Table 6-2: Domain setups for rotational flow

Domain ID	x-magnitude [as ratio of L_{LARD}]	z- magnitude [as ratio of L_{LARD}]	z- magnitude [as ratio of L_{LARD}]
1	-1.3 - 1.3	-1.3 - 1.3	-1.3 - 1.3
2	-1.9 - 1.9	-1.9 - 1.9	-1.9 - 1.9
3	-2.5 - 2.5	-2.5 - 2.5	-2.5 - 2.5
4	-2.5 - 2.5	-2.5 - 2.5	-3.8 - 1.3
5	-3.8 - 3.8	-3.8 - 3.8	-3.8 - 3.8

The different patches of the linear and rotational domains are illustrated in Figure 6-3.

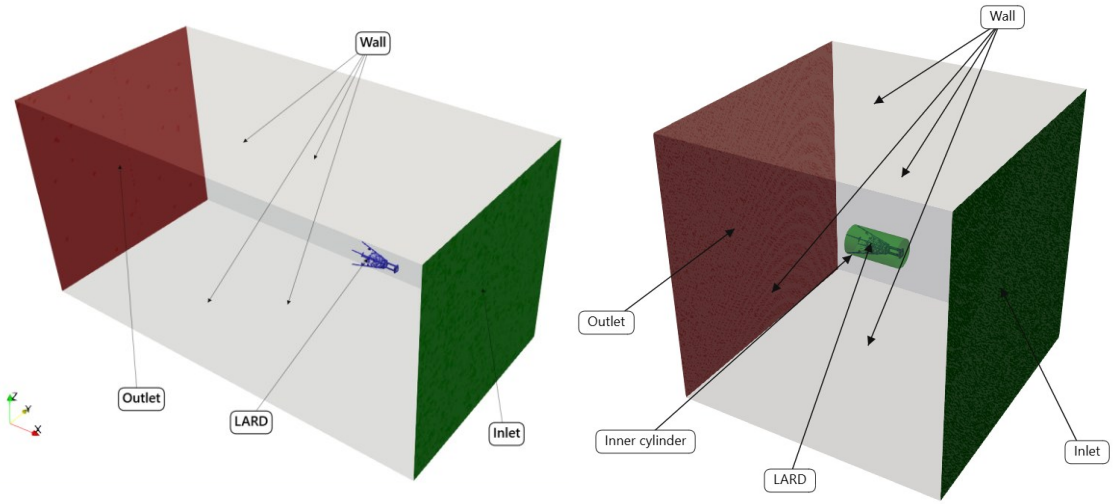


Figure 6-3: Patches of linear (left) and rotational (right) domain

6.1.3 Meshing

This section outlines the meshing procedure while the mesh-sensitivity analysis is reported separately in section 6.2. The meshes are built in two stages. First a structured background grid is generated for the full domain, then locally refined and conformed to the LARD surface. For **translational motions**, a uniform hexahedral background mesh (blockMesh) establishes a clean far field with predictable refinement ratios, low initial skewness and simple boundary patching. The LARD solid is then subtracted so that only the fluid region is meshed, avoiding staircase approximations and ensuring a body-conforming cavity. Local refinement bands are imposed around the body and along the expected wake, producing small cells near the geometry with smooth growth to the far field. The wall functions are described in section 6.1.4. A snapping step projects faces to the CAD surface while preserving detected feature lines, yielding a faithful, fitted boundary. Prismatic boundary-layer cells are inflated on all LARD patches to resolve near-wall gradients. The first-layer height follows a target wall-unit selection using kinematic viscosity, a reference inflow speed and a friction estimate based on the characteristic length of the LARD. Layer count and growth are chosen to bridge smoothly to the outer mesh without collapse in tight gaps. The final mesh for surge direction is illustrated in Figure 6-4.The same setup is reused for sway and heave by reorienting the body in the domain.

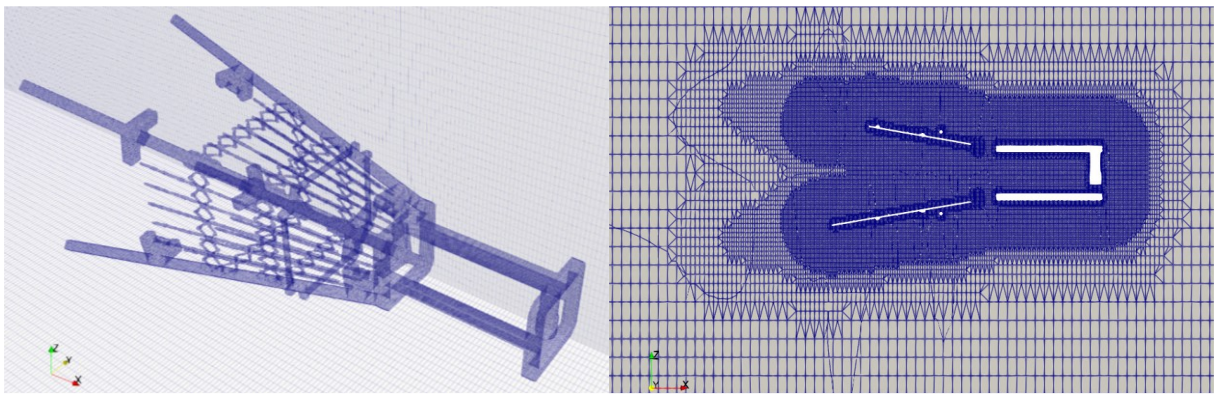


Figure 6-4: linear mesh - left: isometric view; right: longitudinal section at y=0

For **rotational cases**, an inner cylindrical sub-domain rotates rigidly relative to a stationary outer region via a sliding, non-conformal interface. As seen in Figure 6-5 for roll motion, the cubic background mesh contains a coaxial cylindrical sub-domain sized to include the LARD and its boundary layer with margin. The cylinder boundary is split into opposing patches and coupled as a sliding, non-conformal interface. The inner region rotates by the prescribed angle each time step while the outer region remains fixed. Conservative fluxes are exchanged across face overlaps that are recomputed as the cylinder turns, preserving mass and momentum. Stability and accuracy are promoted by matching cell sizes across the interface and by placing the cylinder sufficiently far from sharp features so the full boundary-layer stack lies within the rotating region. As in the linear setup, the solid is subtracted, symmetric refinement bands are applied across the interface to keep cell-size ratios near unity, the surface is snapped and boundary-layer inflation is added on the LARD.

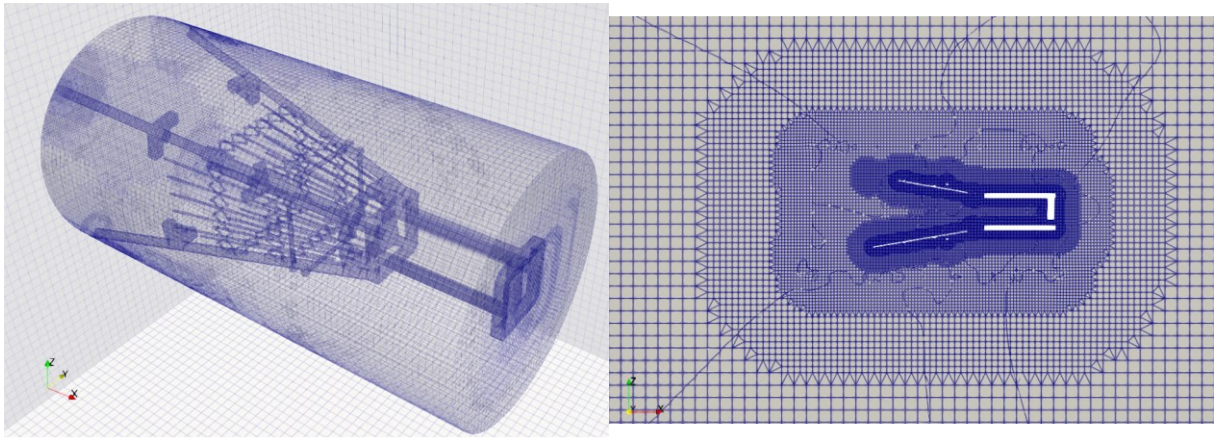


Figure 6-5: rotational mesh (roll) - left: isometric view; right: longitudinal section at y=0

6.1.4 Boundary conditions

This section specifies the boundary conditions and how the imposed motion (velocity for the linear domains and angular velocity for rotational domains) is used to generate a controlled acceleration for hydrodynamic coefficient identification. For **translational cases** the domain features patches Inlet, Outlet, Walls (lateral, top and bottom). The Inlet velocity uses a time-dependent *uniformFixedValue* (spatially uniform, tabulated in time). An acceleration of 0.1 m/s^2 was selected for the linear domain. This is applied to the DoF under consideration for 0.1 s. This results in the inlet velocity over time shown in Table 6-3 using the example of surge.

For sway the velocity is correspondingly defined in the y direction (v) and for heave in the z direction (w). Time steps of 0.01s were selected for the simulation.

Table 6-3: Inlet velocity over time for surge flow

Time [s]	**u** [m/s]	**v** [m/s]	**w** [m/s]
0.0	-1.00	0.00	0.00
5.0	-1.00	0.00	0.00
5.1	-1.01	0.00	0.00

The Outlet employs *inletOutlet*, acting as *zeroGradient* for outflow and switching to a user-specified inflow value under backflow. The reference pressure is *fixedValue p=0* at the Outlet and *zeroGradient* elsewhere. Walls act as a far field with *zeroGradient* for both velocity and pressure and the LARD surface is *noSlip*. Added mass runs use a short inlet-velocity ramp to realize a prescribed acceleration while leaving other boundaries unchanged. Turbulence is modelled with SST k– ω, blending k– ω near walls with k–ε in the free stream and a shear-stress limiter. On the LARD patch, near-wall turbulence is treated with *kqRWallFunction, omegaWallFunction* and *nutkWallFunction* with uniformly initialised reference values $k = 1.215 * 10^{-4}\,\frac{\mathrm{m}^2}{\mathrm{s}^2}$, $\omega = 14.37\,\frac{1}{\mathrm{s}}$ and $\nu = 1.56 * 10^{-6}\,\frac{\mathrm{m}^2}{\mathrm{s}}$. Inlet turbulence quantities are set from an intensity–length-scale specification. Some of the main boundary conditions for the linear domain are shown in Table 6-4.

Table 6-4: Boundary conditions for linear domain - velocity (U) and pressure (p)

Patch	**U**	**p**
Inlet	*uniformFixedValue*	*zeroGradient*
Outlet	*inletOutlet*	*fixedValue*
Wall	*zeroGradient*	*zeroGradient*
LARD	*noSlip*	*zeroGradient*

For **rotational cases**, a rigidly rotating inner cylinder encloses the body and its boundary layer inside a stationary outer box. On the LARD and rotating solid boundaries the velocity is *movingWallVelocity* and on the sliding, non-conformal interface it is *movingWallSlipVelocity*. Pressure uses *zeroGradient* on walls and interface and *fixedValue p=0* at the Outlet. The cylinder's angular speed $\omega(t)$ is prescribed via a short time table $\omega(t) = \omega_0\, scale(t)$ to produce a controlled angular acceleration $\alpha(t) = \frac{d\omega}{dt}$ (see Table 6-5).

Table 6-5: Rotational velocity over time

Time [s]	**scale** [-]	ω [rad/s]
0.000	1.0000	0.0250000
0.250	1.0000	0.0250000
0.251	1.0001	0.0250025

Time steps of 0.0001s were selected for the simulation. Turbulence is modelled with the $k-\varepsilon$ model and standard wall functions on the LARD using *kqRWallFunction, epsilonWallFunction* and *nutkWallFunction.* The fields are initialised uniformly with $k = 3.75 * 10^{-3}\,\frac{\mathrm{m}^2}{\mathrm{s}^2}$,

$\varepsilon = 1.755 * 10^{-2} \frac{m^2}{s^3}$ and $\nu = 1.56 * 10^{-6} \frac{m^2}{s}$. Some of the main boundary conditions for the rotational domain are shown in Table 6-6.

Table 6-6: Boundary conditions for rotational domain - velocity (U) and pressure (p)

Patch	U	p
Inlet	*fixedValue*	*zeroGradient*
Outlet	*inletOutlet*	*fixedValue*
Wall	*noSlip*	*zeroGradient*
Inner Cylinder	*movingWallSlipVelocity*	*zeroGradient*
LARD	*movingWallVelocity*	*zeroGradient*

6.1.5 Solver and numerical settings

All simulations are transient, incompressible and use pressure–velocity coupling with PIMPLE algorithm, which blends PISO's inner pressure corrections with SIMPLE-type outer iterations and under-relaxation to enable robust time marching at controlled Courant numbers with non-orthogonality corrections. In practice, each time step performs a number of outer correctors and, within each, one or more pressure–momentum corrections until continuity and momentum are satisfied on the current mesh.

For the **linear cases**, time advancement uses first-order Euler. Spatial gradients are Gauss linear, viscous terms use Gauss linear with corrected surface-normal gradients and momentum convection employs *linearUpwind* scheme with gradient reconstruction to achieve nominal second-order behaviour while damping spurious oscillations. Turbulence transport uses the same upwind-biased family. Linear solvers are field-segregated. Pressure is solved with *GAMG* (Geometric-Algebraic Multi-Grid), while velocity and turbulence scalars use a *smoothSolver* with symmetric Gauss–Seidel and tight absolute tolerances. Residual controls within PIMPLE terminate inner loops early once specified thresholds are met. The representative solver controls are two outer PIMPLE iterations, two inner pressure corrections and three non-orthogonal corrections per step with residual-based early exit.

Rotational cases adopt nearly the same temporal and spatial schemes with only two changes. First switch turbulence advection to upwind for robustness across the sliding, non-conformal interface and second limit non-orthogonal correction at the gradient level to stabilise flux transfer. Two additional solver roles are applied each time step. A pressure-flux consistency correction (*pcorr*, i.e. *correctPhi*) that enforces conservative face fluxes after mesh motion, typically with tight absolute and zero relative tolerance. And a moving-mesh flux solve (*MeshPhi*) that accounts for mesh velocity and converts between absolute and relative frames in the moving mesh before the main pressure update. The representative solver controls are two outers and one inner pressure correction, no explicit non-orthogonal loop and explicit *pcorr* and *MeshPhi* for flux-correction solves each step to maintain continuity on the moving/non-conformal mesh.

6.2 Mesh Study

To demonstrate mesh independence, the computational meshes for the linear and rotational cases are evaluated using standard quality metrics like cell count, aspect ratio, skewness, non-orthogonality and boundary-layer resolution. Because such metrics do not by themselves guarantee accurate solutions, a systematic grid-refinement (mesh-convergence) study is

performed to quantify discretization uncertainty and establish mesh-converged estimates of key outputs. Together, these analyses show that the selected mesh resolves the flow around the LARD with sufficient fidelity for the reported results. Due to the extent of the work, an exact description of the individual meshes is not provided. The chosen mesh is illustrated using some example detailed views of the LARD.

6.2.1 Linear domain

Three successively refined meshes (M1, M2 and M3) were prepared for the linear-domain mesh study using flow in surge direction as an example. M1 applies distance-based refinement around the body without prism layers. M2 adds a ten-layer prismatic boundary-layer stack. M3 further refines the surface and truss members and increases the boundary-layer resolution to twenty-five prisms. The background block mesh and refinement bands have identical extents in all cases so that differences arise solely from resolution and layering. The meshes properties are given in Table 6-7.

Table 6-7: Mesh properties - linear domain

	M1 (7 mio cells)	**M2 (11 mio cells)**	**M3 (22 mio cells)**
Number of cells	6,689,324	11,125,567	21,972,619
Max aspect ratio	8.45	7.00	5.50
Max skewness	30.29	5.91	4.00
Max Faces with Skewness	198	44	1
Non–orthogonality check	OK	OK	OK
Number of layers	0	10	25
Required computing time [h] (6 cores)	11	43	143

With increasing resolution, maximum aspect ratio and skewness decreased, while skewness hotspots shrink from 44 faces on M2 to a single face on M3. Non-orthogonality checks were passed by all meshes. Near walls, the absence of prisms in M1 limits wall-stress accuracy. The ten layers in M2 provide a smooth wall-function field and M3's twenty-five layers thicken the resolved viscous sublayer and prevent layer collapse in tight gaps. M1 thus serves as a coarse baseline, M2 introduces adequate wall-normal resolution and M3 yields the most uniform quality and true representation of the LARD's geometry. The improved geometric fidelity of the grid with increasing number of cells can be observed for example at the scissor-like struts and narrow gaps (see Figure 6-6).

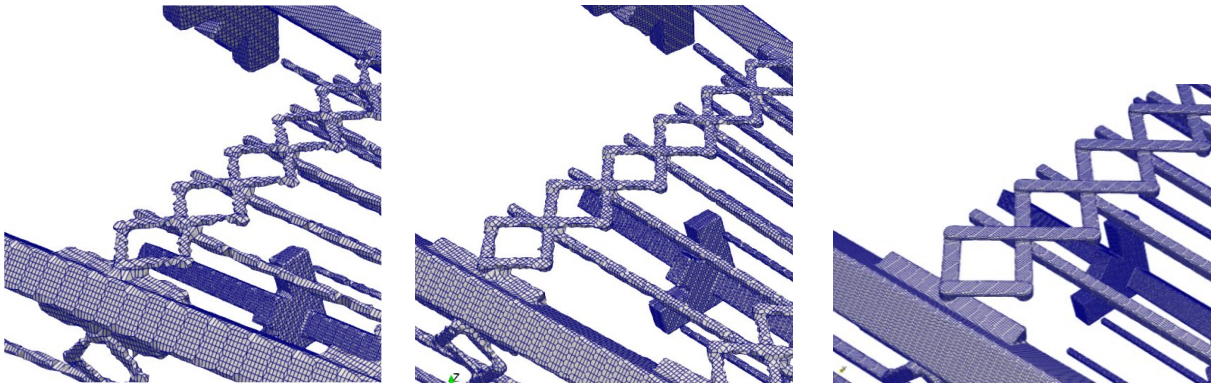


Figure 6-6: Detailed view on scissor-like struts M1 (left), M2 (middle) and M3 (right)

Figure 6-7 presents the force time history for the three meshes under a surge inflow of 1 m/s. Only the force in x-direction (aligned with the imposed velocity and acceleration) is shown, as the remaining load-vector components are negligible. A more detailed description of all force components is presented in section 6.3.

Using M2 as example Figure 6-8 shows that the acceleration applied at t=5 s does not affect long-time convergence. Simulations with and without the acceleration yield similar end-time forces. Accordingly, the mesh study for the linear domain is performed using the example of surge flow based on simulations with acceleration.

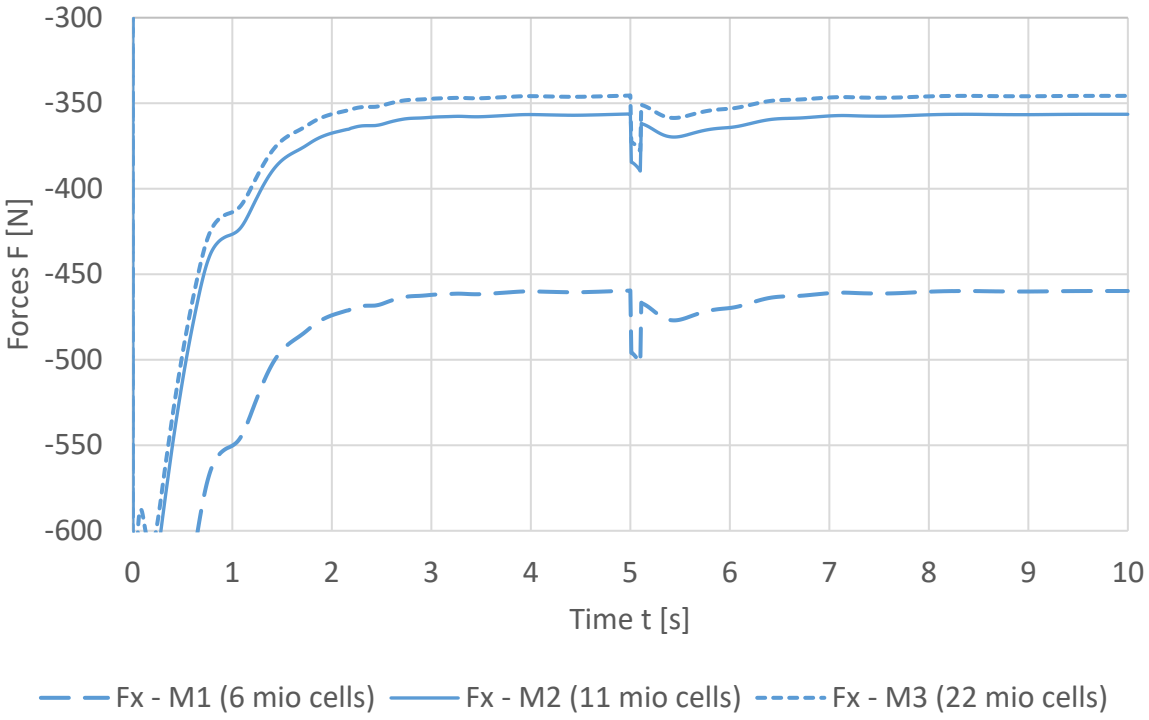


Figure 6-7: Mesh study for surge flow of 1 m/s

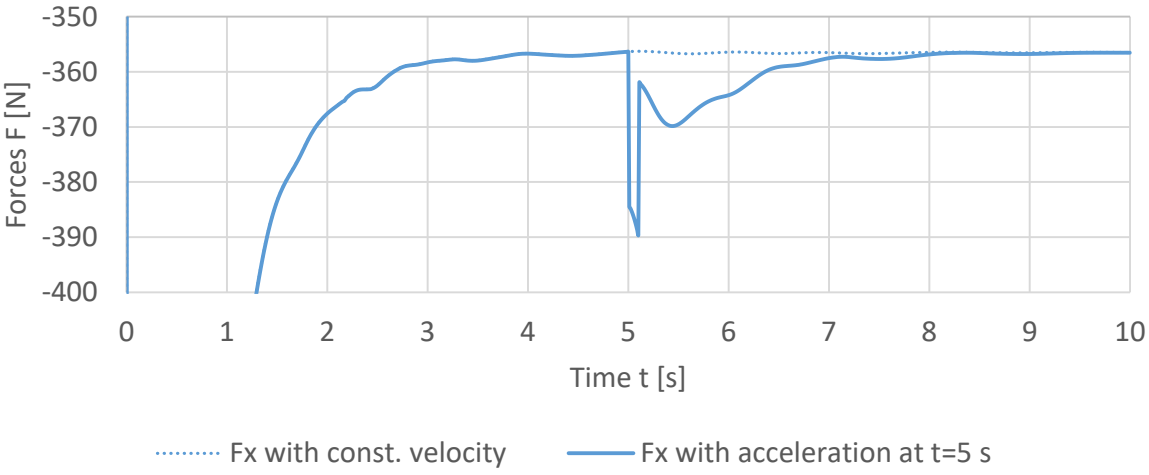


Figure 6-8: Convergence comparison M2: constant surge velocity vs acceleration at t=5 s

Table 6-8 summarizes the results for the three meshes in terms of streamwise drag and added mass. Mesh M2 was selected because it deviates by only about 3 % from the finest mesh (M3)

while requiring substantially fewer resources (M3 needs roughly 3.3 times the computing effort of M2). Residual histories were also considered in the decision. In addition, a Grid Convergence Index was computed across the successively refined grids to quantify discretization uncertainty and supported the decision for M2.

Table 6-8: Mesh dependent results for surge flow

	M1	**M2**	**M3**
Fx [N]	-459.9	-356.3	-345.8
Added mass [kg]	363.1	281.5	273.0

6.2.2 Rotational Domain

The same mesh study strategy as for the translational cases was applied to the rotational cases with the corresponding mesh properties reported in Table 6-9. In the rotational setup, the LARD is placed inside a rotating inner cylinder that is coupled to a stationary outer box via a sliding non-conformal interface. Three successively refined meshes were generated. Version M1 defines the distance-based refinement inside the inner cylinder but does not include prism sublayers. M2 adds a ten-layer wall-normal prism stack on both the LARD and the inner-cylinder wall and increases the tessellation density at the sliding patches. M3 further refines all feature lines on the truss members and increases the boundary-layer resolution to fifty prism layers. The cylinder dimensions and the background block mesh remain identical across all versions, so differences arise purely from local resolution and layering.

Table 6-9: Mesh properties - rotational domain

	M1	**M2**	**M3**
Number of cells	3,428,481	12,138,760	32,136,920
Max aspect ratio	9.0	7.0	2.5
Max skewness	6.8	6.0	2.5
Max Faces with Skewness	30	11	0
Non–orthogonality check	OK	OK	OK
Number of layers	0	10	50
Required computing time [h] (20 cores)	9	15	57

Table 6-9 summarises the principal mesh statistics. In terms of surface resolution, M1 captures the overall frame but under-resolves the slender truss members. M2 sharpens edges and small gaps and largely removes faceting at fillets. M3 resolves individual struts and narrow passages cleanly, which influences local pressure distributions and the resulting pressure-moment response. Near the wall, M1 lacks prism layers and thus limits the accuracy of wall-stress prediction. From M1 to M3 the face sizes at the non-conformal sliding interface become progressively better matched, which reduces flux-mapping errors and keeps pressure jumps across the interface negligible during rotation. The same improvement trend as in the linear cases is observed in the near-wall resolution and Grid Convergence Index.

The moment time history for the three meshes under a pitch flow of 0.025 rad/s is illustrated in Figure 6-9. As M2 remains within about 5 % of M3 in the moment response while reducing the computational cost by roughly 74 % in terms of core-hours, it was selected for the further analysis of the LARD. This residual mesh dependence is treated as a numerical uncertainty and is therefore accounted for in the discussion of the results. This numerical uncertainty is considered alongside other sources of modelling uncertainty that are not reduced by mesh

refinement, such as turbulence-modelling and wall-function assumptions, boundary-condition sensitivity and the geometric idealisations applied during CAD simplification.

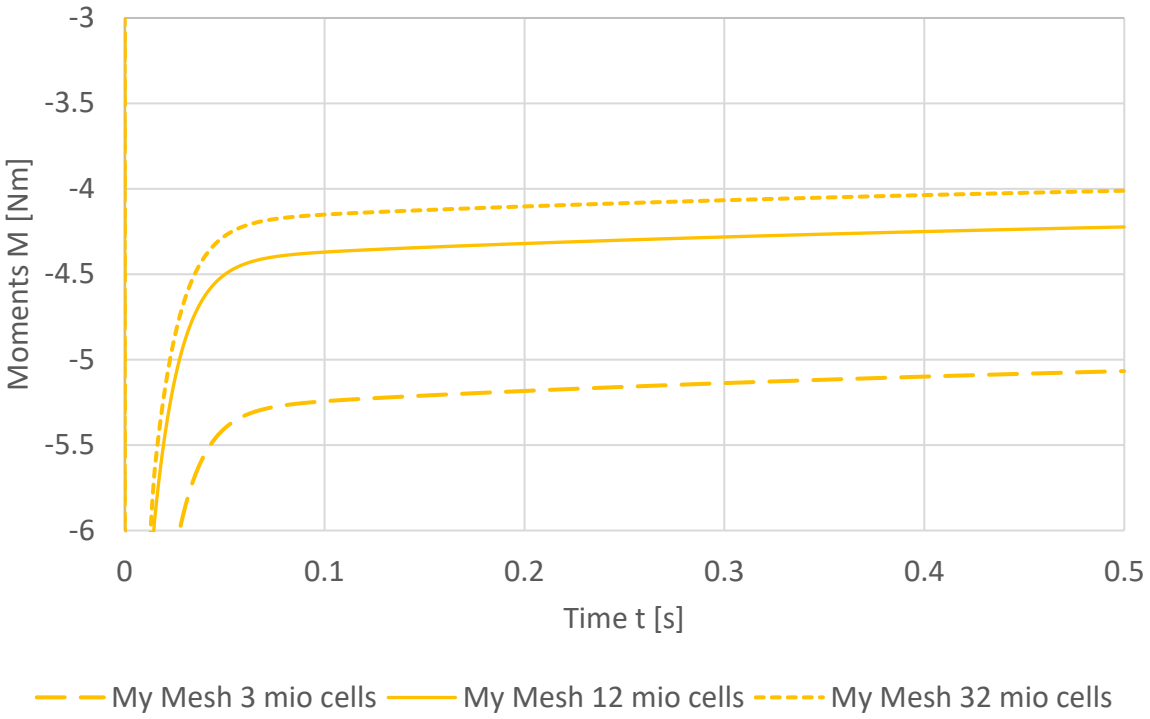


Figure 6-9: Mesh study for pitch flow of 0.025 rad/s

6.3 Numerical Results

This section presents the quantitative results of the LARD simulations in terms of the hydrodynamic parameters introduced at the beginning of the chapter. The data processing and post-processing workflow are described in detail at the start of section 6.3.1 (translational domain), including the evaluation procedure, the force time histories and the pressure distributions. The results for the remaining DoF are then reported and summarised, as they were obtained using the same workflow. An exception is the first rotational degree of freedom discussed in section 6.3.2, where the numerical setup changes, although the underlying evaluation procedure remains the same as for the translational cases. Section 6.3.3 analyses the impact of the chosen velocity on the hydrodynamic coefficients.

6.3.1 Translational degrees of freedom

The forces and moments at a surge flow of 1 m/s are shown in Figure 6-10. With the exception of the force in the x-direction (Fx), all other forces and moments in the remaining DoF are approximately zero and are therefore not considered further. A detailed view of the time history of the force in the x-direction is shown in Figure 6-11.

Using the converged force, simulation parameters and LARD's projected area as obtained from the CAD model, the drag coefficient is determined as follows:

$$C_{D_x}^t = \frac{2\,F_{D_x}}{\rho\, v_{b_x}\,|\,v_b|\,A_x} = \frac{2 * 356.3447\ \mathrm{N}}{1025\ \frac{\mathrm{kg}}{\mathrm{m}^3} * 1\ \frac{\mathrm{m}}{\mathrm{s}} * \left|1\ \frac{\mathrm{m}}{\mathrm{s}}\right| * 1.0741\ \mathrm{m}^2} = 0.6461 \tag{6.6}$$

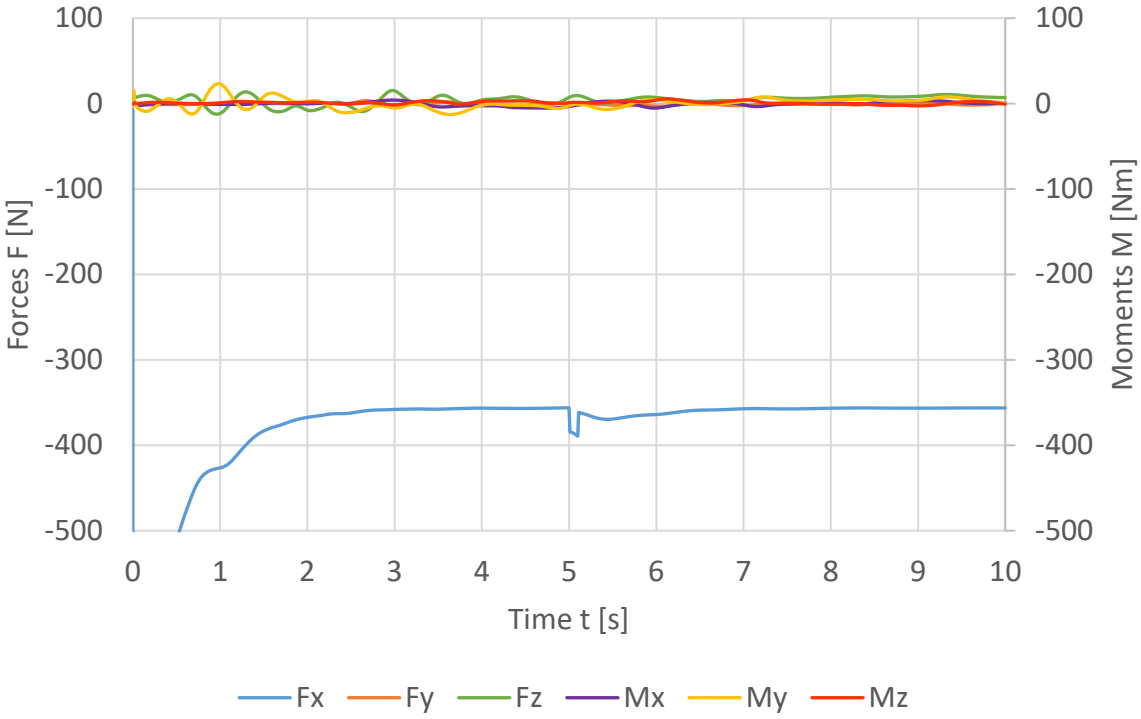


Figure 6-10: Forces and moments of surge flow

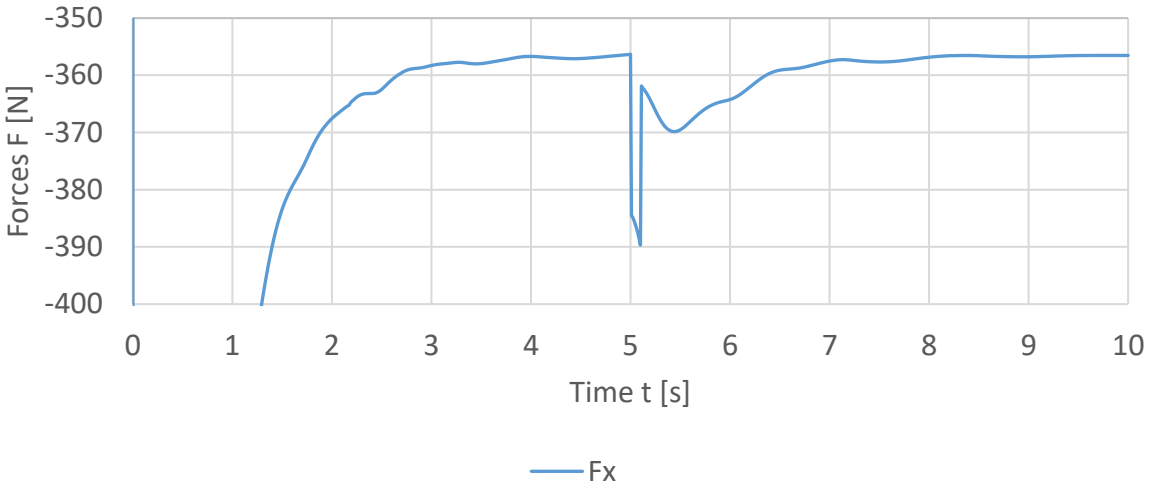


Figure 6-11 Force Fx of surge flow (detailed view)

This converged force is also used to determine the unit damping force:

$$UDF_x = \frac{F_{DA_x}}{v_{b_x}} = \frac{356.3447\ \text{N}}{1\ \frac{\text{m}}{\text{s}}} = 356.3447\ \frac{\text{Ns}}{\text{m}} \tag{6.7}$$

Figure 6-12 shows the pressure distribution on the LARD at a simulation time of 4.9 s, that is, just before the onset of acceleration. The corresponding velocity field is presented in Figure 6-13 as a cross-section along the longitudinal axis of the device. In the head region of the device, a flow directed opposite to the towing velocity can be identified, which is considered beneficial for the docking process, as it may induce a suction effect on the AUV and thereby help to draw it into the device. However, the flow field would change once an additional body, such as the AUV, is introduced.

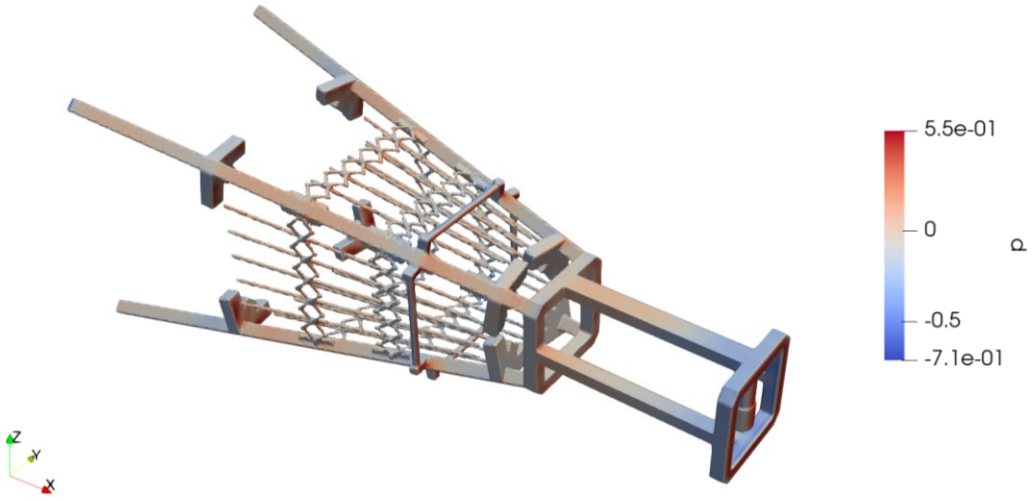


Figure 6-12: LARD pressure distribution for surge flow of 1 m/s at t=4.9 s (isometric view)

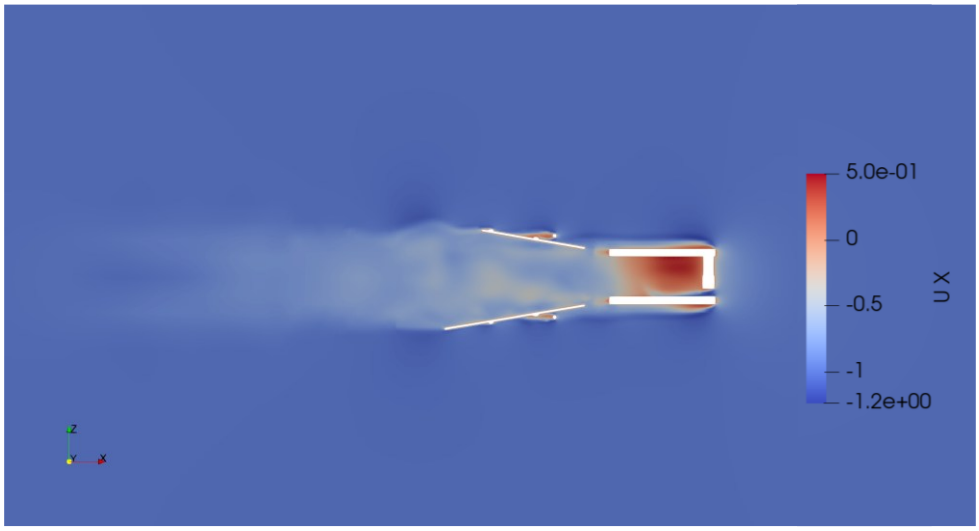


Figure 6-13: Velocity profile at t=4.9 s for surge flow of 1 m/s – x-z-plane at y=0

Figure 6-14 shows the force Fx including the available data points. The plot represents a

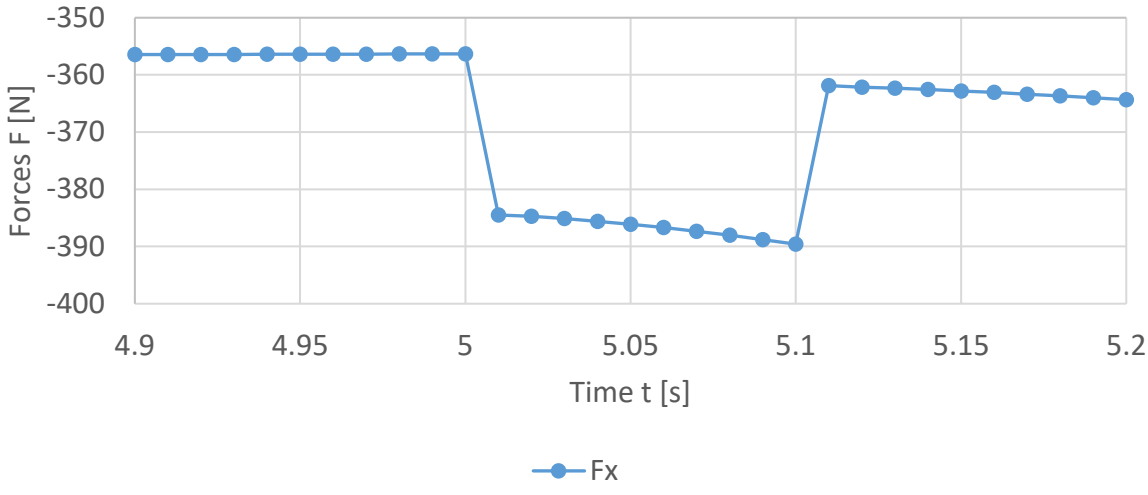


Figure 6-14 Force Fx of surge flow (zoom)

zoomed-in view around the acceleration phase, where a constant velocity is maintained up to a simulation time of 5 s, followed by an acceleration phase of 0.1 s with an acceleration of 0.1 m/s². Based on the force shift, the added mass can be determined as:

$$m_{a_x} = \frac{F_{2_x} - F_{1_x}}{a_{s_x}} = \frac{384.4904\ \text{N} - 357.3447\ \text{N}}{0.1\ \frac{\text{m}}{\text{s}^2}} = 281.4569\ \text{kg} \tag{6.8}$$

F_{2_x} is sampled at the time step directly before the acceleration is applied. F_{1_x} is then sampled at the first instant immediately after the acceleration is imposed. This procedure isolates the step change in the force time history, visible in Figure 6-14, which is attributable to the added mass based on the imposed acceleration. Leading to the added mass coefficient in x-direction:

$$C_{a_x}^t = \frac{m_{a_x}}{\Delta_b} = \frac{281.4569\ \text{kg}}{125.4297\ \text{kg}} = 2.2439 \tag{6.9}$$

Following the same procedure, the hydrodynamic coefficients are also computed for the remaining DoF. Figure 6-15 presents the forces and moments obtained for a sway inflow. It should be noted that, not only a force in the y-direction, which is relevant for the calculations of the drag, damping and added mass coefficient, occurs, but also a moment about the z-axis occurs. This moment arises because the body does not appear symmetric to its COG, when subjected to a lateral (sway) inflow. The different lever arms result in a moment. A similar behaviour is observed for heave flow. In contrast, this effect does not occur for surge, since the body is symmetric to its COG in the corresponding y-z-plane.

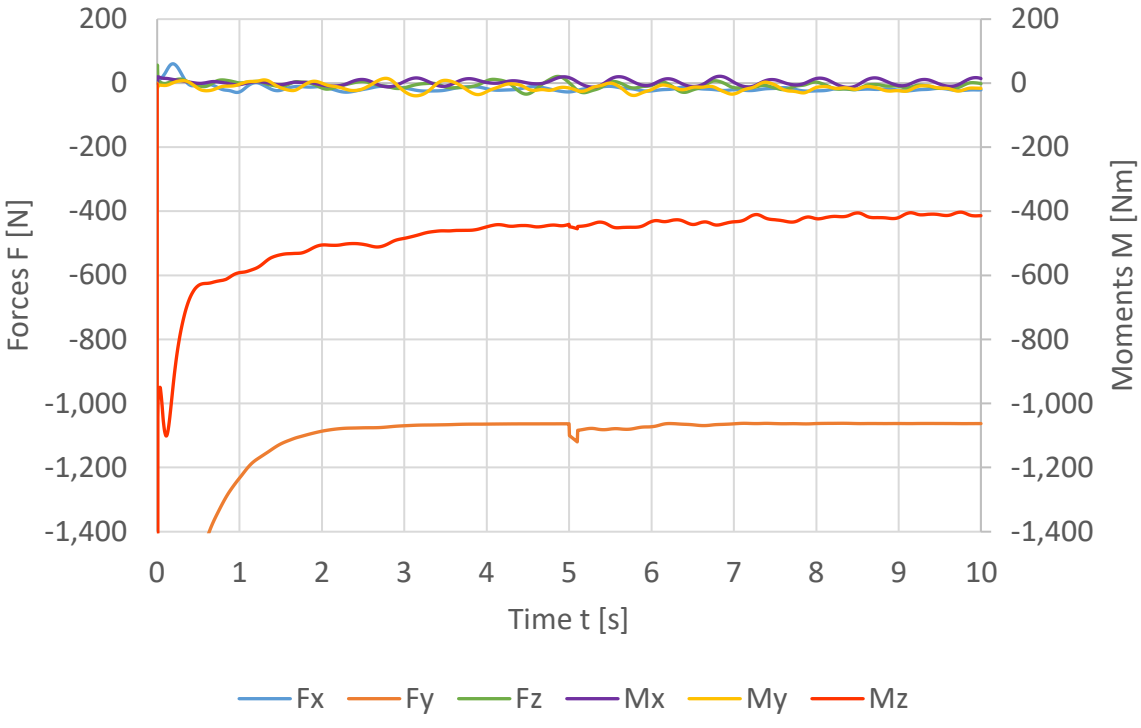


Figure 6-15: Forces and moments of sway flow

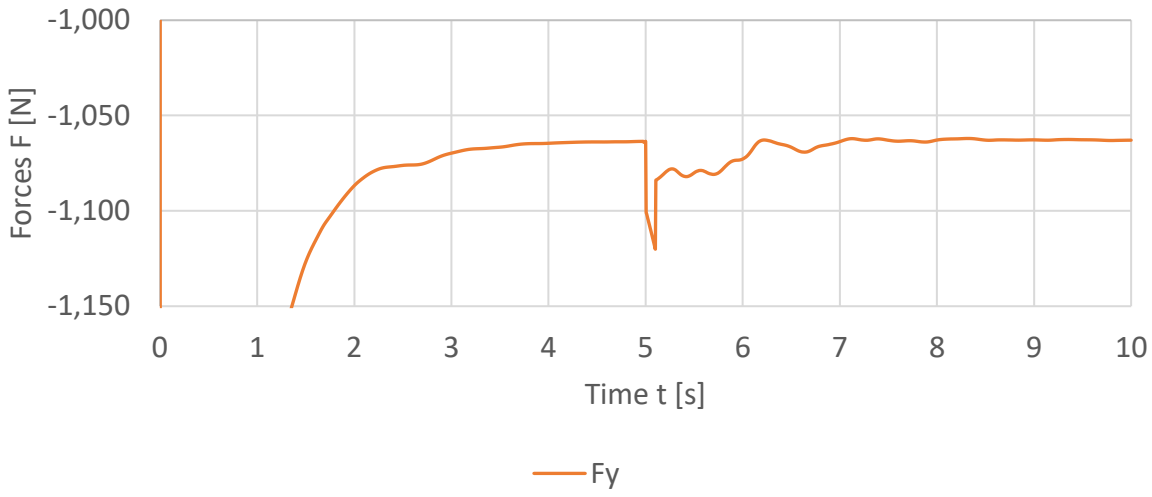


Figure 6-16: Force Fy of sway flow (detailed view)

Based on the force Fy seen in Figure 6-16 the hydrodynamic coefficients can be determined to:

$$C_{D_y}^t = \frac{2\,F_{D_y}}{\rho\, v_{b_y}\,|\,v_b|A_y} = \frac{2 * 1063.5497\ \text{N}}{1025\ \frac{\text{kg}}{\text{m}^3} * 1\ \frac{\text{m}}{\text{s}} * \left|1\ \frac{\text{m}}{\text{s}}\right| * 1.3427\ \text{m}^2} = 1.5426 \tag{6.10}$$

$$UDF_y = \frac{F_{DA_y}}{v_{b_y}} = \frac{1063.5497\ \text{N}}{1\ \frac{\text{m}}{\text{s}}} = 1063.5497\ \frac{\text{Ns}}{\text{m}} \tag{6.11}$$

$$m_{a_y} = \frac{F_{2_y} - F_{1_y}}{a_{s_y}} = \frac{1100.5727\ \text{N} - 1063.5497\ \text{N}}{0.1\ \frac{\text{m}}{\text{s}^2}} = 370.2300\ \text{kg} \tag{6.12}$$

$$C_{a_y}^t = \frac{m_{a_y}}{\Delta_b} = \frac{370.2300\ \text{kg}}{125.4297\ \text{kg}} = 2.9517 \tag{6.13}$$

The velocity field in the x–y plane at t= 4.9 s is shown in Figure 6-17.

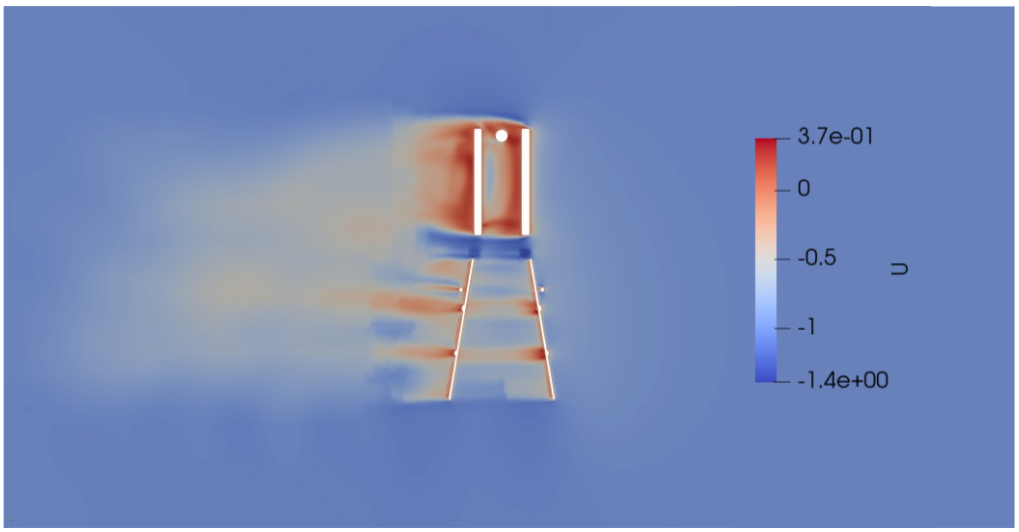


Figure 6-17: Velocity profile at t=4.9 s for sway flow of 1 m/s – x-y-plane at z=0

Due to the strong geometric similarity of the LARD in the x–y plane (sway flow) and the x–z plane (heave flow), the heave-flow simulations yield results that are qualitatively comparable to those obtained for sway. The differences that do occur are limited to small details and can be attributed to small geometric deviations, since the two planes are not fully identical. The most pronounced differences arise from the design of the guiding mechanism, which is slightly shorter on the upper side of the LARD to provide space for AUV superstructures and from the mounting of the USB system, which is attached to the front of the upper beam of the LARD. These features lead to minor deviations between sway and heave results. The results are presented in Figure 6-18 and Figure 6-19.

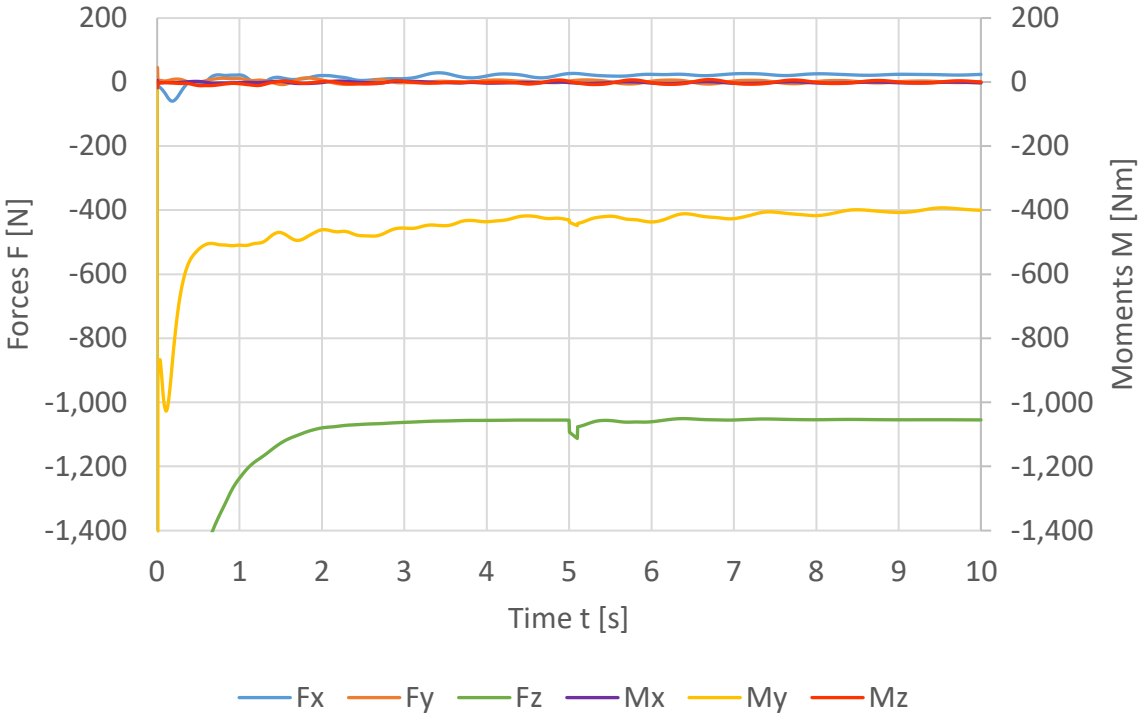


Figure 6-18: Forces and moments of heave flow

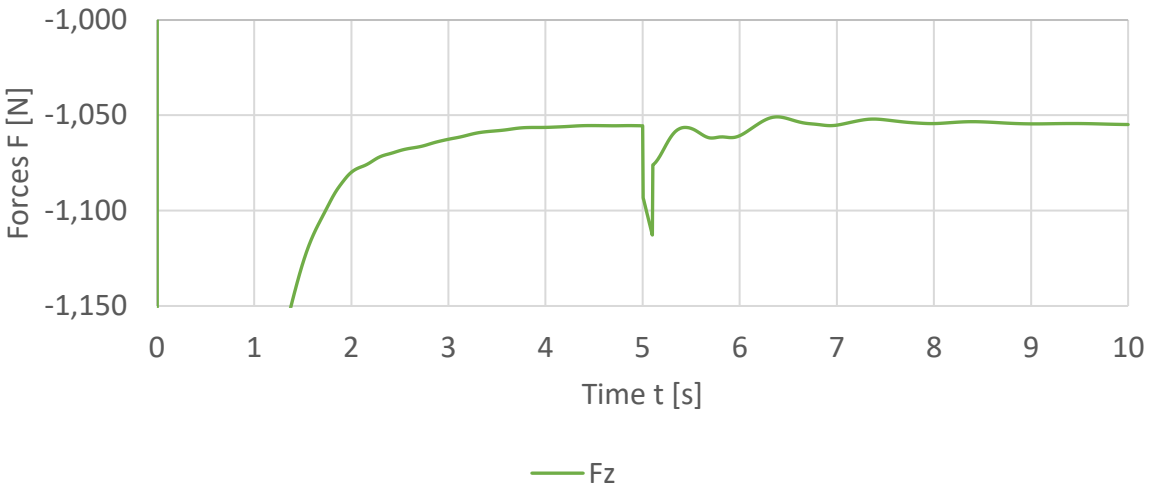


Figure 6-19: Force Fz of heave flow (detailed view)

$$C_{D_z}^t = \frac{2\,F_{D_z}}{\rho\, v_{b_z}\,|\,v_z|A_z} = \frac{2 * 1055.5394\ \text{N}}{1025\ \frac{\text{kg}}{\text{m}^3} * 1\ \frac{\text{m}}{\text{s}} * \left|1\ \frac{\text{m}}{\text{s}}\right| * 1.3254\ \text{m}^2} = 1.5510 \tag{6.14}$$

$$UDF_z = \frac{F_{DA_z}}{v_{b_z}} = \frac{1055.5394\ \text{N}}{1\ \frac{\text{m}}{\text{s}}} = 1055.5394\ \frac{\text{Ns}}{\text{m}} \tag{6.15}$$

$$m_{a_z} = \frac{F_{2_z} - F_{1_z}}{a_{s_z}} = \frac{1093.1220\ \text{N} - 1055.5394\ \text{N}}{0.1\ \frac{\text{m}}{\text{s}^2}} = 375.8264\ \text{kg} \tag{6.16}$$

$$C_{a_z}^t = \frac{m_{a_z}}{\Delta_b} = \frac{375.8264\ \text{kg}}{125.4297\ \text{kg}} = 2.9963 \tag{6.17}$$

In summary, the results for the hydrodynamic coefficients in the translational DoF are presented in Table 6-10.

Table 6-10: Translational hydrodynamic coefficients

DoF	$\boldsymbol{C_{D_i}^t}$ **[-]**	$\boldsymbol{UDF_i}$ **[N/(m/s)]**	$\boldsymbol{C_{a_i}^t}$ **[-]**
Surge	0.6461	356.3447	2.2439
Sway	1.5426	1063.5497	2.9517
Heave	1.5510	1055.5394	2.9963

6.3.2 Rotational degrees of freedom

For the rotational DoF, the same evaluation procedure as described previously for the translational DoF in section 6.3.1 is applied. Figure 6-20 shows the time histories of forces and moments for the simulation with a roll motion of 0.025 rad/s.

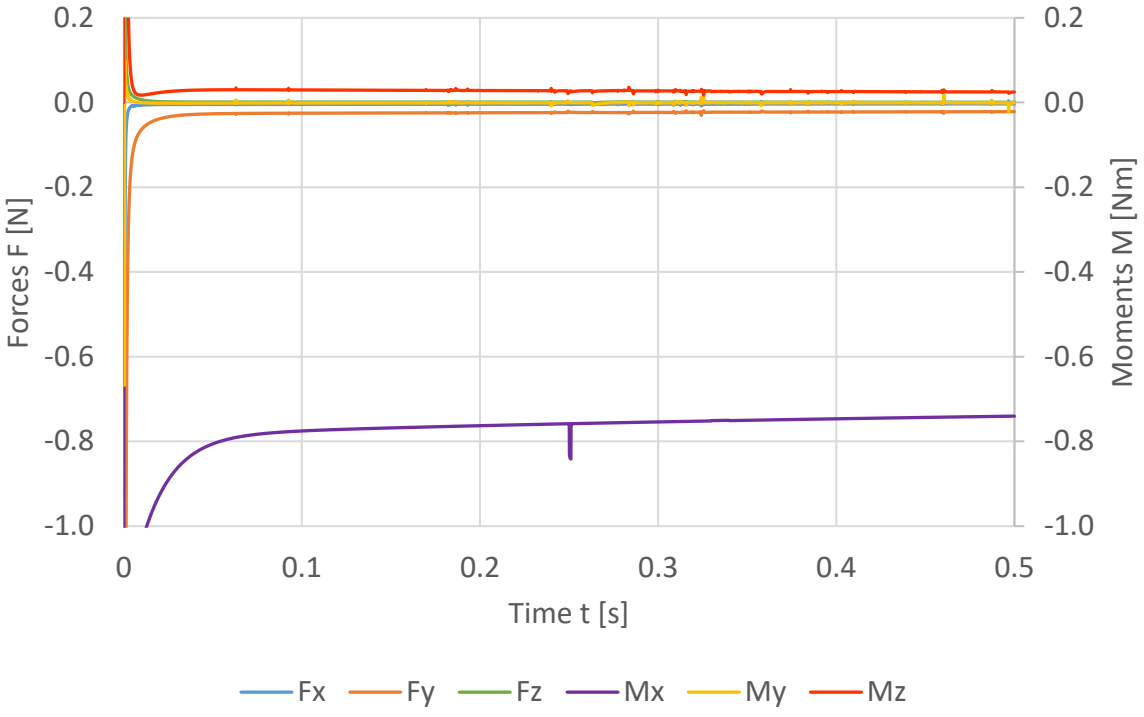


Figure 6-20: Forces and moments of roll flow of 0.025 rad/s

The moment Mx, which is relevant for the coefficient identification for roll motion, is shown in greater detail in Figure 6-21 with data points around the acceleration period.

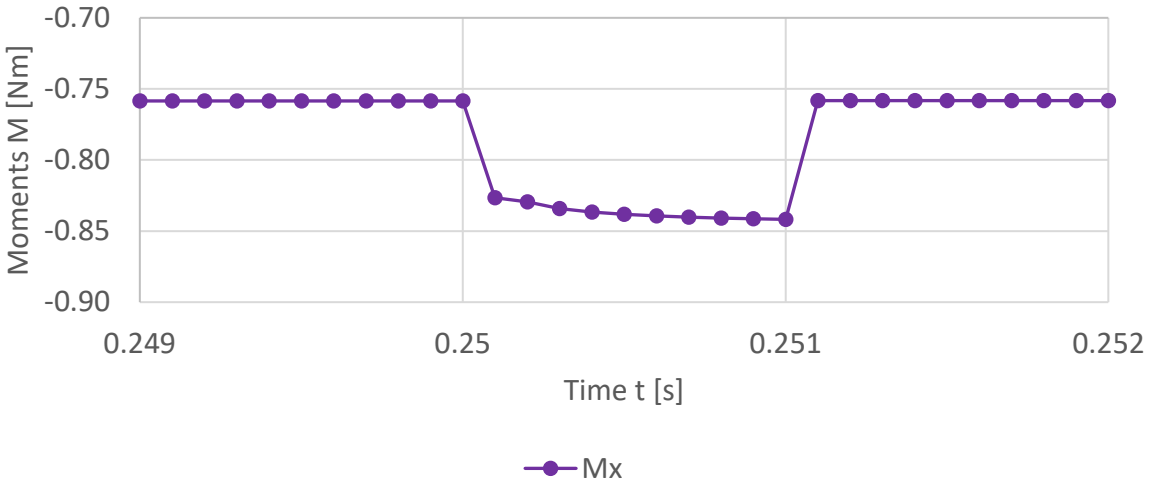


Figure 6-21: Moment Mx of roll flow (zoom)

$$C_{D_x}^r = \frac{2\,M_{D_x}}{\rho\,|\omega_b|^2\,AM_x} = \frac{2 * 0.7405\ \text{Nm}}{1025\ \frac{\text{kg}}{\text{m}^3} * \left|0.025\ \frac{\text{rad}}{\text{s}}\right|^2 * 0.0437\ \text{m}^5} = 52.9007 \tag{6.18}$$

$$UDM_x = \frac{M_{D_x}}{\omega_{b_x}} = \frac{0.7405\ \text{Nm}}{0.025\ \frac{\text{rad}}{\text{s}}} = 29.6194\ \frac{\text{Ns}}{\text{rad}} \tag{6.19}$$

$$m_{a_x} = \frac{F_{2_x} - F_{1_x}}{\dot{\omega}_{s_x}} = \frac{0.8265\ \text{Nm} - 0.7584\ \text{Nm}}{0.0025\ \frac{\text{rad}}{\text{s}^2}} = 27.2487\ \text{kg} \tag{6.20}$$

$$C_{a_x}^r = \frac{m_{a_x}}{\Delta_b} = \frac{27.2487\ \text{kg}}{125.4297\ \text{kg}} = 0.2172 \tag{6.21}$$

The moment history My for pitch flow is shown in Figure 6-17.

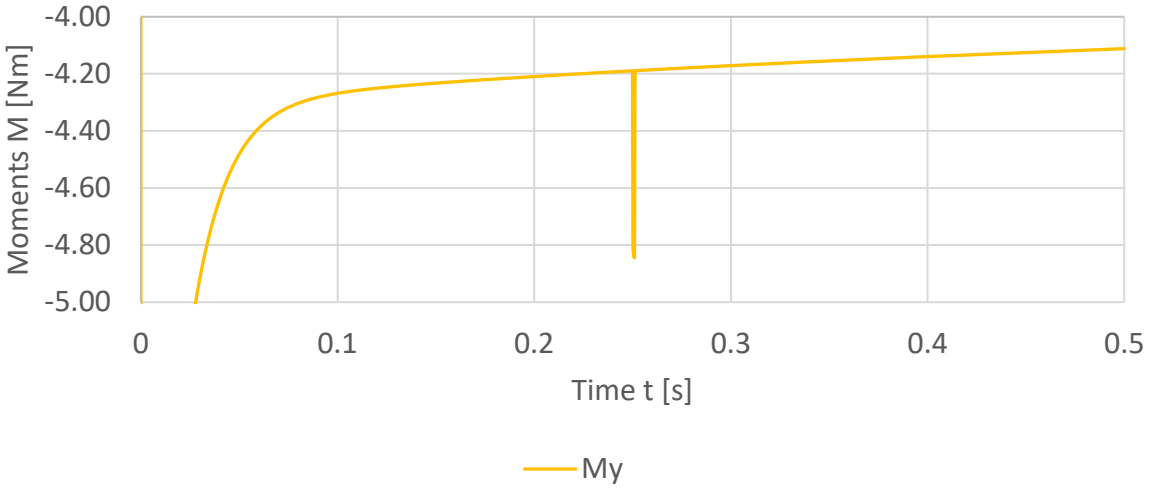


Figure 6-22: Moment My of pitch flow (detailed view)

The moment history Mz for yaw flow is presented in Figure 6-19. The hydrodynamic coefficients for pitch and yaw are obtained an analogous manner to the roll results and summarised in Table 6.11.

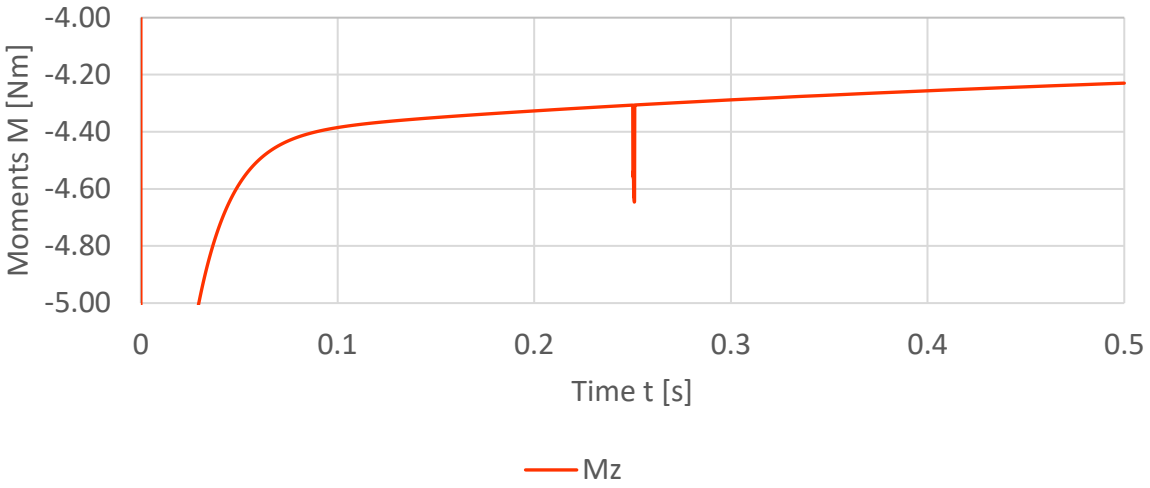


Figure 6-23: Moment Mz of yaw flow (detailed view)

Table 6-11: Rotational hydrodynamic coefficients

DoF	$C^r_{D_i}$ **[-]**	UDM_i **[N/(rad/s)]**	$C^r_{a_i}$ **[-]**
Roll	52.9007	29.6194	0.2172
Pitch	210.0340	167.5919	1.9483
Yaw	195.3676	169.1915	1.0832

The substantially larger rotational drag coefficients in pitch and yaw compared with roll indicate that the LARD produces markedly higher resistance moments about the y- and z-axes, consistent with its geometry providing larger effective lever arms and more separation-prone projected features for pitch/yaw rotations. Moreover, the rotational added-mass coefficients show that the hydrodynamic moment-of-inertia contribution is strongest in pitch and yaw, whereas roll remains comparatively weak, which is plausible because roll predominantly accelerates fluid closer to the body centreline, while pitch and yaw mobilise larger fluid volumes at greater radii. Compared to canonical cylinders, which provide a qualitative benchmark for "order-of-magnitude" reasoning, the LARD's open-frame, multi-member geometry makes its rotational coefficients expectedly larger and more anisotropic than those of simple analytical bodies.

6.3.3 Velocity study

To assess the influence of the prescribed simulation velocity on the hydrodynamic parameters, two velocity studies were carried out for the heave and pitch DoF. In each case, velocities corresponding to 50 % and 150 % of the previously used velocity for the translational and rotational simulations were considered. No further modifications to the simulation setup were introduced. The resulting force histories for the heave flow are shown in Figure 6-24. The corresponding overview of the hydrodynamic coefficients is provided in Table 6-12.

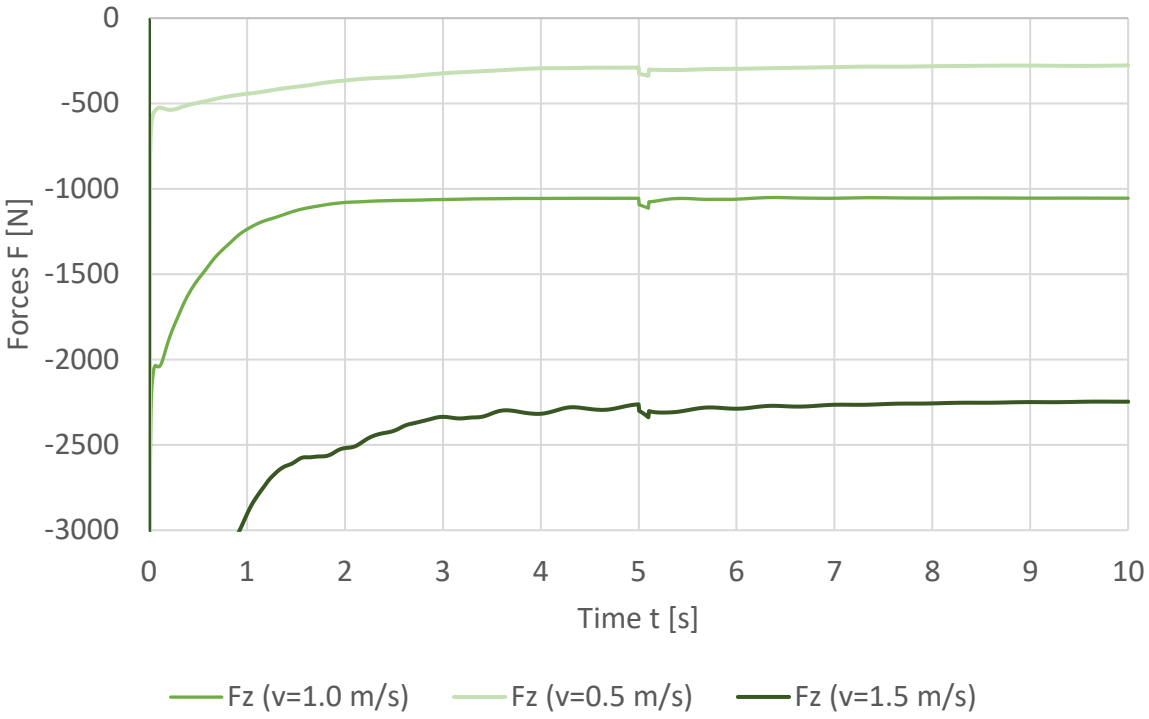


Figure 6-24: Heave velocity study - forces

Table 6-12: Heave velocity study - hydrodynamic coefficients

v [m/s]	$C_{D_i}^t$ **[-]**	UDF_i **[N/(m/s)]**	$C_{a_i}^t$ **[-]**
0	-	0	-
0.5	1.6302	554.7493	2.9542
1	1.5510	1055.5394	2.9963
1.5	1.4680	1498.6206	3.0376

With respect to the drag coefficient, deviations of approximately ± 5 % are obtained for both the lower velocity of 0.5 m/s and the higher velocity of 1.5 m/s when compared to the reference simulation at 1.0 m/s. This trend (a slight reduction of $C_{D_i}^t$ with increasing velocity) is consistent with Reynolds-number effects. At higher Re, the boundary layer typically becomes more resistant to adverse pressure gradients, which can delay separation and reduce wake size, thereby lowering the pressure-drag contribution to $C_{D_i}^t$ [191]. Moreover, for attached-flow portions, the skin-friction contribution to the drag coefficient generally decreases with increasing Re [192]. In practice, the net change in $C_{D_i}^t$ results from the balance between separation-related pressure drag and skin friction and therefore remains modest over the present velocity range. Nevertheless, the residual sensitivity of $C_{D_i}^t$ should be treated as an evaluation uncertainty when interpreting resistance-related coefficients.

For the added mass coefficient, the deviations are considerably smaller, on the order of ± 1 % and can therefore be neglected in this context. It is thus assumed that both coefficients are effectively independent of velocity and the values derived from the simulation at 1.0 m/s are used in this work.

For the unit damping forces, a linear fit is employed based on the drag force derived from the simulation with 1 m/s flow velocity. The fitted line must pass through the origin, since the unit

damping force is 0 at a velocity of 0 m/s. The grey dashed line shown in Figure 6-25 is therefore defined solely by the origin and the unit damping force obtained for a velocity of 1 m/s. The simulation results for the three simulated velocities are represented as green dots in Figure 6-25. Due to the good fit of the simulation results of 0.5 m/s and 1.5 m/s into the linear interpolated grey dashed line the linear interpolation approach is considered sufficiently accurate for the purposes of this study.
This choice is supported by comparative studies on AUV hydrodynamic damping by Gibson et al. [193] which show that a linear model provides competitive accuracy at moderate speeds while substantially reducing the identification effort compared with fully coupled quadratic formulations. [193]

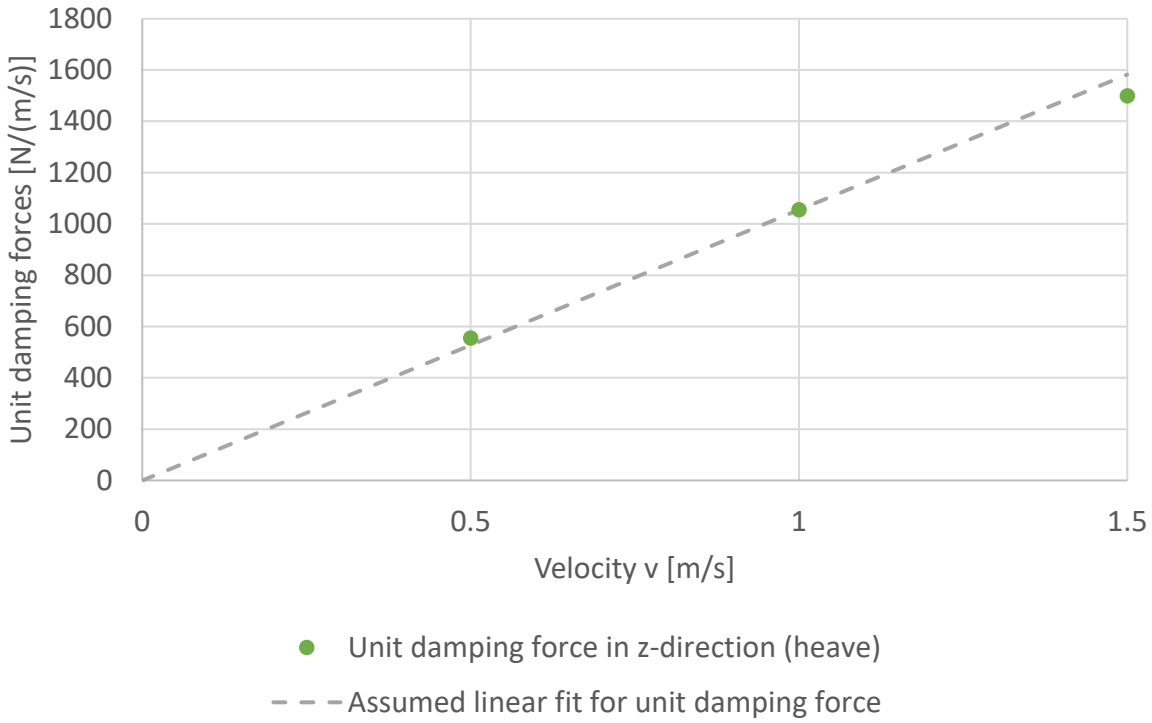


Figure 6-25: Heave velocity study – unit damping forces

Similar observations were made in the velocity study for pitch. The corresponding moment histories are shown in Figure 6-26. As illustrated in Figure 6-27 the deviations between the simulated values (yellow dots) and the linear fit of the unified damping moment (grey dotted line) are a bit larger compared to the heave velocity study. Nevertheless, the resulting accuracy is considered sufficient for the purposes of this work and is adopted in order to reduce the computational effort, since otherwise two additional simulations per degree of freedom would be required to perform a quadratic fit of the unified damping moment.

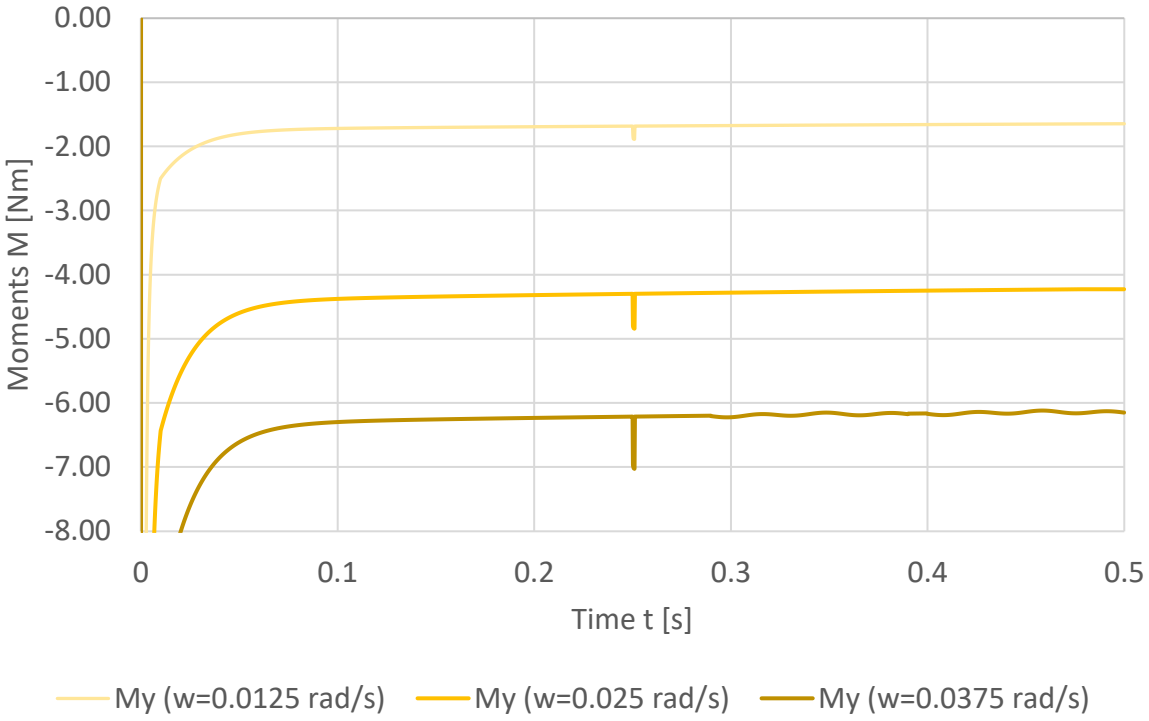


Figure 6-26: Pitch velocity study - moments

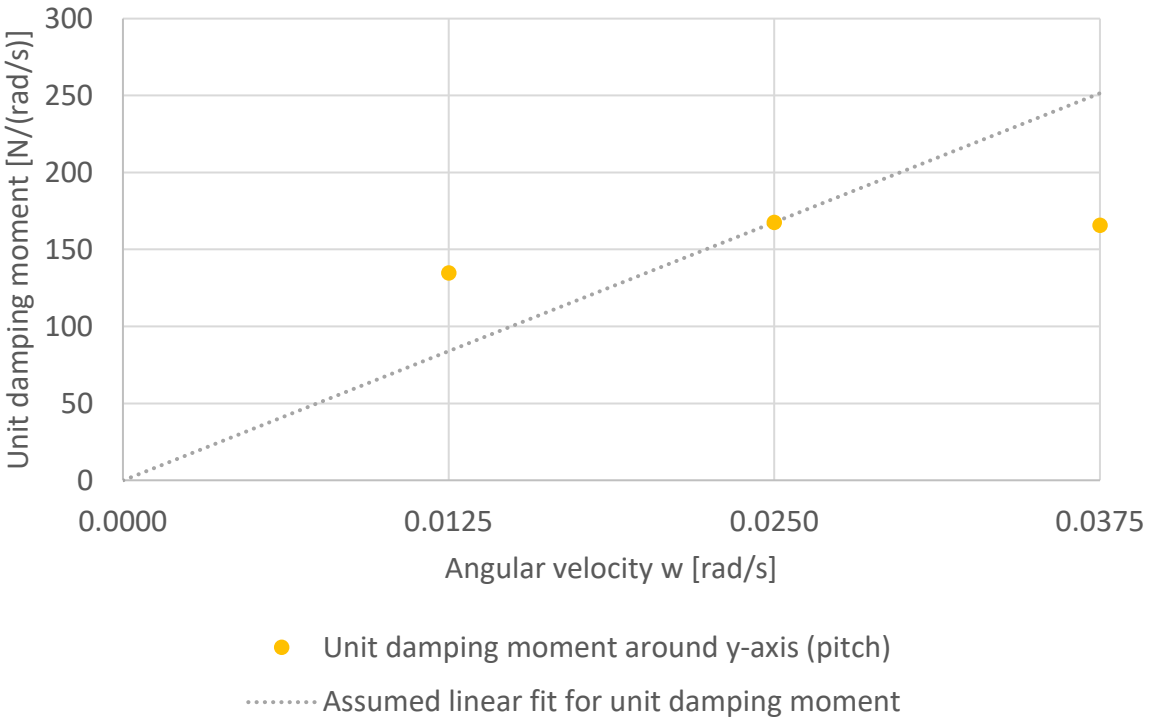


Figure 6-27: Pitch velocity study – unit damping moments

6.4 Experimental Validation

The objective of the experimental programme is to validate the hydrodynamic properties of the LARD. In addition to a qualitative assessment of the physical plausibility of these properties in view of the device geometry, a towing tank test campaign was carried out. This campaign comprises steady-towing tests to determine drag coefficients and forced oscillation tests (see section 4.4.2) to quantify added mass and hydrodynamic damping.
The experiments were restricted to translational degrees of freedom, as implementing a corresponding setup for rotational motions would be excessively complex. Consequently, measurements were conducted in surge and sway. Heave tests were omitted due to the geometric similarity of the body in the sway and heave directions and the very similar hydrodynamic coefficients obtained from the CFD simulations. For this reason, no additional experimental validation of the heave hydrodynamic coefficients is performed within the scope of this work.
This section is structured as follows. First, the experimental setup is introduced. Next, the results of the steady-towing tests used to determine the drag coefficients are presented, followed by the findings of the forced oscillation tests, from which hydrodynamic damping and added mass are derived. Finally, deviations between the numerically predicted and experimentally determined values are discussed.

6.4.1 Experimental Setup

The model of the LARD was manufactured at a 1:3 scale and is shown in Figure 6-28. It replicates the geometry of the full-scale device, including the articulated joints that allow different opening angles to be adjusted. For all experiments, the maximum opening angle of the LARD was selected. The same configuration was used in the CFD simulations, such that the numerical and experimental investigations are based on an identical geometry. This opening angle also corresponds to the configuration intended for the subsequent multibody analysis of the towing behaviour.

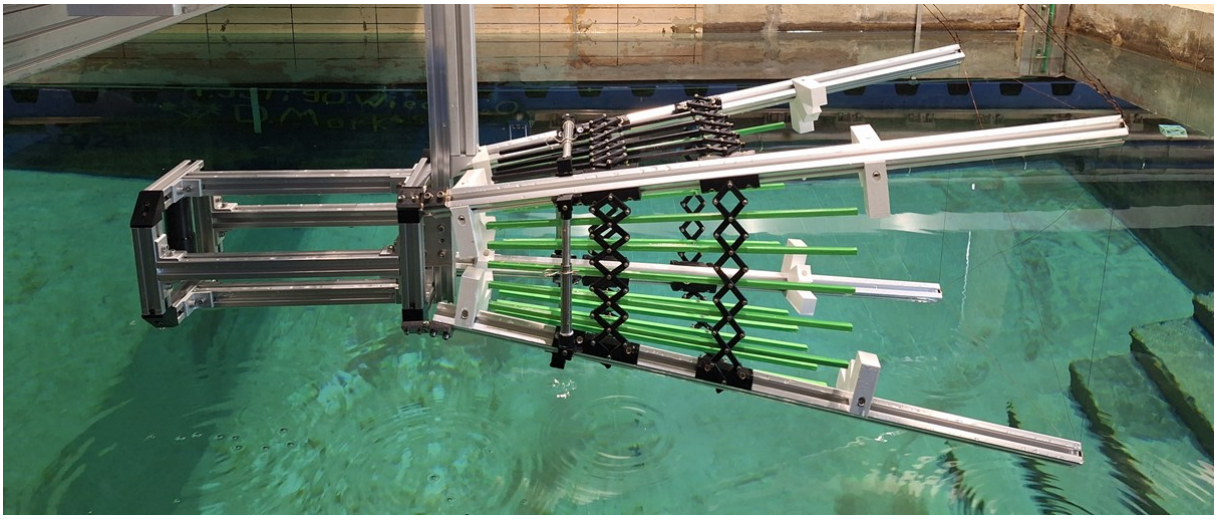


Figure 6-28: LARD model (1:3) - side view

The choice of similarity laws follows the discussion in Section 4.4.1. Dynamic similarity is sought such that the ratios of the dominant forces acting on the fluid are comparable between

model and prototype. Since the body is fully submerged and towed at a sufficient distance below the free surface, the influence of wave and gravitational effects described by Froude similarity is not of importance. Instead, Reynolds similarity is adopted, as viscous and inertial interactions govern the flow in this configuration. The model dimensions and test conditions were selected so that the resulting velocities and accelerations are feasible within the capabilities of the towing tank at the University of Rostock. The towing speeds in the experiments, as well as the characteristic velocities in the simulations, are chosen with respect to the density and kinematic viscosity of the respective working fluid, such that the Reynolds number of the model matches that of the full-scale LARD as closely as possible.
Within this framework, the experimental programme consists of two types of motion. Drag tests are performed at constant streamwise towing speed, while added mass and damping tests are carried out using a prescribed forced oscillation trajectory, in which a sinusoidal lateral displacement is superimposed on a constant longitudinal towing velocity. The four investigated motion patterns are illustrated in Figure 6-29.

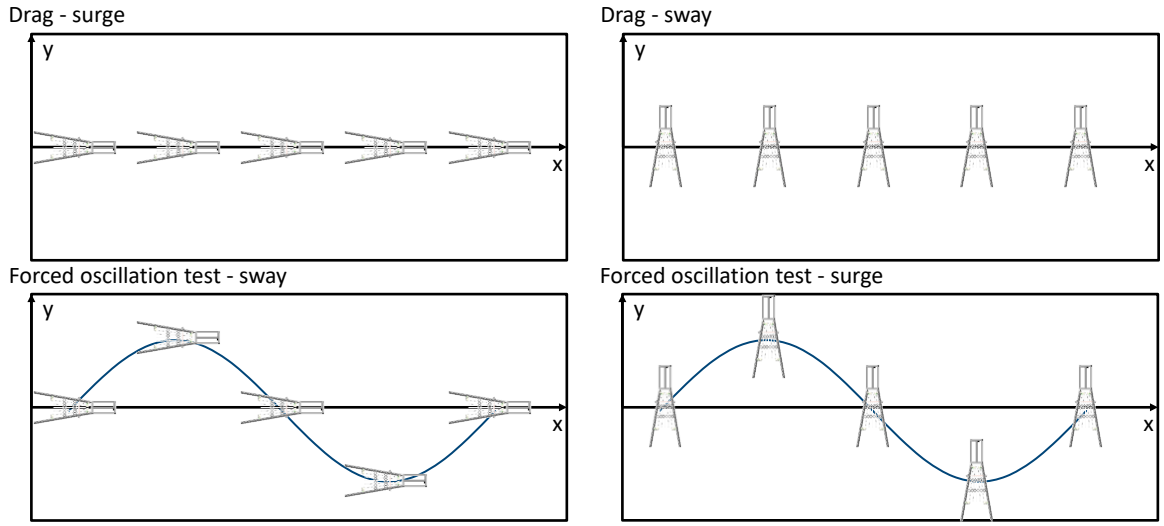


Figure 6-29: Investigated motion patterns

During the initial tests, imperfections in the model manufacture and assembly were observed. Due to clearance in the joints and limited fabrication accuracy, the struts of the model sagged downward. In addition, relative motion within the strut joints was detected, which led to changes in the opening angle and thus in the position of the struts relative to the LARD head during the experiments. To mitigate these effects, the geometry of the model was stabilised using additional wires. This reinforcement was introduced to better reproduce the behaviour of the full-scale device, in which the joints are significantly stiffer and do not permit such unintended motion. At the same time, the wires ensured that the experimental geometry, in particular the opening angle and alignment with respect to the inflow, matched the configuration used in the numerical simulations.
For the mounting arrangement of the LARD on the towing carriage, two configurations were used. One configuration enabled surge drag measurements and sway forced oscillation tests (see Figure 6-30), while the other configuration was applied for sway drag measurements and surge forced oscillation tests (see Figure 6-31). In the CAD representation, the LARD is shown in blue, the support structure including the force measuring unit on the towing carriage is coloured in green, the link between the support structure and the LARD model in grey and the reinforcing wires in yellow.

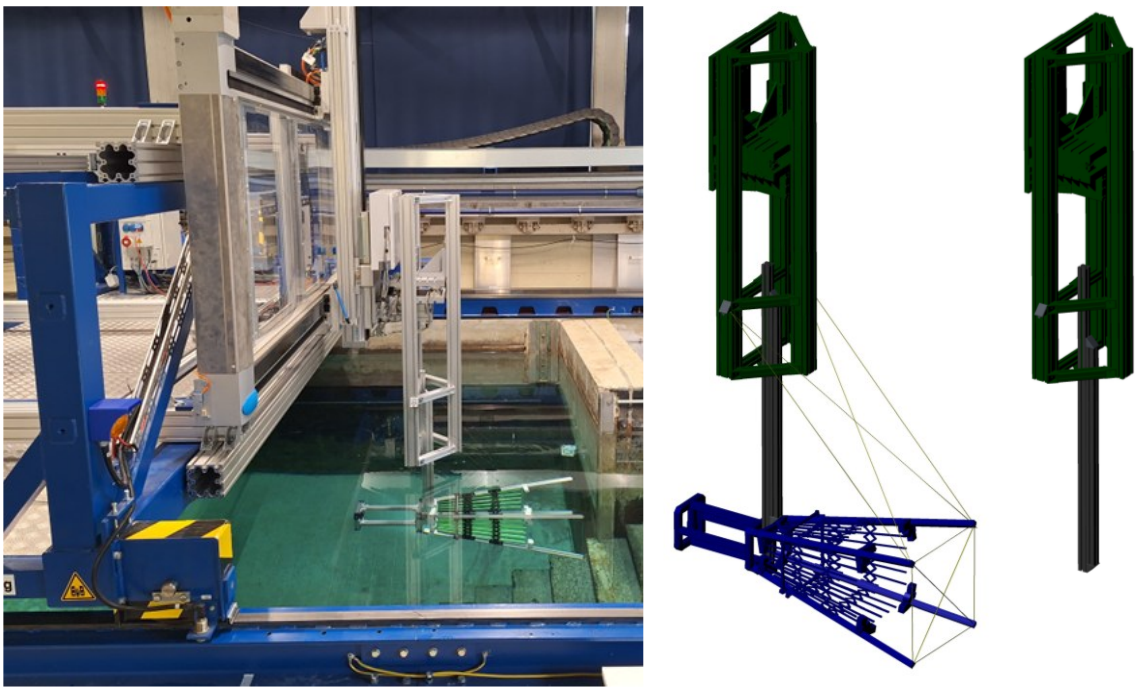


Figure 6-30: Towing carriage arrangement (surge drag and sway forced oscillation tests)
Left: picture of experimental setup; middle: CAD representation LARD mounting on the towing carriage; right: CAD representation baseline measurement configuration

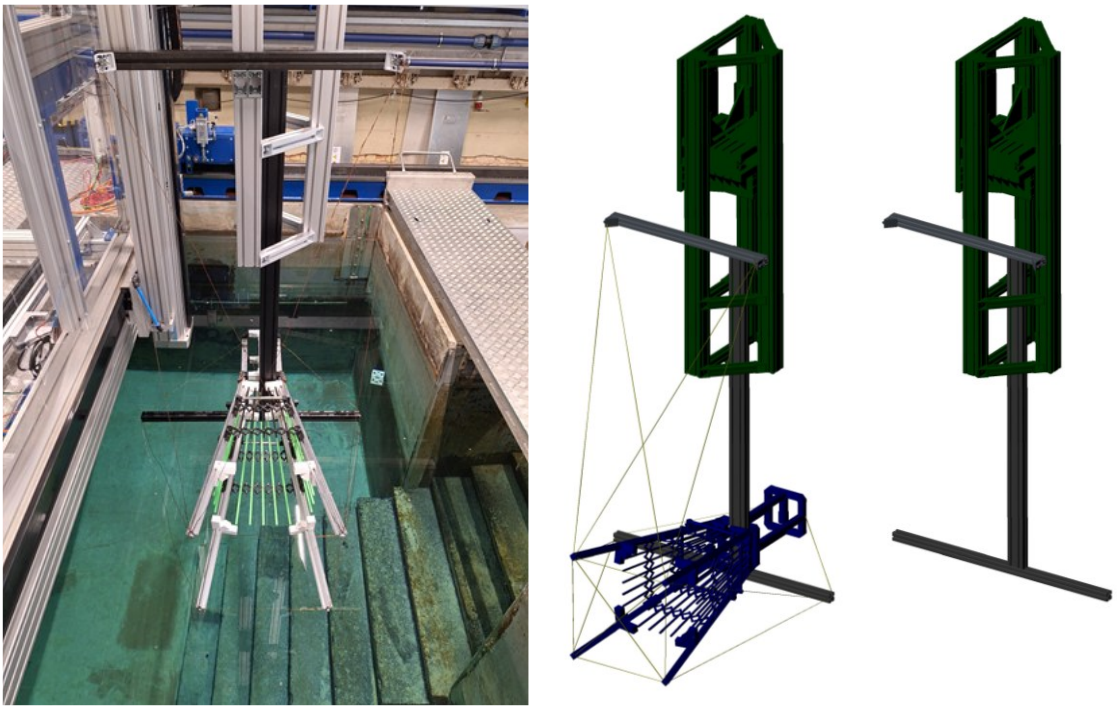


Figure 6-31: Towing carriage arrangement (sway drag and surge forced oscillation tests)
Left: picture of experimental setup; middle: CAD representation LARD mounting on the towing carriage; right: CAD representation baseline measurement configuration

To account for the hydrodynamic influence of the support structure, additional tests were conducted with the mounting alone (baseline measurements), without the model attached. These configurations are illustrated on the right-hand side of Figure 6-30 and Figure 6-31. The measured forces from these runs were subsequently subtracted from the forces obtained with the complete setup including the LARD. In this way, the resistance contribution of the support

structure could be removed, isolating the hydrodynamic loads acting on the model itself. This subtraction removes the stand-alone resistance of the support structure, but it does not fully eliminate interaction effects between the mounting and the LARD. The flow fields around both bodies mutually influence each other. The resulting "support-corrected" loads should be interpreted as an approximation rather than the exact loads. Specifically, the presence of the mounting alters the local approach flow and pressure field along the LARD, such that the flow that would develop without the support cannot be perfectly reconstructed by subtracting the baseline mounting-only measurements. This limitation is most pronounced in the vicinity of the attachment region, but it may also affect downstream portions of the LARD due to the upstream deflection and turbulence introduced by the support.

All experiments were conducted in freshwater with the model fully submerged. The water temperature was monitored periodically throughout the campaign and remained stable, with variations of less than 0.7 °C. The observed temperature variations remain within ITTC (International Towing Tank Conference) recommendations and induce only negligible changes in density and viscosity. The thermal conditions can therefore be considered effectively constant, supporting the repeatability and reliability of the measured hydrodynamic forces.

6.4.2 Drag coefficient

At the beginning of each test series, suitable maximum velocities and accelerations were determined based on preliminary observations and inspection of the measured force histories. Previously the immersion depth of the model was set once for all test runs. For all runs, the LARD's longitudinal centreline was positioned at an immersion depth of 1.05 m below the still-water level. This choice reflects a compromise between submerging the body as deeply as possible, in order to minimise any influence on the free surface and to treat the LARD as fully submerged and, on the other hand, limiting the submerged length of the vertical support strut to reduce its hydrodynamic resistance. In addition, the support structure, including the force-measuring unit on the towing carriage, was kept sufficiently far above the water surface to avoid wave interaction and splash-induced contact with the water. The vertical range of the carriage was also taken into account, as the LARD model needed to be lifted completely out of the water when returning from the end position to the start position.
To allow the flow in the tank to return to a comparable state between runs, a pause interval of 15 minutes was introduced between consecutive experiments. This waiting time ensured that residual waves and turbulence generated by the preceding run had largely decayed before the next run commenced, such that all tests were conducted under similar flow conditions. Only runs that were preceded by another run (15 minutes earlier) were considered in the analysis. The first tests of a given day, for which the water surface was particularly calm, were discarded in order to maintain consistent conditions and ensure comparability of the results.

The LARD was tested in surge and sway. Surge runs were conducted with the model aligned head-first with the towing direction, while sway runs were performed with the flow approaching from the port side. Owing to the symmetry of the geometry in the horizontal plane, the choice of port versus starboard inflow is not expected to affect the hydrodynamic response. In surge, the target towing speed of 3 m/s resulting from the Reynolds-scaling procedure could be achieved. In sway, however, it was not possible to reach the same 3 m/s without risking excessive deformation or damage to the model. During the experimental campaign, the sway speed was therefore increased stepwise and limited to values for which the structural integrity of the model and its support remained acceptable. To further stabilise the model, an additional

support structure (shown in Figure 6-31) was introduced. This structure consists of a longitudinal strut located below the model and aligned with the flow direction, from which additional wires are attached and tensioned to brace and stiffen the model.

Each towing tank run followed a standardised procedure. First, for setup and pre-zeroing, the model was submerged to the prescribed depth and held stationary. At least 15 s of data were recorded in this rest condition to verify signal stability and to determine the initial zero of the force dynamometer. The carriage then accelerated smoothly to the target speed in an acceleration zone. Once the target velocity was reached, the measurement phase began while the model remained at a fixed lateral position in drag tests. After the measurement phase, the carriage decelerated to rest, where the run ended. A further at-rest period of 15 s was recorded to confirm the post-run zero and to support offset and drift correction.

The post-processing of the force measurements comprised several steps. First, the dynamometer output, recorded as electric charge, was converted into mechanical forces. The sensor provides eight charge channels in picoCoulombs, with a predefined assignment of channels to force components. For each force direction, the relevant charge channels were summed and divided by the corresponding calibration sensitivity supplied by the manufacturer, yielding forces in newtons.
Second, the converted force signals were filtered using a low-pass Butterworth filter to suppress high-frequency noise while preserving the slowly varying, physically meaningful dynamics. A third-order Butterworth design was adopted because of its maximally flat passband. When applied in a zero-phase manner, the effective magnitude response is equivalent to that of a sixth-order filter, providing a steep attenuation of approximately 120 dB per decade above the chosen cut-off frequency without introducing phase distortion into the force time series.
Third, the start and end of each towing run were detected from a reference signal using the absolute time gradient and a peak-picking procedure. Computing the gradient emphasises the rapid transitions at the beginning and end of the run and suppresses constant offsets and slow drift. Peaks in the gradient were identified subject to constraints on width, distance and height to ensure robust detection in the presence of noise and small fluctuations. The first detected peak was interpreted as the start transition and the second as the stop transition, providing anchor indices from which all relevant analysis windows, including the steady measurement window, were defined.
Fourth, offset and drift correction were applied. The raw sensor output can exhibit a constant bias (offset) and a slow time-dependent drift arising from temperature effects or mechanical creep. If uncorrected, these effects can shift the apparent force level and introduce artificial trends. To estimate and remove both contributions, the at-rest segments recorded before and after each run were used to fit a linear trend, which was then subtracted from the entire signal. In this way, the corrected force time series is referenced to a consistent zero level over the full duration of the run.
Fifth, the drag force was extracted from the force component aligned with the flow. The mean value was calculated for each measuring window.

For each operating condition, at least three nominally identical runs were carried out consecutively. For every run, the force time series was processed using the workflow described above, including offset and drift correction, transient removal and identification of a steady measurement window. The per-run value used in the subsequent analysis corresponds to the mean of the signal over this steady window. Since the three runs for a given condition were processed identically and exhibited similar steady-window lengths, the reported value for that

condition is the simple arithmetic mean of the three per-run results. This approach is consistent with the ITTC Recommended Procedures, which state that, when repeat tests are available, the mean of multiple runs should be adopted as the best estimate of the measured quantity [194]. In the present study, the at least three per-run means were mutually consistent, showed no systematic trend with run order and fell within a narrow range, confirming satisfactory repeatability of the towing tank measurements (see Figure 6-33 and Table 6-13).

Finally, baseline measurements were performed to quantify the contribution of the test rig to the recorded forces. In towing, the rig itself generates drag. If this contribution is not measured and removed, the derived LARD drag coefficients are biased. The baseline was obtained by repeating the same test protocol as in the full system measurements, but with the LARD model removed. The holder construction, long support profile, towing speeds and immersion depths were kept identical to the main tests. A first-order correction for drag was then computed by subtracting the baseline force from the total measured force to compute the LARD force.

A representative time history for a surge drag run at 3 m/s, processed and filtered with a 5 Hz low-pass Butterworth filter, is shown in Figure 6-32. The middle plateau corresponds to the measurement window from which the final drag value is derived. Figure 6-33 illustrates the steady measurement window for the four surge drag runs conducted for the LARD including the baseline at 3 m/s, after applying a 5 Hz low-pass Butterworth filter. The time histories show very similar trends, with a characteristic force peak at the beginning of the window followed by a force signal fluctuating around the same mean level. The small deviations between the individual runs are visible but remain limited, underscoring the good repeatability of the measurements within this operating condition.

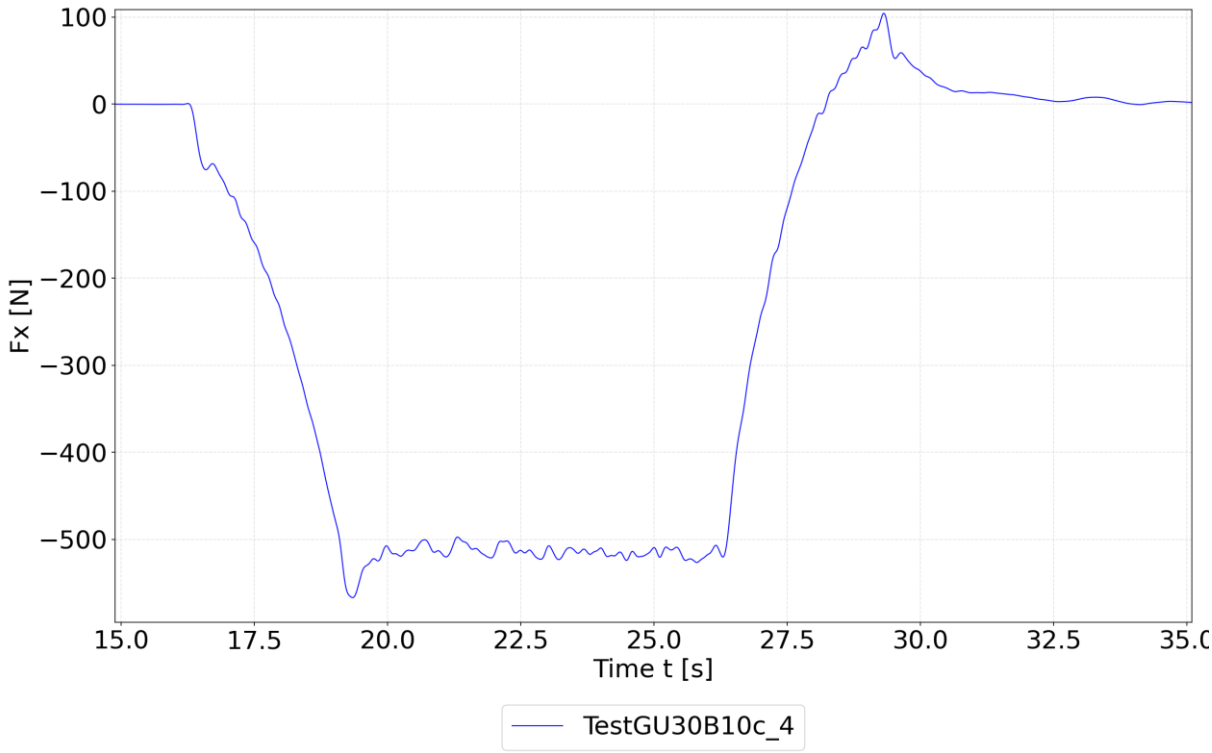


Figure 6-32: Force history Fx for surge drag run at 3 m/s
(filtered with a 5 Hz low-pass Butterworth filter)

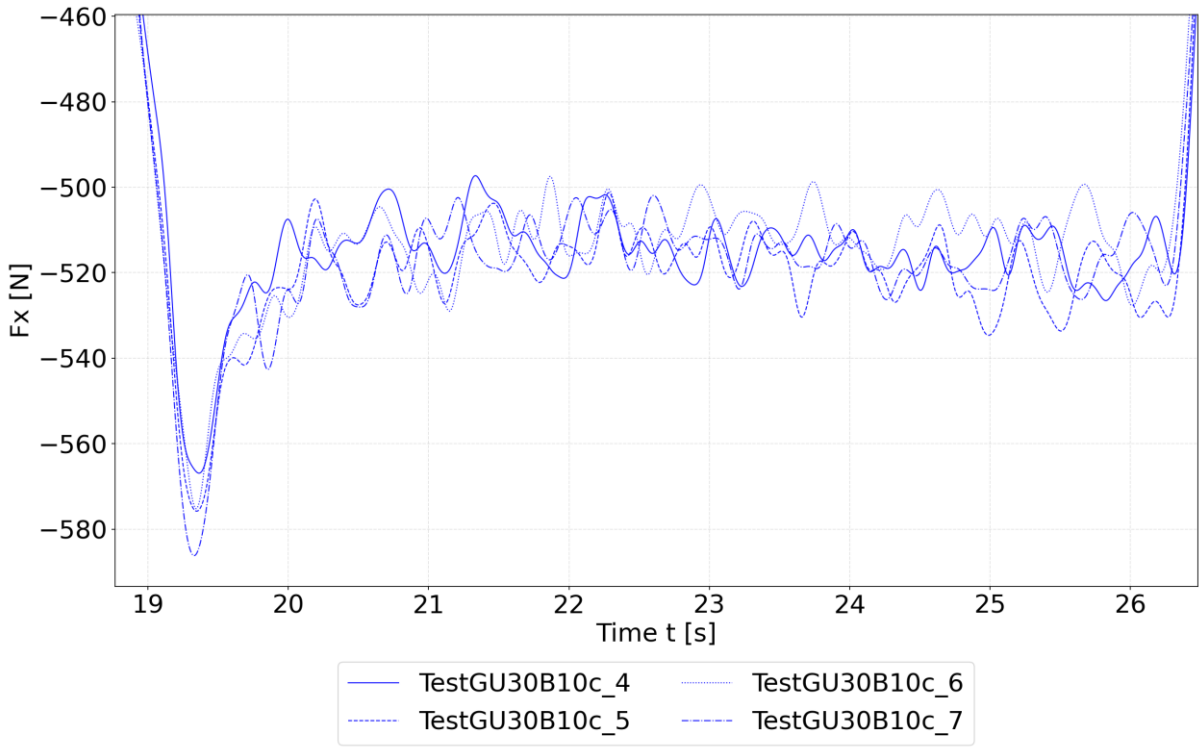


Figure 6-33: Comparison of force histories Fx for surge drag runs at 3 m/s
(filtered with a 5 Hz low-pass Butterworth filter)

The results of the individual towing runs are summarised in Table 6-13, grouped by DoF and experimental setup. For each run, the table reports the internal run ID and the mean force component in the streamwise direction, evaluated over the selected steady measurement window. For a given setup and degree of freedom, the mean force over all corresponding test runs is then listed, together with the deviation of each per-run mean from this setup-mean value. This representation provides a compact overview of both the central tendency and the scatter of the measured forces and thus of the repeatability of the experiments.

Table 6-13: Drag run results

DoF	Setup	Run ID	Mean force per run [N]	Mean force per setup [N]	Deviation to mean setup [%]
Surge	Full system	TestGU30B10c_4	513.33	513.97	0.12
		TestGU30B10c_5	517.70		-0.73
		TestGU30B10c_6	510.49		0.68
		TestGU30B10c_7	514.34		-0.07
	Baseline	BLGU30B10c_20	89.86	89.98	0.14
		BLGU30B10c_21	89.89		0.10
		BLGU30B10c_22	89.74		0.27
		BLGU30B10c_23	90.44		-0.51
Sway	Full system	TestU10B10c_11	166.40	166.67	0.16
		TestU10B10c_12	167.12		-0.27
		TestU10B10c_13	166.48		0.11
	Baseline	BLGU10B10c_41	17.12	16.64	-2.92
		BLGU10B10c_42	16.37		1.59
		BLGU10B10c_43	16.50		0.81
		BLGU10B10c_45	16.55		0.51

On this basis, Table 6-14 presents the resulting drag forces attributed to the LARD, obtained after subtraction of the baseline measurements, along with the corresponding drag coefficients.

Table 6-14: Experimental drag coefficients

DoF	Velocity [m/s]	Force [N]	$C_{D_i}^t$ [-]
Surge	3.00	423.98	0.7910
Sway	1.00	150.03	2.0153

The quality of the drag measurements is evaluated using the root-mean-square error (RMSE) of the drag coefficient within the selected steady measurement window. For surge, the RMSE is 0.07, indicating only minor scatter in the measured force signal and resulting in comparatively tight bounds of the inferred drag coefficient (approximately 0.72 to 0.86). In contrast, the RMSE for sway is 0.72 (36 % of the mean drag coefficient), which reflects a substantially larger variability of the measurements and thus a greater uncertainty in the corresponding drag coefficient.

In addition to the datasets included in Table 6-13 and Table 6-14, further sway measurements are available at a towing speed of 2 m/s. For these runs, which form an incomplete dataset, a drag coefficient of 1.98 would be obtained, with a substantially lower root-mean-square error of 0.17 compared with the sway results for 1 m/s. Although these measurements support the drag coefficient reported for sway in Table 6-14, they are not used in the final evaluation because not all quality criteria were met, in particular the requirement of three successful repeat runs for each operating condition.

6.4.3 Damping & hydrodynamic mass coefficient

The forced oscillation tests were conducted using the experimental setup described in Section 6.4.1. The corresponding test matrices are summarised in Table 6-15 for surge and in Table 6-16 for sway. For each case, the LARD was towed at a constant forward velocity while undergoing a prescribed lateral oscillation. The table lists oscillation frequency (f) and the non-dimensional frequency parameter $\frac{\omega^2 d}{g}$, where ω is the angular oscillation frequency, d is the characteristic length of the LARD and g is the gravitational acceleration. Followed by the amplitude ($\hat{A}$) and the Keulegan–Carpenter number (KC) as the product of the oscillating amplitude multiplied by 2π and divided by the object's characteristic length. The tables further contain the maximum lateral velocity (max u_y), the resulting total maximum velocity magnitude (max $|u|$) and the maximum lateral acceleration (max $\dot{u}_y$).

Table 6-15: Forced oscillation test matrix - surge (u_x = 1 m/s)

f [1/s]	$\frac{\omega^2 d}{g}$	$\hat{A}$ [m]	KC	max u_y [m/s]	max $\|u\|$ [m/s]	max $\dot{u}_y$ [m/s²]
0.133	0.036	0.5	6.28	0.419	1.084	1.084
		0.3	3.77	0.251	1.031	0.251
0.266	0.143	0.1	1.26	0.168	1.014	0.422
0.399	0.321			0.251	1.031	1.205

Table 6-16: Forced oscillation test matrix - sway (u_x = 3 m/s)

f [1/s]	$\frac{\omega^2 d}{g}$	$\hat{A}$ [m]	KC	max u_y [m/s]	max $\lvert u \rvert$ [m/s]	max $\dot{u}_y$ [m/s²]
0.396	0.316	0.5	6.28	1.257	3.253	3.158
		0.3	3.77	0.754	3.093	1.895
		0.1	1.26	0.251	3.010	0.632
0.597	0.718			0.377	3.024	1.421
0.799	1.286			0.503	3.042	2.526
1.000	2.014			0.628	3.065	3.948

The same combinations of dimensional and non-dimensional parameters were realised both for the full system (rig plus LARD model) and for the corresponding baseline rig without the LARD, enabling the isolation of the hydrodynamic added mass and damping associated with the LARD.

To aid the interpretation of the forced oscillation tests, representative motion trajectories are shown for the sway test series at a constant forward velocity of 3 m/s. Figure 6-34 illustrates the trajectory for an oscillation amplitude of 0.1 m over ten periods, corresponding to an excitation frequency of 1 Hz. Figure 6-35 presents the trajectory for a oscillation amplitude of 0.5 m over four periods, corresponding to an excitation frequency of 0.396 Hz.
In the motion plots, the prescribed trajectory y(x) of the model is shown as a solid black line. The individual velocity components Ux(x) and Uy(x) are plotted in green, while the total velocity magnitude U(x) is shown in blue, all as functions of the travelled distance along the tank.
The different phases of each run are indicated by vertical dashed lines. The first dashed line marks the start position, followed by the acceleration phase. Once the target speed is reached, a second dashed line denotes the beginning of the constant-velocity segment. A third dashed line marks the end of this steady-velocity phase and the onset of deceleration and the final dashed line indicates the end of the run. In addition, the axis around which oscillation occurs is shown as a horizontal dashed line and the physical boundaries of the towing tank are represented by horizontal straight lines.

The post-processing of the forced oscillation data follows the same initial steps as for the drag measurements in Section 6.4.2. First, the dynamometer output is converted from electric charge to forces in newtons by summing the relevant charge channels and dividing by the manufacturer's calibration sensitivities. Second, a low-pass Butterworth filter is applied to suppress high-frequency noise while preserving the physically relevant force dynamics. Third, the start and end of each towing run are detected automatically from a reference signal and a steady measurement window is defined within the constant-speed segment. Fourth, offset and drift are removed by fitting a linear trend to the at-rest segments before and after each run and subtracting this trend from the entire time series.

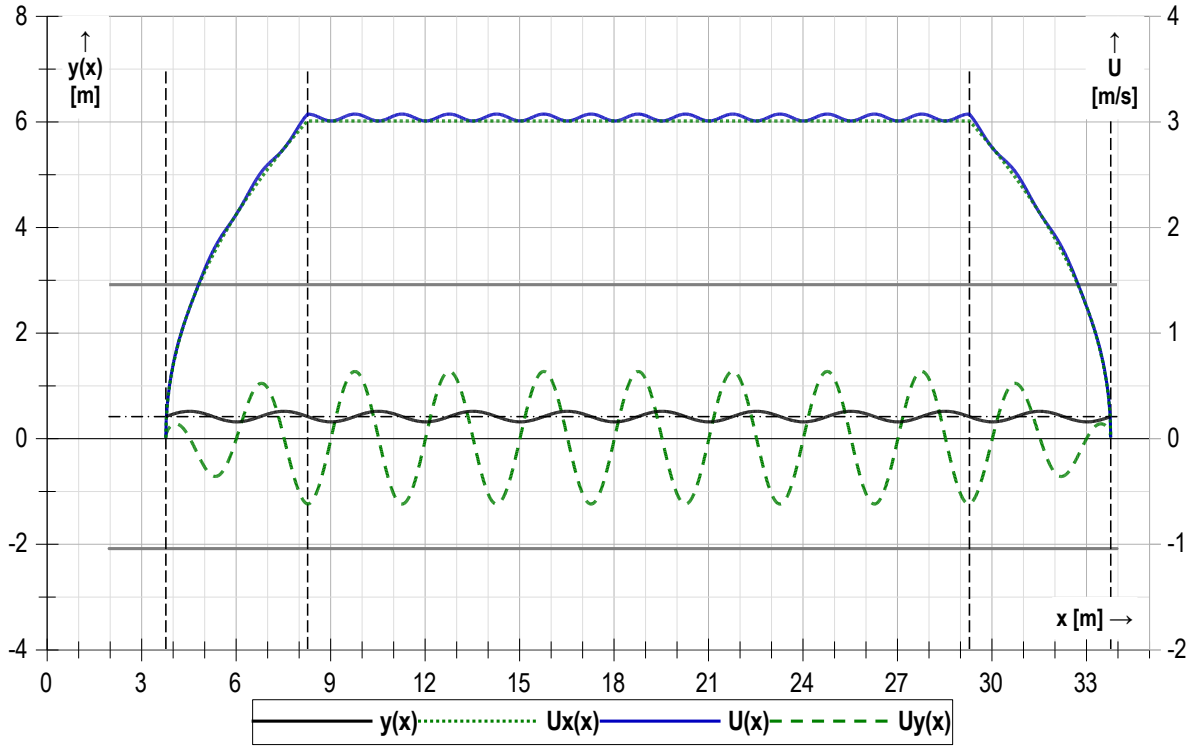


Figure 6-34: Motion trajectory – sway forced oscillation test (f=1 Hz; $\hat{A}$=0.1 m)
(Figure provided by Chair of Fluid Mechanics at the University of Rostock)

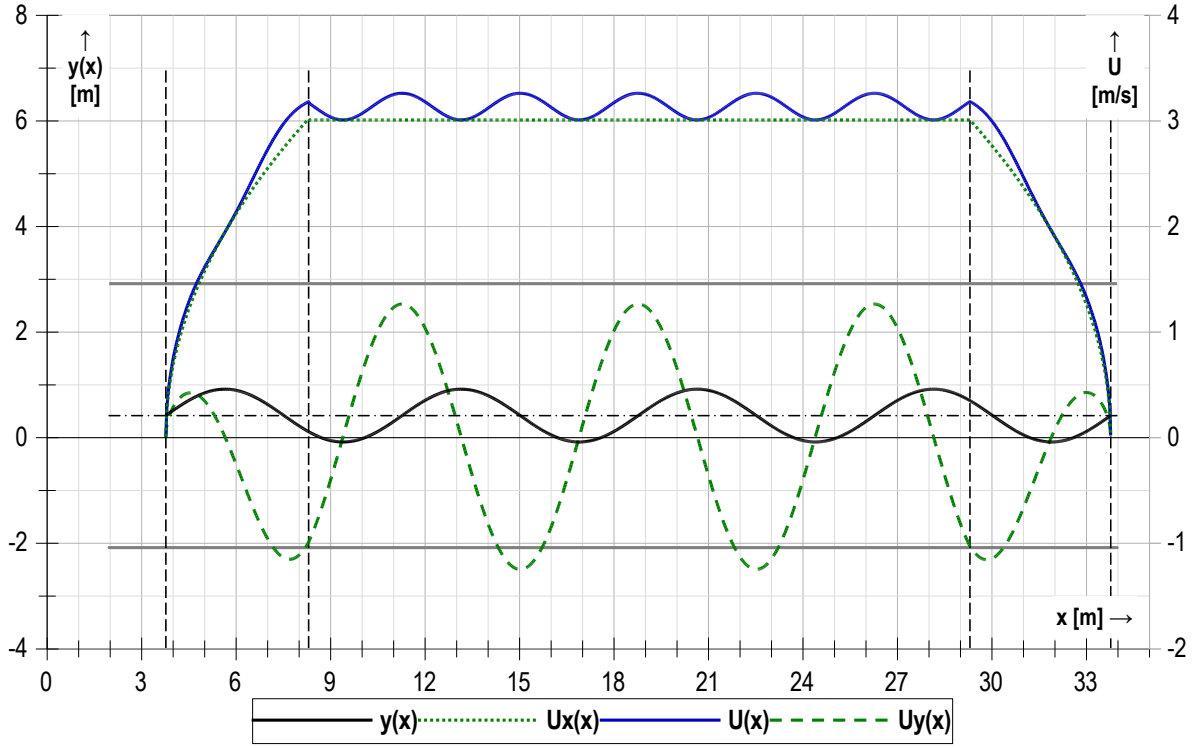


Figure 6-35: Motion trajectory – sway forced oscillation test (f=0.39 Hz; $\hat{A}$=0.5 m)
(Figure provided by Chair of Fluid Mechanics at the University of Rostock)

Beyond these steps, the key element of the forced oscillation analysis is the extraction of the force content at the excitation frequency using the Fast Fourier Transform (FFT). To prevent the zero-frequency component from dominating the spectrum, the mean of this segment is

subtracted prior to the FFT, solely for the purpose of peak detection. A discrete Fourier transform is then computed and only the positive-frequency part of the spectrum is considered. The dominant peak on this positive side is interpreted as the excitation (fundamental) frequency, providing a data-driven estimate that can be compared to the commanded frequency from the motion control.

Once the excitation frequency has been identified, the complex FFT coefficient at the nearest frequency bin is used to extract the force content at that frequency. Under the sign convention adopted in the processing code, the real part of this complex coefficient corresponds to the component in phase with the velocity and is associated with damping, whereas the negative imaginary part corresponds to the component in phase with the acceleration and is associated with inertia. The FFT coefficient is rescaled so that these two components directly represent the amplitudes of the cosine and sine contributions at the fundamental frequency. The result for each run is therefore two scalar quantities: a damping-related force amplitude $F_{damping}$ and an inertia-related force amplitude $F_{inertial}$. These spectral force amplitudes are converted into physical parameters using the known motion kinematics. Let f_0 denote the detected excitation frequency, $\omega = 2\pi f_0$ the corresponding angular frequency and $\hat{A}$ the commanded displacement amplitude. The total effective mass participating in the motion is obtained by normalising the inertia-related force with the peak acceleration amplitude:

$$m_{total} = \frac{F_{inertial}}{\omega^2 \hat{A}} \tag{6.22}$$

m_{total} represents the inertia observed in the force response and includes both the dry mass (m_{dry}) and the added mass (m_a), which is therefore computed as:

$$m_a = m_{total} - m_{dry} \tag{6.23}$$

Similarly, the linear damping coefficient ($C_{B_i}^t$) is obtained by normalising the damping-related force with the peak velocity amplitude:

$$C_{B_i}^t = \frac{F_{damping}}{\omega \hat{A}} \tag{6.24}$$

All quantities are evaluated on the steady, offset- and drift-corrected force segment to avoid bias from shifts, drift or transient behaviour. m_a and B are calculated separately for each run and then summarised as mean values.

The choice of the low-pass cut-off frequency is closely tied to the FFT-based estimation. The filter is not intended to modify the signal at f_0 but only to suppress unrelated high-frequency content so that peak detection and coefficient extraction at f_0 remain robust. For each run, low-pass cut-off frequency was therefore selected comfortably above f_0 to ensure a flat passband around $f_0$while reducing higher-frequency clutter. After setting the cut-off frequency, the amplitude of the Fourier coefficient at f_0 was compared before and after filtering. If any attenuation was detected, the cut-off frequency was increased and the check repeated until the coefficient at f_0 was effectively unchanged by setting the filter.

Figure 6-36 illustrates the repeatability of the sway forced oscillation tests using the example of three runs with an amplitude of 0.1 m and 10 periods, corresponding to an excitation frequency of 1.0 Hz. After the post-processing steps described previously, the three measured force signals lie almost on top of each other. Only small deviations are visible, mainly in the

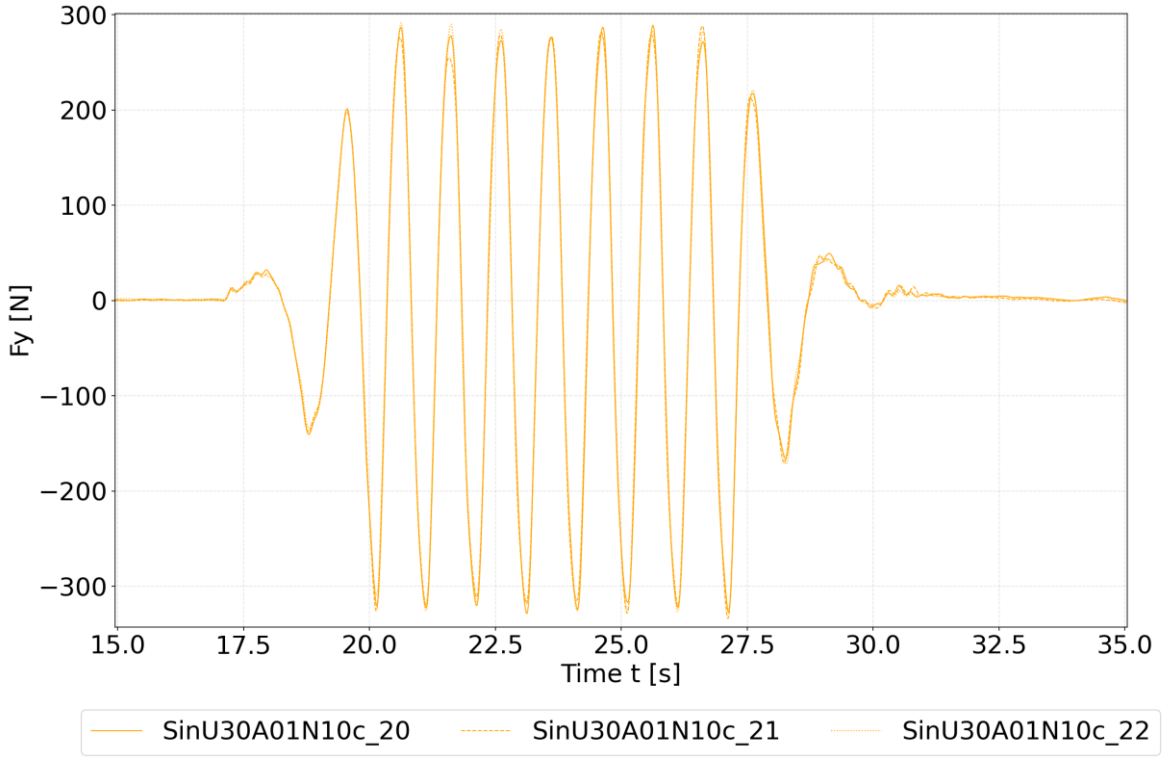


Figure 6-36: Comparison of force histories Fy for sway forced oscillation tests amplitude of 0.1 m and excitation frequency of 1.0 Hz

peak values of the force extrema, while the overall waveform and mean levels are nearly identical. This high level of agreement confirms the good repeatability of the experiments. For reasons of clarity, only one representative run is therefore shown in the subsequent plots for each parameter combination, even though three or more runs were recorded and processed in each case.

The naming convention used in the forced oscillation test series follows a consistent pattern. The prefix “Sin” identifies a sinusoidal motion; “U” denotes the forward velocity, which is 3 m/s for all sway tests presented here; “A” indicates the oscillation amplitude, for example “A01” for an amplitude of 0.1 m, “A03” for 0.3 m and “A05” for 0.5 m. The number of oscillation periods is encoded via an integer parameter “N”, which also determines the excitation frequency. 4 periods (“N04”) corresponds to 0.396 Hz, “N06” to 0.597 Hz, “N08” to 0.799 Hz and “N10” to 1.000 Hz. The trailing “c” can be ignored and the final index after an underscore is simply a running counter that uniquely identifies the individual run.

Figure 6-37 illustrates the measured sway force time histories for forced oscillation tests with four periods at a frequency of 0.396 Hz, but with different amplitudes of 0.1 m, 0.3 m and 0.5 m. The data clearly demonstrate that increasing the oscillation amplitude leads to a corresponding increase in the lateral force amplitude, as expected from the predominantly linear relationship between displacement and restoring hydrodynamic forces.

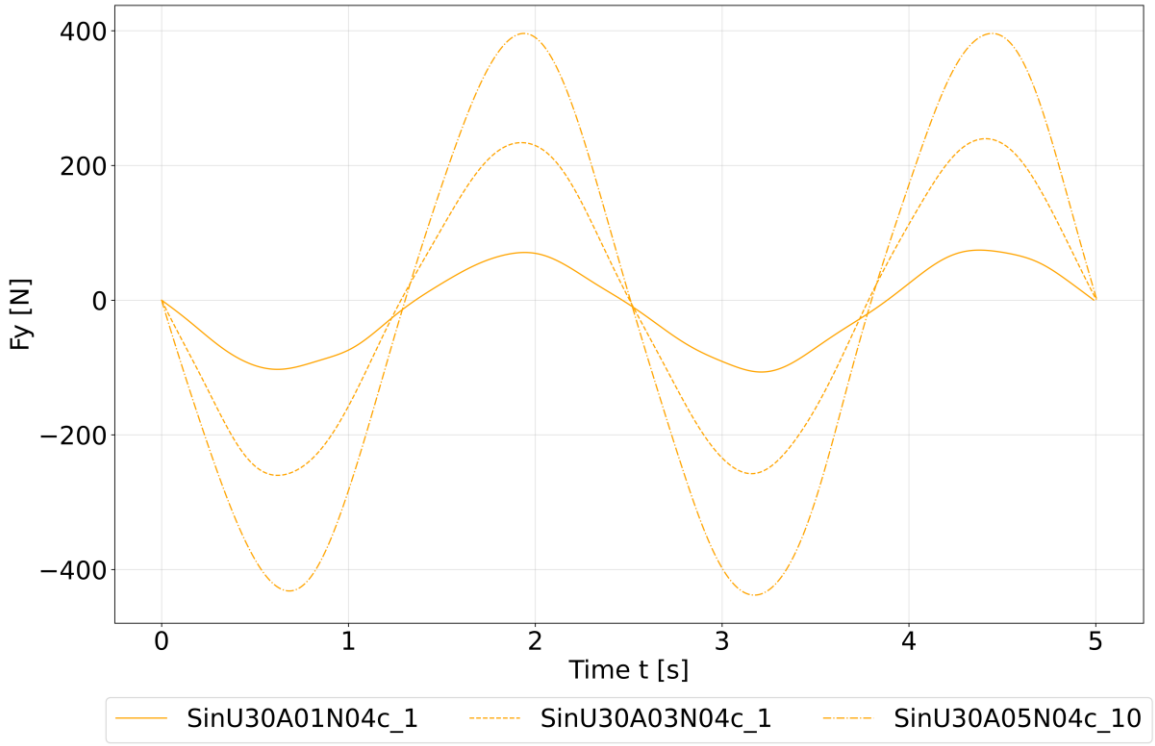


Figure 6-37: Sway forced oscillation tests with different amplitudes

Figure 6-38 shows processed sway force signals for a constant amplitude of 0.1 m, but for different numbers of oscillation periods, which correspond to excitation frequencies of 0.396 Hz, 0.597 Hz, 0.799 Hz and 1.0 Hz, respectively. These results highlight the influence of oscillation frequency on the force response at fixed amplitude.

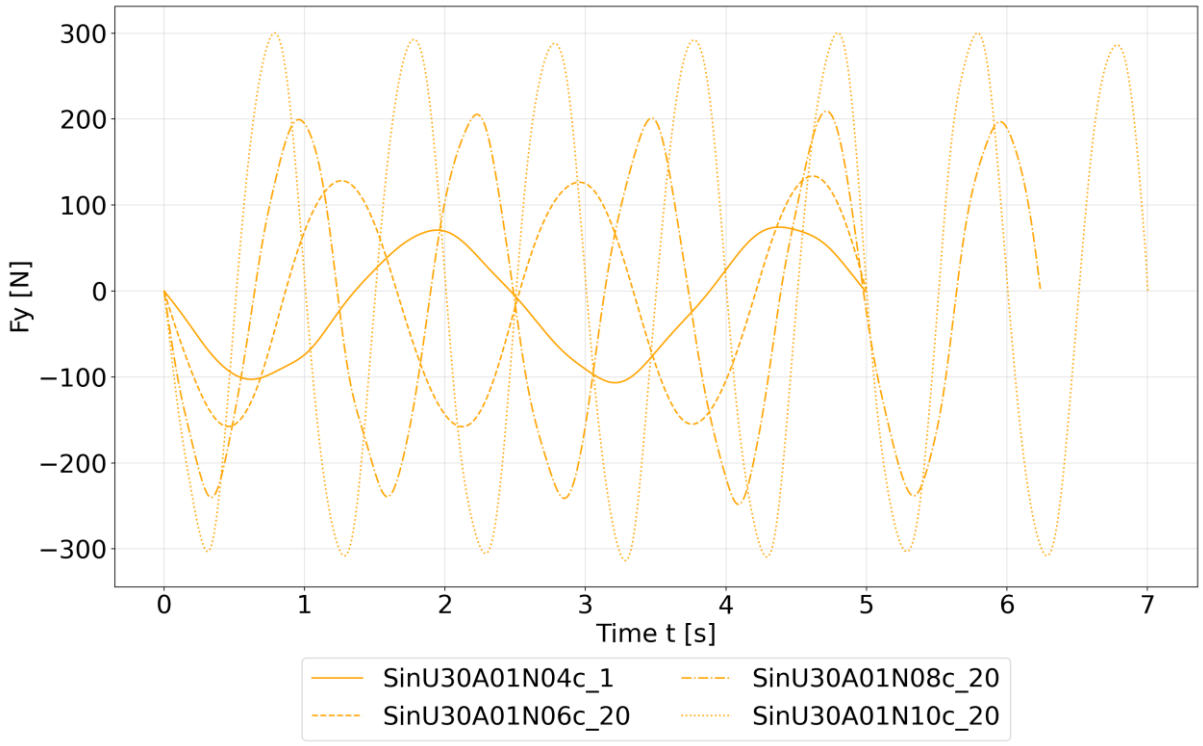


Figure 6-38: Sway forced oscillation tests with different excitation frequencies

As in the drag measurements, baseline corrections are required to remove the hydrodynamic contributions of the rig itself. The baseline is obtained by repeating the identical test protocol with the LARD removed, using the same speeds, immersion depths, amplitudes and frequencies as in the primary measurements. For forced oscillation tests, it is convenient to apply the baseline correction at the level of the hydrodynamic coefficients. First, the time signal of the full system (LARD + rig) is transformed using the FFT and the complex force amplitude at the excitation frequency is converted into an apparent added mass and damping coefficients. The same procedure is applied to the baseline force signal. The net LARD coefficients are then obtained by subtracting the coefficients of the baseline from the coefficients of the full system.

The hydrodynamic coefficients of the LARD model over the investigated range of motion amplitudes and excitation frequencies are summarised in Table 6-17 (surge) and Table 6-18 (sway). To enable a consistent comparison of the damping behaviour with the full-scale configuration, the translational damping coefficient $C_{B_i}^t$ is used. This coefficient is defined as the unit damping force normalised by the product of fluid density, reference area and angular frequency.

Table 6-17: Experimental hydrodynamic damping and added mass - surge

f [1/s]	$\boldsymbol{\frac{\omega^2 d}{g}}$	$\boldsymbol{\hat{A}}$ **[m]**	**KC**	$\boldsymbol{C_{B_x}^t}$ **[-]**	$\boldsymbol{C_{a_x}^t}$ **[-]**
0.133	0.036	0.5	6.28	0.0575	12.1315
		0.3	3.77	0.0020	7.4530
0.266	0.143	0.1	1.26	0.6967	2.3105
0.399	0.321			0.2205	3.6362

Table 6-18: Experimental hydrodynamic damping and added mass - sway

f [1/s]	$\boldsymbol{\frac{\omega^2 d}{g}}$	$\boldsymbol{\hat{A}}$ **[m]**	**KC**	$\boldsymbol{C_{B_y}^t}$ **[-]**	$\boldsymbol{C_{a_y}^t}$ **[-]**
0.396	0.316	0.5	6.28	0.8427	12.4319
		0.3	3.77	0.3287	13.9420
		0.1	1.26	2.1619	15.6094
0.597	0.718			0.7842	8.9572
0.799	1.286			0.0842	5.7593
1.000	2.014			0.1759	4.2631

6.4.4 Comparison of Numerical and Experimental Results

This section compares and discusses the differences between the hydrodynamic coefficients obtained from numerical simulations and those derived from the towing tank experiments. The discussion first addresses the drag coefficients and subsequently considers damping and added mass.

The drag coefficients for surge and sway from CFD and from the experiments are summarised in Table 6-19. The experimental drag exceeds the numerical prediction, with deviations of approximately 18 % in surge and 23 % in sway. For the sway direction, it must be noted that because of the structural deformations and potential damage to the model at higher lateral speeds, multiple sway tests could only be carried out up to a maximum towing velocity of 1 m/s ($Re = 1.43 * 10^6$), whereas strict Reynolds similarity with the CFD setup would require a

speed of 3 m/s ($Re = 4.29 * 10^6$). These Reynolds numbers lie well above the typical laminar and transitional regimes for external flows around bodies. The boundary layer is therefore expected to be predominantly turbulent over most of the wetted surface, with any laminar regions (if present) confined to a limited upstream portion depending on local geometry and pressure gradients. Accordingly, the drag behaviour discussed above is interpreted within a turbulent-flow framework and the remaining Reynolds-number sensitivity is expected to be comparatively weak over the investigated range. A supplementary CFD simulation at reduced inflow velocity was therefore conducted to enforce Reynolds similarity with the 1 m/s model tests ($Re = 1.43 * 10^6$). Under these Reynolds number matching conditions, the remaining deviation between CFD and experiment $C_{D_y}^t$ is about 14 %.

Additional drag model tests were performed at different velocities to examine the speed dependence of the drag coefficient. In surge, the drag coefficient at 2.3 m/s is about 1.9 % higher than at 3 m/s. In sway, the drag coefficient at 1 m/s is approximately 1.4 % higher than a single test run at 2 m/s ($Re = 2.86 * 10^6$). Extrapolating this trend suggests that the sway drag coefficient at 3 m/s would be slightly lower than the value measured at 2 m/s, which would in turn reduce the discrepancy between the CFD and experimental results.

Table 6-19: Drag coefficients – comparison of simulation vs experimental

DoF	**$C_{D_i}^t$ CFD Simulation [-]**	**$C_{D_i}^t$ Experiment [-]**	**Deviation [%]**
Surge	0.6461	0.7910	18.32
Sway	1.5426	2.0153	23.46

Several factors contribute to the observed differences, which generally show a higher experimental value compared to the numerical results. On the CFD side, the deviation is primarily attributed to the simplified geometry used for the simulations (see Figure 6-39). The numerical model retains the main outer surfaces, global edges and overall shape of the LARD, but small-scale details such as fasteners, internal cavities, grooves and sharp corners were either removed or smoothed to obtain a mesh of manageable complexity and to improve numerical stability. These small features, which are present on the physical model, increase form drag in the experiments but are largely absent from the CFD geometry, so that the simulated drag is biased towards lower values. In addition, mesh-sensitivity studies showed that finer grids with a higher cell count produce slightly higher drag forces. The simulations therefore likely still underestimate the true drag to some degree.

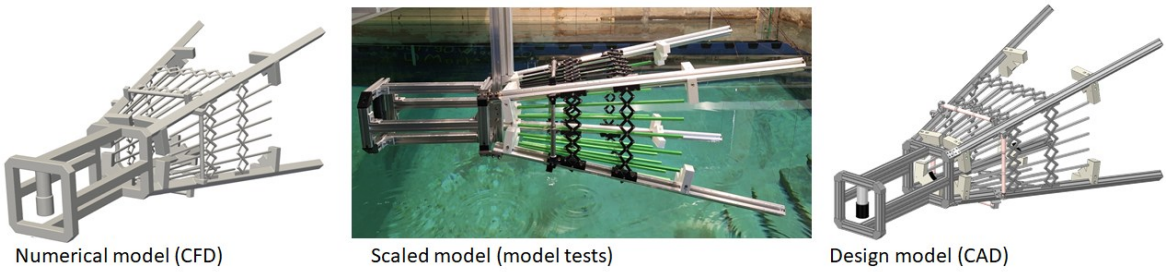


Figure 6-39: Model geometry comparison

On the experimental side, several effects tend to increase the measured drag relative to the numerical prediction. First, model manufacturing tolerances and the selection of individual

components introduce small deviations from the nominal geometry, for example in surface smoothness, alignment and sharpness of edges. Second, slight motion of the model and support structure during the runs can lead to misalignment and imperfect levelling, causing minor yaw or pitch angles that increase the projected area and hence the measured resistance.

The impact of structural deformation on the drag measurements is particularly evident in the sway drag tests. As shown in the left side of Figure 6-40, before adding the additional support structure the model exhibits pronounced twisting even at a velocity of 1 m/s. This deformation significantly alters the effective orientation of the LARD relative to the incoming flow and therefore affects the measured resistance. After introducing the supplementary support structure, this behaviour was substantially reduced. A comparison with the right side of Figure 6-40 shows that less noticeable twisting of the model now occurs only at a higher inflow velocity of approximately 2 m/s. Nevertheless, small residual motions of the model are still expected even at lower velocities and these must be considered as a further source of uncertainty in the interpretation of the sway drag results.

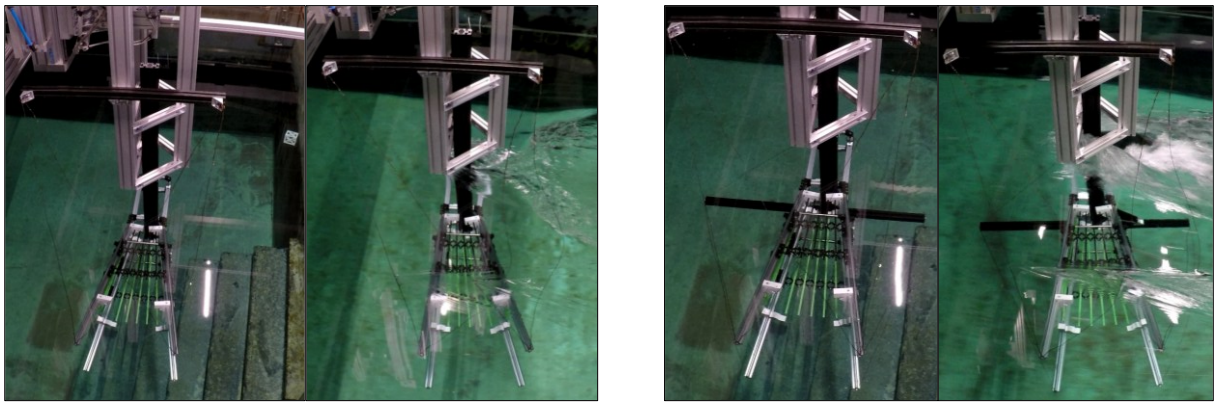


Figure 6-40: Twisting of the model during sway drag tests

Third, support interference plays a significant role. The LARD is mounted on a holder and stabilised by additional struts and wires, which inevitably affect the surrounding flow. Although baseline measurements were performed and subtracted to remove the drag of the support structure, this procedure remains an approximation. In particular, the wires used for model stabilisation could not be mounted in a physically meaningful way without the LARD, so their hydrodynamic influence cannot be fully captured by the baseline. Furthermore, depending on the DoF the baseline drag constitutes a considerable fraction of the full system measurement leading to a relative contribution of the LARD. In this context, the root-mean-square errors and uncertainty intervals reported in Section 6.4.2 must be taken into account.
Additional uncertainty arises from free-surface effects. Although the LARD model was submerged at a depth chosen to minimise interaction with the free surface, some influence cannot be completely excluded. Javanmard and Mansoorzadeh [195] have shown for AUV models that the proximity of the free surface can alter the measured drag coefficient compared with fully deep-water conditions, which provides further indication that residual free-surface effects may contribute to the observed differences. In particular, when a body is towed sufficiently close to the free surface, part of the energy is converted into surface-wave energy (wave-making resistance), which adds to the viscous and pressure components of drag and can therefore increase the inferred drag coefficient compared with an equivalent deep-water case.

Moreover, the presence of the free surface modifies the pressure field and streamline curvature around the body; this changes the local acceleration of the surrounding water and can alter separation and wake development, leading to a different pressure-drag contribution than in an unbounded single-phase flow. Javanmard and Mansoorzadeh explicitly highlight that towing near the free surface can create a wave system and introduce an additional resistance component whose magnitude depends on the resulting wave profile. Consequently, the measured drag and thus the drag coefficient may exceed the corresponding deep-water value even when the model remains nominally “submerged”. [195]

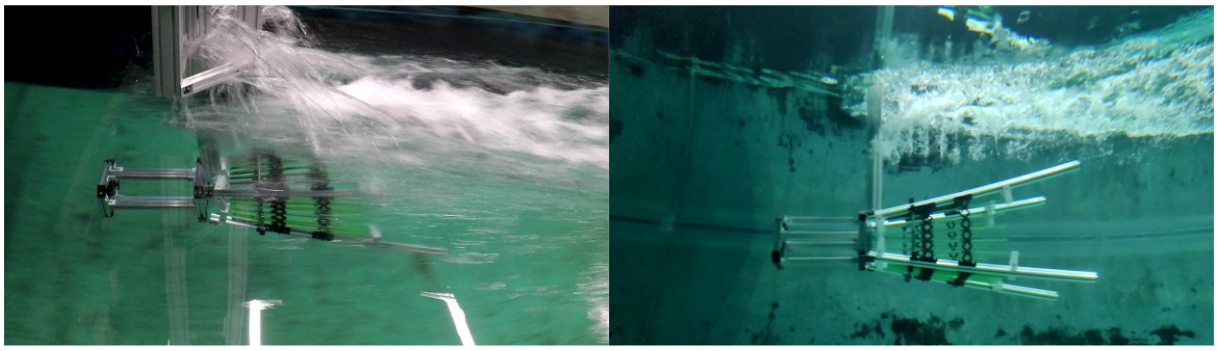


Figure 6-41: Surge drag (3 m/s) experiment run
Left: view from above; right: underwater view

For the drag in sway direction and with respect to Reynolds-number effects, the CFD case corresponds to a higher Re than the sway experiments. The drag of bluff bodies in the post-critical regime, may even increase with Re over parts of this range. Accordingly, the Reynolds-number mismatch is unlikely to be the primary driver of the observed underprediction by CFD. At most, it would be expected to introduce a secondary correction compared with the combined modelling and measurement uncertainties discussed above.

Taken together, there are therefore plausible reasons why the CFD drag tends to be slightly too low, while the experimental drag is likely somewhat too high. The total deviation of 18 % in surge and 23 % in sway can reasonably be interpreted as the combined effect of several smaller modelling and measurement errors on both sides. This interpretation is supported by a validation study using a simpler reference geometry. The same experimental procedures were applied to a circular cylinder with end plates, for which an analytical solution for the drag coefficient is available. In that study, the experimentally derived drag coefficient differed from the analytical value by about 7 %. In this validation setup, no external support structure was required and hence no baseline (“mounting-only”) measurements had to be subtracted. Therefore, the cylinder tests are not subject to mounting–model interaction effects and avoid the uncertainty arising from baseline subtraction. This underlines that even for a simple geometry, a superposition of uncertainties from experiment can lead to deviations of this order and it reinforces the view that the discrepancies observed for the more complex LARD geometry are credible and within a realistic range.

Damping and added mass are not compared directly quantitative between CFD and model tests. Instead, the practical relevance of the CFD- versus experimentally derived coefficients is assessed in terms of conservatism. A comparative study is performed to determine which coefficient set leads to the more conservative predictions of the LARD’s tow response and the outcome of this comparison is reported at the end of this section.
This approach is motivated by the fundamentally different physical regimes represented by the

two identification methods. In the CFD impulse simulations, frequency-independent added-mass coefficients are obtained, representing the inertial response in the limiting case of an impulsive acceleration from rest. The method is rooted in inviscid potential-flow assumptions and deliberately suppresses the development of a viscous boundary layer, flow separation, vorticity generation and vortex shedding.
As discussed by Sarpkaya [196], the resulting coefficients exist only in the instantaneous limit at very short times before viscous effects and separation begin to dominate. Once the flow evolves, the motion of a real body in a viscous fluid becomes strongly time dependent. The added mass becomes a function of time, history or memory effects appear and inertial and viscous contributions interact nonlinearly. In this sense, the inviscid potential-flow coefficient provides an idealised, non-viscous upper bound. [196]
In contrast, the experimental added-mass and damping coefficients were derived from small-amplitude sinusoidal oscillations conducted in a viscous regime. These measurements describe a finite-frequency hydrodynamic response that depends on the Keulegan–Carpenter number and varies with oscillation frequency. The experimental data therefore reflect a viscous, frequency-dependent regime that is strongly influenced by unsteady flow phenomena, whereas the CFD impulse method yields a single, frequency-independent value corresponding to the inviscid infinite-frequency limit by isolating this high-frequency limit by applying very short acceleration pulses that prevent significant boundary-layer growth.

For the forced oscillation tests in surge, it must be noted that the LARD model undergoes both forward and backward motion. The model experiences alternating forward and reverse flow relative to its principal axis as the oscillation proceeds. Owing to the non-symmetric shape of the LARD in the longitudinal direction, the flow topology and resulting hydrodynamic forces differ between the forward and backward phases (see Figure 6-42).

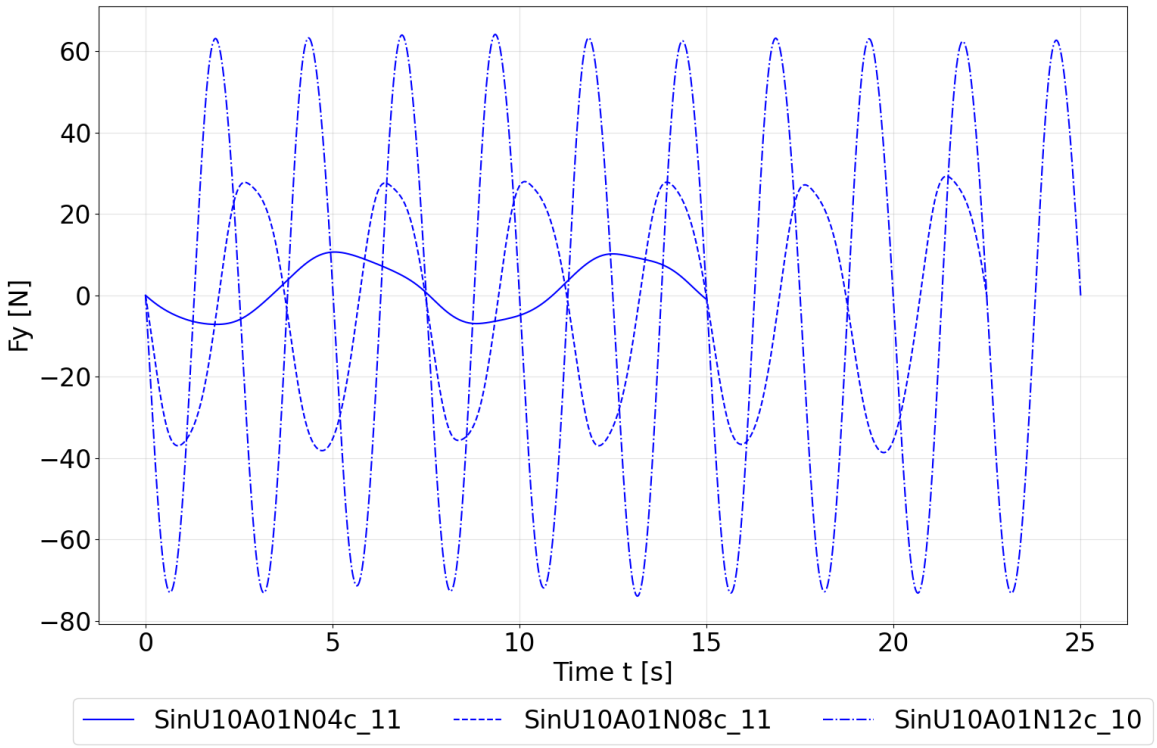


Figure 6-42: Surge forced oscillation tests with different excitation frequencies

Although this introduces additional complexity into the interpretation of the surge forced oscillation data, it is representative of realistic operating conditions, in which the docking device would also be subjected to motions that include components in both the forward and backward directions. In the sway configuration, the motion is symmetric about the centreline, with oscillations to port and starboard. Because the geometry is symmetric in the lateral plane, the sway motion produces a largely symmetric force response for positive and negative displacements.

The selection of hydrodynamic coefficients for the subsequent analyses of the LARD's towing behaviour is based on a comparative study. For this purpose, results obtained using the coefficients from the numerical calculations were compared with those obtained using the coefficients from the model tests for 55 representative parameter combinations considered in the towing behaviour study described in Chapter 7. To avoid anticipating the detailed findings of that chapter, only the conclusion is summarised here. For the analysis of the LARD's towing behaviour, the coefficients derived from the numerical simulations are adopted. Although the experimental coefficients reported in this chapter are higher and may therefore appear "more conservative" at first glance, conservatism in the present context is defined with respect to the predicted tow response rather than e.g. the additional vessel drag. Without anticipating the results of Chapter 7, it is important to note that the towing-performance assessment primarily concerns how readily the body is dynamically excited (either directly by wave-induced loads or indirectly through ship motions transmitted via the towing cable). As hydrodynamic drag, damping and added mass all oppose motion larger values of these coefficients generally reduce the resulting accelerations and response amplitudes for a given external excitation. Consequently, using smaller (rather than larger) drag, damping and added mass values can yield larger predicted motions and thus a less favourable towing behaviour, which constitutes the conservative assumption for the purpose of Chapter 7. So within the scope of this study, the CFD-based coefficients lead to less favourable towing performance and therefore represent the more conservative assumption.
It should be emphasised, however, that this choice is context dependent. If, for example, the primary focus was the additional drag imposed on the towing vessel by the LARD, the larger drag coefficients obtained from the experimental investigations would yield the more conservative estimate and should consequently be used.

7. Towing Behaviour Analysis of the Submerged Towed Docking Device

To assess how well the designed system performs under different conditions, an analysis of the towing behaviour of the submerged towed docking device is carried out. The influence of different boundary conditions on the overall system (illustrated in Figure 7-1) is investigated. The varied parameters include the sea state, wave direction, towing cable length, carrier platform length, the towing velocity, attachment point of the towing cable on the carrier platform and the use of floats and sinkers along the towing cable.
This chapter analyses the towing behaviour of the LARD utilising the multibody simulation software OrcaFlex. First the simulation setup is described, including the different components of the system. Followed by a discussion of the results of the parametric analysis.

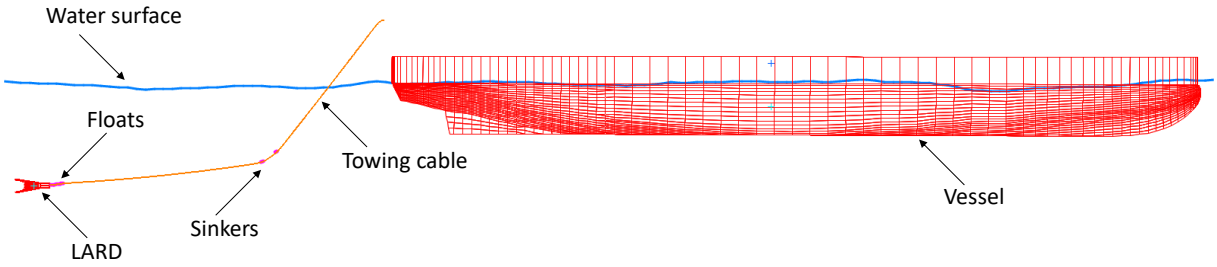


Figure 7-1: Components of the LARS (vessel, towing cable and LARD)

7.1 Simulation Setup

This section provides a detailed description of the simulation model setup. First, the individual components, or subsystems, of the overall system are introduced, namely the vessel, the towing cable and the submerged towed docking device. The incident waves are then defined as boundary conditions. Subsequently, the automation of the simulation process required for the parametric study is described, followed by an outline of the post-processing of the simulation data. Building on this, Section 7.1.7 summarises the limitations, assumptions and simplifications adopted for the multibody analysis.

7.1.1 Vessel

For the numerical representation of the carrier platform, a service vessel for offshore operations is adopted, as this vessel type is suitable for the intended application of the LARD. The main properties of the reference vessel are summarised in Table 7-1. A general view of the vessel hull is shown in Figure 7-2. The geometric data and the hull mesh were provided by the Norwegian research institute SINTEF (Stiftelsen for industriell og teknisk forskning).

Table 7-1: Vessel parameters

Length between perpendiculars	80.80 m
Beam	20.00 m
Draft	5.87 m
Total mass/displaced volume	6.95e6 kg
Longitudinal centre of gravity	-2.83 m
Transverse centre of gravity	0.00 m
Vertical centre of gravity	2.25 m

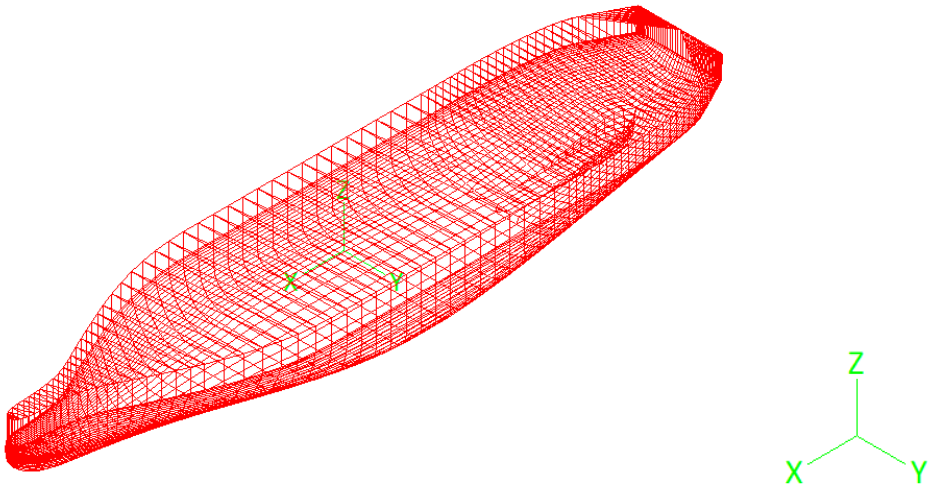


Figure 7-2: Hull geometry

The hydrodynamic behaviour of the vessel is characterised in the frequency domain by RAOs, which are computed using OrcaWave (Orcina). OrcaWave solves the linear potential-flow on the panelised hull surface and evaluates the interaction between the vessel and the incident waves. For each panel of the hull mesh, the linear potential equation is solved and the resulting pressures are integrated to obtain the wave-induced forces and moments.
The RAOs are calculated for different wave periods, ranging from 0.5 s to 15 s in increments of 0.5 s and different wave directions, starting from 0° (following seas) and increasing in steps of 22.5° up to 180° (head seas). The resulting RAOs are tabulated as a function of wave period and direction for the relevant velocity range. If, during the subsequent time-domain simulations in OrcaFlex, the instantaneous wave period or direction does not coincide exactly with one of the tabulated values, OrcaFlex determines the required RAO values by interpolation between the neighbouring entries.
Other environmental loads on the vessel, such as wind, current-induced drift, or additional wave drift forces, are not modelled for the vessel. It is assumed that the vessel's propulsion and station-keeping systems are capable of compensating these external influences so that the dominant excitation of the vessel motion arises from wave action as represented by the RAOs. The implications of these effects on the LARD itself are discussed in section 7.1.4 and the associated limitations of this study are further addressed in section 7.1.7.

To investigate the influence of vessel size on the system response, Froude scaling is used to ensure dynamic similarity between the vessels. The hydrodynamic properties of the scaled vessel lengths of 15 m, 30 m, 50 m are derived from the 80 m reference vessel. By preserving the ratio between inertial and gravitational forces the wave-induced motion characteristics remain identical across different vessel lengths.
As the RAOs are defined as non-dimensional frequency-response functions of vessel motion with respect to wave amplitude, Froude scaling can also be applied. The period (or frequency) axis of the RAOs is adjusted according to the length ratio while preserving the shape of the non-dimensional response curves. This avoids the need for separate hydrodynamic calculations for each vessel length and ensures that the motion behaviour remains dynamically consistent for all scaled vessels. It should be noted that a change in vessel length would in practice almost certainly be accompanied by a change in hull form. In the present example, a 15 m vessel would be unlikely to share the same hull geometry as the 80 m vessel considered here. However, to isolate and investigate the influence of ship length, the same hull form is deliberately retained

and examined at different lengths. If different hull forms were selected for each vessel length, a direct comparison would not be possible, since the response to wave excitation would differ for each hull geometry.
Furthermore, a subset of simulations is carried out with the vessel RAOs set to zero to isolate the role of vessel motion on the towing process. In these cases, the ship does not respond dynamically to the waves and the towing point follows a purely prescribed trajectory at constant position and towing speed relative to the mean water surface. It should be noted that this approach suppresses wave-induced vessel motions but does not introduce a modified local wave field around the hull; effects such as wave breaking and wave reflection/diffraction at the ship hull are therefore not represented. By comparing simulation results obtained with and without wave-induced vessel motions, the influence of the ship's motion on the towing behaviour of the cable and the LARD can be quantified systematically.

7.1.2 Waves

To represent the complex wave conditions in the North Sea, including wave shape, height and period, the JONSWAP wave spectrum is employed (see Section 4.2.2). Within the scope of this work, sea states 1–6 are considered using the values (listed in Table 7-2) derived from the sea state analysis in the North and Baltic Sea (outlined in Section 5.2).

Table 7-2: Significant wave height and peak period

Sea state	H_s [m]	T_p [s]
0	0.00	-
1	0.09	4.39
2	0.36	4.46
3	0.80	5.06
4	1.60	6.25
5	2.90	7.61
6	4.50	9.45

The adopted wave spectrum describes the distribution of wave energy over different frequencies. The resulting wave motion is obtained by superposing the individual frequency components of the JONSWAP spectrum. The surface elevation is defined relative to the mean sea level. Figure 7-3 illustrates the wave amplitude at a fixed spatial location for sea state 4 with a selected simulation duration of 420 s. To ensure comparability between different simulations, the same wave train is used in all cases.
To ensure that the investigations are representative, larger individual waves contained in the spectrum must also be accounted for. In this context, the ratio of maximum observed wave height to defined significant wave height should be at least 1.86. This threshold originates from linear random-wave theory. If individual wave heights are assumed to follow a Rayleigh distribution, the most probable maximum wave height among 1000 waves (commonly associated with a quasi-stationary 3 h sea-state realisation) is expected to be about 1.86 times the significant wave height [197]. Requiring a ratio of maximum observed wave height to significant wave height of at least 1.86 therefore serves as a practical representativeness criterion, indicating that the simulated time series contains at least one comparatively rare, large wave rather than sampling only typical waves.
This condition is satisfied for all examined cases. Using the example illustrated in Figure 7-3, a maximum surface elevation of approximately 2.63 m is observed at around 311 s. Together with the subsequent wave crest of about 2.16 m, this yields a maximum observed wave height

of approximately 4.79 m. This leads to a ratio of maximum observed wave height to significant wave height of 2.99 and thus significantly exceeds the required value of 1.86. Even under consideration of the largest wave height associated with sea state 4 within the Douglas sea state scale (2.5 m), the resulting ratio is 1.92 exceeding 1.86. It can therefore be concluded that, within the chosen simulation duration of 420 s, waves of sufficient height are captured for the study to be regarded as representative.

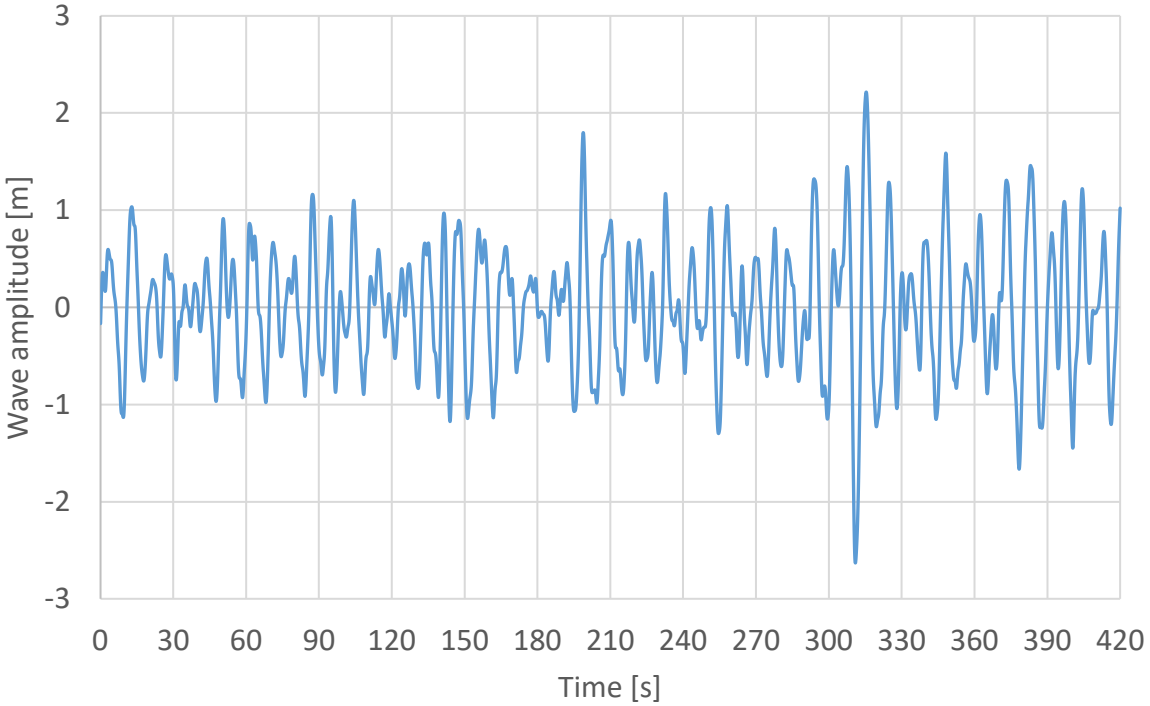


Figure 7-3: Wave amplitude over time - example for sea state 4 (H_S=1,6 m)

To define an appropriate simulation duration, not only the range of waves considered but also the influence of the simulation time on the results is examined. For this purpose, 283 parameter combinations from the parametric analysis described in Section 7.2 are selected and simulated with different total simulation times of 210 s, 420 s, 840 s, 1680 s and 3360 s. The resulting data are evaluated using the towing behaviour metrics introduced the further course of Section 7.1.

When the simulation time is doubled from 210 s to 420 s, substantial differences are observed in both evaluation metrics: one metric decreases by an average of 3.5 %, while the other increases by 7.5 %. This behaviour is partly explained by the fact that the previously described large wave event occurs only at approximately 310 s and is therefore not captured in the 210 s simulations. Significantly smaller deviations are obtained when the simulation time is increased from 420 s to 840 s, for which the first metric decreases by only 0.35 % on average and the second metric increases by 0.09 % on average. Further doublings of the simulation time yield similarly small changes. For an increase from 840 s to 1680 s, mean deviations of 0.24 % and −0.02 % are observed. For the final step from 1680 s to 3360 s the deviations reduce further to 0.04 % and 0.06 %. Based on these observations of how the results evolve with increasing simulation time and in view of the very small gradients beyond 420 s, a simulation duration of 420 s is adopted for all simulations as a compromise between accuracy and computational effort. For a towing velocity of 1 m/s, the 420 s simulations correspond to encountering approximately 107 dominant wave cycles, which is markedly fewer than the 1,000 waves

typically contained in a 3 h sea-state realisation used for high-confidence long-term statistics. Accordingly, the present duration is selected because the chosen towing-behaviour metrics exhibit negligible mean changes beyond 420 s for a large ensemble of cases, indicating that the metrics of interest are sufficiently stable for comparative performance assessment within the scope of this study.

It should be noted, that the number of encountered wave cycles depends on the vessel's velocity since total simulation time is fixed. Faster runs experience more wave cycles within 420 s, whereas slower runs provide fewer cycles. This primarily affects the statistical robustness of response metrics (e.g. maxima, percentiles and spectral estimates). With fewer encountered cycles, extreme-value and variance estimates become less stable and may exhibit increased scatter, even if the underlying dynamics are unchanged.

7.1.3 Towing cable

In the numerical model, the towing cable is represented as a steel wire rope. Its basic design is derived from an order-of-magnitude calculation of the total load of all components to be supported. This load comprises the weight of the docking device, which is conservatively rounded up to account for water retained on the structure during recovery, the AUV displacement and the clump weights attached to the cable. The function of these clump weights is discussed in more detail below. A safety factor of 5 is adopted in accordance with the guidelines of DIN EN 13414 and API 2C [198, 199]. On this basis, a steel wire rope with the properties listed in Table 7-3 is selected.

A key design objective is to minimise the pitching tendency of the docking device by ensuring an approximately horizontal cable segment immediately upstream of the LARD. In this configuration, the line of action of the towing force passes through the centre of gravity of the

Table 7-3: Towing cable properties

Parameter	**Value**
Diameter	0.008 m
Minimum breaking load	67.74 kN
Mass per unit length	0.378 kg/m
X and Y direction bending stiffness	0.189 kNm²
Axial stiffness	4,224.96 kN
Torsional rigidity	25 kNm²
Drag coefficient in X and Y directions	1.2
Drag coefficient in Z-direction	0.005

docking device, so that no additional pitch moment is generated. If the cable were inclined in this region, the towing force would act with a lever arm relative to the centre of gravity and thus induce an unwanted pitch moment. The horizontal cable segment therefore reduces the resulting moment and improves the towing behaviour by preventing the LARD from tilting. This principle is also described by Helmond for minimising the pitch motion of towed bodies [200]. Figure 7-4 illustrates the difference between an inclined cable (blue) and the desired horizontal segment (orange), together with the associated lines of action of the towing forces.

The desired cable shape is realised by a combination of sinkers (clump weights) and floaters (buoyancy elements). The clump weights provide downward force, while the buoyancy elements lift the cable in the region immediately ahead of the LARD. The interaction of these two elements produces a largely horizontal cable section between the last clump and the LARD.

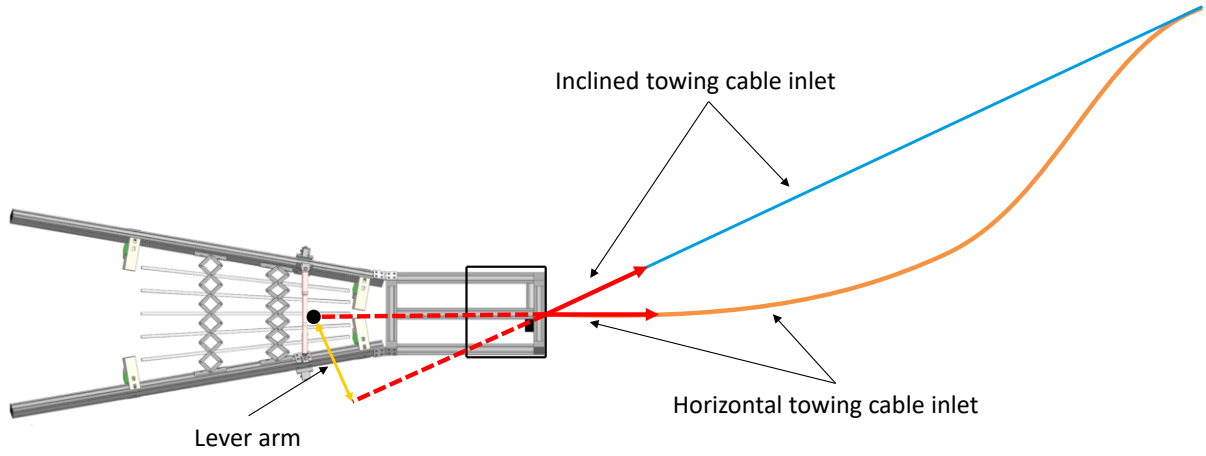


Figure 7-4: Towing cable arrangements

This configuration has the additional advantage that the cable becomes less sensitive to ship motions which act predominantly perpendicular to the cable axis. In general, a cable aligned predominantly horizontally (for example due to a large total cable length) is less sensitive to horizontal vessel motions but reacts more strongly to vertical motions. [200]
The buoyancy elements are modelled as spheres. The clump weights are modelled as cylinders made of lead due to its high density. Mass and volume of the floats and sinkers are chosen with reference to commercially available products to ensure realistic properties. The specified drag and hydrodynamic mass coefficients for the spherical floats and cylindrical clump weights are taken from Hoerner [192], Fackrell [201] and Bruschi et al. [202].

To model the towing cable accurately an appropriate number of cable segments must be chosen. If too few segments are used, the dynamic behaviour of the cable, including its curvature and local tension variations, is poorly resolved. If too many segments are used, the computational cost increases unnecessarily. For this reason, a convergence study on the number of segments is carried out. Within this study, the cable is successively discretised with smaller segment lengths and a convergence criterion of 1 % is imposed. This means that the quantity of interest is required to change by less than 1 % between two successive refinements before the segmentation is accepted.

The position of the cable–vessel attachment point is another critical design variable. In a coupled towing system, the exact location at which the cable is connected to the vessel strongly influences the dynamic response. To represent both idealised and practically feasible operational configurations, three attachment points are considered: a mid-stern attachment, a starboard-side attachment and an attachment point located at the stern one third of the vessel beam off the stern centreline towards starboard. The different towing cable attachment pointsare illustrated in Figure 7-5.
In the mid-stern configuration, the cable is attached at the aft-most point on the vessel centreline. In this case, the attachment point is aligned with the transverse centre of flotation (COF), so that roll motions have a comparatively small influence on the position of the attachment point, whereas pitch motions have a more pronounced effect. In the starboard-side configuration, the cable is attached laterally on the starboard side, aligned with the longitudinal COF. Here, roll motions have a significantly stronger influence on the motion of the attachment point, while pitch plays a less dominant role. In practice, the actual attachment position is determined by the location of the crane or winch used to handle the cable. To reflect this, the

third configuration places the towing point one third of the vessel's beam away from the stern centreline towards starboard. This intermediate position exhibits combined sensitivity to both roll and pitch motions of the vessel.

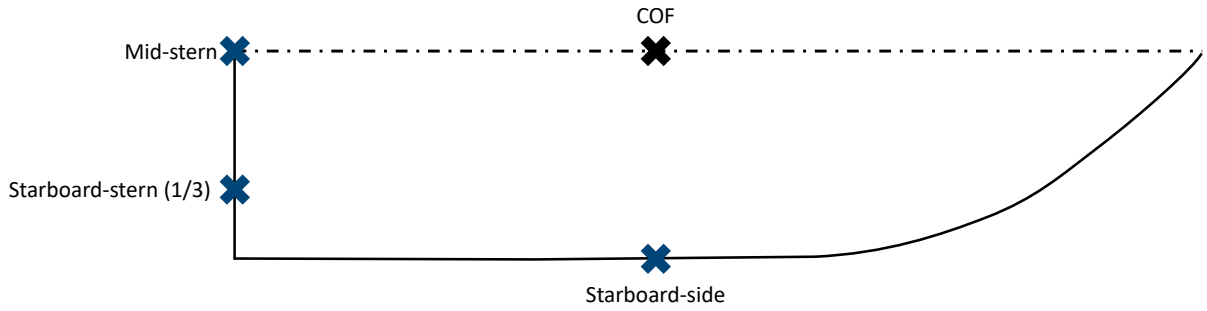


Figure 7-5: Towing cable attachment points

To maintain consistency across different vessel sizes, the coordinates of the cable attachment point at the stern are scaled with the vessel length and beam for all four vessel sizes investigated (15 m, 30 m, 50 m and 80 m). The position and properties of the floats and sinkers are scaled with respect to the cable length.

7.1.4 Submerged Towed Docking Device

In the simulation model, the LARD is represented as a rigid body with six DoF using the lumped-buoy formulation. In this approach, the complex geometry of the docking device is not modelled explicitly. Instead, the body is treated as a point mass whose geometry and inertia properties are represented indirectly through parameters. These include the mass, dimensions, centre of mass, volume, centre of volume and the mass moments of inertia, which are defined on the basis of the detailed engineering design. In addition, the hydrodynamic coefficients determined for the LARD in Chapter 6 are assigned to this lumped body. In this way, the dynamic response of the docking device can be captured realistically without the need to derive the relevant properties directly from a full geometric model.

For visualisation purposes, the docking device is displayed as a wire-frame representation within the simulation environment. This graphical model facilitates the identification of the static position, the tracking of dynamic motions and the overall interpretation of the system configuration. However, the wire-frame visualisation has no influence on the underlying calculations and would only become relevant in the context of explicit contact modelling with other bodies, which is not considered in the present study.

7.1.5 Automation of the simulation runs for the parametric analysis

To conduct the parametric analysis, a large number of simulation cases must be evaluated, which renders manual execution impractical and inefficient. Therefore, an automation framework was developed in Python using the OrcFxAPI, the Python-based application programming interface for OrcaFlex. This interface provides direct access to OrcaFlex functionalities, including model setup, definition of environmental and boundary conditions, execution of simulations and post-processing. In this way, the systematic variation of parameters and the execution of multiple simulation runs can be automated while maintaining a consistent model definition.
The automation framework is organised as a structured workflow. First, a base OrcaFlex data file containing the reference simulation setup is imported. For each parameter configuration

considered in the parametric study, this base model is programmatically updated via the OrcFxAPI to assign the corresponding parameter values and properties. Depending on the selected parameter combination, the environmental and other boundary conditions are modified and, where necessary, scaled for the respective simulation case. To ensure transparency and reproducibility, all boundary conditions and scaled parameter values used in a given run are written to dedicated log files.

Once the model setup is completed for a specific configuration, the simulation is executed for a total duration of 420 s. The solution procedure consists of a static stage from −8 s to 0 s, followed by a dynamic stage from 0 s to 420 s. For each run, the time histories of the LARD motion in all six DoF in 0.1 s increments are exported as structured CSV files for subsequent post-processing in Python. In addition, the corresponding OrcaFlex model files, CSV outputs, log files and simulation result files are stored under uniquely defined simulation names so that all cases can be clearly distinguished and traced. Simulation cases that did not complete successfully are also retained to allow later inspection of the causes of failure.
To improve computational efficiency, the simulations are executed in parallel on multiple cores. This parallelisation reduces the overall computation time while keeping the workflow robust and manageable.

7.1.6 Post-processing of simulation results

The results obtained from the OrcaFlex simulations consist of the time histories of the LARD motion in all six DoF. To derive insightful performance metrics from these data, a systematic post-processing procedure was developed and applied consistently to all simulation cases, enabling a reliable comparison of towing stability and docking performance under varying environmental and design conditions. The post-processing focuses on the towing behaviour of the LARD, using the centre of the docking area as the reference point (see Figure 7-6). The centre of the docking area is defined as the centre of the opening formed by the guiding mechanism at the rear of the LARD, through which the AUV enters an opening of approximately 1 m × 1 m. This point represents the nominal target that the AUV would aim for during docking and is therefore the key quantity for assessing towing performance and docking success.
Because the LARD is modelled in OrcaFlex as a lumped buoy with six DoF, the simulations provide only the time histories of the motion of the lumped point mass, rather than the motion of the opening centre directly. To obtain the centre of the docking area trajectory, a positional vector transformation is applied. Using the known geometric offset between the lumped point mass and the centre of the docking area from the engineering design, together with the simulated time histories of translations and rotations, the global coordinates of the centre of the docking area are reconstructed at every time step of each simulation. Therefore, the simulation outputs (providing the rigid-body position and orientation of the lumped buoy) are post-processed using a Python script. The script applies the known fixed offset vector from the lumped point mass to the docking-area centre (defined in the body-fixed frame) and maps it into the global frame via a rigid-body coordinate transformation (i.e. standard kinematic reconstruction using the simulated rotation and translation). The resulting time series of the docking-area centre coordinates are then exported as a separate dataset containing the corrected position history of the opening centre for subsequent analyses. In this way, the full three-dimensional trajectory and orientation of the opening are computed and is available for further analysis.
The reconstructed centre of the docking area trajectory is then approximated by a three-dimensional fifth-order regression curve (see Figure 7-6 for schematic 2D illustration), which

represents a smoothed path that the AUV is assumed to follow during the final approach. This assumption is motivated by the guidance behaviour of the AUV. At larger distances from the LARD, the control system would typically smooth the commanded trajectory, but in the near-field region that is relevant for the docking phase in this work, it is assumed that the AUV tracks the motion of the opening closely. The regression curve therefore approximates the feasible AUV path in the vicinity of the LARD and serves as the reference trajectory for defining the performance metrics.

This modelling choice reflects the scope of the thesis: the AUV is assumed to provide a reasonable baseline capability for near-field tracking of the docking-area centre. The main contribution therefore lies in shaping the relative motion through system configuration and passive dynamics of the towing arrangement, thereby reducing the control effort required to satisfy the geometric capture conditions. Consequently, docking performance is assessed primarily through relative-motion and geometric capture conditions rather than through classical control metrics.

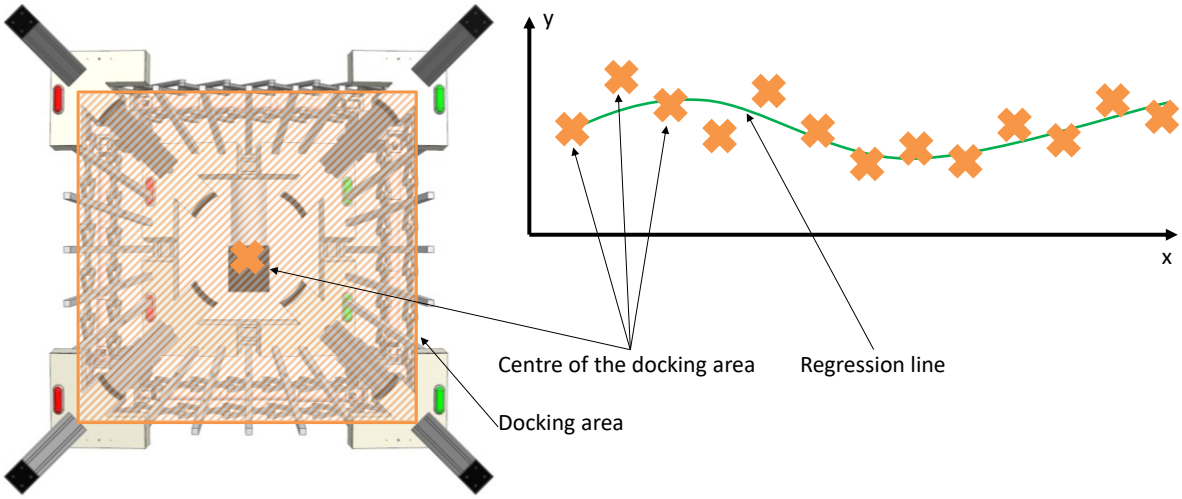


Figure 7-6: Scheme docking area
Left: rear view of docking area; right schematic regression of centre of docking area

For analysing the towing behaviour of the LARD, two main metrics are introduced. The first is the Docking Success (DS), defined as the percentage of the simulation time during which the regression curve lies within, or at least touches, the docking area of the LARD. In practice, the centre of the docking area trajectory is projected onto the plane normal to the towing direction (the YZ-plane) and at each time step it is checked whether the corresponding point on the regression curve is inside the rectangular opening area or on its boundary. Docking is considered possible at a given time step if this condition is met. Evaluating this condition over the entire simulation and across all simulation batches yields a quantitative measure of docking success for each configuration. An illustrative example is provided in Figure 7-7. The areas shaded in green satisfy the criteria for a successful docking and are therefore counted as time steps contributing to the DS metric. In contrast, the red rectangles indicate regions in which the regression line does not lie within the prescribed bounds, so that docking is classified as not possible. The wave surface elevation associated with the example from Figure 7-7 is illustrated in Figure 7-8.

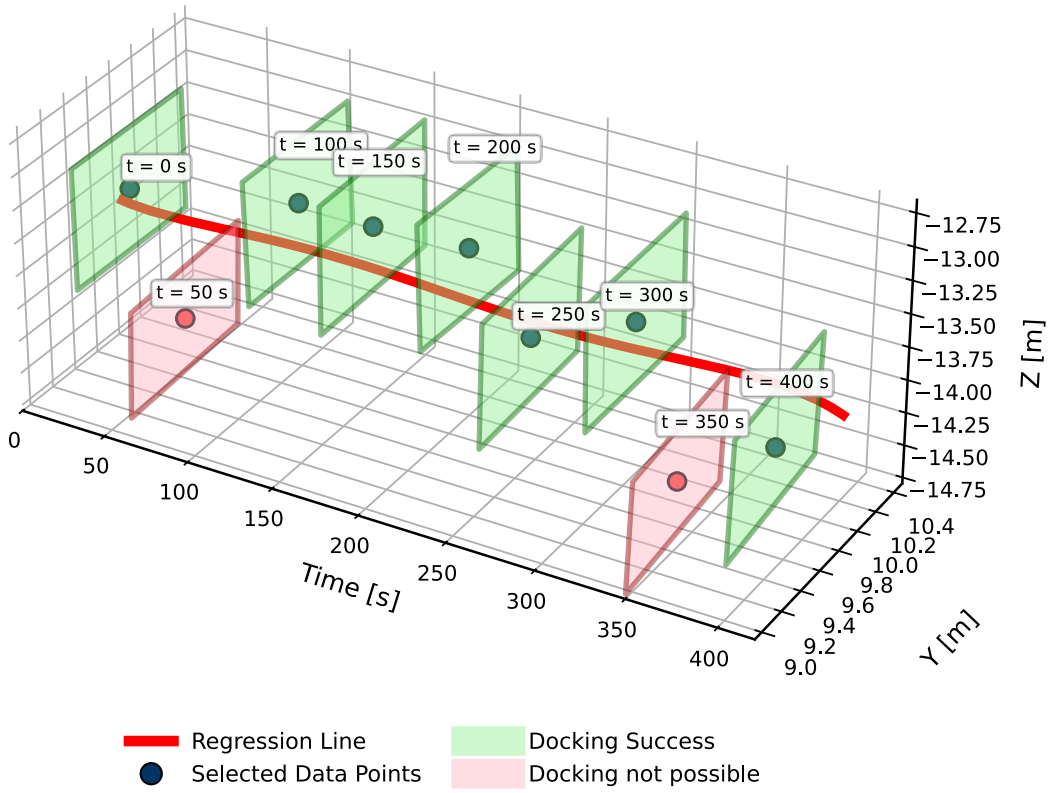


Figure 7-7: Illustration of docking success (DS) metric
(green: docking successful vs. red: docking not possible)

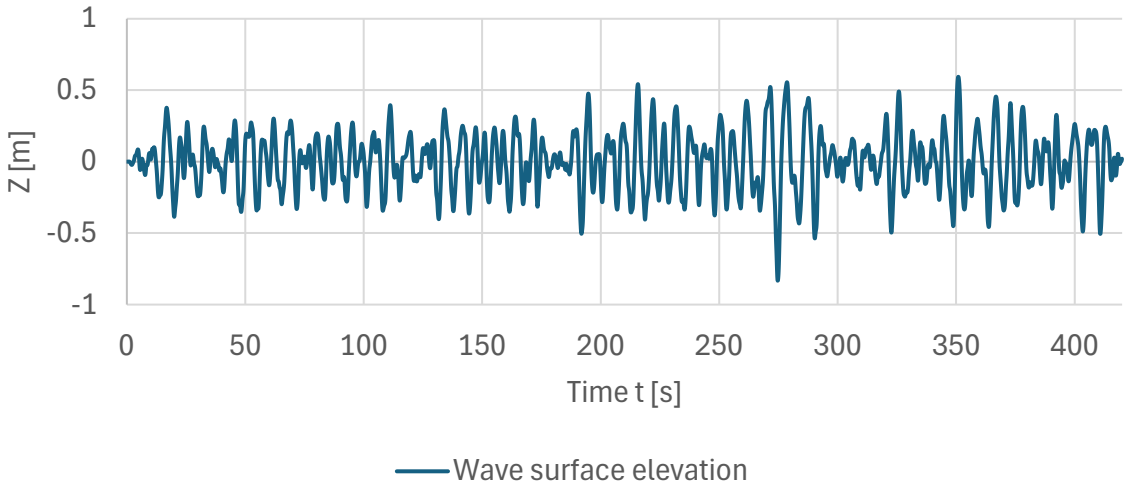


Figure 7-8: Wave surface elevation associated with the example from Figure 7-7

The second metric is the root-mean-square error (RMSE) between the actual position of the centre of the docking area and the regression curve. In this way the RMSE quantifies the magnitude of the deviations of the opening centre from the assumed AUV path. Low RMSE values indicate that the centre of the docking area remains close to the regression trajectory, implying a more stable towing behaviour and more favourable docking conditions. Conversely, higher RMSE values correspond to larger fluctuations of the opening centre around the reference path and thus indicate reduced towing stability. Together, the DS and RMSE provide

complementary measures for assessing the quality of the towing and docking performance across the different simulation scenarios.

7.1.7 Limitations, assumptions and simplifications

The limitations of this study must also be addressed, particularly those arising from the chosen simulation setup, the underlying assumptions and the simplifications that were introduced. In this context, it is important to emphasise that numerical simulations always represent a model of reality and can therefore never reproduce it perfectly. Instead, they approximate selected aspects of the physical system within a defined level of detail and under specific boundary conditions.
For the present work, these limitations concern, in particular, the multibody simulation of the LARD towing system. Certain effects were neglected, others were represented in simplified form and several parameters had to be idealised due to incomplete information or to keep the computational effort within reasonable bounds. These modelling choices influence the quantitative results and must be borne in mind when interpreting the predicted towing behaviour.

To focus on the dynamic loading of the towing cable induced by the vessel motion, the environmental conditions are idealised by assuming constant water temperature, constant water density and constant water depth, a flat seabed and the absence of ocean currents and wind. The model further concentrates on a sufficiently realistic representation of the cable excitation due to wave-induced ship motions, while several effects on the vessel itself are neglected. In particular, external loads, second-order wave drift loads, wave drift damping, second-order sum-frequency loads, manoeuvring forces and associated damping, as well as current- and wind-induced loads on the vessel are not considered.
Additional simplifications are introduced for the towing cable. Internal friction and torsional deformation are neglected and the cable is modelled with linear axial stiffness and linear, isotropic bending stiffness. The LARD is treated as a rigid body, since the expected structural deformations at the low towing speeds considered are small and, in any case, structural deformation is not within the primary scope of this study.

Further sources of uncertainty arise from the modelling of the LARD itself. The hydrodynamic coefficients used for the device are based on numerical values obtained from CFD simulations and were only checked against selected experimental data. Both CFD and model tests are, however, themselves only models of reality, so an associated propagation of error into the multibody simulations must be expected. In addition, the opening and closing motion of the LARD is not represented. Possible changes in the flow field and in the hydrodynamic coefficients due to this motion, particularly during the phase when the AUV enters the device and is being secured, are therefore not captured.

A further limitation is that the AUV is not included in the present multibody simulations. The docking manoeuvre itself is thus not explicitly modelled, even though the inflow conditions and flow topology around the LARD would change significantly once a vehicle approaches and enters the LARD during towing. In the same context, it is assumed that the AUV is able to follow the reference trajectory defined by the regression line used for evaluating the docking success metric and can adjust its motion accordingly.

Additional limitations arise from the assumptions made regarding the ship geometry, as described in Section 7.1.1. In the present study, a single hull form was selected and

subsequently scaled to different dimensions. Although this approach allows the influence of ship length to be investigated systematically, it does not account for the fact that shorter or longer vessels in practice may exhibit distinctly different hull forms. Variations in hull geometry would alter the hydrodynamic response, for example by changing the magnitude and frequency content of roll and pitch motions and thus could significantly affect the towing behaviour of the LARD. As a consequence, the quantitative results obtained here are strictly valid only for the specific hull form considered. Applying the system to other vessel types would require corresponding recalculations with the actual ship geometries.
Similar restrictions apply to the other parameters e.g. the representation of the towing cable. The combined dynamic behaviour of ship, cable and LARD is therefore tailored to this specific configuration of LARD, towing cable and reference vessel. The study thus primarily illustrates the methodology and provides insight into the relative influence of selected parameters. While general qualitative trends can be transferred to other configurations, quantitative predictions for a specific application require that the exact boundary conditions are incorporated into a dedicated simulation model.

For the interpretation of results only the relative motion of the LARD to the assumed path of the AUV are taken into account in terms of DS and RSME. In practical operations, docking performance is influenced not only by the physical relative motion analysed here, but also by navigation uncertainty and measurement latency in the relative pose estimate between AUV and docking divined delayed updates effectively increase the apparent dispersion of the target point that the AUV tracks, thereby reducing the available geometric margin at the entrance. The metrics DS and RMSE can therefore also be interpreted as system-level requirements on the combined envelope of physically induced relative motion and navigation/control uncertainty during the final approach. In this sense, improvements achieved through passive stabilisation directly relax the accuracy and latency demands placed on the near-field homing system.

7.2 Parametric analysis

In this section, the results of the parametric analysis of the towing behaviour of the LARD are presented. The varied parameters are summarised in Table 7-4 and include the Sea State, Wave Direction, towing Cable Length, Vessel Length, Attachment Point of the towing cable, the use of Floats and Sinkers along the cable and the use of Vessel RAOs.

Table 7-4: Datasets for parametric analysis

Parameter	**Dataset1**	**Dataset2**
Sea State	0 - 6	0, 2, 4, 6
Wave Direction	0° -360° in 15° increments	0° -180° in 15° increments
Cable Length	10 m - 70 m in 5 m increments	10 m - 70 m in 10 m increments
Vessel Length	15 m, 30 m, 50 m, 80 m	15 m, 30 m, 50 m, 80 m
Attachment Point	Mid-stern, starboard-side, starboard-stern (1/3)	Mid-stern
Towing Velocity	1 m/s	0.5 m/s, 1 m/s, 1.5 m/s
Floats and Sinkers	Included	Included, not included
Vessel RAOs	Included	Included, not included

Two main datasets were defined. Dataset1 comprises a fine-resolution study to systematically explore the parameters. The sea state was varied from 0 to 6. The wave direction was investigated from 0° to 360° in increments of 15°. The towing cable length ranged from 10 m to 70 m in steps of 5 m and four different vessel lengths were considered (15 m, 30 m, 50 m and 80 m). Furthermore, the three attachment points for the towing cable described in Section 7.1.3 were included. All simulations in Dataset1 were carried out at a towing speed of 1.0 m/s. Floats and sinkers were always placed along the towing cable and the vessel RAOs were consistently taken into account.
Dataset2 focuses on the influence of the towing speed, vessel RAOs and the use of floats and sinkers. In this dataset, towing speeds of 0.5 m/s, 1.0 m/s and 1.5 m/s were analysed. Each case was simulated both with and without floats and sinkers along the cable and both with and without consideration of the vessel RAOs. To limit the computational effort, the remaining parameters were constrained based on the findings from Dataset1. The step size of the cable length was increased to 10 m. Only one towing cable attachment point at the mid-stern of the vessel was considered. Exploiting the vessel's symmetry and the stern attachment, the wave direction was restricted to the range from 0° to 180° in 15° increments, as there is no difference between port and starboard approach for a symmetric hull in this configuration. Only sea states 0, 2, 4 and 6 were investigated.
For both datasets, a few minor exceptions were applied. For sea state 0, only a single wave direction was evaluated, as the direction becomes irrelevant when no wave height is present. Moreover, for the vessel lengths of 50 m and 80 m, some of the shortest cable lengths were excluded because they led to numerical instabilities and non-physical results.

The analysis of both datasets was carried out using the previously defined metrics of DS and RMSE. In all subsequent evaluations, only complete and mutually comparable parameter combinations were considered. Parameter combinations were included in the analysis and visualisation only if they fulfilled a consistency criteria, ensuring that like was compared with like. The division into two datasets requires particular care in this respect, as not all parameters and combinations are present in both datasets. Therefore, the underlying data were systematically filtered prior to plotting and comparison so that only truly comparable configurations were evaluated, thereby avoiding misleading trends or erroneous conclusions.

As a first step, a machine learning (ML) model based on a random forest algorithm was employed to estimate the relative importance of the individual parameters with respect to these metrics. The fundamentals of ML and the random forest algorithm are beyond the scope of this thesis and are therefore not discussed in detail. For further information, reference is made to Breiman [203] and Murphy [204]. The resulting feature importance scores quantify the influence of each parameter on the prediction of the target variables within the framework of the applied random forest model. These scores serve as an initial indicator of the relative impact of the different parameters on the overall system performance. The results are shown in Figure 7-9 and Figure 7-10.
Figure 7-9 for Dataset1 clearly reveals that sea state exhibits by far the highest feature importance score. Within the applied ML model, this indicates that the sea state is the dominant factor governing both DS and RMSE. The second most influential parameter is the towing cable length, whose importance is approximately one fifth of that of the sea state. With a further noticeable decrease, the wave direction follows, then the vessel length. The cable attachment point has the lowest influence on both metrics. This order of relevance is consistent for DS and

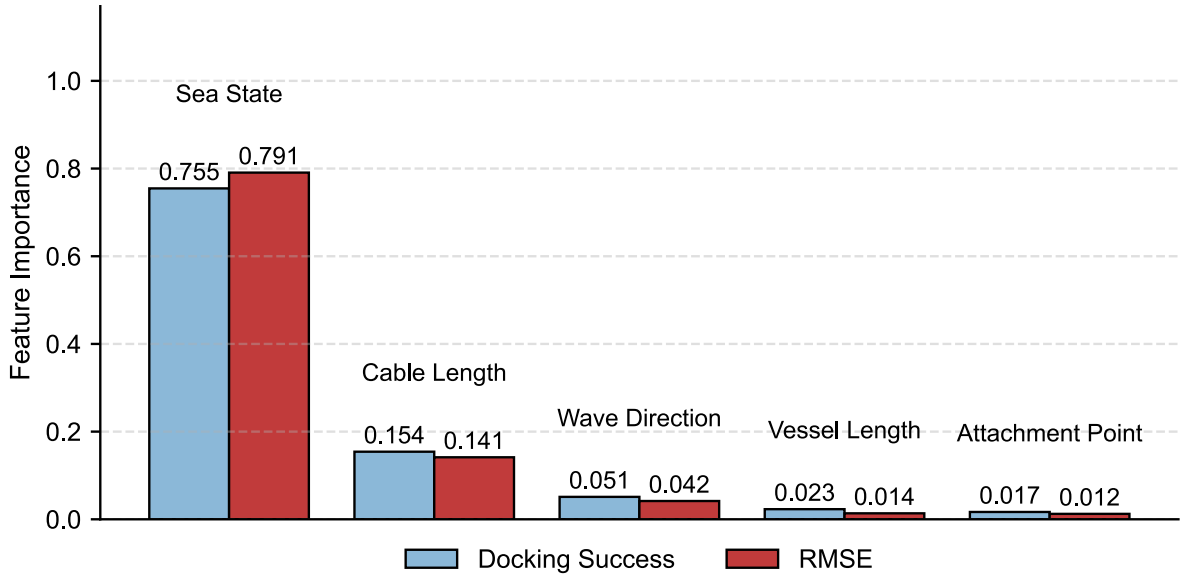


Figure 7-9: Feature importance scores of Dataset1

RMSE, although the absolute feature importance scores differ slightly between the two target variables.

For Dataset2 (see Figure 7-10), the feature importance distribution shows a broadly similar picture. Sea state again emerges as the dominant parameter with the highest feature importance score, followed by towing cable length and wave direction in the same order as for Dataset1. Compared with Dataset1, the absolute importance scores of these leading parameters either decrease slightly or remain unchanged.

In addition, the consideration of vessel RAOs now attains a feature importance level similar to that of vessel length, underlining the role of vessel motions for the towing stability of the LARD in this dataset. The attachment point is not included in the feature importance ranking for Dataset2, as only a mid- stern attachment configuration was analysed. Below vessel length and RAOs, towing speed appears with a very small feature importance, indicating only a minor contribution to the variance of DS and RMSE within the investigated range of speeds. Finally, clump types, i.e. the use or omission of floats and sinkers along the towing cable, shows no

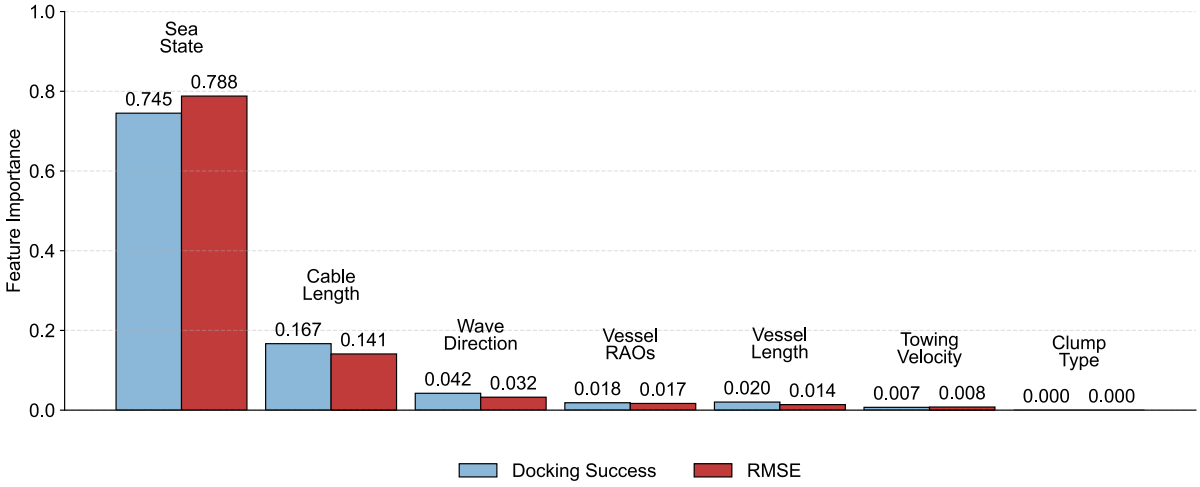


Figure 7-10: Feature importance scores of Dataset2

influence in the random forest model with a feature importance score of 0. It should be noted that the feature importance score only quantifies the relevance of a parameter within the random forest model. In the subsequent analyses, it becomes evident that the inclusion or omission of floats and sinkers does have a discernible effect on the evaluation metrics DS and RMSE. However, in the ML algorithm this influence is marginal compared with the impact of the dominant parameters. The very low feature importance value for the clamp type is therefore best interpreted as a consequence of rounding to three decimal places rather than as a complete absence of effect.

In the following subsections, the influence of sea state, wave direction, towing cable length, vessel length, cable attachment point, use of floats and sinkers and towing speed is presented and discussed in detail. In this context the influence of individual parameters is often evaluated on the basis of dataset mean values. The curves presented for a given parameter typically represent averages over a range of different configurations of the remaining parameters. As a consequence, the underlying data may span a relatively wide range of DS and RMSE values for each mean point. The observed trends should therefore be interpreted as system-level tendencies rather than as exact predictions for any specific parameter combination.

7.2.1 Sea state

As sea state has been identified as the most influential parameter, its effect on system performance is examined first. Figure 7-11 shows the variation of DS and RMSE over the investigated sea states from 0 to 6, based on all simulations contained in Dataset1. The plotted values represent mean results aggregated over a wide range of wave directions, towing cable lengths, vessel lengths and all three cable attachment points.

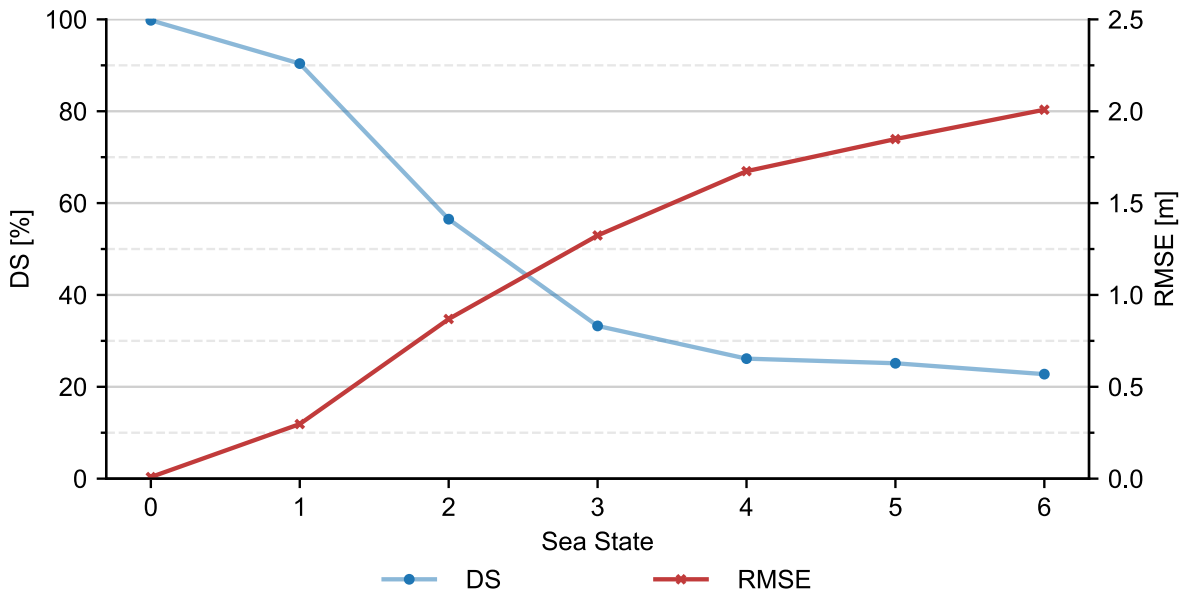


Figure 7-11: DS and RMSE vs Sea State

At sea state 0, DS is 100 %, while the RMSE is 0 m, indicating that under calm conditions the LARD can be positioned and maintained in the target region with very high reliability and no positional deviation. Figure 7-11 shows that DS (blue) decreases monotonically and in a distinctly non-linear manner with increasing sea state. DS drops steeply between sea states 1 and 3, after which the gradient becomes much weaker and the curve approaches a low-success

plateau slightly above 20 % between sea states 3 and 6. In contrast, RMSE (red) increases monotonically with predominantly piecewise quasi-linear behaviour. It rises approximately linearly and reaches values of almost 2 m at sea state 6. Overall, the two metrics exhibit a strong inverse relationship, but DS deteriorates more abruptly than RMSE grows.

This behaviour is consistent with the underlying physics of the system. Higher sea states are associated with larger wave heights and stronger vessel motions, which are transmitted through the towing cable to the LARD. In addition, the orbital motion of the water particles increasingly excites both the cable and the submerged LARD directly. As a result, the motion of the LARD becomes more pronounced, leading to lower DS and larger positional deviations expressed by the RMSE. Given this strong influence, sea state is treated as a key conditioning parameter in the subsequent analyses, where results are systematically stratified by sea state to enable a more detailed interpretation.

7.2.2 Wave heading

Figure 7-12 presents DS and RMSE as functions of wave direction grouped by sea state in the form of polar plots. A wave direction of 0° corresponds to following seas from astern which are waves propagating in the positive x-direction, while 90° denotes waves approaching from starboard (positive y-direction). The analysis again uses all simulations from Dataset1. Each data point therefore represents mean values averaged over all considered towing cable lengths, the four vessel lengths and the three cable attachment points.

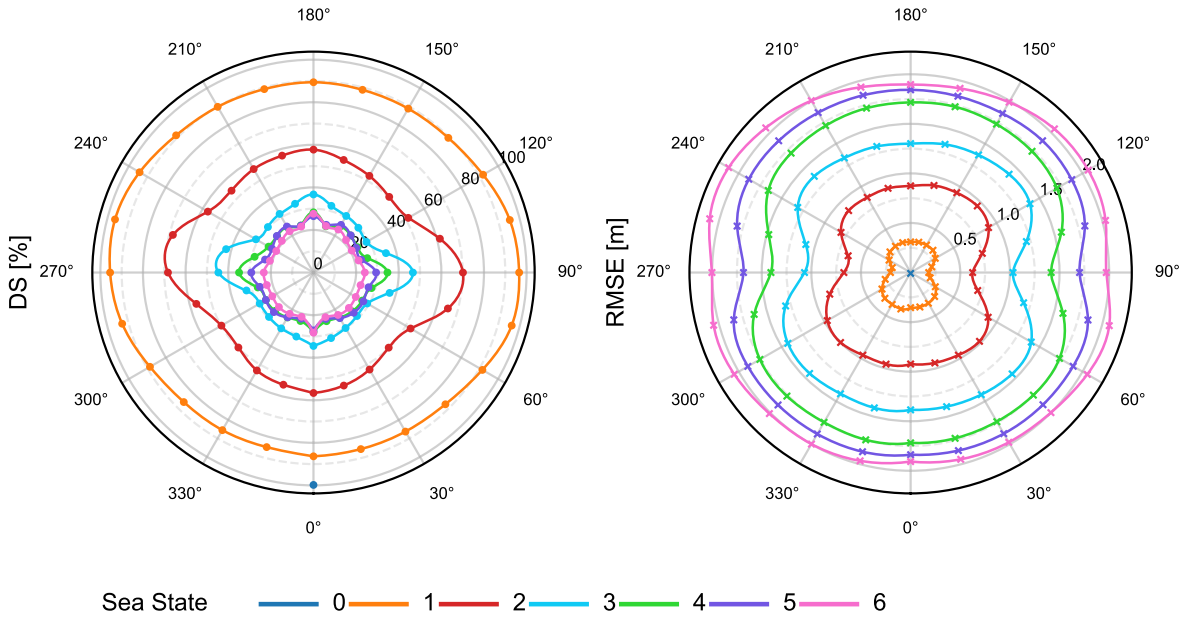


Figure 7-12: DS and RMSE vs Wave direction grouped by Sea State

For sea state 0, only a single point is shown, because in the absence of waves the direction of "no incoming wave" is irrelevant. In this case, DS is 100 % and RMSE is 0 m for all directions. On the DS side (left-hand of Figure 7-12), the previously observed overall decrease in DS with sea state is also evident, but the polar representation reveals the additional influence of wave direction. At sea state 1, DS remains almost direction-independent, with only minor variations around the circle. From sea state 2 onwards, distinct directional patterns emerge. Pronounced local maxima (bulges) appear around 90° and 270°, indicating notably higher DS for beam seas from starboard and port compared with head and following seas at 0° and 180°. With increasing

sea state these local maxima become more pronounced relative to the surrounding directions and from approximately sea state 3 a slight secondary elevation at 0° and 180° can also be observed. Overall, this implies that for low to moderate sea states beam seas are comparatively favourable for the towing and docking performance of the LARD. This behaviour is consistent with the vessel's roll response, which modifies the relative motion between vessel, towing cable and LARD in a way that is, on average, more benign for docking in beam seas than in pure head or following seas.

A similar directional trend is visible in the RMSE distribution (right-hand of Figure 7-12). The RMSE values exhibit an almost circular pattern for most sea states, indicating a relatively weak overall dependence on wave direction. However, already at sea state 1 and more clearly at higher sea states, local reductions in RMSE appear around 90° and 270°, again highlighting the comparatively advantageous towing behaviour in beam seas. Thus, both DS and RMSE consistently point to wave direction in interaction with sea state as a secondary but systematic control parameter, with beam-sea conditions generally providing more favourable operating conditions for the LARD than pure head or following seas.

7.2.3 Towing cable length

Figure 7-13 shows DS as a function of towing cable length, differentiated by sea states 0–6.

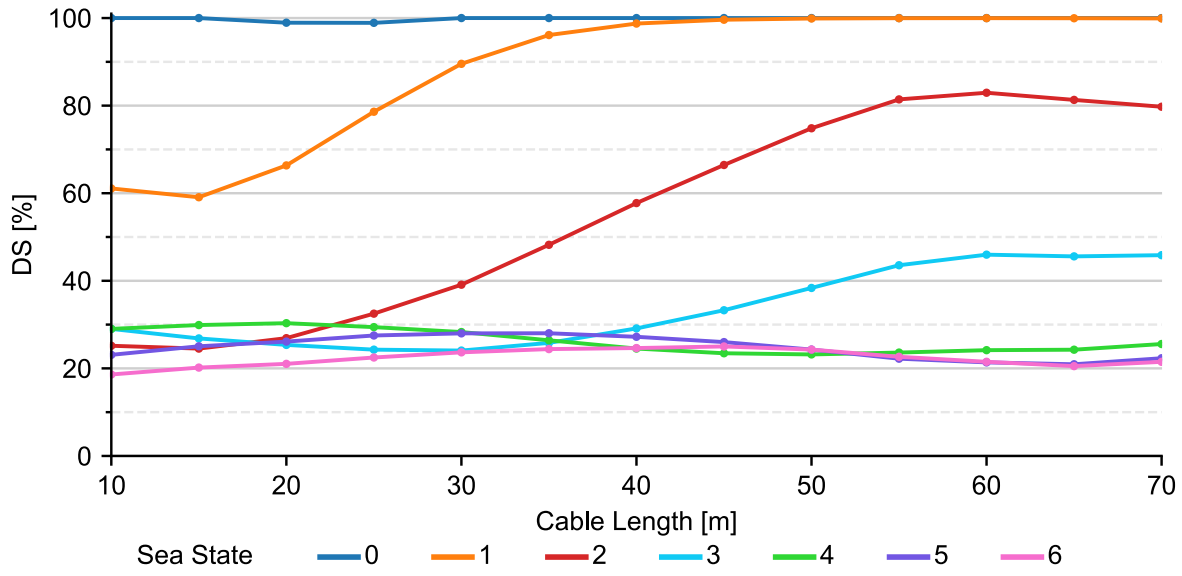


Figure 7-13: DS vs Cable Length grouped by Sea State

For sea state 0, DS remains at 100 % for all cable lengths, confirming that in calm conditions the LARD can always be successfully docked irrespective of the cable configuration. For non-zero sea states, DS generally increases with cable length until it reaches a plateau, beyond which further extension of the cable does not yield additional improvement. An exception occurs at sea state 1 for the shortest cable length of 15 m, where the conspicuous reduction in DS is most likely caused by numerical instabilities in the simulation. In practical terms, this effect is very small. DS decreases by only about 2 percentage points when moving from 10 m to 15 m cable length before increasing again for longer cables and is therefore treated as negligible in the present interpretation. The underlying issue is expected to be associated with the combination of very short cables and stronger transient excitation, which can lead to occasional solver failures or unstable contact/constraint behaviour in individual realisations, particularly when exceptionally large waves occur. Consistent with this explanation, such instabilities were

observed more frequently for the 10 m and 15 m cable cases in the simulations of the larger vessels (50 m and 80 m). This is also the reason why, the cable lengths of 10 m and 15 m were not considered for the 50 m and 80 m vessels in the simulation set.
For sea state 1, DS approaches 100 % once the cable length exceeds approximately 40 m. At sea state 2, a maximum DS of about 80 % is only achieved at cable lengths of around 55 m, while at sea state 3 a DS level of roughly 45 % is reached at the same cable length. For higher sea states (4–6), the influence of cable length is much weaker; DS fluctuates only slightly around values just above 20 % and longer cables cannot compensate for the stronger environmental excitation.

Figure 7-14 depicts RMSE as a function of cable length for the same range of sea states. In general RMSE decreases with increasing cable length. Again, plateau-like regions can be identified. There are ranges in which variations in cable length lead to a pronounced reduction in RMSE and ranges in which further extension or shortening has only a marginal effect. For sea state 0, RMSE remains close to zero and is nearly insensitive to cable length. For sea states 1–3, RMSE shows a strong dependency on cable length and can be significantly reduced by increasing the cable length, consistent with the corresponding rise in DS. For sea states 4 and above, the reduction in RMSE with increasing cable length becomes small, mirroring the limited improvement seen in DS. Overall, the results indicate that increasing cable length is an effective measure to enhance LARD towing and docking performance at low to moderate sea states, while its beneficial effect is strongly diminished in more severe sea conditions.

It should be noted that the curves represent mean values computed from the corresponding time series. Consequently, the increasing wave height and associated wave-induced loads as well as individual large waves can influence the metrics. While the overall excitation level rises, pronounced transient excursions from larger waves that temporarily degrade towing stability. In this way the observed reduction in DS reflects the cumulative effect of more energetic sea conditions rather than solely the presence of rare, particularly high waves.

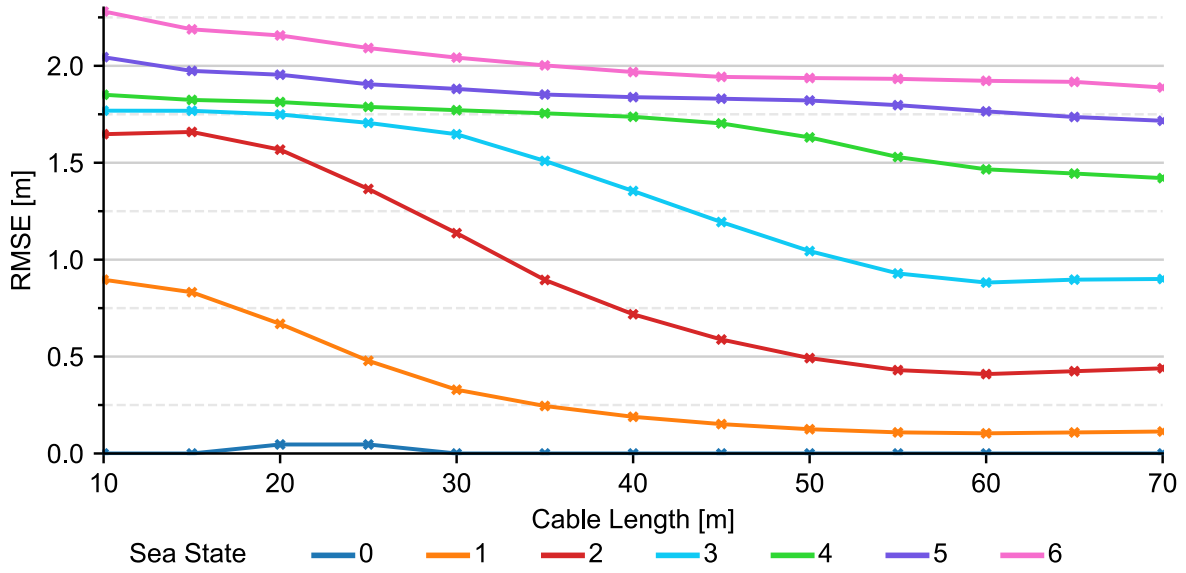


Figure 7-14: RMSE vs Cable Length grouped by Sea State

7.2.4 Vessel length

Analogous to the previous investigation of cable length, Figure 7-15 and Figure 7-16 show DS and RMSE plotted against towing cable length differentiated by sea state and additionally by vessel length (15 m, 30 m, 50 m and 80 m), represented by different line styles. As before, the curves are based on mean values from Dataset1, which denotes averages taken over all available Dataset1 cases that are not explicitly distinguished in the legend. Accordingly, the curves represent mean DS and RMSE values aggregated across the full set of wave headings, attachment-point configurations, towing cable lengths and other Dataset1 parameters (like towing velocity of 1 m/s as well as RAOs & floats and sinkers considered in the simulation), while only sea state and vessel length are shown as differentiating factors in the figures. For clarity, only sea states 2, 4 and 6 are displayed in the figures.

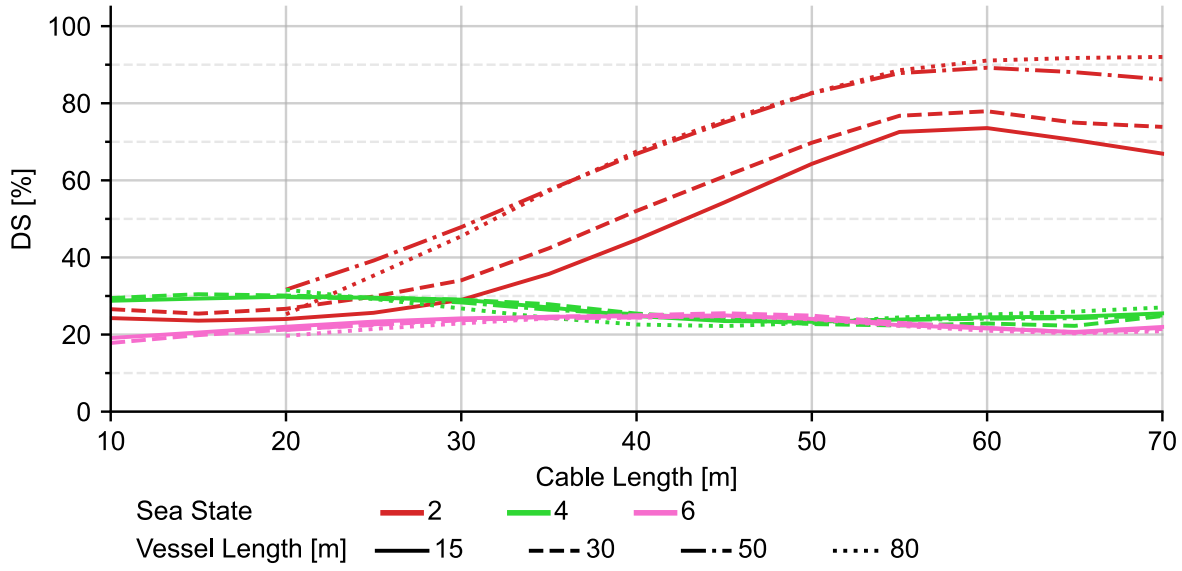


Figure 7-15: DS vs Cable Length grouped by Sea State and Vessel Length

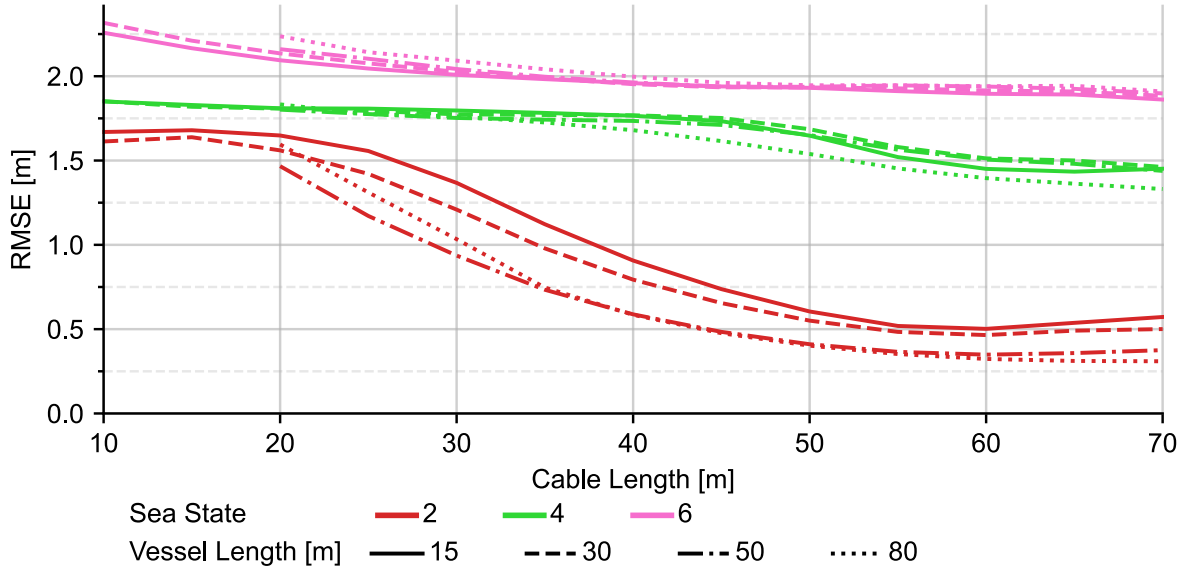


Figure 7-16: RMSE vs Cable Length grouped by Sea State and Vessel Length

Overall, the same qualitative trends as in the cable-length analysis are observed. For each sea state, DS generally increases and RMSE decreases with increasing cable length, with both metrics tending towards plateau regions at larger cable lengths. The curves for the different vessel lengths lie very close to each other, particularly at sea states 4 and 6, where the effect of vessel length on DS and RMSE is minor compared with the dominant influence of sea state and cable length. At sea state 2, a somewhat larger spread between the vessel-length curves can be seen. Here, a general tendency emerges that longer vessels are associated with slightly higher DS and correspondingly lower RMSE values. In these cases, the maximum differences between the shortest and longest considered vessel length are approx. 20 % on DS and 0.8 m in RMSE.

To quantify the influence of vessel motions in waves on the towing behaviour of the LARD, additional simulations were carried out in which the vessel RAOs were set to zero. In this configuration, the vessel is not excited by the incident waves and therefore moves at a constant forward speed without any roll, pitch or yaw motion, irrespective of sea state. Figure 7-17 and Figure 7-18 present DS and RMSE, respectively, as functions of wave direction for sea states 2, 4 and 6, comparing cases with considered vessel RAOs to cases with RAOs set to zero. The results are based on mean values from Dataset2 and thus represent averages over the corresponding combinations of the remaining parameters.
With exception of the characteristic bulge at and around 90° wave direction for vessel lengths with active RAOs the cases with RAOs set to zero consistently exhibit significantly higher DS and markedly lower RMSE than the corresponding cases. This indicates that vessel motions in moderate seas contribute substantially to the degradation of towing and docking performance. This trend is particularly noticeable at sea state 2 and 4. While a similar, though less pronounced, trend is observed at sea state 6, where the differences between both configurations are still evident, especially in terms of DS. This suggests that, in more severe sea conditions, the relative contribution of vessel motions to the overall excitation diminishes and the direct wave loading on the towing cable and the LARD itself becomes the dominant factor governing DS and RMSE.

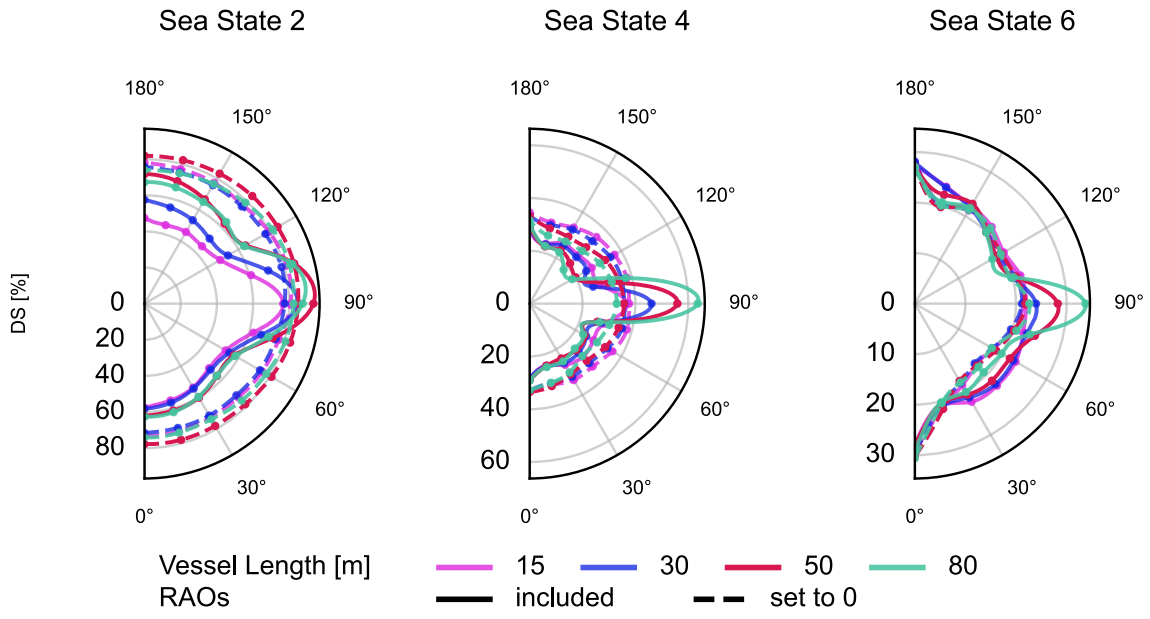


Figure 7-17: DS vs Wave Direction grouped by Vessel Length and Vessel RAOs

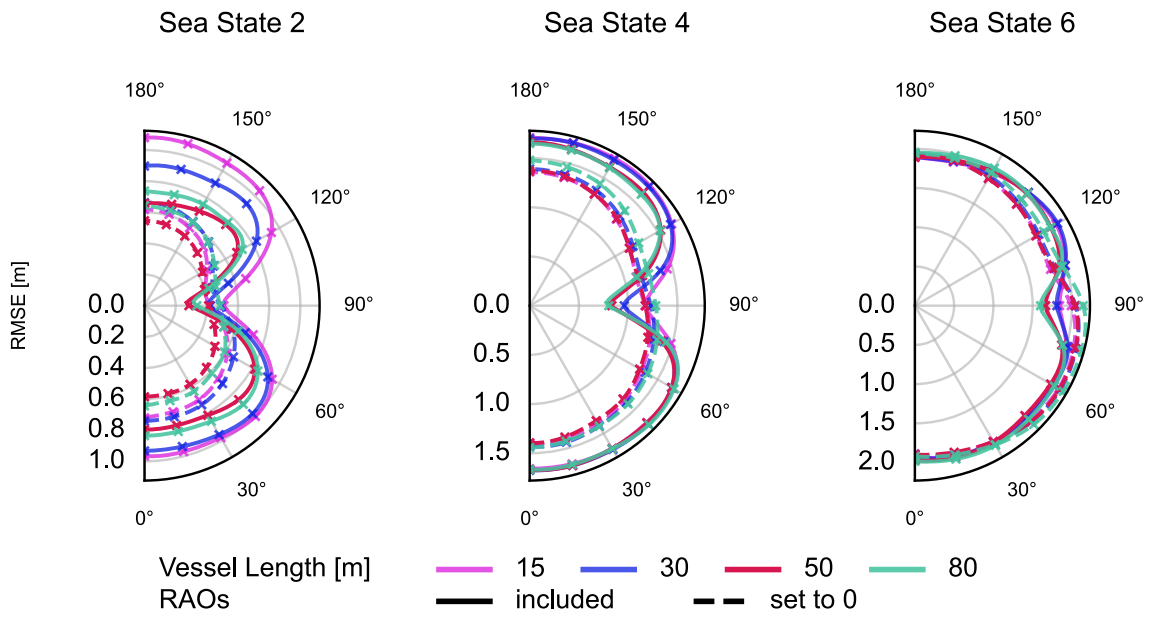


Figure 7-18: RMSE vs Wave Direction grouped by Vessel Length and Vessel RAOs

It is further noted that the curves obtained with RAOs set to zero are not necessarily symmetric about 90° wave direction axis, with this effect being most pronounced at sea state 6 for both DS and RMSE. Since vessel motions are suppressed, these asymmetries might originate from the wave excitation of the towing cable and LARD itself. The relative wave kinematics experienced by the towed body differ between head seas and following seas. This speed-induced difference between opposing directions (e.g. waves approaching from ahead versus from astern) becomes increasingly relevant in more energetic seas, which provides a plausible explanation for the stronger asymmetry observed at sea state 6.

Figure 7-19 shows DS and RMSE as functions of towing cable length for sea state 2.

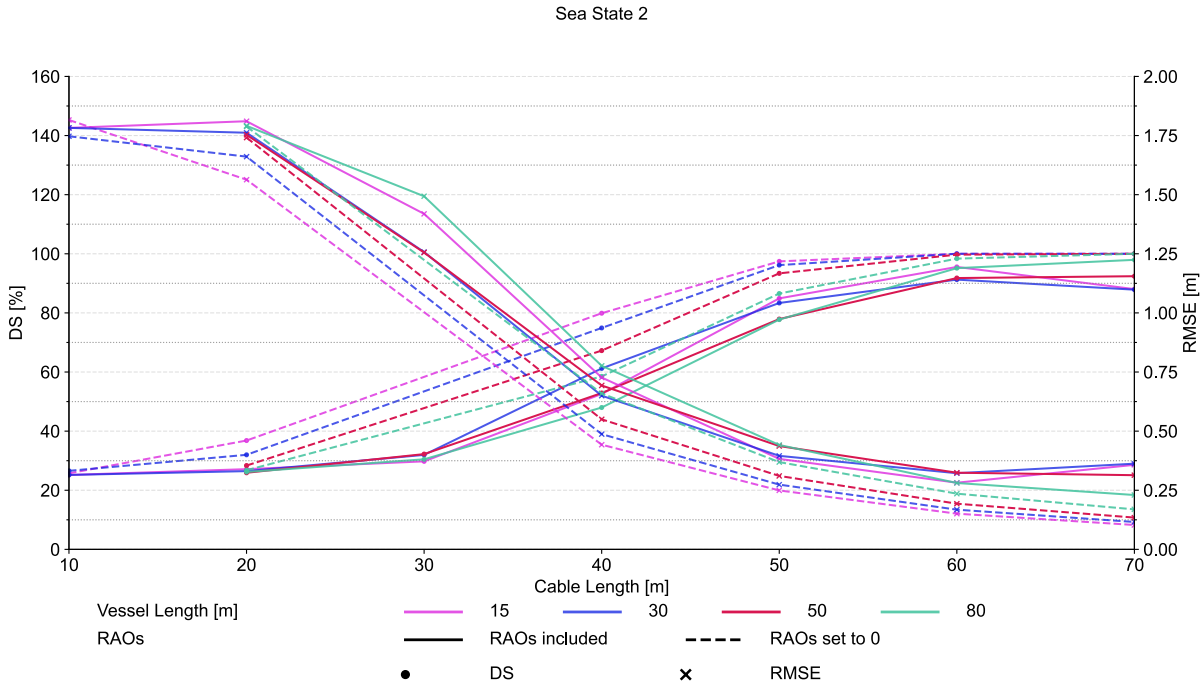


Figure 7-19: DS and RMSE vs Cable Length grouped by Vessel Length and Vessel RAOs

Different vessel lengths (15 m, 30 m, 50 m and 80 m) are distinguished by line colour, while the line style indicates whether vessel RAOs are included or set to zero. DS values are marked by circular symbols (left y axis) and RMSE values by crosses (right y axis). Overall, DS and RMSE configurations follow a very similar qualitative trend over cable length. For DS, the curves corresponding to simulations with RAOs set to zero lie consistently above those with active RAOs. In both cases, DS increases with cable length and tends towards a plateau. When vessel motions are suppressed (RAOs = 0), DS approaches 100 % for all vessel lengths at cable lengths of approximately 60 m and above. For the cases with active RAOs, the curves also tend towards saturation but do not fully reach 100 %; only the 80 m vessel comes close to this level. The RMSE curves exhibit an analogous behaviour. All configurations show a decreasing RMSE with increasing cable length, again following similar trajectories. However, whenever the vessel RAOs are set to zero, the RMSE levels remain systematically lower than for the corresponding cases with active RAOs.

The vertical offset between the two sets of curves quantifies the contribution of vessel motions to the overall excitation of the towing system. At the same time, the RMSE does not vanish, even for long cables and RAOs = 0. This indicates that a residual positional error persists purely due to direct wave excitation of the towing cable and the LARD itself. The remaining differences between the 0-RAO curves for different vessel lengths can be attributed to the vertical position of the attachment point. The cable is always connected at a defined height above the waterline that scales with vessel size. Consequently, the length of cable actually submerged and exposed to wave loading varies with vessel length, as does the relative position of the LARD with respect to the vessel. These geometric effects explain the slight systematic differences observed between the individual 0-RAO curves for different vessel lengths.
A similar behaviour for DS and RMSE is observed at higher sea states, although the differences between the configurations become progressively less pronounced as sea state increases.

7.2.5 Attachment point

To assess the influence of the cable attachment point on the metrics DS and RMSE, simulations were carried out using the three attachment configurations introduced in Section 7.1.3: mid-stern, starboard side and stern 1/3 starboard. The three cable attachment points are illustrated in

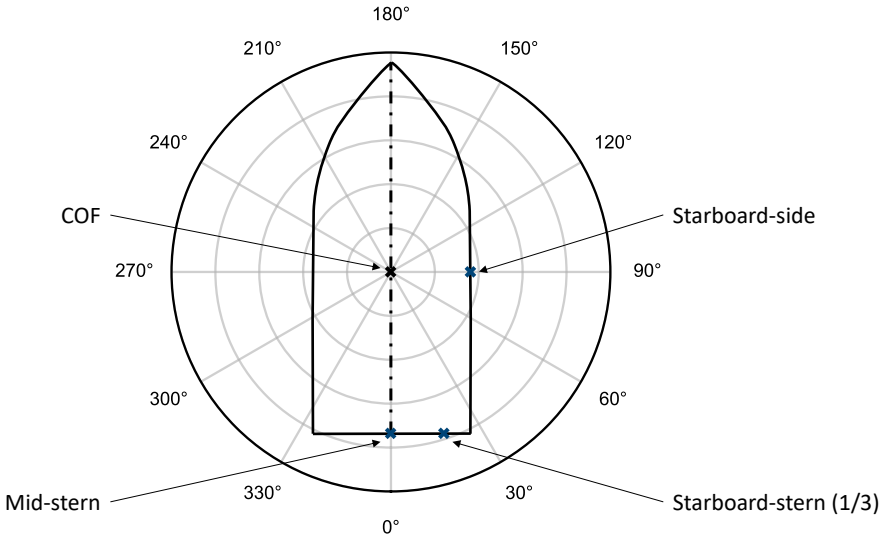


Figure 7-20: Towing cable attachment points in respect to the wave direction

respect to the wave direction in Figure 7-20. For each of the considered vessel lengths (15 m, 30 m, 50 m and 80 m), DS and RMSE are plotted as functions of wave direction and subdivided by sea state and attachment point. The DS distributions are shown in Figure 7-21 and the corresponding RMSE distributions in Figure 7-22. The curves are based on mean values from Dataset1. The wave direction was varied from 0° to 360°, such that for the starboard-side and stern 1/3 starboard attachments both windward and leeward situations of the LARD relative to the incident waves are captured. Previously discussed general trends with respect to sea state and wave direction are not repeated as the focus is on the differences between attachment points.

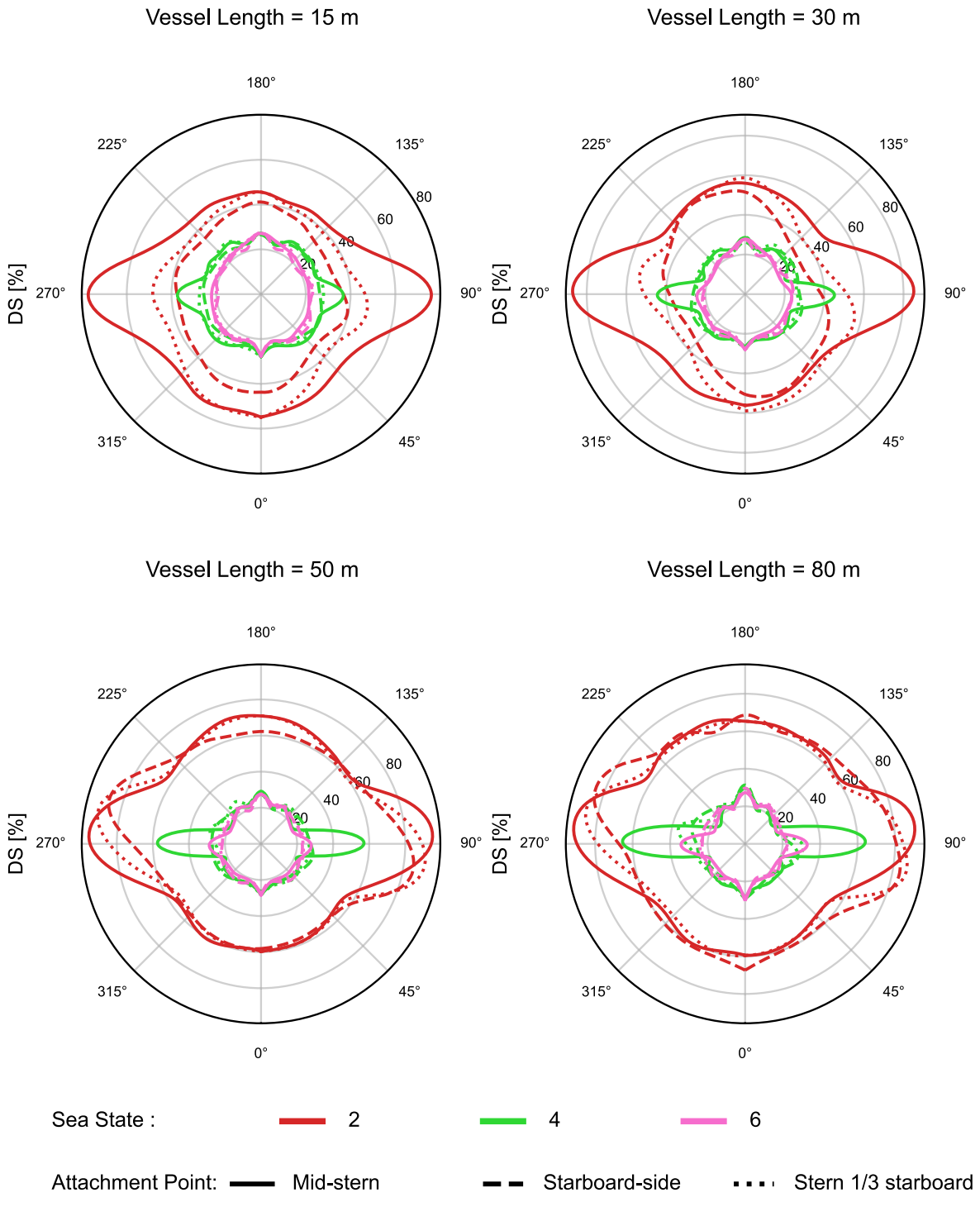


Figure 7-21: DS vs Wave Direction grouped by Sea State and Attachment Point

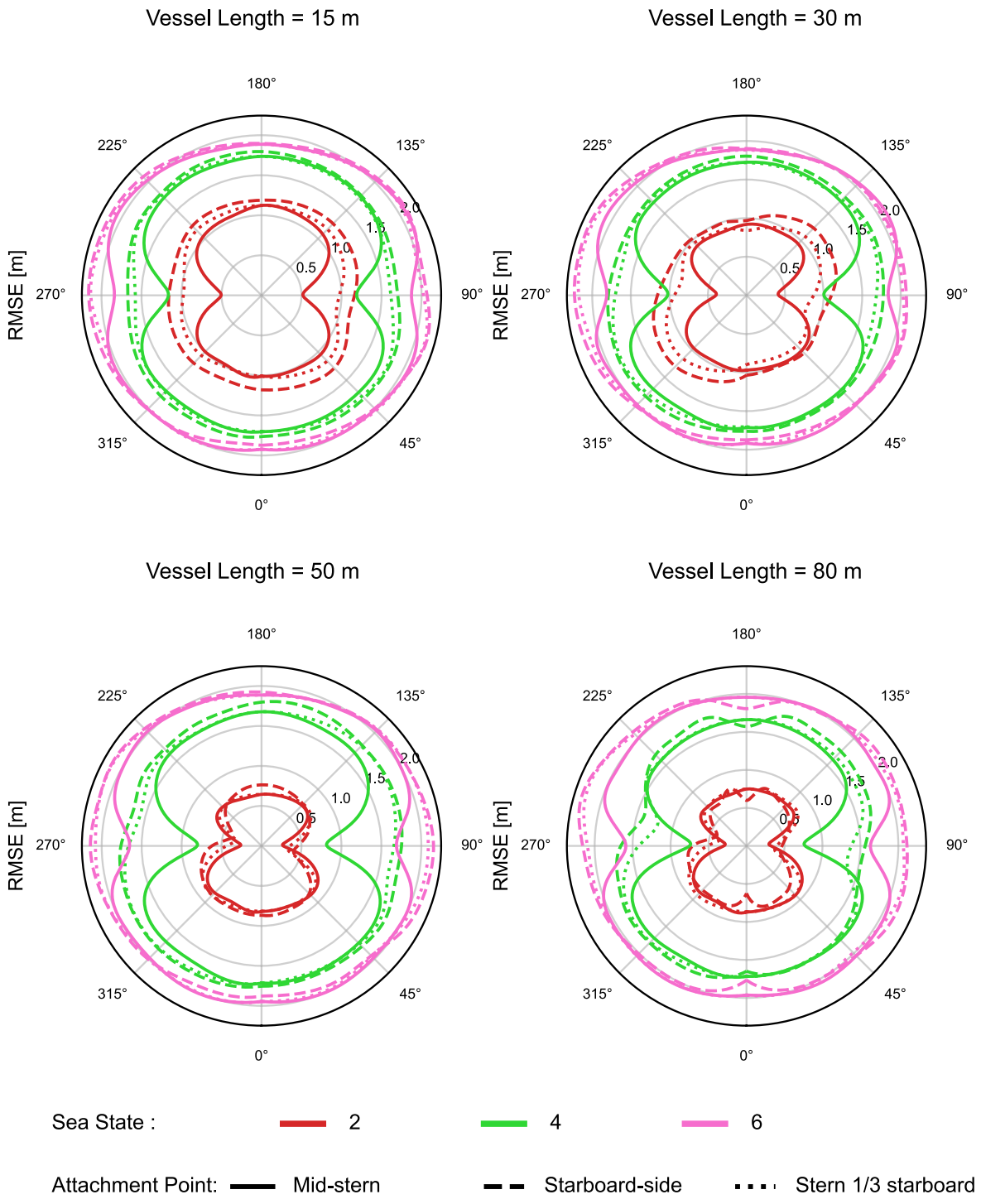


Figure 7-22: RMSE vs Wave Direction grouped by Sea State and Attachment Point

For the mid-stern attachment point pronounced improvements of DS and RMSE are consistently observed for beam seas (around 90° and 270°) across all vessel lengths. This behaviour is attributed to the directional coupling between wave excitation, vessel response and tow-point motion. For beam seas, the vessel response is dominated by roll motion. The dependency of this effect on the attachment-point location is particular evident by comparing beam and head as well as following seas. For the mid-stern attachment, which lies within the roll axis of the vessel, the reduction in RMSE at 90° and 270° is most pronounced, whereas it is weakest for the starboard-side attachment, which is farthest from the roll axis and thus

experiences the largest roll-induced tow-point excursions. In contrast, for the starboard-side attachment point an improvement in DS and RMSE can be observed for head and following seas (around 0° and 180°). This is attributed to the fact that the attachment is located closer to the vessel's pitch axis. For these wave directions, the pitch motion induces comparatively smaller tow-point excursions at the starboard-side location than at the other attachment points, for which the same wave directions lead to little or no improvement. This effect is particularly evident in the DS and RMSE distributions of the 80 m vessel, where the starboard-side attachment exhibits a clear reduction in response measures at 0° and 180° compared with the mid-stern and stern 1/3 starboard configurations.

As expected for the mid-stern attachment, both DS and RMSE are always symmetric about the vessel longitudinal centreline irrespective of vessel length. In these cases, the response is identical for waves approaching from port and starboard and the curves in the polar plots are mirror-symmetric with respect to the vertical axis. For the off-centre attachments (starboard side and stern 1/3 starboard), this symmetry is broken and clear differences emerge between wave directions in which the LARD is located on the windward side of the vessel and those in which it is on the leeward side.

A plausible additional contributor to these windward–leeward differences is a vessel "shielding" (or "shadow-zone") effect. When waves approach from the side opposite to the LARD, the hull can partially reflect and diffract the incident wave field, locally reducing wave heights on the lee side and thereby weakening the direct wave loading on the cable–LARD system. Such lee-side sheltering is well known in offshore operations and is actively exploited by selecting headings that maximise the calm region on the lee side for lifting and recovery tasks. However, the degree of shelter depends on wavelength relative to vessel length, wave steepness and diffraction around the hull, such that a complete "wave block" is not expected. Accordingly, the observed attachment-dependent asymmetries can be interpreted as a combined effect of direction-dependent vessel motion transfer to the tow point and direction-dependent modification of the local wave environment at the LARD by hull-induced reflection/diffraction, i.e. a partial shielding effect. [205]

This effect is particularly evident for the 30 m vessel at sea state 2. In the DS plot (top right hand corner of Figure 7-21), the variation of DS with wave direction is no longer symmetric to the vertical axis. Instead, DS reaches noticeably higher values in the sector between approximately 45° and 90° than in the opposite sector between about 270° and 315°. In this example, the higher DS occurs for waves approaching from the side on which the LARS is installed. The corresponding RMSE distribution for the same configuration (top right hand corner of Figure 7-22) shows a consistent pattern. The RMSE is reduced in the same favourable sector where DS is enhanced, indicating improved towing stability of the LARD when it is located on the wave-facing side of the vessel for waves coming from astern with an angle. For waves coming from bow-quartering directions, the example of the 30 m vessel at sea state 2 reveals higher DS values for configurations in which the LARS is installed on the leeward side of the vessel (compare 105°-150° to 195°-255° of the top right hand plots in Figure 7-21 and Figure 7-22). So quartering seas from astern tend to favour the leeward side, while quartering seas from ahead tend to favour the weather side. Similar, though less pronounced, trends can be identified for the other vessels and sea states, both in terms of DS and RMSE. Overall, the results show that while sea state and cable length remain the dominant parameters, the choice of attachment point can introduce systematic, direction-dependent variations in DS and RMSE.

Despite these described benefits of placing the LARS on the wave-facing or leeward side, the operational constraints on board the carrier vessel must be taken into account. If the crane is located on the side from which the waves approach, the towline may be pressed against the vessel hull, which either requires a sufficiently large crane outreach or may lead to frequent contact between the towing cable and the ship side. While such contact might be tolerable during simple straight-line towing, it becomes critical during the actual lifting process, when the LARD with the captured AUV approaches both the vessel and the free surface and the risk of collision between LARD and hull increases. In addition, the cable routing must always ensure that the towing cable does not pass in the vicinity of the propeller or rudder. A minimum clearance to these critical components is essential to avoid entanglement or damage and thus imposes practical limits on the favourable positioning of the LARD and the associated lifting system.

7.2.6 Floats and sinkers

Within Dataset2, the effect of floats and sinkers along the towing cable was investigated. Figure 7-23 shows DS and RMSE plotted against towing cable length for sea state 2. Vessel length is distinguished by line colour, while the line style indicates whether floats and sinkers are included or omitted. DS values are marked by circular symbols and RMSE values by crosses. At short cable lengths of approximately 10–20 m, the DS curves with and without floats and sinkers lie close to each other, indicating only minor differences in performance in this range. With increasing cable length, DS increases as observed previously. However, the relative ranking between both configurations is not strictly monotonic. In intermediate ranges, configurations without floats and sinkers can temporarily exhibit slightly higher DS than those with floats and sinkers. One example is the 50 m vessel, where this behaviour is visible for cable lengths of roughly 20–45 m. At larger cable lengths, the trend becomes consistent: configurations with floats and sinkers systematically achieve higher DS than configurations without them.

The RMSE results provide a clearer distinction between both configurations. With the exception of the 30 m vessel, omitting floats and sinkers leads to noticeably higher RMSE

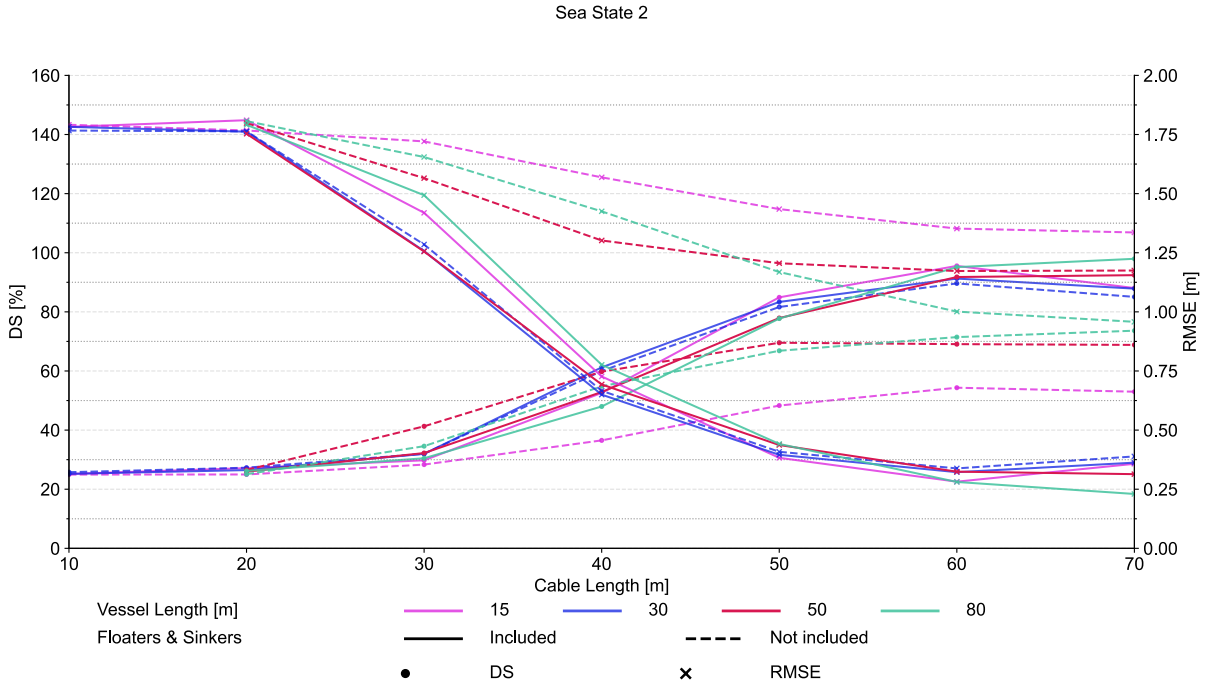


Figure 7-23: DS and RMSE vs Cable Length grouped by Vessel Length and Clump Type

values, indicating poorer towing stability and larger positional deviations of the LARD. For the 30 m vessel, both DS and RMSE remain very similar regardless of whether floats and sinkers are included. For the other vessel lengths, the separation between the curves with and without floats and sinkers is more pronounced. A comparable pattern for DS and RMSE is found at higher sea states. However, the differences between the configurations diminish progressively as the sea state increases.

7.2.7 Towing velocity

Three different towing velocities of 0.5, 1.0 and 1.5 m/s were investigated. Therefore the towing speed of the host vessel was changed, while the LARD hydrodynamic coefficient set was kept. This is justified by the preceding velocity study (see section 6.3.3) and the velocity independence of the coefficients. Figure 7-24 and Figure 7-25 present DS and RMSE,

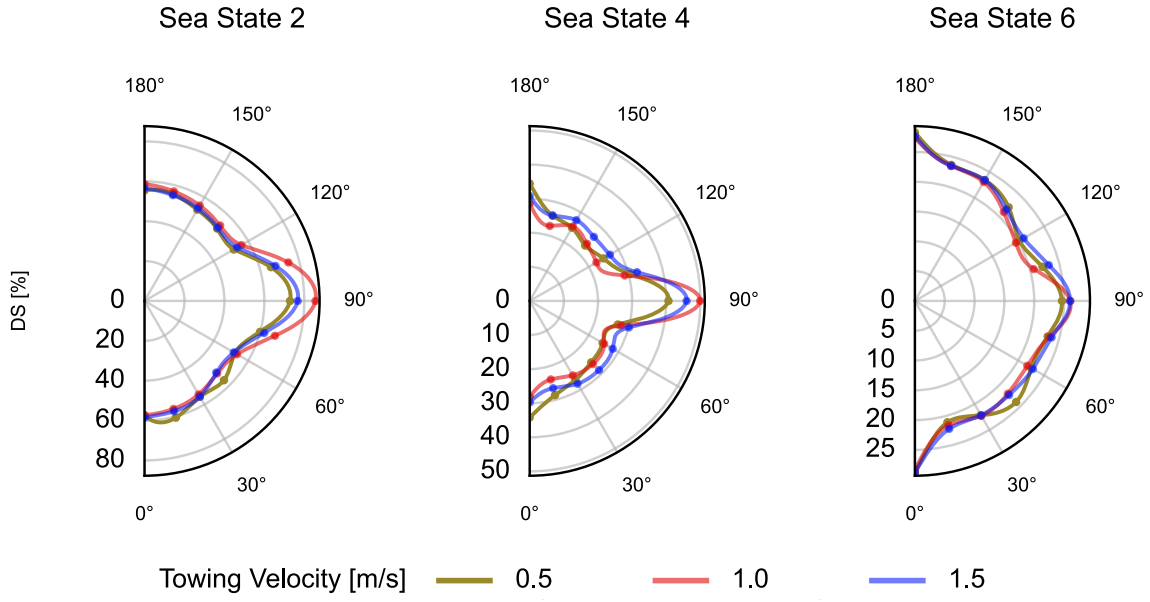


Figure 7-24: DS vs Wave Direction grouped by Sea State and Towing Velocity

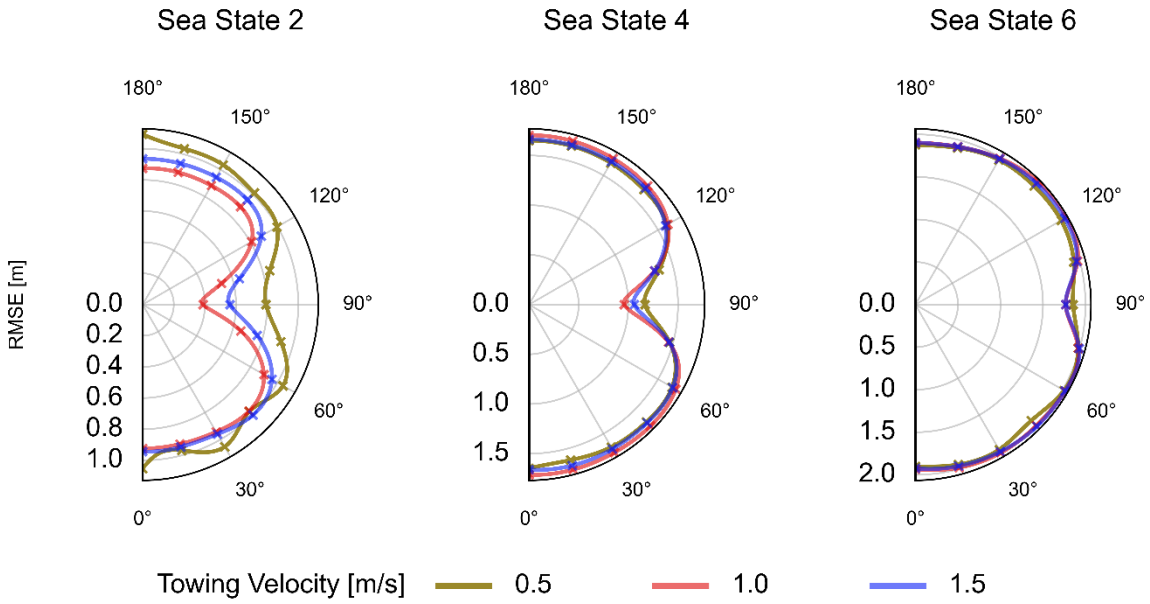


Figure 7-25: RMSE vs Wave Direction grouped by Sea State and Towing Velocity

respectively, in polar plots as functions of wave direction for sea states 2, 4 and 6, distinguished by towing speed. In both figures, the curves for the three speeds lie very close to one another, indicating that the ±50 % variation around the reference velocity of 1.0 m/s produces only modest changes in overall LARD performance. The ranking of the speeds is not uniform across all conditions. For sea state 2, DS is generally highest at 1.0 m/s, particularly in the sector between roughly 60° and 180°. At sea state 4, DS at 90° is again maximised at 1.0 m/s. However, in the neighbouring angular range around 30°-75° and 115°-150°, the higher speed of 1.5 m/s becomes slightly more advantageous, whereas in head and following seas (around 0° and 180°) the lower speed of 0.5 m/s tends to yield better DS. At sea state 6, the three curves practically collapse onto each other and no systematic speed-dependent differences in DS can be discerned.
The RMSE distributions exhibit analogous behaviour. At sea state 2, RMSE generally attains its lowest values at 90° with 1.0 m/s, consistent with the corresponding DS trends. For sea states 4 and 6, the RMSE curves for the three towing speeds are almost indistinguishable over most wave directions, with only small deviations, for example near 90°. Overall, the results confirm the very low feature importance of towing speed identified in the random forest analysis. Within the investigated range of parameters, towing speed has only a minor influence on DS and RMSE compared with dominant parameters such as sea state and cable length.

Overall, the analyses have clarified how the different parameters affect the general towing and docking behaviour of the LARD. It must be kept in mind that the presented curves are based on mean values over multiple combinations of the remaining parameters, so each data point represents an underlying range of possible DS and RMSE outcomes. For reasons of clarity, this spread is not explicitly visualised (e.g. by error bars or confidence intervals), as this would significantly reduce the readability of the figures. Consequently, the results should be interpreted as system-level trends rather than as exact predictions for specific configurations.

Within this framework, robust global trends and parameter sensitivities were identified. At the same time, inspection of individual parameter combinations shows that substantially higher DS values and lower RMSE levels can be achieved than illustrated by the aggregated mean curves. This is particularly relevant in view of the sometimes rather small mean DS and comparatively large RMSE values. Embedded in these averages are configurations that are considerably more favourable. The analysis therefore underlines the practical importance of systematically selecting advantageous parameter settings such as cable length, wave direction relative to the vessel heading, or attachment configuration under given, non-controllable boundary conditions (e.g. sea state). These findings highlight the scientific and operational relevance of the parametric study, as they provide concrete guidance on how to adjust controllable parameters to enhance the probability of successful LARD operation and, ultimately, the safe L&R of AUVs.

8. Conclusions

The central challenge in AUV L&R of safely establishing an initial physical connection between a free-moving AUV and a LARS (on a dynamically excited host platform) under realistic offshore conditions has been addressed by deliberately shifting the main robustness mechanism away from complex on-board autonomy and towards system configuration. The thesis focuses on the system design and performance analysis of the LARD and its behaviour within the coupled vessel–towing cable–LARD system. This framing is important because it clarifies what the thesis contributes at system level. Rather than optimising docking through increasingly sophisticated algorithms, the developed concept aims to shape the relative-motion environment at the docking interface through mechanical and hydromechanical design choices. Within the scope of this thesis, a realistic baseline capability for navigation, guidance and control on the vehicle side is assumed. Therefore, no dedicated GNC system for the AUV is designed or analysed in detail.
In practical terms, the LARD acts as a passive stabilising element that reduces relative motion and misalignment during the critical capture phase, thereby lowering demands on the AUV's active control effort and making the establishment of first contact more repeatable, reliable and robust under environmental excitation.
Against this background, the thesis pursued two tightly linked objectives: first, to develop a concept for initial physical contact that meets functional and operational requirements with respect to automation, universality and resilience in higher sea states. And second, to identify and demonstrate a coherent methodological framework for estimating the probability of successful operation across varying environmental and operational boundary conditions. The resulting contribution is therefore not only a device concept, but also a transferable assessment procedure that can be re-applied to other vessels, towing arrangements and operational scenarios in a structured and quantitative way.

Best-practice interpretation for realistic North Sea and Baltic Sea operations can be derived based on the consolidated findings of Chapter 7, creating the link between results, trade-offs and operational outcomes. They should be read as configuration logic under the uncertainty described in section 7.1.7. Sea state is an external constraint that can be forecasted but not controlled, whereas cable length, wave heading relative to the vessel, towing velocity as well as the optional use of floats and sinkers are controllable levers that can be adjusted to increase the likelihood of successful docking. Depending on the (lifting) capabilities available on board, different cable attachment points may also be used. Furthermore, the optimal vessel (depending on the dimension) could also be selected if several different ones were available for the recovery of the AUV. Importantly, the aggregated curves presented in the parametric analysis results (section 7.2) reflect mean values over multiple combinations of remaining parameters. Each point therefore represents an underlying distribution of outcomes. The results must be interpreted as system-level trends rather than exact predictions for any single configuration and the practical value lies precisely in systematically selecting advantageous parameter settings within those trends.

As sea state was identified as the dominant feasibility driver, an operationally meaningful interpretation of the results begins with explicit sea-state-dependent decision-making. Recovery should be planned within an operating window and if the forecasted sea state exceeds the range in which controllable levers produce meaningful gains, the preferred "best practice" is not to attempt to compensate through minor tuning but to defer recovery or switch to alternative

procedures.
Within the controllable levers, towing cable length emerges as the strongest and most actionable parameter. In low to moderate sea states, systematically increasing cable length can materially improve docking performance because the cable acts as a dynamic filter between vessel motion and the submerged device, reducing the transmission of motion from the carrier platform towards the LARD and in this way enabling a more stable relative-motion regime at the docking interface. Operationally, this implies that cable management should be treated as a primary control variable during recovery. The system should be brought to a cable-length regime where performance approaches a plateau, rather than maximising or minimising length ad hoc. From a design perspective, this directly supports concrete requirements like sufficient winch range, safe handling procedures and the ability to reliably reach and maintain the favourable length regime under realistic constraints (such as deck layout, safe working loads and potential restrictions due to finite water depth). The associated trade-off is that longer cables increase handling complexity and may introduce additional constraints (e.g., risk of seabed contact in shallow water and increased swept volume), so the best practice is not “as long as possible”, but “long enough to enter the favourable dynamic regime while remaining operationally safe”.
Wave heading relative to the vessel provides a second major operational lever. The parametric results demonstrate that the docking success probability and the deviation measures can vary substantially with wave direction, which is consistent with the fact that vessel motions and therefore excitation transmitted into the tow system are directionally dependent. The decision implication is immediate and practical: whenever mission constraints permit, recovery should be executed in a wave-heading sector that minimises the vessel motion components most detrimental to capture and wave heading should be selected jointly with cable length rather than as an afterthought. This joint tuning is especially relevant because “good” headings can amplify the benefits of advantageous cable settings, while “bad” headings can suppress them and effectively shift the system towards an excitation-dominated regime in which configuration levers have reduced effect.
The analysis results for vessel itself matter both in early design and in operational selection of host platforms. Even within the scope of a single investigated vessel, the study highlights that seakeeping characteristics and their influence on transmitted excitation are central. In broader terms, this means that results must be embedded into concrete vessel choices. When planning operations in areas, where moderate to rough conditions occur more frequently (like the North Sea), selecting a host platform with favourable motion characteristics for the expected conditions can be more impactful than fine-tuning secondary parameters. Conversely, in areas, where operational windows with lower to moderate sea states are more common (like the Baltic Sea), configuration levers such as cable length and wave heading can more often be exploited to reach robust docking behaviour. Of course, advantageous motion characteristics of the vessel have beneficial effects in all sea areas. In this regard, it is more appropriate to comprehend that under more demanding environmental conditions which cannot be influenced, the motion characteristics of the vessel can be less easily compensated by adjustable parameters.
The attachment point of the towing cable adds another controllable, yet operationally constrained lever. Different attachment points change the kinematic and dynamic coupling between vessel and tow system and can therefore shift docking performance. In practice, however, the feasible set of attachment points is bounded by the position of the lifting devices as well as clearance, safe towline routing, deck layout and collision avoidance. If more than one option is available, the parametric insights can be utilised to select attachment options that reduce relative motion and improve DS under the given conditions.

Floats and sinkers, can be interpreted as robustness enhancers that further shape the towline dynamics, for example by the transmission of vessel motions through the line. The practical implication is again decision-relevant. These elements are useful “add-ons” when operations are within the regime where configuration sensitivity is high (typically low to moderate sea states), yet their ability to compensate for dominant excitation diminishes as sea states increase. Hence, best practice is to include them as available operational options and to treat their selection as part of a systematic configuration strategy.
In contrast, towing velocity appears as a comparatively weak lever within the investigated range from 0.5 m/s up to 1.5 m/s. This matters for operational decision-making because it clarifies prioritisation: speed should primarily be chosen based on mission constraints and safety considerations and only secondarily used for fine tuning where sensitivity is demonstrated. In other words, best practice is to first set the high-impact levers like sea-state-dependent timing, wave heading, cable length and feasible attachment configuration before spending operational effort on speed optimisation, which the study indicates has only minor influence.

Taken together, these consolidated findings provide a concrete “best practice” narrative for typical operations. For low to moderate sea states, the practical emphasis lies on exploiting controllable levers to enter and maintain favourable dynamic regimes. The most important influencing factors are choosing a wave heading to limit vessel excitation, adjusting cable length into the beneficial range and optionally usage of floats/sinkers to further stabilise the tow system. For higher sea states, the emphasis shifts towards stricter sea-state-dependent gating and toward platform/heading choices that reduce transmitted excitation, because the environment more frequently approaches regimes where configuration sensitivities diminish. In both contexts, the key practical message is that the parametric database is not merely descriptive. It can serve as a decision basis by casting the results into rule sets, lookup maps, or decision-support tools that recommend feasible configurations and rank alternatives when ideal settings cannot be achieved due to technical or operational constraints.

As emphasised repeatedly in section 7.2, the consolidated observations derived from the parametric study represent trends obtained from averaged responses across a large number of simulations. Each point on the aggregated curves therefore reflects a mean value over multiple combinations of the remaining parameters and, by implication, an underlying distribution of outcomes. These generalised statements are consequently not expected to hold for every individual case in a strict sense. The practical value of the simulation campaign lies precisely in using the results as a structured decision basis for specific operational boundary conditions. The appropriate way to exploit the results is to use the parametric analysis as a structured database. The results are most effectively exploited through a database that maps non-controllable inputs (i.e., the external boundary conditions that cannot be influenced during recovery) to an optimal combination of controllable configuration parameters. In the present context, this means that, once sea state, vessel characteristics (dimensions) and wave direction are specified or measured, the database can be queried to identify advantageous settings of the parameters that can be adjusted by the operator or by onboard systems, most notably the vessel heading relative to the incoming waves (where feasible), towing cable length, the optional use of floats and sinkers and towing velocity. Depending on the lifting and deck-handling capabilities available on the host platform, alternative towing cable attachment points may also be selectable. Moreover, if multiple candidate host vessels were available for a given mission, the same database logic could support vessel selection by favouring platforms that yield more benign towing dynamics under the expected conditions.

The parametric analysis in section 7.2 is based on a large number of simulations with varying settings. The more than 25,000 simulated cases cannot be discussed individually in this work. In order to suggest not only the previously derived general trends but also the framework within which these trends apply or even in some cases not, the practical application of the database is presented by three representative examples. The purpose of the following examples is therefore not to restate the complete dataset, but to illustrate how the database operationalises the findings of section 7.2 and turns them into concrete configuration guidance for three representative scenarios.

In the first example, sea state 4 is assumed, with only a single host vessel of 80 m length available for recovery. Under these boundary conditions, the database predicts a maximum achievable DS of 87 %. Since DS denotes the percentage of time during which docking would be feasible according to the adopted criteria, a value of 87 % indicates a favourable operating regime for the given scenario. This optimum is achieved for waves from 90° or 270° (beam seas), a cable length of 50 m, towing at 1.0 m/s, using floats and sinkers and selecting mid-stern attachment point. The sensitivity to configuration choices becomes immediately apparent when individual controllable levers are constrained or modified. In the following comparison, only one parameter is changed at a time while all others correspond to the setting described above for the maximum DS. For example, omitting floats and sinkers reduces DS to 19 %. Further, while towing speed was identified as a comparatively weak lever in the global trends, the database reveals that in specific cases it can still produce meaningful changes. Under the parameter set for the maximum DS of 87 %, reducing speed to 0.5 m/s lowers DS to roughly 53 %, whereas increasing speed to 1.5 m/s yields around 73 %, confirming an optimum near 1.0 m/s under the investigated rage. An analogous case-specific sensitivity is observed for cable length. Shortening the cable to 20 m reduces DS to approximately 30 %. Finally, isolating the effect of wave direction illustrates why the database is required beyond the generalised trends. With all parameters fixed at their value for the optimum DS except wave direction, waves from 120°/240° lead to a particularly unfavourable outcome of 8 % DS, while head seas yield around 32 % DS.
In this context, it should be noted that the comparisons were conducted under the assumption that only a single parameter was varied, while all remaining parameters were fixed at the values previously identified as yielding the maximum achievable DS of 87 %. This represents a substantial constraint on this example. The implication can be illustrated by treating head-sea condition as fixed in addition to the considered sea state 4 and an 80 m host vessel. In this scenario a DS value of 46 % can still be achieved by selecting a cable length of 25 m, a starboard-side attachment, the use of floats and sinkers and a towing velocity of 1 m/s.
This example demonstrates both the practical relevance of the general trends and the necessity of case-specific optimisation. It therefore underscores that the broad tendencies described in section 7.2 are recognisable, yet the ranking and the magnitude of effects are strongly case dependent. Consequently, the best configuration for a given set of non-controllable conditions must be determined through targeted querying of the data basis.

A second example considers milder conditions at sea state 2 on a smaller host platform with a length of 30 m. For a towing cable length of 25 m, beam seas (90°/270°), a towing speed of 1.0 m/s, the mid-stern attachment point and the use of floats and sinkers, the database predicts a DS of approximately 78 %. If, under otherwise identical conditions, the waves approach from ahead, DS reduces to about 37 %, reinforcing the practical importance of heading selection when feasible. Under beam-sea conditions, but for alternative attachment points, DS again

drops substantially, to about 23 % for starboard-side attachment and 29 % for starboard-stern attachment, indicating that attachment configuration can remain influential even at relatively low sea states when the system operates near threshold conditions. The same scenario also illustrates the practical value of cable-length adjustability. Increasing the cable length by only 5 m (from 25 m to 30 m) under otherwise identical conditions raises DS from 78 % to approximately 87 %. When varying towing speed for the case with the 30 m cable, the database indicates that 0.5 m/s yields only about 44 % DS, whereas 1.5 m/s produces around 72 %. In combination, this example shows how the database supports operational compromise: if a preferred wave heading cannot be maintained, or if the attachment point is fixed by deck layout, the remaining levers can be re-optimised to recover as much performance as possible within the feasible configuration space.

The third example examines an extreme scenario with sea state 6 on a 50 m vessel to demonstrate the limits of configurability. For beam seas (90°/270°), a cable length of 60 m, a towing speed of 1.0 m/s, the mid-stern attachment point and the use of floats and sinkers, the predicted DS is approximately 38 %. In this regime, the database reflects the trend that configuration sensitivity diminishes as environmental excitation becomes dominant. Increasing towing speed to 1.5 m/s does not improve performance in a meaningful way (remaining at about 38 %), while reducing speed to 0.5 m/s decreases DS slightly to around 33 %. However, some configuration changes remain clearly detrimental even under severe excitation. Keeping all other parameters fixed but shortening the cable from 60 m to 25 m reduces DS to roughly 19 %, indicating that, even under very adverse conditions, some configuration choices remain strongly detrimental. However, the attainable best-case performance remains limited by the sea state.

Taken together, the three examples demonstrate how the database-based use of the simulation campaign resolves the apparent contradiction between general trends and case-specific behaviour. The consolidated observations from section 7.2 remain valuable as guidance for prioritising levers and understanding physical sensitivities, yet the optimal configuration for a specific recovery attempt must be derived for the actual combination of boundary conditions at hand. Importantly, the database can also accommodate additional practical constraints. If, for example, a particular vessel heading must be maintained due to parallel operations, if towing speed is constrained, if only one attachment point is available, or if cable length is limited by onboard equipment, the optimisation can be performed within the restricted parameter space to identify the most stable and most robust achievable towing configuration. In this way, the simulation campaign provides not only physical insight, but also enables structured, repeatable decision-making for real operations.

The following outlines the main outcomes of the work and the methodological framework used to develop and validate the system. Building on a comprehensive review of existing L&R technologies and research, the thesis first established a clear baseline of the state of the art and identified current limitations with respect to automation, universality and operation in higher sea states. Based on this review and on the operational context, a structured set of requirements for the LARS was derived and discussed. These requirements formed the reference against which the developed concept and the subsequent analyses were evaluated.

The first main outcome of the thesis is the LARD design and the associated development of a concept for safely establishing the physical connection between the AUV and the LARS that fulfils the identified requirements. The concept is designed to operate in a fully automated manner and to be universally applicable to different AUV types, sizes and masses, without

relying on additional dedicated hardware on the vehicles. Furthermore, the concept explicitly targets operation in rougher sea conditions and aims to minimise restrictions caused by high sea states. In doing so, it seeks to increase AUV utilisation rates and to enable efficient and cost-effective operation of the carrier platforms.

The second major outcome of the thesis is the development and application of a coherent methodological framework for analysing the performance of the LARS and for estimating the probability of successful operation across a range of boundary conditions. This framework builds on several groups of methods that are consistently linked throughout the work.
First, methods from product development were used to generate, structure and refine solution principles. These methods supported the systematic creation and evaluation of concept variants, leading to the selection and elaboration of a preferred LARS configuration that meets the defined requirements. Second, methods from detailed mechanical design were applied to dimension the components, to select suitable components and to perform simplified strength and load calculations. These analyses ensured that the concept is not only functionally viable but also mechanically feasible for realistic loads and operating conditions.
Third, CFD methods were employed to determine key hydrodynamic parameters of the LARD, such as drag, added mass and damping coefficients. These simulations provided the hydrodynamic input data required for subsequent dynamic analyses. Fourth, dedicated model tests were designed and carried out to validate the numerical CFD results. The experimental programme included drag as well as forced oscillation tests. This validation step increased confidence in the numerical model and clarified where conservative assumptions are appropriate.
Finally, the validated hydrodynamic data were used as input to multibody dynamics simulations of the coupled system comprising the towing vessel, tow cable and LARS. These simulations formed the core of a parametric analysis investigating the influence of environmental and operational boundary conditions on the towing behaviour of the developed system. The varied parameters include sea state, wave direction, length of the towing cable, vessel length, attachment point of the towing cable on the vessel, the use of floats and sinkers and towing velocity. The detailed results of this study are presented and discussed in Section 7.2 and are therefore not repeated here. Based on the simulations, the probability of successful establishment of the physical connection can be estimated for the considered parameter combinations.

Within the scope of this work, the evaluation procedure was applied to a specific LARS configuration, allowing both general and configuration-specific patterns in the system response to be identified and discussed. The results demonstrate that the developed system exhibits substantial resilience to disruptive environmental conditions. In combination with its high degree of automation and its universal applicability to different AUV types, this confirms that all three main development objectives have been achieved.
At the same time, the analyses underline that the conclusions are, in a strict sense, valid for the investigated combination of vessel, towing cable and LARD. When other boundary conditions are considered, for example, a different vessel with a significantly different hull form, or alternative cable types, the performance of the LARS must be re-analysed using the same methodological framework in order to obtain reliable predictions. Therefore, the necessary methods are not only presented but their practical application using representative data was also illustrated, thereby providing a blueprint for future studies and for the adaptation of the system to other platforms and operating scenarios.

In summary, the work has achieved its primary objectives. A concept for safely establishing a physical connection between an AUV and a LARS has been developed that fulfils the requirements for automation, universal applicability and operation in demanding environmental conditions. In addition, suitable methods and procedures have been identified, combined and demonstrated for analysing the performance of the developed LARS and for assessing the probability of successful operation under varying environmental and operational boundary conditions. Together, the concept and the associated evaluation framework form a coherent contribution that supports the design, assessment and future optimisation of automated LARS solutions for AUVs.

8.1 Perspective

The outlook can be structured into three main directions. First, ways to extend and refine the investigations already carried out are presented. This includes refining the existing models, expanding the investigated range of parameters and performing additional studies to improve the robustness of the findings. Second, the broader context of the L&R process is considered. Beyond the primary focus of this work on establishing the physical contact between the AUV and the LARS, further interfaces to other disciplines arise, for example with AUV control and handling operations. These interfaces define where additional development work is required to ensure a reliable and safe end-to-end L&R operation. Finally, procedures to use the results obtained to advance and enable both support of the human operator and autonomous decision-making during the establishment of physical first contact are presented. In particular, the derived data can serve as a basis for decision-support tools or automated control strategies of the L&R operation.

The **extension and refinement of the analyses performed** in the investigation of the towing behaviour of the LARD can comprise several measures. Further parameter variations and extensions could be examined to improve the robustness of the identified trends and derive new conclusions. A straightforward next step would be adding smaller step sizes for the already investigated parameters. This would allow potential irregularities to be identified more clearly and would sharpen the interpolated trends. However, this approach has to be assessed in terms of computational effort.
In addition, the parameter ranges themselves could be further expanded. For example, higher sea states, longer cable lengths or different ship lengths and ship types could be considered. As discussed in Chapter 7, the current analysis is based on a single vessel and three specific attachment points of the towing cable. Future studies could therefore include other hull forms and additional cable attachment locations, thereby generating a broader and more generalisable understanding of the system behaviour.
In this context, there is also significant potential for the optimisation of individual design parameters. Besides alternative cable types, different cable materials with improved damping properties could be investigated. Likewise, the arrangement and the properties of floats and sinkers along the towing cable could be systematically varied. Both the positions and the magnitudes of buoyancy and weight forces may be adjusted with the aim of further reducing the transmission of vessel motions through the towing cable to the LARD. Given the large number of possible combinations, such studies would require a systematic optimisation strategy or a carefully designed design-of-experiments approach. This would make it possible to evaluate, in short parameter intervals, how specific modifications to the location or properties of buoyancy modules and weights influence the damping behaviour.

In principle, there are few strict limits to the extension of the current simulations. Various additional boundary conditions could be incorporated. A particularly relevant example is the investigation of finite water depth. Here, the interaction between cable length and water depth must be considered to avoid contact with the seabed. Further the use of winches with integrated heave compensation, which help mitigate the effects of vessel motion on the excitation of the trailing cable could be taken into account. Furthermore, the L&R from another UUV can also be considered. These aspects represent the most immediate and practically relevant extensions that can be derived from the current findings but can in turn be complemented by many further parameter variations.

A second direction for the extension and refinement of the analyses is the coupling of the multibody simulations with high-fidelity numerical flow analyses. In the present study, the focus was placed on the LARD, while the AUV itself was not explicitly included in the multibody analysis. To obtain a more complete picture of the coupled dynamics, the AUV could be integrated into the model, such that both the influence of the LARD on the AUV and the influence of the AUV on the LARD are captured. This is particularly relevant in the critical phase when the AUV approaches and enters the LARD. Such interactions could be examined both within the multibody framework and by means of additional CFD simulations. For instance, the wake behind the LARD could be analysed in more detail, with a specific focus on how this wake changes when the AUV penetrates into the flow field. A further option would be modelling selected cases from the multibody analysis by CFD methods in order to resolve the stern wake of the vessel. This would allow to analyse the influence of propeller-induced flow on the LARD and the whole towing process.

Finally, model tests offer a promising method to validate and extend the parametric multibody analysis. While the present experimental effort focused on the hydrodynamic characterisation of the LARD, future tests could address the entire system consisting of vessel, towing cable and LARD. For such experiments, a sufficiently long and large towing tank would be required to allow initial transients to decay and stable towing conditions to be established. As an alternative to testing a full ship model, the vessel motions at the cable attachment point could be imposed directly by the towing carriage. In this approach, the ship motions in waves would first be determined numerically. The resulting motion trajectory at the attachment point would then be prescribed as scaled motion input to the towing carriage. The physical model in the tank would thus consist only of the towing cable and the LARD, while the carriage reproduces the ship-induced motions at the attachment point. If the towing tank is equipped with a wave generator, the influence of waves on the towing process could also be incorporated. However, these experimental campaigns would require substantial effort and resources. Consequently, it may also be reasonable to consider the construction of a prototype in full-scale and to test it under real sea conditions, thereby directly assessing the performance and robustness of the system in its intended operational environment without the risk of scaling or modelling errors affecting the analysis.

Beyond the direct findings of this work, the results must be embedded into the **broader context of the overall L&R process** and the interfaces to the remaining disciplines must be clearly defined to enable a fully functional system. This includes, the alignment of the AUV with the LARD. Future work may combine the mechanically robust, passively stabilised towing configuration with advanced docking guidance and control approaches (e.g., adaptive or model-predictive strategies) to further increase capture robustness under uncertainty and time-varying disturbances.

Further, once physical first contact has been established and the AUV is secured inside the LARD, the complete system consisting of LARD and enclosed AUV must be recovered onto the host platform. This lifting operation introduces additional challenges related to crane-based or ramp-based handling under offshore conditions. However, in this area are many similar use cases from various sectors, so existing approaches can be applied. In this context, reference is made to work on offshore lifting operations like for example Szczotka [206].
By ensuring well-defined and consistent interfaces between the individual process steps, the smooth functioning of the overall LARS can be achieved. In the context of the present work, the establishment of an initial physical contact must be coordinated with both the preceding process of guiding the AUV into the LARD and the subsequent lifting operation, so that all stages interact reliably as parts of one integrated system.

Finally, the results presented in this thesis can be used to **advance and enable both support of the human operator and autonomous decision-making** during establishing initial physical contact. An important question in this context is at which stage these findings should be integrated. One application lies in the early design phase of a vessel. The insights into the towing behaviour of the LARD can be used, for example, to identify favourable positions for cranes or ramps that lead to more stable towing conditions of the LARD. In doing so, the specific hull form and its seakeeping characteristics must be taken into account, as well as the constraints imposed by other ship design requirements. This inevitably involves trade-offs between competing objectives, but it offers a systematic way to consider the L&R of AUVs already during the conceptual design of the host vessel. The methodology developed in this work can be transferred to a given hull form and used to perform dedicated analyses to support such design decisions.

A further application concerns the operational phase of LARS. The knowledge gained about the behaviour of the LARD under different environmental and system conditions can assist operators in selecting suitable operating windows and parameter settings. The parametric database generated in this work can be used as the basis for a ML algorithm that predicts the towing motion behaviour of the LARD even for combinations of conditions that were not explicitly covered in the original simulations. For a given set of external boundary conditions, provided either manually via a human–machine interface or automatically by the ship's systems, the algorithm can recommend optimal values for the controllable parameters of the LARS. If the ideal configuration is not feasible due to technical or operational constraints, the algorithm can rank alternative configurations according to their estimated probability of successful docking, thereby directly supporting the operator's decision-making.
The initial database derived from simulations can be continuously extended by measurements collected during real-world operation of the LARS. In this way, the underlying ML model is gradually refined and the ML algorithm can provide reliable predictions. At the same time, comparing measured system responses with the expected behaviour from the combined simulation and operational database allows deviations to be identified and used for fault detection and maintenance planning.
The same data basis can also be exploited on the AUV side. The motion patterns of the LARD, predicted from the environmental conditions and the system configuration, can be used by the AUV's guidance and control algorithms to plan an optimal approach and docking trajectory. Depending on the available computational resources, these predictions may either be calculated on board the AUV or on the host platform and then transmitted to the vehicle via an underwater communication link, such as an acoustic positioning and communication system. In both cases,

the AUV benefits from a more accurate forecast of the LARD motion and can adapt its own manoeuvres accordingly, which increases the robustness and reliability of the docking process. The underlying concept can be extended beyond the establishment of physical first contact to include the subsequent lifting operation using a crane or ramp. By incorporating environmental data and system states, the same framework can be used to determine favourable conditions and strategies for lifting, such as suitable headings in waves, the use or omission of forward speed and appropriate winch speeds.

In summary, there is substantial potential to extend the studies conducted in this work, to refine the interfaces with adjacent process steps and to further exploit the derived data and insights in both the design and operational phases of LARS. At the same time, the system design and performance analysis developed in this work provide a key foundation for enabling automated L&R of AUVs using a submerged towed docking device.

Bibliography

[1] E. Zereik, M. Bibuli, N. Mišković, P. Ridao and A. Pascoal, "Challenges and future trends in marine robotics," *Annual Reviews in Control,* vol. 46, pp. 350-368, 2018.

[2] A. F. Molland, Ed., "Chapter 10 - Underwater vehicles," in *The Maritime Engineering Reference Book*, Oxford, Butterworth-Heinemann, 2008, pp. 728-783.

[3] M. Seidel, T. Frey and J. Greinert, "Underwater UXO detection using magnetometry on hovering AUVs," *Journal of Field Robotics,* vol. 40, pp. 848-861, 2023.

[4] Y. Cong, C. Gu, T. Zhang and Y. Gao, "Underwater robot sensing technology: A survey," *Fundamental Research,* vol. 1, pp. 337-345, 2021.

[5] T. Sands, "Development of Deterministic Artificial Intelligence for Unmanned Underwater Vehicles (UUV)," *Journal of Marine Science and Engineering,* vol. 8, p. 578, July 2020.

[6] M. Jacobi, "[In German:] Fahrzeugführung für die automatisierte Unterwasser-Inspektion," Universitätsverlag Ilmenau, 2020.

[7] R. Chakrabarti, "[In German:] Abhandlungen über den Nutzen, den Aufbau und den Betrieb autonomer Unterwasserfahrzeuge," Technical University of Berlin, Berlin, 2015.

[8] Planungsamt der Bundeswehr, "[In German:] UNMANNED UNDERWATER VEHICLES - Sachstand und Perspektiven für militärische Unterwasserwirkmittel," 2017.

[9] T. Song and R. Zheng, "Autonomous Launch and Recovery System for Underwater Towed Vehicle Based on USV," in *2019 3rd International Conference on Robotics and Automation Sciences (ICRAS)*, 2019.

[10] J. Heo, J. Kim and Y. Kwon, "Technology Development of Unmanned Underwater Vehicles (UUVs)," *Journal of Computer and Communications,* vol. 05, pp. 28-35, January 2017.

[11] D. Mischnick, "[In German:] Aussetz- und Bergevorrichtung für das autonome Unterwasserfahrzeug PreToS," Technical University of Berlin, Berlin, 2013.

[12] L. W. Hanyok and T. C. Smith, "LAUNCH AND RECOVERY SYSTEM LITERATURE REVIEW," 2010.

[13] G. Griffiths, N. Bose, J. Ferguson and D. R. Blidberg, "Insurance for autonomous underwater vehicles," *As resubmitted after review Published in Underwater Technology,* vol. 27, pp. 43-48, June 2007.

[14] J. Liu, F. Yu, B. He and C. G. Soares, “A review of underwater docking and charging technology for autonomous vehicles,” *Ocean Engineering,* vol. 297, p. 117154, 2024.

[15] S. Liu, H. Xu, Y. Lin and L. Gao, “Visual Navigation for Recovering an AUV by Another AUV in Shallow Water,” *Sensors,* vol. 19, 2019.

[16] E. B. Bermudez, “Terminal homing for autonomous underwater vehicle docking,” 2016.

[17] “www.oceaneering.com,” Oceaneering International, Inc., [Online]. Available: https://www.oceaneering.com/de/rov-services/rov-systems/. [Accessed 19 06 2024].

[18] “www.saabseaeye.com,” Saab Seaeye Ltd , [Online]. Available: https://www.saabseaeye.com/solutions/underwater-vehicles/sabertooth-double-hull. [Accessed 25 06 2024].

[19] “www.kongsberg.com,” Kongsberg Discovery, [Online]. Available: https://www.kongsberg.com/discovery/autonomous-and-uncrewed-solutions/auv/hugin/. [Accessed 19 06 2024].

[20] “www.teledynemarine.com,” Teledyne Marine Technologies Incorporated, [Online]. Available: https://www.teledynemarine.com/brands/webb-research/slocum-glider. [Accessed 19 06 2024].

[21] “www.eiva.com,” EIVA a/s, [Online]. Available: https://www.eiva.com/products/equipment/hardware/rotv-solutions/scanfish-3d-steering. [Accessed 19 06 2024].

[22] “www.eiva.com,” EIVA a/s, [Online]. Available: https://www.eiva.com/products/equipment/hardware/rotv-solutions/viperfish. [Accessed 19 06 2024].

[23] C. Glenn, “Pushing subsea boundaries with hybrid AUV/ROV,” *Hydro International - Volume 27 - Issue 4 2023,* pp. 9-11, 2023.

[24] J. Osse, S. Pai, A. Maguer, M. Chitre, M. DeBoni, P. Guerrini and J. Potter, “Autonomous Launch And Recovery System (AutoLARS) for AUVs,” 2010.

[25] B. R. Page and N. Mahmoudian, “Simulation-Driven Optimization of Underwater Docking Station Design,” *IEEE Journal of Oceanic Engineering,* vol. 45, pp. 404-413, April 2020.

[26] P. Bernalte Sánchez, M. Papaelias and F. P. García Márquez, “Autonomous underwater vehicles: Instrumentation and measurements,” *IEEE Instrumentation & Measurement Magazine,* vol. 23, pp. 105-114, April 2020.

[27] “www.geomar.de,” GEOMAR Helmholtz-Zentrum für Ozeanforschung, [Online]. Available: https://www.geomar.de/tlz/auv-autonome-unterwasserfahrzeuge/auv-poseidon. [Accessed 28 06 2024].

[28] “www.atlas-elektronik.com,” ATLAS ELEKTRONIK GmbH, [Online]. Available: https://www.atlas-elektronik.com/solutions/mine-warfare-systems/seacat.html. [Accessed 25 06 2024].

[29] “www.cellula.com,” Cellula Robotics Ltd., [Online]. Available: https://www.cellula.com/solus-lite. [Accessed 25 06 2024].

[30] “www.cellula.com,” Cellula Robotics Ltd., [Online]. Available: https://www.cellula.com/solus-lr. [Accessed 25 06 2024].

[31] “www.cellula.com,” Cellula Robotics Ltd., [Online]. Available: https://www.cellula.com/solus-mr. [Accessed 25 06 2024].

[32] “www.ecagroup.com,” ECA GROUP, [Online]. Available: https://www.ecagroup.com/en/solutions/a18-d-auv-autonomous-underwater-vehicle. [Accessed 25 06 2024].

[33] “www.evologics.com,” EvoLogics GmbH, [Online]. Available: https://evologics.com/robotics. [Accessed 25 06 2024].

[34] “www.gdmissionsystems.com,” General Dynamics Mission Systems, Inc. , [Online]. Available: https://gdmissionsystems.com/products/underwater-vehicles/bluefin-9-autonomous-underwater-vehicle. [Accessed 25 06 2024].

[35] “www.gdmissionsystems.com,” General Dynamics Mission Systems, Inc. , [Online]. Available: https://gdmissionsystems.com/products/underwater-vehicles/bluefin-12-unmanned-underwater-vehicle. [Accessed 25 06 2024].

[36] “www.gdmissionsystems.com,” General Dynamics Mission Systems, Inc. , [Online]. Available: https://gdmissionsystems.com/products/underwater-vehicles/bluefin-21-autonomous-underwater-vehicle. [Accessed 25 06 2024].

[37] “www.gdmissionsystems.com,” General Dynamics Mission Systems, Inc. , [Online]. Available: https://gdmissionsystems.com/products/underwater-vehicles/bluefin-hauv. [Accessed 25 06 2024].

[38] “www.graaltech.com,” Graal Tech Srl, [Online]. Available: https://www.graaltech.com/products/x-300-auv/. [Accessed 25 06 2024].

[39] “www.graaltech.com,” Graal Tech Srl, [Online]. Available: https://www.graaltech.com/products/x-300-mcm-compact/. [Accessed 25 06 2024].

[40] “www.ise.bc.ca,” International Submarine Engineering Ltd., [Online]. Available: https://ise.bc.ca/product/explorer/. [Accessed 25 06 2024].

[41] “www.ise.bc.ca,” International Submarine Engineering Ltd., [Online]. Available: https://ise.bc.ca/product/theseus-auv/. [Accessed 25 06 2024].

[42] “www.iquarobotics.com,” IQUA Robotics, [Online]. Available: https://iquarobotics.com/girona-500-auv. [Accessed 25 06 2024].

[43] “www.iquarobotics.com,” IQUA Robotics, [Online]. Available: https://iquarobotics.com/sparus-ii-auv. [Accessed 25 06 2024].

[44] “www.kongsberg.com,” Kongsberg Discovery, [Online]. Available: https://www.kongsberg.com/discovery/autonomous-and-uncrewed-solutions/auv/hugin/#key-features. [Accessed 25 06 2024].

[45] “www.kongsberg.com,” Kongsberg Discovery, [Online]. Available: https://www.kongsberg.com/discovery/autonomous-and-uncrewed-solutions/auv/autonomous-underwater-vehicle-hugin-edge/. [Accessed 25 06 2024].

[46] “www.kongsberg.com,” Kongsberg Discovery, [Online]. Available: https://www.kongsberg.com/discovery/autonomous-and-uncrewed-solutions/auv/autonomous-underwater-vehicle-hugin-endurance/. [Accessed 25 06 2024].

[47] “www.kongsberg.com,” Kongsberg Discovery, [Online]. Available: https://www.kongsberg.com/discovery/autonomous-and-uncrewed-solutions/auv/autonomous-underwater-vehicle-hugin-superior/. [Accessed 25 06 2024].

[48] “www.naval-technology.com,” Verdict Media Limited, [Online]. Available: https://www.naval-technology.com/projects/thunderfish/?cf-view. [Accessed 25 06 2024].

[49] “www.l3harris.com,” L3Harris Technologies, Inc., [Online]. Available: https://www.l3harris.com/all-capabilities/iver3-standard-system-auv. [Accessed 25 06 2024].

[50] “www.l3harris.com,” L3Harris Technologies, Inc., [Online]. Available: https://www.l3harris.com/all-capabilities/iver4-580-auv. [Accessed 25 06 2024].

[51] “www.l3harris.com,” L3Harris Technologies, Inc., [Online]. Available: https://www.l3harris.com/all-capabilities/iver4-900-auv. [Accessed 25 06 2024].

[52] “www.lockheedmartin.com,” Lockheed Martin Corporation, [Online]. Available: https://www.lockheedmartin.com/en-us/products/marlin.html. [Accessed 25 06 2024].

[53] “www.saab.com,” Saab AB, [Online]. Available: https://www.saab.com/products/auv62-at. [Accessed 25 06 2024].

[54] “www.saab.com,” Saab AB, [Online]. Available: https://www.saab.com/products/double-eagle. [Accessed 25 06 2024].

[55] “www.saab.com,” Saab AB, [Online]. Available: https://www.saab.com/products/sabertooth. [Accessed 25 06 2024].

[56] “www.saabseaeye.com,” Saab Seaeye Ltd, [Online]. Available: https://www.saabseaeye.com/solutions/underwater-vehicles/sabertooth-single-hull. [Accessed 25 06 2024].

[57] “www.seaber.fr,” SEABER S.A.S, [Online]. Available: https://seaber.fr/yuco-ctd. [Accessed 25 06 2024].

[58] “www.seaber.fr,” SEABER S.A.S, [Online]. Available: https://seaber.fr/yuco-pam. [Accessed 25 06 2024].

[59] “www.teledynemarine.com,” Teledyne Marine Technologies Incorporated, [Online]. Available: https://www.teledynemarine.com/en-us/products/Pages/gavia-auv.aspx. [Accessed 25 06 2024].

[60] “www.teledynemarine.com,” Teledyne Marine Technologies Incorporated, [Online]. Available: https://www.teledynemarine.com/en-us/products/Pages/osprey-auv.aspx. [Accessed 25 06 2024].

[61] “www.teledynemarine.com,” Teledyne Marine Technologies Incorporated, [Online]. Available: https://www.teledynemarine.com/en-us/products/Pages/searaptor-auv.aspx. [Accessed 25 06 2024].

[62] “www.whoi.edu,” Woods Hole Oceanographic Institution, [Online]. Available: https://www.whoi.edu/what-we-do/explore/underwater-vehicles/auvs/orpheus/. [Accessed 25 06 2024].

[63] “www2.whoi.edu,” Woods Hole Oceanographic Institution, [Online]. Available: https://www2.whoi.edu/site/osl/vehicles/remus-100/. [Accessed 25 06 2024].

[64] “www2.whoi.edu,” Woods Hole Oceanographic Institution, [Online]. Available: https://www2.whoi.edu/site/osl/vehicles/remus-600/. [Accessed 25 06 2024].

[65] “www2.whoi.edu,” Woods Hole Oceanographic Institution, [Online]. Available: https://www2.whoi.edu/site/osl/vehicles/remus-3000/. [Accessed 25 06 2024].

[66] “www2.whoi.edu,” Woods Hole Oceanographic Institution, [Online]. Available: https://www2.whoi.edu/site/osl/vehicles/remus-6000/. [Accessed 25 06 2024].

[67] “ndsf.whoi.edu,” National Deep Submergence Facility, [Online]. Available: https://ndsf.whoi.edu/sentry/. [Accessed 25 06 2024].

[68] J. G. Bellingham, “Autonomous Underwater Vehicle Docking,” in *Springer Handbook of Ocean Engineering*, Dordrecht Heidelberg London New York, Springer Cham, 2016, pp. 387-406.

[69] E. I. Sarda and M. R. Dhanak, “Launch and Recovery of an Autonomous Underwater Vehicle From a Station-Keeping Unmanned Surface Vehicle,” *IEEE Journal of Oceanic Engineering,* vol. 44, pp. 290-299, April 2019.

[70] T. K. Podder, M. Sibenac and J. G. Bellingham, “Applications and challenges of AUV docking systems deployed for long-term science missions,” *Monterey Bay Aquarium Research Institute,* 2019.

[71] M. Zuo, G. Wang, Y. Xiao and G. Xiang, "A unified approach for underwater homing and docking of over-actuated AUV," *Journal of Marine Science and Engineering,* vol. 9, p. 884, 2021.

[72] M. F. Yahya and M. R. Arshad, "Robust recognition of targets for underwater docking of autonomous underwater vehicle," in *2016 IEEE/OES Autonomous Underwater Vehicles (AUV)*, 2016.

[73] M. F. Yahya and M. R. Arshad, "Tracking of Multiple Light Sources Using Computer Vision for Underwater Docking," *Procedia Computer Science,* vol. 76, pp. 192-197, 2015.

[74] S. Fan, C. Liu, B. Li, Y. Xu and W. Xu, "AUV docking based on USBL navigation and vision guidance," *Journal of Marine Science and Technology,* vol. 24, p. 673–685, 2019.

[75] G. Vallicrosa, J. Bosch, N. Palomeras, P. Ridao, M. Carreras and N. Gracias, "Autonomous homing and docking for AUVs using Range-Only Localization and Light Beacons," *IFAC-PapersOnLine,* vol. 49, pp. 54-60, 2016.

[76] S. Fan, B. Li, W. Xu and Y. Xu, "Impact of Current Disturbances on AUV Docking: Model-Based Motion Prediction and Countering Approaches," *IEEE Journal of Oceanic Engineering,* vol. 43, pp. 888-904, October 2018.

[77] A. Maguer, R. Been, A. Tesei, J. Alves, V. Grandi and S. Biagini, "Recent Technological Advances in Underwater Autonomy," 2018.

[78] H. Singh, J. Bellingham, F. Hover, S. Lemer, B. Moran, K. von der Heydt and D. Yoerger, "Docking for an autonomous ocean sampling network," *Oceanic Engineering, IEEE Journal of,* vol. 26, pp. 498-514, November 2001.

[79] M. R. Dhanak and N. I. Xiros, Springer Handbook of Ocean Engineering, Dordrecht Heidelberg London New York: Springer Cham, 2016, pp. 387-406.

[80] V. Yakimov, O. Gaidai, F. Wang and K. Wang, "Arctic naval launch and recovery operations, under ice impact interactions," *Applications in Engineering Science,* vol. 15, p. 100146, 2023.

[81] C. G. Rauch, M. J. Purcell, T. Austin and G. J. Packard, "Ship of opportunity launch and recovery system for REMUS 600 AUV's," in *OCEANS 2008*, 2008.

[82] P. E. Hagen, N. Størkersen, K. Vestgård and A. S. Kongsberg, "HUGIN MRS in the Royal Norwegian Navy," 2004.

[83] C. KENNETH, "Method and apparatus for deploying and recovering water borne vehicles". USA Patent US000005253605A, 21 12 1992.

[84] G. Meinecke, *[In German:] H-ROV-LARS: Entwicklung eines Aussetz- und Bergesystems mit integrierter, neuartiger Kommunikation und Ortung für das Hybrid-ROV (LARS), Schlussbericht.,* Bremen: MARUM – Center for Marine Environmental Sciences, 2019.

[85] O. Landstad, H. S. Halvorsen, H. Øveraas, V. Smines and T. A. Johansen, "Dynamic positioning of ROV in the wave zone during launch and recovery from a small surface vessel," *Ocean Engineering,* vol. 235, p. 109382, 2021.

[86] R. D. Hooper, J. T. Gilchrist, W. A. Chambers and T. R. Doolittle, "PORTABLE UUV LAUNCH AND RECOVERY ASSEMBLY". USA Patent US 20220258841A1, 18 02 2021.

[87] M. Pfitzner, "Ships salvaging equipment for floating objects having there own eyes". Germany Patent DE000019544656C1, 30 11 1995.

[88] "www.hhenriksen.com," H. Henriksen AS, [Online]. Available: https://hhenriksen.com/mus-launch-and-recovery-auv-capture-hook/. [Accessed 08 11 2024].

[89] D. BORGWARTH and B. BREEGGEMANN, "Launch and recovery system". USA Patent US000007350475B2, 18 09 2006.

[90] S.-C. HESSE, "AUTONOMOUS SUBMERSIBLE VEHICLE AND METHOD FOR PULLING IN SAME". Germany Patent WO002014173392A1, 30 10 2014.

[91] H. Treyde, "VEHICLE SYSTEM COMPRISING A MOTHER SHIP AND AN UNMANNED WATERCRAFT, AND METHOD FOR RECOVERING AN UNMANNED WATERCRAFT". GERMANY Patent US 020170259887 A1, 14 09 2017.

[92] C. ZHANG, H. CHENG, P. XU, W. CHENG, Y. SHEN and Y. DING, "Apparatuses and methods for recovering autonomous underwater vehicle by steering cable-based unmanned vehicle". United Kingdom Patent GB000002581091B, 19 10 2022.

[93] "www.deckmarinesystems.com," DECK Marine Systems, [Online]. Available: https://www.deckmarinesystems.com/ailarstm-artificially-intelligent-launch-and-recovery-system-for-auvs/. [Accessed 05 07 2024].

[94] S. Ritz, "DEVICE FOR ATTACHING A COUPLING DEVICE TO A FREE-FLOATING OBJECT". EU Patent EP 3 512 767 B1, 11 09 2017.

[95] M. Pfitzner, "[In German:] Vorrichtung zum Bergen eines Unterwasserfahrzeugs". GERMANY Patent DE 000010045911 B4, 07 10 2004.

[96] B. GUNNAR, "Recovery apparatus and allocated method". USA Patent US000011447209B2, 20 09 2022.

[97] S. Brizzolara and C. Chryssostomidis, "Design of an Unconventional ASV for Underwater Vehicles Recovery: Simulation of the motions for operations in rough seas," in *ASNE International Conference, Linthicum (MD)*, 2012.

[98] S. Rosie, *EVALUATION OF AN AUTONOMOUS UNDERWATER VEHICLELAUNCH AND RECOVERY SYSTEM,* 2007.

[99] M. Luccioni, V. Ciausu, V. Rigaud and L. Artzner, “INSTALLATION AND METHOD FOR RECOVERING AN UNDERWATER OR MARINE VEHICLE”. USA Patent US 2010/0018449 A1, 25 07 2007.

[100] B. Allen, T. Austin, N. Forrester, R. Goldsborough, A. Kukulya, G. Packard, M. Purcell and R. Stokey, “Autonomous Docking Demonstrations with Enhanced REMUS Technology,” 2006.

[101] J. Guo, M. Liu, X. Pan, J. Zhu, J. Liu, H. Xu, Z. Peng and J.-H. Cui, “Moored underwater docking system for resident UUVs with acoustic guidance: Design and experiment,” *Ocean Engineering,* vol. 294, p. 116802, 2024.

[102] J. Guo, R. Zheng, X. Yu, A. Wei and B. Yang, “Autonomous underwater vehicle docking system based on wired transmission,” in *2018 WRC Symposium on Advanced Robotics and Automation (WRC SARA)*, 2018.

[103] K. Sun and Z. Han, “Autonomous underwater vehicle docking system for energy and data transmission in cabled ocean observatory networks,” *Frontiers in Energy Research,* vol. 10, 2022.

[104] T. Zhang, D. Li and C. Yang, “Study on impact process of AUV underwater docking with a cone-shaped dock,” *Ocean Engineering,* vol. 130, pp. 176-187, 2017.

[105] L. Wu, Y. Li, S. Su, P. Yan and Y. Qin, “Hydrodynamic analysis of AUV underwater docking with a cone-shaped dock under ocean currents,” *Ocean Engineering,* vol. 85, pp. 110-126, 2014.

[106] L. Meng, Y. Lin, H. Gu, G. Bai and T.-C. Su, “Study on dynamic characteristics analysis of underwater dynamic docking device,” *Ocean Engineering,* vol. 180, pp. 1-9, 2019.

[107] D. J.-P. Barre, X. F. Y. Delahousse and A. H. A. Meirier, “[In German:] Vorrichtung und Verfahren zum Aussetzen und Bergen eines Unterwasserfahrzeuges”. GERMANY Patent DE000060208256T2, 01 02 2007.

[108] A. BRIGHENTI, R. GALLETTI and L. ZUGNO, “DOCKING DEVICE FOR SELF-PROPELLED AUTONOMOUS UNDERWATER VEHICLES”. Patent WO002000071415A1, 30 11 2000.

[109] Abeking & Rasmussen Schiffs- und Yachtwerft, “[In German:] Vorrichtung zum Aussetzen und Aufnehmen eines tauchfähigen Wasserfahrzeuges, Vorrichtung zum Schleppen eines tauchfähigen Wasserfahrzeuges sowie Überwasserfahrzeug mit einer solchen Vorrichtung”. Germany Patent DE000020316247U1, 07 04 2005.

[110] F. CADALEN, O. JEZEQUEL and M. JOURDAN, “DOCKING DEVICE FOR AN UNDERWATER VEHICLE”. USA Patent US020220063780A1, 03 03 2022.

[111] A. ALCOCER PENÃS, O. P. HJELMSTAD and F. SANTANA LIMA, “A MARINE STRUCTURE COMPRISING A LAUNCH AND RECOVERY SYSTEM”. Norway Patent WO002020058408A1, 26 03 2020.

[112] F. TAKAHIRO and T. KENJI, “STORAGE DEVICE AND STORAGE METHOD FOR UNDERWATER VEHICLE”. Japan Patent JP002015231779A, 24 12 2015.

[113] China Patent CN000114426088B, 09 12 2022.

[114] J. LICHT, “DEVICE AND METHOD FOR HAULING IN AN UNMANNED SUBMERSIBLE”. GERMANY Patent WO002013092216A1, 27 06 2013.

[115] W. RUGGABER, “Apparatus and Method for Deploying and Recovering an Underwater Vehicle, and Method for Docking an Underwater Vehicle to a Recovery Apparatus”. USA Patent US020080302292A1, 11 12 2008.

[116] X. DU, Z. LAN, G. PAN and B. SONG, “Autonomous underwater vehicle (AUV) launch and recovery device driven by elastic linkage mechanism for extra-large unmanned underwater vehicle (XLUUV)”. USA Patent US000011377183B2, 05 07 2022.

[117] J. Kalwa, “ECOVERY METHOD FOR THE RECOVERY OF AN SUBMARINE WATERCRAFT, RECOVERY ARRANGEMENT, SUBMARINE WITH RECOVERY ARRANGEMENT, SUBMARINE WATERCRAFT THEREFOR AND SYSTEM THEREWITH”. GERMANY Patent EP000002838788B1, 19 09 2018.

[118] S. J. JACK, “Underwater recovery vehicle”. USA Patent US000003367299A, 06 02 1968.

[119] A. LEATT, C. MACKINNON and A. WATT, “Apparatus and method for deploying, recovering, servicing, and operating an autonomous underwater vehicle”. USA Patent US000006189476B1, 20 02 2001.

[120] N. Dahn, C. Gaudig, T. Lehr, N. Pech, P. Kampmann, L. Christensen and F. Kirchner, “Autonomous Docking between a Mobile Subsea Docking Station and an AUV while in Motion,” in *OCEANS. OCEANS MTS/IEEE Conference (OCEANS-2024), September 23-26, Halifax, Kanada, Canada*, 2024.

[121] S. Ritz, J. Pleger, I. Cebulla, B. Blum-Thomas and E. Rentzow, “Concept Design for a New Approach of a Subsurface Docking Station,” in *International Conference on Drones and Unmanned Systems (DAUS' 2025)*, Granada, Spain, 2025.

[122] S. GRALL, “SYSTEM FOR DEPLOYING AND RECOVERING AN AUTONOMOUS UNDERWATER DEVICE, METHOD OF USE”. France Patent WO002019207263A1, 31 10 2019.

[123] Y. Xu, W. Shi, Y. Song and H. Hou, “Hydrodynamics of a Remora-inspired autonomous underwater vehicle approaching and docking to a benchmark submarine,” *Ocean Engineering,* vol. 291, p. 116447, 2024.

[124] J. Currie, C. B. Gillis, J. A. Carretero, R. Dubay, T. Jeans and G. D. Watt, “DYNAMICS OF TWO ACTIVE AUTONOMOUS DOCK MECHANISMS FOR AUV RECOVERY,” *Transactions of the Canadian Society for Mechanical Engineering,* vol. 38, pp. 213-226, 2014.

[125] P. W. Kimball, E. B. Clark, M. Scully, K. Richmond, C. Flesher, L. E. Lindzey, J. Harman, K. Huffstutler, J. Lawrence, S. Lelievre, J. Moor, B. Pease, V. Siegel, L. Winslow, D. D. Blankenship, P. Doran, S. Kim, B. E. Schmidt and W. C. Stone, "The ARTEMIS under-ice AUV docking system," *Journal of Field Robotics,* vol. 35, pp. 299-308, 2018.

[126] M. Wirtz, M. Hildebrandt and C. Gaudig, "Design and test of a robust docking system for hovering AUVs," 2012.

[127] N. Palomeras, T. Peñalver, M. Massot-Campos, G. Vallicrosa, P. Negre, J. J. Fernandez, P. Ridao, P. Sanz, G. Oliver and A. Palomer, "I-AUV Docking and Intervention in a Subsea Panel," 2014.

[128] "Under-actuated AUV underwater automatic recovery device based on cable capture". China Patent CN000115009473B, 07 06 2024.

[129] C. E. S. Koch and M. Bande Firvida, "Active manipulator-aided docking of underactuated autonomous underwater vehicles," in *OCEANS MTS/IEEE Conference 2024. OCEANS MTS/IEEE Conference (OCEANS-2024), September 23-26, Halifax, Canada*, 2024.

[130] E. I. Sarda, "Automated Launch and Recovery of an Autonomous Underwater Vehicle from an Unmanned Surface Vessel," 2016.

[131] U. Kuckartz and S. Rädiker, [In German:] Qualitative Inhaltsanalyse. Methoden, Praxis, Computerunterstützung, 5. Auflage, Weinheim Basel: Beltz, 2022.

[132] "www.schottel.de," Schottel, [Online]. Available: https://www.schottel.de/portfolio/referenzen/referenz-detail/fugro-venturer. [Accessed 09 07 2024].

[133] "www.thyssenkrupp-marinesystems.com," thyssenkrupp Marine Systems, [Online]. Available: https://www.thyssenkrupp-marinesystems.com/en/products-services/innovations/mum-modifiable-underwater-mothership. [Accessed 09 07 2024].

[134] T. I. Fossen, Handbook of marine craft hydrodynamics and motion control, Trondheim, Norway: Norwegian University of Science and Technology, 2021.

[135] G. Antonelli, Underwater Robots, Heidelberg: Springer, 2014.

[136] L. Paull, S. Saeedi, M. Seto and H. Li, "AUV Navigation and Localization: A Review," *EEE Journal of Oceanic Engineering,* no. 39, pp. 131-149, 2014.

[137] B. Bender and K. Gericke, Eds., [In German:] Pahl/Beitz Konstruktionslehre: Methoden und Anwendung erfolgreicher Produktentwicklung, 9 ed., Berlin, Heidelberg: Springer Vieweg Berlin, Heidelberg, 2021.

[138] Association of German Engineers, "VDI 221: Design of technical products and systems - Model of product design," Beuth Verlag, Düsseldorf, 2019.

[139] P. Naefe, [In German:] Einführung in das Methodische Konstruieren, Wiesbaden: Springer Fachmedien Wiesbaden, 2012.

[140] U. C. E. Zanke, [In German:] Hydromechanik der Gerinne und Küstengewässer, Wiesbaden: Vieweg+Teubner Verlag , 2002.

[141] A. A. Osinowo, E. C. Okogbue, E. A. Adefisan and O. A. Ogunrayi, "On the statistical characterization of sea surface conditions in the mid Atlantic," *Modeling Earth Systems and Environment,* pp. 1487-1507, 23 06 2018.

[142] O. Faltinsen, Sea Loads on Ships and Offshore Structures, Trondheim: Cambridge Ocean Technology Series, 1993.

[143] Orcina Ltd, "OrcaFlex Help," 2024. [Online]. Available: https://www.orcina.com/webhelp/OrcaFlex/Default.htm. [Accessed 17. 10. 2024].

[144] J. H. Spurk and N. Aksel, [In German:] Einführung in die Theorie der Strömungen, 1996.

[145] J. Wissink and W. Rodi, Direct numerical simulations of transitional flow in turbomachinery, 2006.

[146] P. Balakumar, "Direct numerical simulation of flows over an NACA-0012 airfoil at low and moderate Reynolds numbers," in *47th AIAA fluid dynamics*, 2017.

[147] K. Ghaib, [In German:] Einführung in die numerische Strömungsmechanik, Wiesbaden: Springer Vieweg, 2019.

[148] O. Haag, "[In German:] Studie zur Anwendung von Turbulenzmodellen in Gasturbinenbrennkammern," TU Darmstadt, Darmstadt, 2003.

[149] H. Martin, [In German:] Numerische Strömungssimulation in der Hydrodynamik: Grundlagen, Heidelberg: Springer Verlag, 2011.

[150] C. Greenshields, OpenFOAM v3 User Guide, London, UK: The OpenFOAM Foundation, 2015.

[151] D. C. Wilcox, "Formulation of the k-omega Turbulence Model Revisited," *AIAA Journal Vol. 46, No. 11,* pp. 2823-2838, 2008.

[152] J. Leitão, P. Pereira, R. Campilho and A. Pinto, "Estimation of the Raya UUV Hydrodynamic Coefficients using OpenFOAM," in *OCEANS 2024 - Halifax*, 2024.

[153] L. Hong, X. Wang, D. Zhang and H. Xu, "Numerical Study on Hydrodynamic Coefficient Estimation of an Underactuated Underwater Vehicle," *Journal of Marine Science and Engineering,* vol. 10, p. 1049, July 2022.

[154] G. Jiawei, L. Chuan, Y. Shifeng, C. Zhiyuan and C. Jibo, "Structural Design and Hydrodynamic Coefficient Calculation of Observation-class ROVs," *Journal of Engineering Research and Reports,* vol. 25, pp. 104-113, June 2023.

[155] J. Amini Foroushani and M. Sabzpooshani, “An approach for the estimation of hydrodynamic coefficients of an underwater vehicle in off-design velocities,” *Journal of Marine Science and Technology,* vol. 26, pp. 1-14, June 2020.

[156] J. Gadelho, J. M. Rodrigues, A. Lavrov and C. Guedes Soares, “Determining hydrodynamic coefficients of a cylinder with Navier-Stokes equations,” 2014, pp. 1001-1007.

[157] S. Sutulo, J. Rodrigues and C. Guedes Soares, “Computation of inertial and damping characteristics of ship sections in shallow water,” *Ocean Engineering,* no. 36, pp. 1098-1111, 2009.

[158] Y.-H. Lin and Y.-C. Chiu, “The estimation of hydrodynamic coefficients of an autonomous underwater vehicle by comparing a dynamic mesh model with a horizontal planar motion mechanism experiment,” *Ocean Engineering,* vol. 249, p. 110847, 2022.

[159] K. Vikestad, J. K. Vandiver and C. M. Larsen, “Added mass and oscillation frequency for a circular cylinder subjected to vortex induced vibration and exernal disturbance,” *ournal of Fluids and Structures,* vol. 14, pp. 1071-1088, 2000.

[160] C. Ewelina and D. Pawel, “Modelling of the viscosity effect of heave plates for floting wind turbines by hydrodynamic coefficient,” *acta mechanica et automatica,* vol. 17, 2013.

[161] O. Voldsund, “Estimation and Verification of Hydrodynamic Parameters of an ROV using CFD,” University of Bergen, 2023.

[162] “www.lsm.uni-rostock.de,” Chair of Fluid Dynamics - University of Rostock, [Online]. Available: https://www.lsm.uni-rostock.de/ressourcen/versuchsanlagen/schleppkanal-mit-hochleistungsschleppsystem-hlss/. [Accessed 21 11 2025].

[163] G. Rill, T. Schaeffer and F. Borchsenius, [In German:] Grundlagen und computergerechte Methodik der Mehrkörpersimulation, Wiesbaden: Springer Vieweg, 2023.

[164] F. Kong, Y. Guo and W. Lyu, “Dynamics Modeling and Motion Control of an New Unmanned Underwater Vehicle,” *IEEE Access,* vol. 8, pp. 30119-30126, 18. 02. 2020.

[165] A. Böge and W. Böge, [In German:] Technische Mechanik, Wiesbaden: Springer Vieweg Wiesbaden, 2024.

[166] K. J. Rawson and E. C. Tupper, Basic Ship Theory, Oxford: Butterworth-Heinemann, 2001.

[167] A. Armudi, W. C. Marques and P. Oleinik, “ANALYSIS OF SHIP BEHAVIOR UNDER INFLUENCE OF WAVES AND CURRENTS,” *Revista de Engenharia Térmica,* no. 16, p. 18, 10. 2018.

[168] C. Brennen, “A Review of Added Mass and Fluid Inertial Forces,” 1982.

[169] Orcina Ltd, "OrcaWave Help," 2024. [Online]. Available: https://www.orcina.com/webhelp/OrcaWave/. [Accessed 06. 01. 2025].

[170] C. Rapp, "[In German:] Einführung in die Potentialtheorie," in *Hydraulik für Ingenieure und Naturwissenschaftler: Ein Kurs mit Experimenten und Open-Source Codes*, Wiesbaden, Springer Fachmedien Wiesbaden, 2017, pp. 37-43.

[171] G. Clauss, E. Lehmann and C. Östergaard, Offshore Structures, London: Springer London, 1992.

[172] V. Bertram, Practical Ship Hydrodynamics, Oxford: Butterworth-Heinemann, 2000.

[173] J. H. A. M. Vervoort, "Modeling and Control of an Unmanned Underwater Vehicle," University of Canterbury, Christrchurch, New Zealand, 2008.

[174] M. Hall and A. Goupee, "Validation of a lumped-mass mooring line model with DeepCwind semisubmersible model test data," *Ocean Engineering,* vol. 104, pp. 590-603, 2015.

[175] S. Vöth, "[In German:] Systemparameter," in *Dynamik schwingungsfähiger Systeme*, Wiesbaden, Vieweg, 2006, pp. 14-27.

[176] D. H. Hops, A. Ott, C. Rühle and M. Sackmann, "[In German:] Vorrichtung zur Aufnahme eines unbemannten Unterwasserfahrzeugs". Germany Patent DE 10 2023 126 292 A1, 27 03 2025.

[177] D. H. HOPS, A. OTT, C. RÜHLE and M. SACKMANN, "DEVICE FOR RECEIVING AN UNMANNED UNDERWATER VEHICLE". Patent WO002025067969A1, 03 04 2025.

[178] Federal Maritime and Hydrographic Agency, "www.bsh.de," [Online]. Available: https://www.bsh.de/DE/THEMEN/Beobachtungssysteme/Messnetz-MARNET/Seegang/seegang_node.html. [Accessed 12 12 2024].

[179] K. Roos, "[In German:] Konstruktion einer Vorrichtung zum Aussetzen und Bergen eines autonomen Unterwasserfahrzeuges," Jade Hochschule, Wilhelmshaven, 2024.

[180] J.-M. Preibisch, "[In German:] Konzeptentwicklung eines Spann- und Haltesystems für einen klappbaren LARS-Prototypen zur Sicherung eines AUVs unter Wasser," Hochschule Emden/Leer, Emden, 2024.

[181] H. Wittel, D. Muhs, D. Jannasch and J. Voßiek, [In German:] Roloff/Matek Maschinenelemente, Wiesbaden: Vieweg+Teubner Verlag - Springer Fachmedien, 2009.

[182] C. R. Teeneti, T. T. Truscott, D. N. Beal and Z. Pantic, "Review of Wireless Charging Systems for Autonomous Underwater Vehicles," *IEEE Journal of Oceanic Engineering,* vol. 46, pp. 68-87, 2021.

[183] F. Rémouit, P. Ruiz-Minguela and J. Engström, “Review of Electrical Connectors for Underwater Applications,” *IEEE Journal of Oceanic Engineering,* 2017.

[184] R. Kories and H. Schmidt-Walter, [In German:] Taschenbuch der Elektrotechnik, Haan: Europa-Lehrmittel, 2022.

[185] W. Song and W. Cui, “An Overview of Underwater Connectors,” *Journal of Marine Science and Engineering,* vol. 9, p. 813ff, 2021.

[186] W. Song, C. Yang, W. Cui, Y. Lei, J. Hong, Z. Wang and Z. Hu, “Study of pressure-balanced oil-filled (PBOF) technology,” *Ocean Engineering,* no. 260, 2022.

[187] M. Kadivar, D. Tormey and G. McGranaghan, “A review on turbulent flow over rough surfaces: Fundamentals and theories,” *International Journal of Thermofluids,* no. 10, 2021.

[188] G. Zhang, M. Zhu, H. Liu, X. Qiang and J. Teng, “The impact of variable fillets on corner separation in a liner compressor cascade,” *Journal of the Global Power and Propulsion Society,* 2024.

[189] T. Yoshida1 and T. Watanabe, “Numerical Simulation of Flow over an Open Cavity with Self-Sustained Oscillation Mode Switching,” *Open Journal of Fluid Dynamics,* no. 6, pp. 361-370, 2016.

[190] K. Maki, F. Zhao, P. Horn, J. Banks, J. Martio, B. Starke, Z. S, D. Villa, M. Vitola, H. S. Yoon., Y. Jiang and S. Shingo, “Practical Guidelines for Ship CFD Applications,” ITTC - International Towing Tank Conference, Switzerland, 2024.

[191] R. J. Shyne, “Experimental Study of Boundary Layer Behavior in a Simulated Low Pressure Turbine,” NASA - National Aeronautics and Space Administration, Cleveland, 1998.

[192] S. F. Hoerner, Fluid-Dynamic Drag, Großbritannien, 1965.

[193] S. B. Gibson, B. McCarter, D. J. Stilwell and a. W. L. Neu, “A comparison of hydrodynamic damping models using least-squares and adaptive identifier methods for autonomous underwater vehicles,” *OCEANS 2015,* pp. 1-7, 2015.

[194] ITTC (International Towing Tank Conference), “Recommended Procedures 7.5-02-02-02: Resistance Test Uncertainty Analysis,” ITTC - International Towing Tank Conference, 2017.

[195] E. Javanmard and S. Mansoorzadeh, “A Computational Fluid Dynamics Investigation on the Drag Coefficient Measurement of an AUV in a Towing Tank,” *Journal of Applied Fluid Mechanics,* vol. 12, no. 3, pp. 947-959, 2019.

[196] T. Sarpkaya, “Chapter 2: Review of the fundamental equations and concepts,” in *Wave Forces on Offshore Structures*, 2010.

[197] Y. Goda, “Design wave height selection in intermediate-depth waters,” *Coastal Engineering,* no. 66, 2012.

[198] Deutsches Institut für Normung e. V., *[In German:] DIN EN 13414-1: Drahtseile für Anschlagmittel – Sicherheit – Teil 1: Anschlagseile aus Stahldrahtseilen.,* Berlin: Beuth-Verlag, 2020.

[199] American Petroleum Institute, *Offshore Pedestal-mounted Cranes.,* Washington D.C.: API Publishing Services, 2012.

[200] I. Helmond, “Towed Vehicles,” *Encyclopedia of Ocean Sciences (Second Edition),* pp. 65-74, 2001.

[201] S. Fackrell, *Study of the Added Mass of Cylinders and Spheres,* Windsor: University of Windsor, 2011.

[202] G. Bruschi, T. Nishioka, K. Tsang and R. Wang, *A Compraison of Analytical Methods. Drag Coefficient of A Cylinder,* San Diego: University of California, 2003.

[203] L. Breiman, “Random Forests,” *Machine Learning,* no. 45, pp. 5-32, 2001.

[204] K. P. Murphy, “Machine learning - a probabilistic perspective,” *Adaptive computation and machine learning series,* 2012.

[205] T. Wang, R. Skulstad, F. T. Holmeset, K. H. Halse, H. P. Hildre and H. Zhang, “ull-scale experimental research on wave shielding effect of RV Gunnerus for offshore operations,” *Ocean Engineering,* no. 320, 2025.

[206] M. Szczotka, “AUV launch & recovery handling simulation on a rough sea,” *Ocean Engineering,* vol. 246, p. 110509, 2022.

This dissertation additionally incorporates information from patents filed by the author and academic theses supervised by the author, which were not publicly available at the time of its submission.

Statement on the use of AI-assisted writing tools

Language-related tasks, including spelling and grammar correction as well as stylistic refinement and paraphrasing of draft text, were supported by the following AI-powered applications:

- QuillBot (https://quillbot.com)
- ChatGPT (https://chatgpt.com)
- DeepL - Translate & Write (https://www.deepl.com)

The use of these tools was strictly limited to language editing. The intellectual content of this dissertation including the problem formulation, development of research ideas, methodological choices, numerical and experimental work, data analysis, derivation of results and scientific conclusions is solely attributable to the author.